

NORTHWESTERN UNIVERSITY

Design and Installation of Sorptive Sites in Metal-Organic Framework Adsorbents.

A DISSERTATION

SUBMITTED TO THE GRADUATE SCHOOL IN PARTIAL FULFILLMENT OF THE  
REQUIREMENTS

for the degree

DOCTOR OF PHILOSOPHY

Field of Chemistry

By

Cornelius Okatahi Audu

EVANSTON ILLINOIS

March 2019

© Copyright by Cornelius O. Audu 2018

All Rights Reserved

## ABSTRACT

### Design and Installation of Sorptive Sites in Metal-Organic Framework Adsorbents.

Cornelius Okatahi Audu

In the design of efficient adsorbents for the sequestration of toxic molecules and the separation of volatile organic compounds, two important criteria are: high porosity and high density of sorptive sites. The work in this thesis showcases how metal-organic frameworks (MOFs) can be used as porous adsorbent templates where many types of sorptive interactions can be incorporated at high densities. These features can be incorporated by: (1) coordination to the metal-nodes, (2) complexation at the organic linkers, and (3) van der Waals (vdW) interactions within the MOF pores. With the bottom-up construction of MOFs, a wide range of building blocks can be used to engender a single framework to not only exhibit high uptake kinetics and capacity, but also chemoselectively target multiple analytes that require a diverse set of sorptive interactions.

The first chapter of this thesis introduces the concept of using MOFs as a template to design efficient adsorbents with high porosities and sorptive-site density. Chapter two describes the successful utilization of a metal node and organic linker in a zirconium-based MOF framework (specifically UiO-66) to chemoselectively capture arsenic species ( $\text{As}^{\text{III}}$  and  $\text{As}^{\text{V}}$ ) from water. This work, however, also revealed that analyte diffusion to all sorptive sites in MOFs can be hindered by small pore apertures. To improve diffusion kinetics, the pores can be enlarged by elongating the organic linkers and/or forming missing-node defects. Chapter three discloses in more detail how the latter strategy also affects the overall pore structure and stability of the UiO-66 framework

using a combination of experimental and computational studies. The fourth chapter then focuses on the utilization of the pore environment in another model MOF (ZIF-8) for the separation of linear alkanes. Here, the diffusivities for these hydrocarbons ( $C_{5-16}$ ) through ZIF-8 thin films were correlated to the level of strong vdW interactions between the aliphatic pores and the incoming analyte. The final chapter summarizes the major findings disclosed in this thesis and suggests new directions in the design of efficient adsorbents.



## ACKNOWLEDGEMENTS

I want to thank my graduate advisors, Profs. Joseph T. Hupp and SonBinh T. Nguyen for their constant mentorship, support, and encouragement throughout my graduate career. I am also thankful to have the advice and guidance of Prof. Omar Farha, who is like my third advisor. He has taught me to see every challenge as an opportunity to improve myself. In addition, I would like to extend my gratitude to my committee members, Profs. Randall Snurr, Fraser Stoddart, and Franz Geiger (Chair for my Qualifier Exam) for their invaluable insights every step along my PhD journey.

I am blessed to have the love and support of my family, especially my parents, Dr. and Mrs. Audu, during my 5 years in graduate school. Their continued support and prayers during my matriculation through the Northwestern PhD program here, have sustained me on days that I was overwhelmed with stress. I thank to the group members in the Hupp and Nguyen labs for the opportunities to collaborate on projects outside my thesis work. From these group members, I would like to highlight my friendship with Ashlee Howarth (mentor and “boating instructor”), Aaron Peters (“The extreme critic of my paper figures”), Paula Garcia (“The Instigator”), Cassandra Buru (“ClassySassyCassie”), Amanda Mahoney (“Lady Awesome”), Giang Nguyen, Rungmai Limvorapitux, and Lily Mao. I would also like to give special thanks to my studious undergraduate researcher and friend, Mengtan Liu for continuing and developing a research side-project that is dear to my heart – even to the point of manuscript submission. I would also like to thank Tim “T33gs” Hawkins and Danny “TorchRed” Cullen, two friends amongst several from the *pogo* community, who aided me with a place to stay during my transition from graduate school.

## TABLE OF CONTENTS

<b>ABSTRACT</b> .....	<b>3</b>
<b>ACKNOWLEDGEMENTS</b> .....	<b>5</b>
<b>TABLE OF CONTENTS</b> .....	<b>8</b>
<b>LIST OF TABLES</b> .....	<b>11</b>
<b>LIST OF FIGURES</b> .....	<b>13</b>
<b>LIST OF SCHEMES</b> .....	<b>27</b>
<b>Chapter 1 Introduction to sorptive interactions in metal-organic frameworks</b>	<b>28</b>
1.1 Metal-organic frameworks for adsorbent design .....	29
1.2 Sorptive interactions in MOFs .....	31
1.3 Sorbent-related challenges addressable with MOFs .....	32
1.4 Thesis overview .....	33
<b>Chapter 2 Employing sorptive interactions at the inorganic node and organic linker of Zr-based MOFs for the removal of arsenic species</b>	<b>35</b>
2.1 Introduction.....	36
2.2 Acid-modulated synthesis of UiO-66 .....	38
2.3 Chelation of As <sup>V</sup> by the inorganic Zr-containing node.....	40
2.4 Improving accessibility to node sites via linker elongation: UiO-67.....	45
2.5 Chelation of As <sup>III</sup> by the organic thiol-containing linker .....	47
2.6 The binding reversibility of As <sup>III</sup> and As <sup>V</sup> .....	50
2.7 Conclusion .....	51

2.8 Experimental Section .....	52
<b>Chapter 3 Delineating pore architectures in defect-containing UiO-66 derivatives and its significance to adsorbent design.</b>	<b>53</b>
3.1 Introduction .....	54
3.2 Preparation and experimental analyses of defect-containing UiO-66 derivatives .....	58
3.3 Construction of the computational models for defect-containing UiO-66 derivatives ..	62
3.4 Simulated N <sub>2</sub> adsorption isotherms and their use in structure elucidation of samples ..	65
3.5 Molecular modelling-assisted property-prediction .....	72
3.6 Correlation to pore-size distributions, framework stability, and crystallinity .....	76
3.7 Conclusion .....	78
<b>Chapter 4 Correlating transport diffusion of linear hydrocarbons through MOF pores to their level of van der Waals interactions with the pore environment</b>	<b>81</b>
4.1 Introduction and Overview .....	82
4.2 Synthesis and characterization of ZIF-8 thin films .....	85
4.2 Determining the intracrystalline diffusivity in thin films .....	87
4.4 Rate-limiting interface permeation?.....	90
4.5 Determining the intracrystalline diffusivity in coarser thick films .....	93
4.6 Conclusion .....	96
4.7 Experimental section.....	98
<b>Chapter 5 Epilogue</b>	<b>99</b>
5.1 Overview .....	100

5.2 Outlook.....	101
5.2.1 Towards complete structural elucidation of defect-containing MOFs.....	102
5.2.2 Towards hierarchical defect-free MOFs for As <sup>III/V</sup> capture .....	102
5.2.3 Towards the selective separation of linear hydrocarbons. ....	103
<b>Appendices</b>	<b>130</b>
Appendix A Supplementary to Chapter 2 .....	131
Appendix B Supplementary to Chapter 3.....	173
Appendix C Supplementary to Chapter 4.....	204
Appendix D Supplementary to Chapter 5 .....	224
<b>References</b>	<b>104</b>
<b>CURRICULUM VITAE.....</b>	<b>235</b>

## LIST OF TABLES

<b>Table 3.1</b>	Summary of measured properties for UiO-66 samples and simulated properties in the corresponding <i>in silico</i> models. Simulated values in parenthesis.	72
<b>Table A1</b>	Preparative data for HCl-UiO-66 <sub> x/12</sub> ( $[\text{Zr}_6\text{O}_4(\text{OH})_4(\text{L})_x]$ ) <sup>a</sup>	140
<b>Table A2</b>	Pore and surface properties of MOFs	148
<b>Table A3</b>	Adsorption rates of As <sup>V</sup> in UiO-66 <sub> x/12</sub> MOFs	162
<b>Table A4</b>	Tested desorption conditions for As <sup>V</sup> -treated HCl-UiO-66 <sub> 9/12</sub>	169
<b>Table A5</b>	Tested desorption conditions for As <sup>III</sup> -treated HCl-UiO-66(SH) <sub>2</sub>	170
<b>Table B1</b>	Sample calculation for Zr content in BzOH-UiO-66.	185
<b>Table B2</b>	Samples for the BDC:MA NMR calibration curve, as prepared from DMSO- <i>d</i> <sub>6</sub> stock solutions of BDC (12 mM) and MA (12 mM).	187
<b>Table B4</b>	Linker-node (L/N) ratio as determined from data obtained from NMR and ICP-OES in comparison to the TGA-based values (defect-free = 6)	190
<b>Table B5</b>	Lennard-Jones (LJ) parameters for the framework atoms	194

## LIST OF FIGURES

- Figure 1.1** A 3D representation of a MOF highlighting where potential sorptive sites can be introduced into the framework. 29
- Figure 1.2** A schematic showing the advantages of a porous adsorbent. Not only are all potential sorptive sites accessible, but the quantity of these sites can be directly correlated to the total sorbates observed. 31
- Figure 2.1** A schematic representation that suggests how MOFs can be tailored to coordinate anionic  $\text{As}^{\text{V}}$  moieties at the node while binding neutral  $\text{As}^{\text{III}}$  with the linkers. 37
- Figure 2.2** Representative views (see Appendix A, Figure A.19 for other possible binding motifs) of a unit cell of UiO-66, with either 12-coordinated ideal nodes  $[\text{Zr}_6\text{O}_4(\text{OH})_4(-\text{CO}_2)_{12}]$  or imperfect nodes  $[\text{Zr}_6\text{O}_4(\text{OH})_x(-\text{CO}_2)_y]$ , which result from missing linkers. Each purple “bond” indicates a coordinating carboxylate from the terephthalate linker. 39
- Figure 2.3**  $\text{As}^{\text{V}}$ -uptake profiles for MOF samples (10 mg) that have been exposed to  $\text{As}^{\text{V}}$ -containing solutions (30 mL; 50 ppm initial concentration). The total amounts of bound  $\text{As}^{\text{V}}$  per node is indicated on the right. Each data point is an average of 3-4 different experiments. 41
- Figure 2.4** The  $\text{As}^{\text{V}}$ -adsorption isotherms for AcOH-UiO-66<sub>|11/12</sub> (a) and HCl-UiO-66<sub>|9/12</sub> (b) at short (0.5 h) and long (24 h) exposure time, plotted as bar graphs with the  $\text{As}^{\text{V}}:\text{Zr}_6$  ratios indicated at the top of each bar. Experimental conditions: batch exposure of a sample of MOF (10 mg) to the appropriate  $\text{As}^{\text{V}}$ -containing solution (30 mL). 42
- Figure 2.5** DRIFTS spectra of HCl-UiO-66<sub>|9/12</sub> sample before and after  $\text{As}^{\text{V}}$  treatment, showing the presence of  $-\text{As}-\text{O}-\text{H}$  bonds after exposure. Spectra for powder  $\text{Na}_2\text{HAsO}_4 \cdot 7\text{H}_2\text{O}$  are included as reference. Data for AcOH-UiO-66<sub>|11/12</sub> can be found in the Appendix A, Figure A14. 46
- Figure 2.6** (a)  $\text{As}^{\text{III}}$ -uptake profiles by thiolated UiO-66 samples and non-functionalized analogues confirming the important role of the soft thiol ligands in capturing  $\text{As}^{\text{III}}$ . While the AcOH-UiO-66<sub>|11/12</sub> and HCl-UiO-66<sub>|9/12</sub> controls show some initial uptake of  $\text{As}^{\text{III}}$ , this appears to be semi-reversible, not unexpectedly if we consider the weaker binding nature of the soft  $\text{As}^{\text{III}}$  ion to the hard missing-linker sites of the nodes, especially under slightly acidic conditions. (b-c) In

sequential exposures to As<sup>V</sup> (b) and As<sup>III</sup> (c), HCl-UiO-66(SH)<sub>2</sub> shows good uptakes for both As<sup>V</sup> and As<sup>III</sup> compared to HCl-UiO-66<sub>[9/12]</sub>, which only binds As<sup>V</sup>. See Figure A9 for data concerning the reverse exposure order. Experimental conditions: batch exposure of a sample of MOF (10 mg) to the appropriate As-containing solution (30 mL; 50 ppm initial concentration).

49

**Figure 3.1** An illustration of how modifications of the pore architecture can affect the pore-filling process in a gas-adsorption experiment and introduce discernable changes in the adsorption isotherm. For pore architecture A, the first and second isotherm steps reflect monolayer formation (dark blue spheres) and pore filling (red spheres). For pore architecture B, a third and fourth steps are introduced due to the monolayer formation (light blue spheres) and pore filling (yellow spheres) occurring in the newly introduced larger pore. While the spheres are color-coded to correlate with the different steps in the adsorption process, they represent molecules of the same type (e.g., N<sub>2</sub>).

57

**Figure 3.2** A schematic of the UiO-66 unit cells comprising perfect UiO-66 regions (UiO-66-*fcu*),<sup>62,71</sup> “missing-linker” regions (UiO-66-*ml*),<sup>60,81</sup> and “missing-cluster” regions (UiO-66-*reo*).<sup>81,108</sup>

60

**Figure 3.3** Experimentally obtained N<sub>2</sub> isotherms for AcOH-UiO-66<sub>[5.2/6]</sub>, HCl-UiO-66<sub>[4.2/6]</sub>, and BzOH-UiO-66<sub>[4.0/6]</sub> plotted on a normal scale (a) and a semi-log scale (b) of just the adsorption-branch data. The N<sub>2</sub>-adsorption isotherm for the defect-free UiO-66 model was generated using grand canonical Monte Carlo simulations with the open source code RASPA.<sup>142,143</sup>

61

**Figure 3.4** The ideal UiO-66 supercell (a) and a set of seven *in silico* structural models for AcOH-UiO-66 with different defective regions based on either missing linker or missing cluster defects (b-h). Models b and f were constructed by removing linkers from the ideal UiO-66 supercell, but not nodes. The locations of removed linkers that are noticeable in this 2D view are circled. Models c, d, e, g, and h were constructed by removing nodes and the associated linkers (i.e., generating missing-cluster defects). In the *AcOH-UiO-66*<sub>(*l*/*n*)</sub> notation, *l* indicates the total number of linkers and *n* indicates the total number of nodes in the supercell. Models a and g correspond to UiO-66-*fcu* and UiO-66-*reo*, respectively. Models g and h have similar missing-cluster defects but *AcOH-UiO-66*<sub>(96/24)*c*</sub> possess defect regions that coalesced together.

64

**Figure 3.5** Simulated N<sub>2</sub>-adsorption isotherms along with “step-related” simulation snapshots for *UiO-66*<sub>(192/32)</sub> and *AcOH-UiO-66*<sub>(168/30)</sub>. (a) For the defect-free *UiO-66*<sub>(192/32)</sub>, the steps correspond to filling of the tetrahedral pores by N<sub>2</sub> molecules (purple objects in the snapshots), followed by filling of the

octahedral pores. (b) For  $AcOH-UiO-66_{(168/30)}$ , which represents a UiO-66 sample that has a low density of missing clusters (2 out of 32), the steps correspond to filling of the tetrahedral pores, filling of the octahedral pores, formation of a  $N_2$  monolayer around the cavities created by missing-cluster defects, and filling of these cavities, successively

66

**Figure 3.6** Comparison between the simulated isotherms for models with similar L/N ratio of four. a) Comparing  $AcOH-UiO-66_{(96/24)}$  to  $AcOH-UiO-66_{(128/32)}$  shows that the most notable difference is in their respective saturation loadings. The former represents a sample with missing-cluster defects whereas the latter represents a sample with missing-linker defects. b) Comparing  $AcOH-UiO-66_{(96/24)}$  to  $AcOH-UiO-66_{(96/24)c}$  reveals that the most notable difference is in the isotherm steps. Both models exhibit missing-cluster defects, but the former corresponds to the traditional UiO-66-*reo* representation, whereas the latter corresponds to consecutive or “coalesced” missing-clusters.

67

**Figure 3.7** Comparison of experimentally obtained isotherm for  $AcOH-UiO-66|^{5.2/6}$  with simulated isotherms in  $AcOH-UiO-66_{(l/n)}$  supercell models.

68

**Figure 3.8** Best match between measured and simulated isotherms for each tested sample. The model representing each sample is shown as inset in each panel. a) Measured isotherm in  $AcOH-UiO-66|^{5.2/6}$  vs. simulated isotherm in  $AcOH-UiO-66_{(168/30)}$ . b) Measured isotherm in  $HCl-UiO-66|^{4.2/6}$  vs. simulated isotherm in  $FOH-UiO-66_{(114/25)}$ . c) Measured isotherm in  $BzOH-UiO-66|^{4.0/6}$  vs. simulated isotherm in  $BzOH-UiO-66_{(96/24)c}$

72

**Figure 3.9** Comparison between measured isotherms for each post-synthetically modified (decapped) sample of  $BzOH-UiO-66|^{4.0/6}$  ( $BzOH-UiO-66_{(96/24)c}$ ) and the simulated isotherms in the corresponding models predicted based on the expected changes in the structure due to differences in treatment. a) Measured isotherm in *de*- $BzOH-UiO-66|^{4.0/6}$  and simulated isotherm in  $FOH-UiO-66_{(96/24)c}$ . b) Measured isotherm in *de'*- $BzOH-UiO-66|^{4.0/6}$  and simulated isotherm in  $H_2O/OH-UiO-66_{(96/24)c}$  and  $HCl-UiO-66_{(96/24)c}$ . The experiment-simulation match was comparable to the one obtained for the non-treated versions (Figure 3.8), indicating our prediction to be correct, which was further verified by subsequently obtained experimental data.

75

**Figure 3.10** a) Nomenclature for schematics in panel *b*. Square size represents a unit cell size. b) Schematics summarizing the structural changes in the supercells of UiO-66 samples as a result of missing-cluster types (top panel) and pore sizes (bottom panel). c) Pore size distributions (PSDs) obtained by applying classical density functional theory (DFT) to the measured isotherms, along with PSDs obtained geometrically in the structural model representing the



sample. Note that the missing cluster region type II has a higher density of defects than the type I.

77

**Figure 4.1** A schematic showing how a QCM can be used to obtain key properties pertaining to MOF thin films (i.e., mass and thickness) and subsequent analyte diffusion studies (i.e., mass/molecule uptake and diffusivities)

84

**Figure 4.2** (a) ZIF-8 thin film fabrication via solvothermal growth with an SEM image of the surface of the Au-QCM sensor. (b) XRD patterns of the ZIF-8 thin films grown solvothermally on the Au-QCM electrodes. (c) Plot of thicknesses of solvothermally grown films (determined by QCM) as a function of number of growth cycles. (d) Cross-sectional SEM image of a QCM electrode after 8 growth cycles

86

**Figure 4.3** (a) Linear diffusion model used to evaluate the alkane uptake by flat, compact, solvothermally grown films of ZIF-8. (b) Schematic representation of intra- versus inter-crystalline through films of ZIF-8. (c) Experimental uptake (DA method) of hexane in the presence of air, hexane in the presence of cyclohexane vapor, and cyclohexane in the presence of air. (d) Measurement and fit of the hexane uptake plot to Equation C2, Appendix C.

88

**Figure 4.4** Fractional uptake versus  $t^{1/2}$  for (a) *n*-pentane through *n*-decane and (b) *n*-dodecane and *n*-hexadecane. (c) Semi-log plot of the obtained diffusivities for C<sub>5-16</sub> versus carbon chain length (please see Appendix C, Figure C11 for the corresponding *D* values and section C4 for further discussion on their reproducibility). Diffusivities for all guests were determined from application of Equation 4.3 to the plots in panels *a* and *b* in the region of initial uptake. On average, each additional carbon decreases the transport diffusivity by a factor of two. Closer examination appears to indicate an “odd-even” effect, where alkanes having even numbers of carbon atoms display transport diffusivities that are larger than one would expect based on comparisons to alkanes having odd numbers of carbons.

91

**Figure 4.5** (a) Schematic representation of electrophoretic deposition of ZIF-8 nanoparticles onto a QCM support. (b) Schematic depiction of radial diffusion model used to obtain transport diffusivities from mass versus time plots for EPD films. (c-d) SEM images of the top surfaces of ZIF-8 films prepared via EPD (c) or grown solvothermally (d). (e-f) Time course of heptane uptake by QCM-supported ZIF-8 films prepared by electrophoretic deposition (e) or by solvothermal growth (f). Note the roughly 100-fold shorter timescale for uptake by the EPD film.

95

- Figure A1** PXRD patterns of as-prepared UiO-66 analogues before and after exposure to aqueous  $\text{As}^{\text{V}}$  solutions for at least 24 h. The simulated PXRD pattern for UiO-66 is also included for comparison. As suggested by this data, the UiO-MOF samples are still crystalline after long exposures to aqueous  $\text{As}^{\text{V}}$  solution. 145
- Figure A2** PXRD patterns of as-prepared  $\text{HCl-UiO-66}|_{\text{x}/12}$  derivatives. 146
- Figure A3** (a) PXRD patterns of as-prepared  $\text{HCl-UiO-67}|_{9/12}$  before and after exposure to solutions of  $\text{As}^{\text{V}}$ . Good PXRD data can be obtained for  $\text{As}^{\text{V}}$ -exposed  $\text{HCl-UiO-67}|_{9/12}$  upon solvent exchange to acetone from water and subsequent thermal activation.<sup>58</sup> Although UiO-67 has been reported to be unstable in water or mild acid/base aqueous solutions,<sup>63</sup> this data suggest that our  $\text{HCl-UiO-67}|_{9/12}$  retains crystallinity under our testing conditions. The simulated PXRD pattern for UiO-67 is also included for comparison. (b) PXRD patterns of as-prepared functionalized UiO-66 analogues ( $\text{AcOH-UiO-66}(\text{SH})_2$ ,  $\text{HCl-UiO-66}(\text{SH})_2$  and  $\text{HCl-UiO-66}(\text{OH})_2$ ). The simulated PXRD pattern for UiO-66 is also included for comparison. 146
- Figure A4**  $\text{N}_2$  isotherms for the UiO-66 analogues used in Chapter 2. 147
- Figure A5** Relative pore size-distribution profiles for the UiO-66 analogues grown with different acid modulators. Data were collected on a Tristar II 3020 instrument, which does not allow for accurate evaluate of pore sizes  $< 8 \text{ \AA}$ . In comparison to the nearly defect-free  $\text{AcOH-UiO-66}|_{11/12}$  sample,  $\text{HCl-UiO-66}|_{\text{x}/12}$  derivatives, which have many missing-linker sites, clearly have additional larger pores (12-16  $\text{ \AA}$ ) that can increase accessibility to the internal binding sites. The appearance of these additional pores as a result of missing linker formation is in agreement with the analysis reported by Katz *et al.* for UiO-66 samples with up to four missing linkers.<sup>59</sup> We note that while the main micropore peak for  $\text{AcOH-UiO-66}|_{11/12}$  ( $\sim 10 \text{ \AA}$ ) appears to be  $\sim 1\text{-}1.5 \text{ \AA}$  greater than the reported value for UiO-66,<sup>59, 73, 233</sup> this is an artificial limitation of the instrumentation and does not affect the conclusion shown in Chapter 2. Consistent with this analysis,  $\text{HCl-UiO-67}$ , which has a larger diphenyl dicarboxylate linker than  $\text{HCl-UiO-66}$ , expectedly has a larger main pore (12  $\text{ \AA}$ ) which is consistent with the reported value (11.5  $\text{ \AA}$ ).<sup>59</sup> 147
- Figure A6a** Left panels: SEM images of  $\text{AcOH-UiO66}|_{11/12}$  and  $\text{HCl-UiO66}|_{\text{x}/12}$  MOFs. Right panels: The corresponding SEM-derived particle-size-distribution profile for the MOF samples; each profile was constructed based on measurements of  $>70$  particles. 149

**Figure A6b** Left panels: SEM images of AcOH-UiO-66-(SH)<sub>2</sub>, HCl-UiO-66-(SH)<sub>2</sub>, HCl-UiO-66-(OH)<sub>2</sub>, and HCl-UiO-67|<sub>9/12</sub> MOFs. Right panels: The corresponding SEM-derived particle-size-distribution profile for each of the MOF samples; each profile was constructed based on measurements of >70 particles.

150

**Figure A7** The calculation of number of missing linkers for MOFs with [Zr<sub>6</sub>O<sub>4</sub>(OH)<sub>4</sub>(BDC)<sub>n</sub>] compositions based on TGA profiles. (a) A representative TGA profile (green) for one AcOH-UiO-66|<sub>11/12</sub> sample and the first derivative (red-dotted line) of this profile, used to identify the point of complete linker degradation; where the only materials left is presumably ZrO<sub>2</sub>. The total mass loss due to the organic linker is calculated from the mass at 320 °C, at which point the MOF is fully activated to the dehydroxylated [Zr<sub>6</sub>O<sub>6</sub>(BDC)<sub>n</sub>] compositions,<sup>62, 145</sup> to the point of complete linker degradation. (b) A table showing theoretical % mass loss as a function of n. These % mass losses are the corrected values for the formation of ZrO<sub>2</sub> (instead of ZrO when derived directly from the [Zr<sub>6</sub>O<sub>6</sub>(BDC)<sub>n</sub>] formula (*ca.* 5.9% mass difference)). (c) Plot of the theoretical % mass vs n as best-fitted ( $R^2 = 1$ ) to a polynomial equation. With this equation, convenient estimates of the amounts of missing linkers can be qualitative obtained from experimental data with a precision of  $11.0 \pm 0.1$  linkers per node, as determined from six repetitive measurements of the same batch of AcOH-UiO-66|<sub>11/12</sub>. Attempts to corroborate this data using the weight percent of Zr in a relatively small (4.5 mg, digestion of larger samples can lead to safety hazards in our equipments) sample of activated AcOH-UiO-66|<sub>11/12</sub> gave us 32 wt % Zr which is 1 wt % off from the theoretical 33 wt % Zr for [Zr<sub>6</sub>O<sub>4</sub>(OH)<sub>4</sub>(BDC)<sub>5.5</sub>(AcO<sup>-</sup>)<sub>0.5</sub>]. While this value is in agreement with our formula unit, the error in the ICP-OES method, due to the reliance on accurate mass measurement of a very hygroscopic solid under ambient conditions and/or complete MOF digestion, prevents us from determining the accurate number of missing linkers. In contrast, the use of TGA allows us to use a much larger sample (20-30 mg) where adsorbed water and solvents can be completely removed prior to the decomposition temperature, and bypass these sources of error. As such, we estimated our amounts of missing linker present in the MOF using linker mass loss from 320-500 °C. It is important to note that the specific surface areas of these MOF samples correlate very well with the number of missing linkers (i.e., the more linkers missing in the sample, the higher the surface area) and these results are in agreement with previously reported observations.<sup>59-60, 145</sup>

154

**Figure A8** (a-c) TGA profiles of AcOH-UiO-66|<sub>11/12</sub> (a), HCl-UiO-66|<sub>x/12</sub> derivatives (b), and HCl-UiO-67|<sub>9/12</sub> (c). For the TGA profile of HCl-UiO-67|<sub>9/12</sub>, we set the linker-mass-loss point as 320 °C (dotted line) to be consistent with those for the UiO-66 samples, which were carried out under the same oxygen-enriched

atmosphere. While our TGA profile for this sample does not exhibit a clear organic-mass-loss step at  $\sim 500$  °C as reported by Katz *et al.*,<sup>59</sup> their experiments were carried out in a  $N_2$  atmosphere where complete oxidation of the organic is difficult. (d-f) TGA profiles for AcOH-UiO-66(SH)<sub>2</sub> (d), HCl-UiO-66(SH)<sub>2</sub> (e), and HCl-UiO-66(OH)<sub>2</sub> (f). As the TGA profiles of both thiolated MOFs show a gradual degradation with indistinct steps, predicting the amount of linkers present in them using TGA, as discussed in the caption of Figure A7, is difficult. As such, we relied on the ICP-OES determination of the Zr:S ratio, which does not rely on weight % measurements and should accurately reflect the node/linker ratio in each sample. For both AcOH-UiO-66(SH)<sub>2</sub> and HCl-UiO-66(SH)<sub>2</sub>, the Zr:S ratio were 1:(1.78  $\pm$  0.03), suggesting that both samples have similar number of missing-linker defects ( $\sim 10.5/12$  carboxylates per node; a non-defective sample would yield a 1:2 Zr:S ratio, corresponding to 12/12 carboxylates per node). We note in passing that this analysis results in a higher number of missing-linker defects for our AcOH-UiO-66(SH)<sub>2</sub> sample than that reported by Yee *et al.*,<sup>52</sup> for a materials synthesized at  $3 \times [Zr]$  and with a smaller amount of AcOH modulator. Yee *et al.* also estimated node/linker ratio using a combination of TGA under nitrogen flow and CHN combustion analysis, techniques that require estimates of trapped solvent or water.

155

**Figure A9** (a,b) These panels are reproductions of Figure 2.6b-c in the main text for convenience of the readers. Time-dependent arsenic-uptake profiles for HCl-UiO-66|<sub>9/12</sub> and HCl-UiO-66(SH)<sub>2</sub> samples in sequential exposure to As<sup>V</sup> first (a), then As<sup>III</sup> (b). (c,d) Time-dependent arsenic-uptake profiles for HCl-UiO-66|<sub>9/12</sub> and HCl-UiO-66(SH)<sub>2</sub> samples in the reverse exposure order (As<sup>III</sup> first (c), then As<sup>V</sup> (d)). Experimental conditions for all experiments: batch exposure of a sample of MOF (10 mg) to the appropriate As-containing solution (30 mL; 50 ppm initial concentration, pH  $\sim 7$  for As<sup>V</sup> stock solution and pH  $\sim 5$  for As<sup>III</sup> stock solution<sup>236</sup>).

156

**Figure A10** (a,b) The time-dependent uptake profiles at different concentrations for AcOH-UiO-66|<sub>11/12</sub> (a) and HCl-UiO-66|<sub>9/12</sub> (b). (c,d) As<sup>V</sup>-adsorption profiles (in mg/g) for AcOH-UiO-66|<sub>11/12</sub> (c) and HCl-UiO-66|<sub>9/12</sub> (d). The green dashed line across the y axis represents the theoretical As<sup>V</sup>-uptake capacity based on the amount of missing linkers present in the sample. (e,f) % removal of As<sup>V</sup> oxyanions from 30 mL solutions at different times and at low initial As<sup>V</sup>-exposure concentrations for AcOH-UiO-66|<sub>11/12</sub> (e) and HCl-UiO-66|<sub>9/12</sub> (f). Experimental conditions: batch exposure of a sample of MOF (10 mg) to the appropriate As<sup>V</sup>-containing solution (30 mL; 50 ppm initial concentration).

157

**Figure A11** Initial As<sup>V</sup>-uptake profiles for MOF samples that have been exposed to a 50 ppm initial concentration of As<sup>V</sup>. Given the long sampling time of the data-taking processes, only the first 3 data points could be used in the fits to get initial rate data before the pseudo-first-order assumption becomes invalid for HCl-UiO-66<sub>|9/12</sub> and HCl-UiO-67<sub>|9/12</sub> (over 25% of the As<sup>V</sup> in solution adsorbed). These data clearly show that the rates for HCl-UiO-66<sub>|9/12</sub> and HCl-UiO-67<sub>|9/12</sub> are several times faster than AcOH-UiO-66<sub>|11/12</sub>. We attribute this difference to two different effects: 1) The large particle size differences between AcOH-UiO-66<sub>|11/12</sub> and the HCl-capped MOFs: HCl-UiO-66<sub>|9/12</sub> and HCl-UiO-67<sub>|9/12</sub> have particles that are 4 times smaller in comparison to those for AcOH-UiO-66<sub>|11/12</sub>. 2) The fast diffusion into the first few layers of the MOF particles as a result of larger amounts of defects (hence larger pore sizes) in the HCl-prepared MOFs (see Figures A12-13 for further discussion).

159

**Figure A12** (a) Lagregren pseudo-first-order and (b) pseudo-second-order model fitting of the initial (within 30 mins) uptake data for samples of UiO-66 and analogues. In all cases (including the other two HCl-UiO-66<sub>|x/12</sub> derivatives, data not shown), the Lagregren pseudo-first-order model provided the best fit to this initial uptake data.

160

**Figure A13** (a,b): The As<sup>V</sup>-adsorption profiles for AcOH-UiO-66<sub>|11/12</sub> and the three HCl-UiO-66<sub>|x/12</sub> derivatives under conditions that favor the missing-linker-based uptake mechanism. HCl-UiO-66<sub>|x/12</sub> samples with similar particle sizes (Figure A6a) displayed similar initial (i.e., first 30 mins) uptake profiles (a) but diverge at longer times (b). This divergence (i.e., starting at 3 h with HCl-UiO-66<sub>|10.6/12</sub> having the lowest uptake) suggests that As<sup>V</sup>-uptake capacity increases with larger amounts of defect density. This is presumably due to the additional binding sites present and larger “average” internal spaces that facilitate As<sup>V</sup> diffusion. AcOH-UiO-66<sub>|11/12</sub>, which have particle sizes that are 4 times as large (Figure A6a), has a significantly slower initial uptake profile. These observations suggest that both the particle size and defect density can play important roles in As<sup>V</sup> uptake but their relative contributions change at different stages of the adsorption. (c,d): The best fits of the adsorption profiles to the Lagregren pseudo-first-order (30 min uptake, c) and pseudo-second-order (24 h uptake, d) models. Similarly to that in Figure A11, the initial adsorption profiles for all four MOFs samples fit best to the pseudo-first-order model (bottom left panel) supports our hypothesis that initial uptake is mainly governed by chemisorption to the binding sites on the surface of the MOF particles. This conclusion is also consistent with literature findings<sup>238-239</sup> for Fe-BTC and other porous adsorbents for As<sup>V</sup>. However, the total adsorption profiles over 24 h fit better to a pseudo-second-order model (bottom right panel), affirming the presence of a second, diffusion-limited process (i.e., binding to the accessible internal binding sites).

161

**Figure A14** (a) DRIFT spectra of MOF samples before and after As<sup>V</sup> treatment suggest successful As<sup>V</sup> encapsulation. After As<sup>V</sup> treatment (24 h of exposure to 30 mL of a solution of 50 ppm initial As<sup>V</sup> concentration), samples were washed with DI water (2 × 30 mL) and acetone (1 × 30 mL) and activated at 120 °C overnight. (c) The broad stretch at ~880 cm<sup>-1</sup>, which is attributed to As-O bonds,<sup>237, 240</sup> appears in both As<sup>V</sup>-treated MOF samples with an increased relative intensity in the HCl-UiO-66|<sub>9/12</sub> sample (top gold dotted plot). Additionally, the appearance of new peaks at the bridging hydroxide region (b, 3680-3630 cm<sup>-1</sup>) in the DRIFT spectra of the MOFs after exposure to As<sup>V</sup> suggest the presence of new As(OH) and AsO···H species that are similar to the As<sup>V</sup>-O···H···OM species reported by Myneni *et al.*,<sup>240</sup> and the PO···H···OZr species reported by Deria *et al.*<sup>19</sup>

163

**Figure A15** As3d XPS spectra of MOFs and TiO<sub>2</sub> samples that have been exposed to a solution (30 mL) of 50 ppm initial As<sup>V</sup> concentration for 24 h (i.e., at the point of highest As<sup>V</sup> uptake in our study, see Chapter 2, Figure 2.3). The XPS chemical shift for our As<sup>V</sup>-exposed Ti sample is consistent with data previously obtained for As<sup>V</sup>-TiO<sub>2</sub> surface complexation.<sup>39</sup> Together with the data for the parent MOF before exposure and Na<sub>2</sub>HAsO<sub>4</sub>·7H<sub>2</sub>O, the data for the As<sup>V</sup>-exposed MOF samples strongly support the presence of bound As<sup>V</sup>. While it is tempting to note that the binding energies of As<sup>V</sup> bound to the UiO analogues (middle and right spectra) are shifted in a manner that is consistent with the increased presence of bound As<sup>V</sup> (either Zr-O-As or As oligomers) in the MOF (by ~0.34 and ~0.53 eV for HCl-UiO-66|<sub>9/12</sub> and HCl-UiO-67|<sub>9/12</sub> respectively), these shifts are comparable to the ultimate resolution of our spectrometer (0.4 eV).

164

**Figure A16** Ti2p and Zr3d XPS spectra of the TiO<sub>2</sub> and MOFs, before and after As<sup>V</sup> exposure (24 h of exposure to 30 mL of a solution of 50 ppm initial As<sup>V</sup> concentration).

164

**Figure A17** O1s XPS spectra of the TiO<sub>2</sub> and MOFs, before and after As<sup>V</sup> exposure (24 h of exposure to 30 mL of a solution of 50 ppm initial As<sup>V</sup> concentration).

165

**Figure A18** Left panels: TEM images of AcOH-UiO-66|<sub>11/12</sub> exposed to water and AcOH-UiO-66|<sub>11/12</sub> and HCl-UiO-66|<sub>9/12</sub> exposed to As<sup>V</sup> solution (30 mL of a solution of 100 ppm initial As<sup>V</sup> concentration) for 24 h. Right panels: The corresponding EDS linescans showing the amount of arsenic present with respect to zirconium. These data correspond to the scans that are traced by the orange dashed lines in the images on the left.

165

**Figure A19** A schematic illustration showing other potential coordination motifs of As<sup>V</sup> to the nodes of UiO-66 as the exact binding mode was not investigated by

direct methods (e.g., pair distribution function). It is quite possible that some combinations of these binding modes will form rather than the energetically unfavorable displacement of the  $\mu^3$ -OH moiety.

166

**Figure A20** (a) A schematic representation<sup>52</sup> of the node of UiO-66(SH)<sub>2</sub> where the linkers are shown to have four thiols (as opposed to two) due to potential rotational disorders in the simulated crystal structure.<sup>52</sup> When the pre-oriented thiols are pointing into the same pore, the bond distances are close enough for synergistic complexation of As<sup>III</sup>. (b) A schematic illustration showing the proposed binding motif for As<sup>III</sup> in UiO-66(SH)<sub>2</sub>. Note that while it may take ~2-3 rightly oriented thiols to bind one As<sup>III</sup> in a strong, “chelated” fashion,<sup>69</sup> some of the As<sup>III</sup> may be bound more weakly through only one As-S linkage.

166

**Figure A21** (a) A schematic illustration of possible As<sup>V</sup>-binding behavior to the defective nodes in HCl-UiO-66<sub>x/12</sub> MOFs. (b) A perspective view into the first few layers of a MOF particle that is exposed to an As<sup>V</sup> solution over time. As time passes, the pore aperture becomes more constricted, slowing down the diffusion rates of As<sup>V</sup> ions into the internal binding sites.

167

**Figure A22** Qualitative investigation of the effect of pH on the desorption of As<sup>V</sup>. The plots show the amount of As desorbed, expressed as ppm concentrations in the supernatant, as a function of time in acidic, neutral, and basic solutions. (Full desorption would yield 112 ppm for As<sup>V</sup>-treated AcOH-UiO-66<sub>11/12</sub> and 135 ppm for As<sup>V</sup>-treated HCl-UiO-66<sub>9/12</sub>.) No Zr<sup>IV</sup> ions leached out at pH 7 and 12, and only trace amounts (<1%) was found in the supernatant s after 24 h at pH 2. Experimental conditions: 50 mg of each As<sup>V</sup>-treated UiO-66 sample was placed in a volume (30 mL) of un-buffered solution (pH = 2, 7, or 12), which was gently agitated using a Barnstead Thermolyne Labquake Shaker Rotisserie Model T400110 (Barnstead International, Dubuque, IA). ICP analysis was carried out on aliquots of the supernatant of the mixture after centrifuging at various time points.

168

**Figure B1** In-house (a) and synchrotron (b) PXRD patterns of as-prepared UiO-66 variants in comparison to the simulated *fcu* and *reo* PXRD patterns for UiO-66. In-house data was obtained from a STOE’s STADI-MP powder X-ray diffractometer.

180

**Figure B2** In-house PXRD patterns of as-prepared of BzOH-UiO-66 variants in comparison to the simulated *fcu* and *reo* PXRD patterns for UiO-66. In-house data was obtained from a Rigaku X-ray diffractometer.

181

- Figure B3**  $N_2$  isotherms for the BzOH-UiO-66 samples on a normal scale (a) and a semi-log plot scale (b), before and after post-synthesis decapping treatment. The hysteresis in the sample decapped in HCl/DMF (*de*-BzOH-UiO-66) is not observed in the sample decapped in HCl/*n*-butanol (*de'*-BzOH-UiO-66) in the normal scale plot. 181
- Figure B4** SEM-images for the UiO-66 variants used in Chapter 3. 182
- Figure B5** The approximation of L/N ratios in the variants of UiO-66 with  $[Zr_6O_4(OH)_4(BDC)_n]$  compositions based on TGA profiles.<sup>36</sup> (a) A representative TGA mass-loss profile (red) for the AcOH-UiO-66<sup>5.2/6</sup> sample and the corresponding first derivative (red-dotted line), plotted as functions of time (bottom x-axis) and temperature (top x-axis).<sup>242</sup> These were used to identify the point of complete linker degradation, where the only materials left is presumably  $ZrO_2$ . The total mass loss due to the organic linker is calculated from the mass at 345 °C (at which point the MOF presumably forms the dehydroxylated  $[Zr_6O_6(BDC)_n]$  compositions<sup>62, 145</sup>) to the point of complete linker degradation (600 °C). (b) A table showing theoretical % mass loss as a function of *n*. These % mass losses are the corrected values for the formation of  $ZrO_2$  (instead of  $ZrO$  when derived directly from the  $[Zr_6O_6(BDC)_n]$  formula.<sup>243</sup> (c) Plot of the theoretical % mass vs *n* as best-fitted ( $R^2 = 1$ ) to a polynomial equation. With this equation, convenient estimates of the L/N ratios (Table B4) can be qualitatively obtained from experimental data with a good precision.<sup>36</sup> These measurements corroborate well with the L/N ratios calculated using a joint NMR/ICP strategy as discussed below. 183
- Figure B6** (a-c) TGA profiles of HCl-UiO-66<sup>4.2/6</sup> (a), BzOH-UiO-66<sup>4.0/6</sup> (b), and *de*-BzOH-UiO-66<sup>4.0/6</sup> (c). For BzOH-UiO-66<sup>4.0/6</sup>, an accurate L/N ratio could not be determined given the non-distinct mass loss step from both the BzOH cap and the BDC linker. 184
- Figure B7** The  $^1H$  NMR spectrum of an HF-digested sample of *de*-BzOH-UiO-66<sup>4.0/6</sup> sample in  $DMSO-d_6$ . (Inset) A calibration curve of concentration of terephthalic acid vs the relative BDC:MA integration ratios (blue circles). The relative BDC:MA integration ratio for a digested MOF sample can then be plotted on this calibration curve (red square) to determine the concentration of BDC in solution. The small peak to the left of the BDC aromatic resonances represents a trace of formic acid that caps the defect sites. 187
- Figure B8** The  $^1H$  NMR spectra of HF-digested AcOH-UiO-66<sup>5.2/6</sup>, HCl-UiO-66<sup>4.2/6</sup>,<sup>245</sup> and BzOH-UiO-66<sup>4.0/6</sup> samples in  $DMSO-d_6$ . Inset shows the acetic acid peak with respect to the internal standard (I.S.). 188



- Figure B9** The  $^1\text{H}$  NMR spectra in  $\text{DMSO-}d_6$  of HF-digested  $de\text{-BzOH-UiO-66}^{4.0/6}$  and  $de'\text{-BzOH-UiO-66}^{4.0/6}$ , obtained after being “decapped” in  $\text{HCl/DMF}$  (top spectrum) and  $\text{HCl}/n\text{-BuOH}$  (bottom spectrum), respectively. The mole ratios of the different species in the top spectrum were obtained from NMR integration against MA internal standards. As shown, formates are no longer present in the bottom spectrum. 189
- Figure B10** Proposed capping of under-coordinated nodes in structural models according to synthesis or post-synthesis treatment. a) Proposed model for the acetate capping of UiO-66 synthesized with acetic acid modulator ( $\text{AcOH-UiO-66}$ ). b) Proposed model for the benzoate capping of UiO-66 synthesized with benzoic acid modulator ( $\text{BzOH-UiO-66}$ ). c-d) Two proposed models for the monodentate capping (i.e.,  $[\mu_1\text{-Cl} + \mu_1\text{-H}_2\text{O}]$ ) (c), formates (d) of UiO-66 synthesized in DMF with hydrochloric acid as modulator ( $\text{HCl-UiO-66}$ ) or post-synthetically treated with hydrochloric acid in DMF or *n*-butanol ( $de\text{-BzOH-UiO-66}$  and  $de'\text{-BzOH-UiO-66}$ ) 191
- Figure B11** *In silico* models for defective UiO-66 domains capped with benzoates, i.e.,  $BzOH\text{-UiO-66}_{(x/y)}$  models where  $x$  indicates the number of linkers and  $y$  indicates number of nodes in the supercell. Models a and g correspond to  $\text{UiO-66-}fcu$  and  $\text{UiO-66-}reo$ , respectively 191
- Figure B12** *In silico* models for defective UiO-66 domains capped with  $[\mu_1\text{-Cl} + \mu_1\text{-H}_2\text{O}]$  groups i.e.,  $\text{HCl-UiO-66}_{(x/y)}$  models, where  $x$  indicates the number of linkers and  $y$  indicates number of nodes in the supercell. Models a and g correspond to  $\text{UiO-66-}fcu$  and  $\text{UiO-66-}reo$ , respectively 192
- Figure B13** *In silico* models for defective UiO-66 domains capped with formate groups, i.e.,  $\text{FOH-UiO-66}_{(x/y)}$  models, where  $x$  indicates the number of linkers and  $y$  indicates number of nodes in the supercell. Models a and g correspond to  $\text{UiO-66-}fcu$  and  $\text{UiO-66-}reo$ , respectively. 193
- Figure B14** A schematic showing how the defective domains, modeled by our *in silico* structures, could be present in UiO-66 crystallites. Ordered defective domains (left) would result in additional, highly intense, and low-angle diffraction peaks as shown in the simulated PXRD pattern in Figure B1 and in literature.<sup>81, 108</sup> Disordered defective domains (right) may exhibit (if at all observed) additional and broader peaks in the low-angle regions of the experimental PXRD patterns with weak intensity.<sup>81</sup> 193

- Figure B15** TraPPE model for nitrogen molecule. This model was parameterized to reproduce vapor-liquid equilibrium curves as well as the quadrupole moment of nitrogen. 194
- Figure B16** Different simulated isotherms for the *in silico* models. Simulated isotherms within each panel correspond to the same capping. 195
- Figure B17** Clustering vs. randomly distributed missing-linker defects in *AcOH-UiO-66*<sub>(l/n)</sub>. Comparison between the simulated isotherms for models with high L/N ratios show that isotherms simulated from a model with randomly distributed missing linkers (*AcOH-UiO-66*<sub>(176/32)</sub>) matches closest to the defect-free UiO-66 (*AcOH-UiO-66*<sub>(192/32)</sub>) simulated isotherm except at the pore-filling of the tetrahedral cavities (purple box region). When compared against the isotherm simulated from a model (*AcOH-UiO-66*<sub>(176/32)c</sub>) comprising of clustering or coalescing missing linkers, the filling of the tetrahedral pore is significantly reduced suggesting the lessened amount of distinct tetrahedral cavities. 195
- Figure B18** Comparisons between the experimentally-collected isotherms and those generated from the *in silico* models where only the most reasonable candidates<sup>249</sup> from the models are shown. Comparison between measured and simulated isotherms for a) HCl-UiO-66<sup>4.2/6</sup> vs. *HCl-UiO-66*<sub>(114/25)</sub> and *FOH-UiO-66*<sub>(114/25)</sub> models respectively and for b) BzOH-UiO-66<sup>4.0/6</sup> vs. select BzOH-UiO-66<sub>(x/y)</sub> models. From these, the best fit simulated isotherm to that of the experimental (Chapter 3, Figure 3.8) can be used to justify the assignment of each UiO-66 derivative to a structural model. 196
- Figure B19** Expected (simulation) vs. measured (experiment) effects due to post-synthesis decapping. a) Measured isotherms in BzOH-UiO-66<sup>4.0/6</sup> and *de*-BzOH-66<sup>4.0/6</sup>, and simulated isotherms in *BzOH-UiO-66*<sub>(96/24)c</sub> and *FOH-UiO-66*<sub>(96/24)c</sub>. These models only differ in the capping groups (benzoate vs formate). b) Measured isotherms in BzOH-UiO-66<sup>5.2/6</sup> and *de'*-BzOH-66<sup>4.0/6</sup>, and simulated isotherms in *BzOH-UiO-66*<sub>(96/24)c</sub> and *HCl-UiO-66*<sub>(96/24)c</sub>. These models only differ in the capping groups (benzoate vs. formate). 197
- Figure B20** Simulation snapshots corresponding to steps in isotherm of *BzOH-UiO-66*<sub>(96/24)c</sub> (model for BzOH-UiO-66<sup>4.0/6</sup>). 198
- Figure B21** Simulation snapshots corresponding to steps in isotherm of *FOH-UiO-66*<sub>(96/24)c</sub> (model for *de*-BzOH-UiO-66<sup>4.0/6</sup>). 198
- Figure B22** Simulation snapshots corresponding to steps in isotherm of *FOH-UiO-66*<sub>(114/25)</sub> (model for HCl-UiO-66<sup>4.2/6</sup>). 199

**Figure B23** All pore size distributions (PSD) geometrically calculated for all structural models studied in this work (FOH-UiO-66 models produced similar PSDs to AcOH-UiO-66 models). The PSD were calculated according to the method of Gelb and Gubbins.<sup>250</sup> In this computational method, random points are selected within the pores of a materials and the largest sphere that encloses each point is determined. The resulting histogram corresponds to the PSD. 200

**Figure B24** Example of detailed BET area calculation from the isotherms of synthesized samples (here AcOH-UiO-66<sup>5.2/6</sup>) and from simulated isotherms corresponding to the *in silico* models (here AcOH-UiO-66<sub>(168/30)</sub>). Left plots are used to select a pressure range that fulfills the second BET criteria, which is indicated by the shaded region. All points within the shaded region are plotted in the right plots. Open-squared points were utilized for the BET calculation. Solid vertical line indicates the pressure corresponding to the calculated monolayer loading  $A_m$  as read from the isotherm. Dashed line indicates the value of  $(1+C)^{1/2}$  which correspond to the pressure predicted by the BET calculation to correspond to monolayer loading. a) Calculation from measured isotherm for AcOH-UiO-66<sup>5.2/6</sup> b) Calculation from simulated isotherm for the corresponding AcOH-UiO-66<sub>(168/30)</sub> model. 201

**Figure B25** (a-d) Water isotherms (left panel) and recyclability saturation-point isotherm plots (right panel) of UiO-66 variants. In a typical experiment, the MOF is activated at 120 °C under reduced pressure ( $10^{-3}$  bar) for 30 min followed by an injection of water vapor at  $P/P_0 = 0.9$  at 25 °C. The mass is allowed to equilibrate over 60 min at 25 °C then the sample is activated again to begin the next trial. 202

**Figure C1** (a) An illustrative schematic showing the solvothermal ZIF-8 thin film synthesis and growth onto the gold coated QCM sensors. (b) Arrangement of precleaned QCM sensors into a vertical slide staining rack filled with a solution containing  $Zn(NO_3)_2 \cdot 6H_2O$  and 2-MeIm. 12–24 sensors can be placed into this tray with two sensors placed back-to-back in one slot to prevent ZIF-8 growth on the back side (i.e., contact electrode). For high reproducibility, the QCM sensors should be placed in the same arrangement from batch to batch as increasing or decreasing the amount of sensors placed in the tray can lead to slight deviations in the ZIF-8 film thickness (see Figures C3 and C4 below for more discussion). 210

**Figure C2** Diffusivity measurements carried out using a custom made QCM based set-up. (a) RQCM monitor can be readily fitted to the QCM holders. (b) For the *direct-addition method*, the QCM holder can be fitted to a jar with a “sealable hole” on the opposite side of the QCM sensor. Using this hole, ~ 1 mL of analyte can be added quickly using a syringe needle, sealed by tape or with

rubber. An alternative method, (c) the *chamber-exchange method*, utilizes two jars, where a second jar containing the analyte is pre-equilibrated for at least 30 min, while the QCM holder is equilibrated in air in the other jar. After 30 minutes, the QCM holder/sensor is then exchanged to the analyte jar exposing the vapor to the sensor as depicted in (d).

211

**Figure C3** Film thickness values obtained via QCM, as described in the main text, and by cross-sectional SEM were plotted and show good agreement, thus verifying that the values obtained from QCM for subsequent experiments are representative of the true film thicknesses.

212

**Figure C4** The combined dataset (including multiple batch runs) of all thin film growth attempts of which the thickness of each film can be controlled by the number of growth cycles (Figure C1a) completed. Each growth cycle on average resulted in an increase in film thickness of *ca.* 43 nm of ZIF-8.

213

**Figure C5** ZIF-8 thin film growth (one batch) of which some films were isolated from the batch at different cycles. The high linear correlation of this plot demonstrates the high level of control that can be obtained by growing the films solvothermally.

214

**Figure C6** (a-f) Representative plots and their corresponding fits (to Equation C2, hence called full fits) of linear hydrocarbon diffusion through ZIF-8 thin films as measured with QCM using the DA method (Figure C2b). Fitting the plots to the top-down Fickian model captures the uptake profile for linear alkanes (C<sub>5-10</sub>).

216

**Figure C7** Comparison between the CE and the DA methods (Figure C2) employed for these studies. Uptake of highly volatile hydrocarbons (e.g., C<sub>5-6</sub>) are slightly faster in the CE method (a) as opposed to the DA method (b). This could be due to the quick perturbations of the pentane vapor during CE (technique limitation). Hence, we note that DA it is better suited for measuring the uptake of smaller hydrocarbons with high vapor pressure. However, in contrast, uptake kinetics of the larger hydrocarbons (e.g., C<sub>12-16</sub>) through ZIF-8 pores can be measured better using the CE method (c) as opposed to the DA method (d). This is because the DA method relies on very fast evaporation which is problematic for heavier hydrocarbons which causes the inflection in earlier time points  $0 < t \text{ (s)} < 12500$  (d). It is worthy of note that despite the better method, diffusion profiles obtained using the CE method still had poor fits to the simple Fickian model for the entire uptake profile. As such we surmised that the diffusivities for the heavier alkanes (> C<sub>10</sub>) can be estimated from the earlier stages of adsorption (see Figure C9 below).

217

- Figure C8** Plotted fits to cyclohexane uptake (using the DA method) in an ~ 300 nm film over a wider range than shown in Figure 4.3c. From the fits, apparent transport diffusivity was determined to be  $3.5 \times 10^{-17} \text{ m}^2/\text{s}$ , which we attribute to the filling of the intercrystalline void spaces, given that its large kinetic diameter would sterically hinder it from permeating through the ZIF-8 pores. 218
- Figure C9** Combined semi-log plots and table containing both the diffusivities (from full fits) with alkane kinetic time plots obtained using CE and DA method. While the values for pentane and hexane are different for both methods, there seems to be a strong correlation from heptane to decane. In all cases, the longer the alkyl chain the smaller the diffusivity which is expected as van der Waals interaction with ZIF-8 pore increases. The observed trends (i.e., decrease in  $D$ , zig-zag pattern for  $C_7$ - $C_{10}$ ) are visible in both methods indicating a possible odd-even effect as delineated in Figure 4.4c, Chapter 4. Representative standard deviations for each alkane diffusivity were determined from duplicate runs on different ~300 nm films per each method used. 218
- Figure C10** (a-b) Representative hexadecane plot analysis showing how diffusivity was estimated for the heavier alkanes ( $>C_{10}$ ) by first plotting the mass uptake vs the  $\sqrt{\text{time}}$  (a) and fitting the slope of the early stages of diffusion (green box in (a)) to Equation 4.3. 219
- Figure C11** Comparison between diffusivities obtained from full fits vs. those fitted to earlier time points on a semi-log plot and table. Differences between the regions are marginal for  $n$ -pentane to  $n$ -decane but are noticeable for  $n$ -dodecane and  $n$ -hexadecane. Values for  $D$  are shown in the adjacent table. For representative standard deviations (from duplicate runs on different ~ 300 nm films) please see the  $D$  values for  $C_6$ ,  $C_{10}$ , and  $C_{12}$  (Figure C13) or from the fits to earlier time points for  $C_{12}$  and  $C_{16}$  in the table. 219
- Figure C12** (a) A schematic of the recyclability experiment showing the diffusion and effusion measurements possible on the ZIF-8 modified-QCM sensors. For each run, the QCM sensor was exposed to the vapor chamber containing hexane and then exposed to air for the hexane to effuse out of the sensors. (b) Plots and statistical data showing reproducibility of the diffusivities obtained 220
- Figure C13** To verify the validity of the diffusivities obtained, we obtained these diffusion coefficients on films with different film thicknesses and plotted on a semi-log plot for hexane (a), decane (b), and dodecane (c). As expected, we do not see a dependence on thickness at least for cases where fits to the initial uptake stages (orange dots) were done. If transport were controlled by rate of crossing vapor/MOF interface (but analyzed as diffusivities following

Equation 4.3 in Chapter 4) then one should see an ~12 fold increase in values for  $D$ . It is worthy of note that fits to full uptake for hexane (a) and decane (b) can be used as good estimates for the true diffusivities around ~300 nm, where they overlap with the  $D$  determined from earlier time points. When fit to full uptake plots, it is apparent that the diffusivities drastically increases with film thickness.

220

**Figure C14** Assuming that only one linear hydrocarbon ( $K_d = 4.3 \text{ \AA}$ ) can pass through the small pore apertures of ZIF-8 (~ 3.4  $\text{\AA}$ ) at a time, then it is conceivable that single-line confinement<sup>158</sup> in addition to pore filling is a possible diffusion mechanism. As such, it is possible that (a) *even* hydrocarbons can stack closer inside the pores of the ZIF-8 pore under saturated vapor conditions as opposed to the *odd*-hydrocarbons which preferentially stack in one direction of the linear molecule to be closely packed. This packing phenomenon, which is known to cause a similar zig-zag trend in the boiling point trends of these  $n$ -alkanes and also in the case of charge transport across different length  $n$ -alkanethiolate based SAMs,<sup>258</sup> could account for the observed zig-zag pattern observed for heptane to decane both in perspective of the diffusivities shown on the semi-log plot (b) and the % condensed mass loadings/uptake (c) of the alkanes in the pores of the MOF.

221

**Figure C15** Diffusion of heptane through EPD film. The first step (boxed section *a*) plateaus near the expected capacities which were determined by correlating the maximum capacity per unit cell (~38  $-\text{CH}_2-$  per UC)<sup>191</sup> to the mass deposited onto the film. Data fits to this first step were then used to obtain intracrystalline diffusivities (Figure 4.5e). The remaining of the uptake profile (boxed section *b*) is a result of the condensation of heptane within the numerous interparticle spaces or voids on the EPD film.

222

**Figure D1** A schematic illustration of alkyl-anchoring MOFs (AAMOFs) in which the identity of the molecular stopper renders additional sensing (Structures 1,2,4) or catalytic (Structure 3) properties to the MOF.

224

**Figure D2** Solvothermal synthesis of ZIF-8 thin films as conducted in a scintillation vial.

228

**Figure D3** Dye substrates (Structure 1-2, Figure D1) were exposed to ZIF-8 as a suspension (a) or thin film (b) in a toluene (20 mL, 1.4 nM ZIF-8, 0.2 nM dye). After a 24 h of exposure, the samples were then analyzed by a PTI QuantaMaster 400 fluorometer (Birmingham, NJ).

228

- Figure D4** Synthesis of ZIF-8 nanoparticles where the embedded SEM image shows the particle sizes of the MOF. The embedded PXRD profile of the crystalline solids is identical to the reported profile for ZIF-8. 230
- Figure D5** PXRD scans on the prepared thin films verify the intentionally coated portion is ZIF-8. 231
- Figure D6** Fluorescence measurements reveal that after the second washing cycle of the ZIF-8 suspension, all residual “untethered” dye molecules (Structure 2, Figure D1) have been washed off. On the bottom right panel, the high fluorescence signals obtained are from the surface functionalized ZIF-8 nanoparticles – in comparison to the control scans. 231
- Figure D7** For visualization, the functionalized ZIF-8 nanoparticles fluoresces when exposed to a 365 UV lamp albeit the distinction is not great (dye emission wavelength = 415 nm). 232
- Figure D8** Fluorescence measurements on the half-coated glass strips (representative trial) showed that the ZIF-8 portion retained the dye molecules more efficiently than the glass surface. 232
- Figure D9** Fluorescence scans on the dye treated thin films. When the long alkyl chain is present (a), we are able to see high retention on the ZIF-8 surface. When the alkyl chain is much shorter (b), very low retention onto the ZIF-8 surface is observed. This shows that the adhesion to the ZIF-8 surfaces is most likely due to the vdW interactions between the alkyl tail (a) and the pores of ZIF-8. 233
- Figure D10** ZIF-8 nanoparticles were exposed to the BODIPY substrates (Structure 3, Figure D1) and evaluated for catalytic activity. Preliminary work shows that the MOF system is catalytically active towards the photooxidative degradation of a chemical warfare agent (CWA) simulant. However, more controls and leaching experiments will have to be completed before any other conclusions can be made. 234

## **Chapter 1**

### **Introduction to sorptive interactions in metal-organic frameworks**



## 1.1 Metal-organic frameworks for adsorbent design

Designing efficient adsorbents for molecular storage, extraction, and separation has led to research interests focused on the high incorporation of accessible sorptive sites into template materials. One of these templates, metal-organic frameworks (MOF),<sup>1-3</sup> a recent class of materials, have gained increasing attention as their structural diversity can facilitate the establishment of design principles for the next generation of adsorbents. MOFs are comprised of inorganic nodes connected by organic linkers, resulting in a porous framework that can be endowed with various kinds of sorbate-sorbent interactions at the node, linker, and in the pores (Figure 1.1).

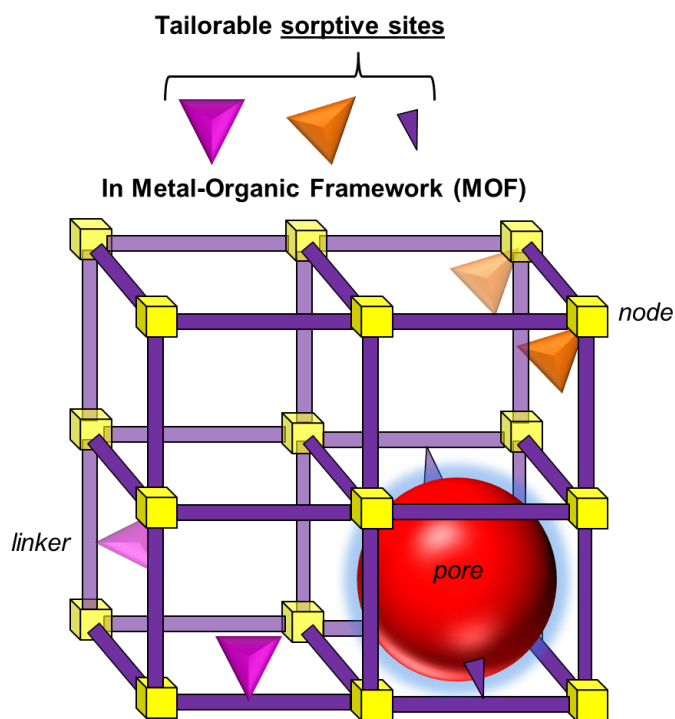


**Figure 1.1** A 3D representation of a MOF highlighting where potential sorptive sites can be introduced into the framework.

Advantages MOFs have over other templates (e.g., metal-oxides,<sup>4</sup> amorphous carbon,<sup>5-6</sup> silica,<sup>7-8</sup>) primarily involve their well-defined structure and its facile tunability to give materials with high crystallinity, excellent porosity, and high thermal and chemical stability. With these tailorable features, delineating optimal sorbent-design principles can be readily achieved. For instance, the well-defined nature of MOFs can aid in the identification of favorable sorbate-sorbent binding motifs. Proposed binding motifs can be easily verified based on the molar ratio of sorptive sites to sorbates assuming that all sorptive sites are accessible in these highly porous materials (as opposed to non-porous materials where the sorptive sites are restricted to the external surfaces, Figure 1.2). The strength of these binding motifs can then be tested in over a broad range of conditions (e.g., heat, acidic, or basic) given the specific MOF used is stable to such conditions. With the large number of MOFs currently known,<sup>9-10</sup> selecting a specific MOF that embodies the aforementioned features can be as simple as choosing one with different inorganic nodes or organic linkers.

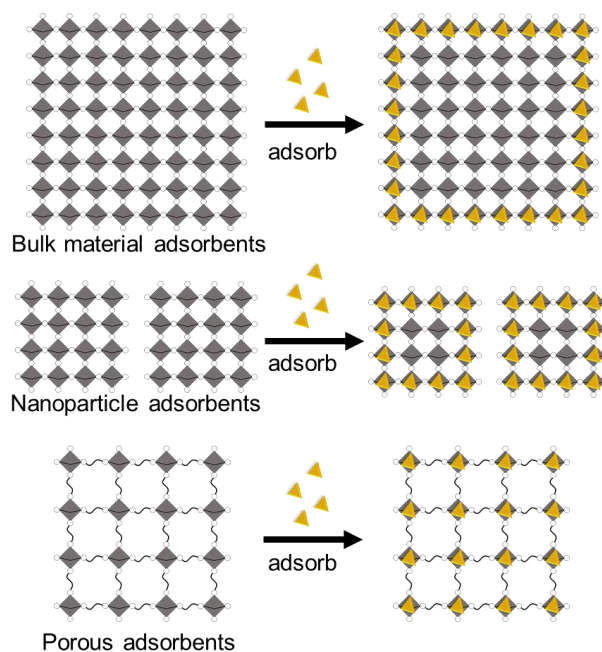


**Figure 1.2** A schematic showing the advantages of a porous adsorbent. Not only are all potential sorptive sites accessible, but the quantity of these sites can be directly correlated to the total sorbates observed.

## 1.2 Sorptive interactions in MOFs

At the start of this thesis work, MOF-based adsorbents were prepared in a way that utilized either the nodes, linkers, or pores to introduce sorptive sites in a framework. At the inorganic nodes, which are typically multivalent metal ions or metal-oxide clusters, sorptive sites can be introduced by modifying the node<sup>11</sup> to engender open-metal (i.e., coordinatively undersaturated) sites,<sup>12-14</sup> metal-hydroxylated/hydrated sites,<sup>15-16</sup> and sites with chelated metal-ions<sup>17</sup> or organic ligands.<sup>18-19</sup> Key examples of node sorptive sites can be seen in the installation of open-metal sites<sup>20</sup> in HKUST-1 and hydroxylated nodes<sup>16</sup> in NU-1000. While the former utilizes the electron-deficient sites to capture electron-rich guest molecules (e.g., O<sub>2</sub>, H<sub>2</sub>, alkenes, etc), the latter takes advantage of the coordinative ability of the hydroxylated node to bind cations and anions alike.<sup>21</sup>

On the other hand, the organic linkers, typically comprised of di-, tri-, or tetrapotic ligands (e.g., carboxylates, imidazolates, phosphonates, pyridyls, etc.),<sup>22-24</sup> can be further chemically functionalized to introduce additional sorptive sites. This functionalization can be done by modifying the linker using organic chemistry and subsequent incorporating it into a MOF via *de novo* crystal growth or by post-synthesis methods (i.e., post-synthesis linker modification,<sup>18, 25-26</sup> solvent-assisted linker exchange<sup>27-28</sup>). This approach proved useful for the development of amine- or amide-containing MOF-based sorbents to remove acidic CO<sub>2</sub> at low pressures.<sup>29-33</sup> Similarly, organic linkers containing phosphates, sulfur, and other chelating groups have been incorporated into water-stable MOFs to remove toxic aqueous moieties (e.g., heavy metals,<sup>34</sup> oxyanions,<sup>21, 35-36</sup>). In fact, via this functionalization route, it is possible to incorporate chemically diverse sites into a single framework, as demonstrated by Yaghi and coworkers, who prepared multivariate MOFs<sup>37</sup> (i.e., the incorporation of multiple linker functionalities in one crystallite of MOF) with the ability to chelate different targets.

### 1.3 Sorbent-related challenges addressable with MOFs

The molecular-level engineering of the node, linker, and pores of MOFs to introduce a wide variety of sorptive sites has given researchers the ability to target challenging issues pertaining sorbents. In particular, this thesis showcases how MOFs can be used for the removal of multispeciatic arsenic oxyanions present in water streams—an arduous task given the high water solubility of these species. Inorganic arsenic species (i.e., arsenite (As<sup>III</sup>) and arsenate (As<sup>V</sup>)) have different binding affinities to known adsorbents<sup>38-39</sup> <sup>40</sup> with preferential uptake for the least toxic species, As<sup>V</sup>.<sup>41-42</sup> One way to address this is to design a single framework with the capability to

remove both species in an orthogonal manner. Such a strategy, if successful, could prove viable in the design of other adsorbents for sensing<sup>20, 43-44</sup> or separating<sup>45-46</sup> structurally similar molecules.

This thesis also addresses a MOF sorbent-related challenge in measuring and quantifying the varying levels of host-guest (HG) interactions between the pore environment and structurally-similar volatile organic compounds like linear alkanes. As alluded to earlier, the use of MOFs for these studies is partially hindered by the inability to simply measure and quantify the level of HG interactions for each different analyte. Overcoming this challenge would then facilitate the design of MOF-based sorbents for the effective separation of linear alkanes. To this end, this thesis shows how the rate of diffusion of these alkanes through MOF thin films can be accurately measured, and correlated to their HG interactions. These results suggest that the pore environment of the MOF can be eventually tuned to facilitate separations of these structurally similar gases.

#### **1.4 Thesis overview**

The work described in this thesis shows how MOFs can be tailored at the node, linker, and pore to become model adsorbents. Chapter 2 focuses on UiO-66 as a model MOF template for capturing two different arsenic species from water: the Zr-OH containing node of UiO-66 can be tuned to selectively capture  $\text{As}^{\text{V}}$  species while its thiol-functionalized linker can be used to capture  $\text{As}^{\text{III}}$  species. This work, however, also revealed that analyte diffusion to all sorptive sites in MOFs can be hindered by small pore apertures. To improve diffusion kinetics, the pores can be enlarged by elongating the organic linkers and/or forming missing-node defects. Chapter 3 discloses in more detail how the latter strategy also affects the overall pore structure and stability of the UiO-66 framework using a combination of experimental and computational studies. Chapter 4 then

focuses on the utilization of the pore environment in another model MOF (ZIF-8) for the separation of linear alkanes. Here, the diffusivities for these hydrocarbons (C<sub>5-16</sub>) through ZIF-8 thin films were correlated to the level of strong vdW interactions between the aliphatic pores and the incoming analyte. The final chapter summarizes the major findings disclosed in this thesis and suggests new directions in the design of efficient adsorbents.

*To raise new questions, new possibilities, to regard old problems from a new angle requires creative imagination and marks real advances in science.*

Albert Einstein.

## Chapter 2

### Employing sorptive interactions at the inorganic node and organic linker of Zr-based MOFs for the removal of arsenic species

Portions of this chapter appear in the following manuscript:

Audu, C. O.; Nguyen, H. G. T.; Chang, C.; Katz, M. J.; Mao, L.; Farha, O. K.; Hupp, J. T.; Nguyen, S. T. “The dual capture of As<sup>V</sup> and As<sup>III</sup> by UiO-66 and analogues” *Chem. Sci.* **2016**, *7*, 6492-6498.

## 2.1 Introduction

Taking advantage of the facile structural tunability of MOFs,<sup>18, 23, 27, 47-48</sup> we first envisioned engineering a single framework with sorptive sites at the inorganic node and organic linker. Individually, these structural components have garnered increasing interest in capture-and-release studies including examples where the inorganic (i.e., metal-cluster) nodes were tailored to capture/release phosphate-based substrates<sup>49-50</sup> or the organic linkers were used to sequester heavy metals.<sup>51-53</sup> However, at the time of this study, introducing both types of sorptive sites into a single framework, one route to improving the efficiency of MOF adsorbents, had not been demonstrated. Thus, we envisioned that a MOF could be designed to remove toxic multispeciated moieties via selective chelation to the node and linkers. To demonstrate this hypothesis, we targeted toxic anionic arsenates ( $\text{As}^{\text{V}}$ ) and neutral arsenites ( $\text{As}^{\text{III}}$ ), both of which exist in ground water (pH 6-8.5).<sup>42</sup> We proposed that the node can be used for binding anionic  $\text{As}^{\text{V}}$  and the linkers can be functionalized to capture neutral  $\text{As}^{\text{III}}$  in a complementary fashion (Figure 2.1). Such a design strategy can serve as a method for developing versatile materials that efficiently capture multiple pollutants or toxic agents that exist as diverse species in contaminated environments.



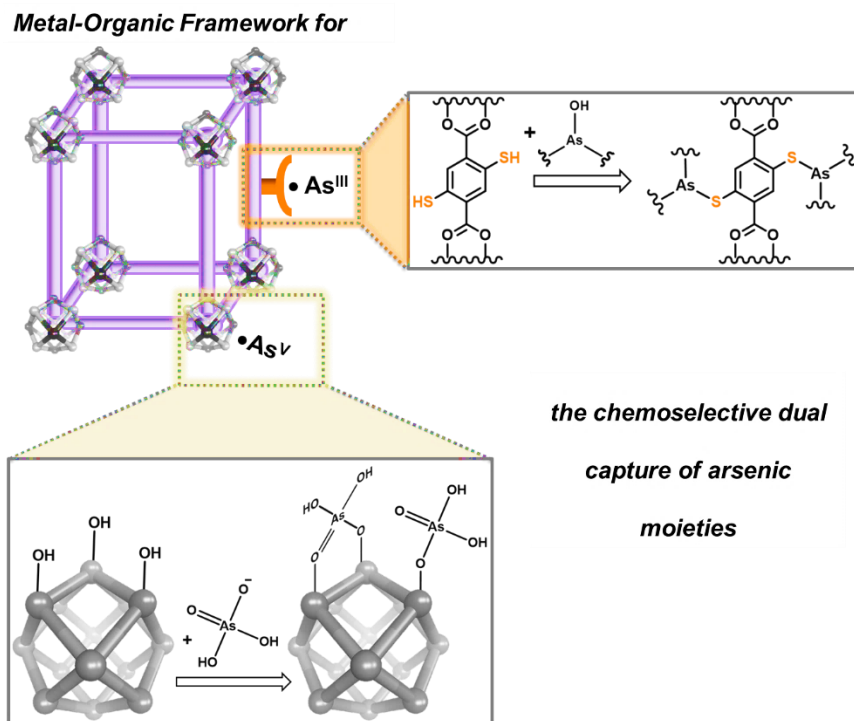


**Figure 2.1** A schematic representation that suggests how MOFs can be tailored to coordinate anionic As<sup>V</sup> moieties at the node while binding neutral As<sup>III</sup> with the linkers.

Given their high chemical stability and hydrophilicity,<sup>54-59</sup> we deemed MOFs with hexazirconium oxo hydroxo ( $Zr_6O_4(OH)_4$ ) cluster nodes, such as UiO-66,<sup>58-64</sup> to be suitable model targets for modifications to capture both As<sup>V</sup> and As<sup>III</sup> from aqueous media. We predicted strong interactions between the nodes of UiO-66 and  $[As^V O_4 H_{3-n}]^{n-}$  oxyanions (Figure 2.2 and Appendix A, Figure A1), based on the observed strong coordination of the  $Zr_6O_4(OH)_4$  cluster nodes<sup>6, 7, 24-27</sup> to phosphonates and phosphates, which are isostructural and have similar Brønsted basicity as arsenates.<sup>19, 24, 49-50, 65-67</sup> In addition, the incorporation of thiol-containing BDC ligands<sup>52</sup> (i.e., 2,5-dimercaptoterephthalic acid) into UiO-66 should facilitate binding to neutral  $[As^{III}(OH)_3]_n$  species,<sup>42</sup> akin to the known arsenophilicity of sulfur-containing enzymes and thiol-rich chelators.<sup>41, 68-70</sup> In this chapter, we report the successful use of HCl-UiO-66-(SH)<sub>2</sub>, a UiO

derivative with thiolated linkers and nodes that are “capped” with weakly binding ligands, to efficiently capture both  $\text{As}^{\text{III}}$  and  $\text{As}^{\text{V}}$  from aqueous media (Figure 2.1). The defect sites on the  $\text{Zr}_6(\text{O})_4(\text{OH})_4$  nodes can serve as excellent binders for  $\text{As}^{\text{V}}$  oxyanions while the thiolated linkers can selectively coordinate  $\text{As}^{\text{III}}$  for dual-capture purposes. The efficiency and capacity of this dual-binding feature is best realized when the binding sites are made easily accessible, either by enlarging the pore aperture size of the MOF or by reducing the particle size of the MOF nanocrystals.

## 2.2 Acid-modulated synthesis of UiO-66

As a model platform for our work, UiO-66 is highly attractive given its excellent synthetic tunability: functionalized derivatives of *p*-benzene dicarboxylate (BDC) can be easily incorporated into the framework either through de novo synthesis<sup>59, 71</sup> or post-synthetically.<sup>25, 28</sup> In addition, the degree of coordinative unsaturation of the nodes can be tuned with the use of organic<sup>60-61, 72</sup> or inorganic<sup>59</sup> acid-modulators. In the current study, we select nearly defect-free AcOH-UiO-66<sub>|11/12</sub> (i.e., AcOH-“capped” UiO-66; see Figure 2.2, top structure in the lower left corner) as a control sample. This material was prepared from  $\text{ZrCl}_4$  and  $\text{H}_2\text{BDC}$  in dimethylformamide (DMF) and in the presence of acetic acid as a modulator. It comprises well-defined octahedral particles with a Brunauer–Emmett–Teller (BET) surface area of  $\sim 1150 \text{ m}^2/\text{g}$ , and a powder X-ray diffraction (PXRD) pattern identical to that of crystalline UiO-66 (Appendix A, Figure A2-A4). Thermogravimetric analysis (TGA) data for this material suggested a formula unit of  $\text{Zr}_6\text{O}_4(\text{OH})_4(\text{BDC})_{5.5}$ , alternatively referred to as  $\text{Zr}_6\text{O}_4(\text{OH})_4(-\text{CO}_2)_{11/12}$ , which suggests that only a small amount of defects (i.e., missing-linker sites) are present (Appendix A, Figure

A7). (The “(-CO<sub>2</sub>)<sub>11/12</sub>” notation is used to indicate 1 missing carboxylate per node or 0.5 missing BDC linker per formula unit). As mentioned above, these missing-linker sites are known to bind well to phosphonates<sup>49</sup> and vanadates,<sup>73</sup> and should also be susceptible toward arsenate binding (Figure 2.2).

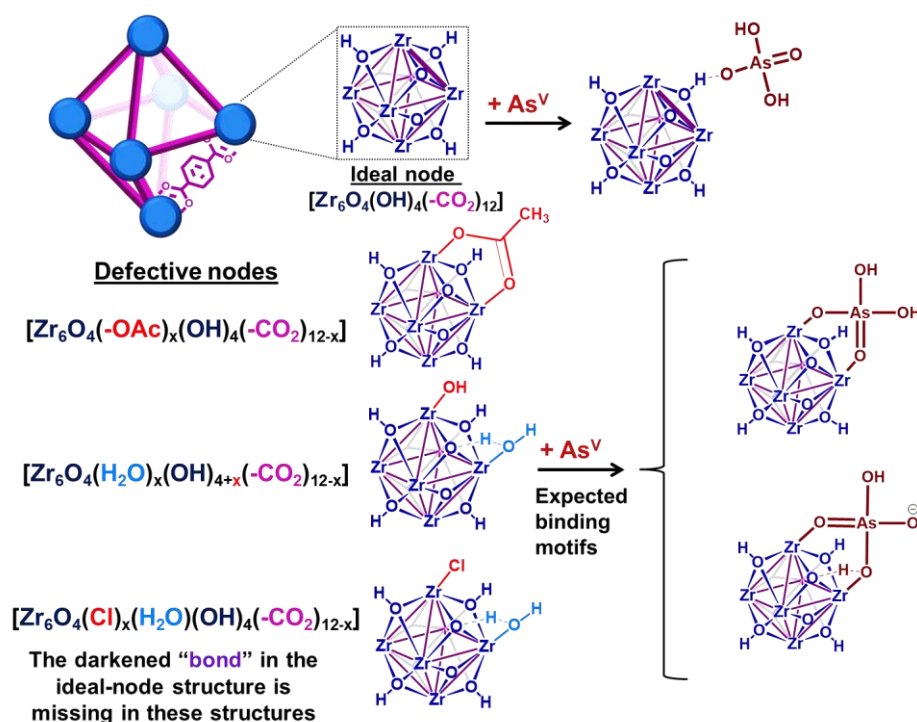


**Figure 2.2** Representative views (see Appendix A, Figure A.19 for other possible binding motifs) of a unit cell of UiO-66, with either 12-coordinated ideal nodes  $[\text{Zr}_6\text{O}_4(\text{OH})_4(-\text{CO}_2)_{12}]$  or imperfect nodes  $[\text{Zr}_6\text{O}_4(\text{OH})_x(-\text{CO}_2)_y]$ , which result from missing linkers. Each purple “bond” indicates a coordinating carboxylate from the terephthalate linker.

To elucidate the ability of the  $\text{Zr}_6\text{O}_4(\text{OH})_4$  node to bind As<sup>V</sup>, we additionally synthesized HCl-UiO-66<sub>|(12-x)/12</sub>, a series of UiO-66 materials where the amount of missing linker (x) was systematically varied using the HCl-modulator strategy.<sup>59</sup> These materials were also prepared

from  $\text{ZrCl}_4$  and  $\text{H}_2\text{BDC}$  in DMF, but with different molar ratios and with HCl as the modulator (see details in Appendix A, Section A2 and Table A1). Notably, we successfully obtained HCl-UiO-66|<sub>9/12</sub>, with ~3 available missing-linker sites per node, presumably being “weakly capped” by either  $\text{HO}^-$ ,  $\text{Cl}^-$ , or  $\text{H}_2\text{O}$  (see Figure 2.2, last two structures in the lower left corner).

### 2.3 Chelation of $\text{As}^{\text{V}}$ by the inorganic Zr-containing node.

$\text{As}^{\text{V}}$ -adsorption experiments were conducted at pH ~7,<sup>74</sup> to simulate the middle range of ground water pH, by exposing samples of the MOFs (10 mg each) to separate 50 ppm solutions (30 mL portions<sup>75</sup>) of  $\text{Na}_2\text{HAsO}_4 \cdot 7\text{H}_2\text{O}$  as the  $\text{As}^{\text{V}}$  source. The amount of  $\text{As}^{\text{V}}$  in the supernatant is monitored using inductively coupled plasma optical emission spectroscopy (ICP-OES) and the per-node uptake of  $\text{As}^{\text{V}}$  by the MOF at time  $t$  can then be calculated. As expected, AcOH-UiO-66|<sub>11/12</sub> showed good uptake of  $\text{As}^{\text{V}}$  (Figure 2.3, green profile) from the  $\text{Na}_2\text{HAsO}_4 \cdot 7\text{H}_2\text{O}$  test solution. The near-stoichiometric  $\text{As}^{\text{V}}:\text{Zr}_6$  uptake ratio (1.1:1  $\text{As}^{\text{V}}:\text{Zr}_6$ ) at 6 h strongly suggests a preferential binding of  $\text{As}^{\text{V}}$  to the missing-linker sites on the  $\text{Zr}_6$  nodes. Assuming that missing-linker sites are the most easily accessible, half of these sites (0.5:1  $\text{As}^{\text{V}}:\text{Zr}_6$ ), presumably those that are closest to the surface of the MOF nanocrystals, would be saturated within the first 30 min (Figure 2.3, green profile). The rate of adsorption slows down as the remaining, internal (i.e., deeper inside the MOF nanocrystals) sites are saturated over the next few hours, consistent with a diffusion-limited behavior. That the 24 h uptake ratio (1.2:1  $\text{As}^{\text{V}}:\text{Zr}_6$ ) slightly exceeds the estimated available binding site suggests the possible involvement of secondary binding pathways—such as formation of As oligomers<sup>42</sup> on the node (see Appendix A, Figure A21a for an illustration), linker displacement by the incoming  $\text{As}^{\text{V}}$  species (see below and Appendix A, Section

A4.2 for additional discussions),<sup>76</sup> and/or anion exchange with the bridging hydroxyl sites of the nodes,<sup>77-78</sup>—although delineating these pathways is beyond the scope of this chapter.

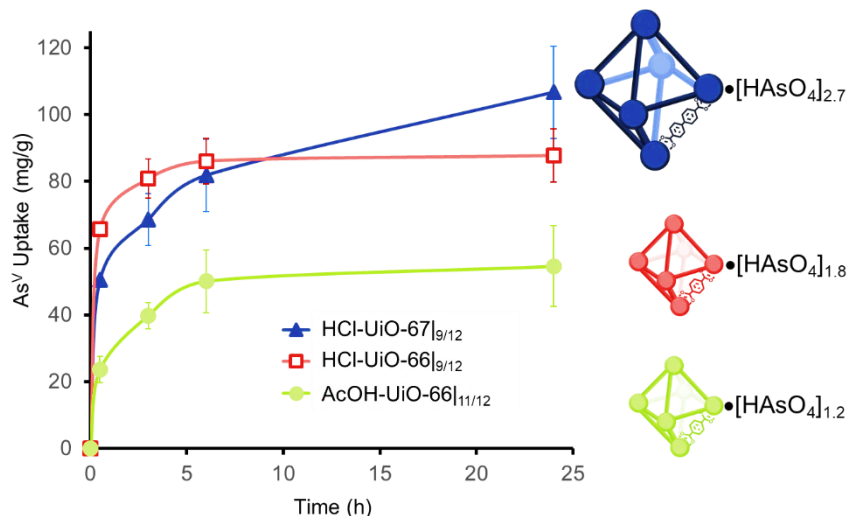


**Figure 2.3**  $\text{As}^{\text{V}}$ -uptake profiles for MOF samples (10 mg) that have been exposed to  $\text{As}^{\text{V}}$ -containing solutions (30 mL; 50 ppm initial concentration). The total amounts of bound  $\text{As}^{\text{V}}$  per node is indicated on the right. Each data point is an average of 3-4 different experiments.

Consistent with our hypothesis that missing-linker sites can also bind arsenates well, HCl-UiO-66|<sub>9/12</sub>, which has 3 missing-linker sites per node, captured  $\text{As}^{\text{V}}$  substantially faster and more (1.4:1  $\text{As}^{\text{V}}:\text{Zr}_6$  or ~46% of the missing-linker sites after 30 minutes) than the nearly defect-free AcOH-UiO-66|<sub>11/12</sub> (Figure 2.3, cf. red and green profiles). Interestingly, the uptake ratio for HCl-UiO-66|<sub>9/12</sub> in our standard 50 ppm initial As-exposure experiment levels out relatively quickly and does not change after 6 h: the  $\text{As}^{\text{V}}$  uptake ratio at this time point, as well as after 24 h of exposure, only amounts to ~60% of the available missing-linker sites (1.8:1  $\text{As}^{\text{V}}:\text{Zr}_6$ ) even though there is still excess  $\text{As}^{\text{V}}$  in solution.<sup>38</sup> These data suggests that the  $\text{As}^{\text{V}}$  uptake in HCl-UiO-66|<sub>9/12</sub> is probably

dominated by an equilibrium-driven process, as demonstrated for organophosphorus<sup>49</sup> and selenates<sup>35</sup> uptakes in UiO-type MOFs. This is indeed the case: as the As-exposure concentration is increased to 100 ppm, all of the available missing-linker sites (3:1 As<sup>V</sup>:Zr<sub>6</sub>) for HCl-UiO-66<sub>9/12</sub> can be filled after 24 h (Figure 2.4).

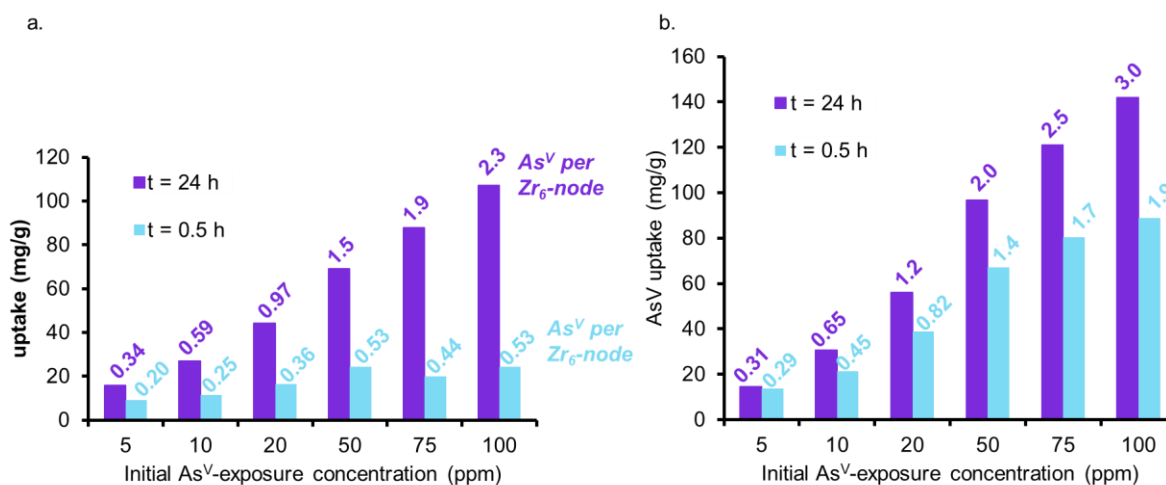


**Figure 2.4** The As<sup>V</sup>-adsorption isotherms for AcOH-UiO-66<sub>11/12</sub> (a) and HCl-UiO-66<sub>9/12</sub> (b) at short (0.5 h) and long (24 h) exposure time, plotted as bar graphs with the As<sup>V</sup>:Zr<sub>6</sub> ratios indicated at the top of each bar. Experimental conditions: batch exposure of a sample of MOF (10 mg) to the appropriate As<sup>V</sup>-containing solution (30 mL).

The combination of equilibrium-driven and secondary uptake mechanisms lead to quite different behaviors for AcOH-UiO-66<sub>11/12</sub> and HCl-UiO-66<sub>9/12</sub> as the initial As-exposure concentration was varied from 5 to 100 ppm (Figure 2.4). While the As<sup>V</sup>-adsorption profiles for HCl-UiO-66<sub>9/12</sub> at different time points all increased in the same manner (see also Appendix A, Figure A10d), the As<sup>V</sup>:Zr<sub>6</sub> uptake ratios never exceeded the per-node number of missing-linker sites, presumably due to sterics.<sup>79</sup> In contrast, the As<sup>V</sup>-adsorption profiles for AcOH-UiO-66<sub>11/12</sub> varied significantly depending on the timing of the measurements: at 0.5 h the As<sup>V</sup>:Zr<sub>6</sub> uptake ratios did not vary much beyond 53% of the available missing-linker sites (0.20-0.53:1 As<sup>V</sup>:Zr<sub>6</sub>)

while that at 24 h varied over a very large 34-235% range (0.34-2.35:1  $\text{As}^{\text{V}}:\text{Zr}_6$ ) (see also Appendix A, Figure A10c as well as the accompanying discussion that follows Figure A10).

The aforementioned large discrepancy in behaviors accentuates the differences in As-uptake mechanisms between HCl-UiO-66<sub>|9/12</sub> and AcOH-UiO-66<sub>|11/12</sub>. While the As uptake by the former is presumably based on filling up missing-linker sites, that for the latter changes between short and long exposure times. We speculate that the As-uptake mechanism for AcOH-UiO-66<sub>|11/12</sub> during the short exposure is also based on filling up missing-linker sites but that for the long exposure is dominated by the secondary binding pathways mentioned above. We note in passing that the large number of defect sites, and presumably larger pores (Appendix A, Figure A5), in HCl-UiO-66<sub>|9/12</sub> are highly advantageous for capturing purposes: the adsorption profiles measured at 3, 6, and 24 h are quite similar (Appendix A, Figure A10d), suggesting that most of the removal occurs during the first 3 h. Under our experimental conditions (Figure 2.4), this means that >90% of the  $\text{As}^{\text{V}}$  oxyanions from a 5 ppm solution can be removed after 0.5 h (0.29:1  $\text{As}^{\text{V}}:\text{Zr}_6$ ; see also Appendix A, Figure A10f), and complete removal (0.31:1  $\text{As}^{\text{V}}:\text{Zr}_6$ ) occurred after 3 h.

TEM-based EDS analyses of AcOH-UiO-66<sub>|11/12</sub> and HCl-UiO-66<sub>|9/12</sub> samples that have been exposed to 100 ppm  $\text{As}^{\text{V}}$  solutions for 24 h are also consistent with the aforementioned uptake contrast. While no visible morphological changes can be observed, the latter sample clearly showed a much higher  $\text{As}^{\text{V}}$  uptake based on the relative As/Zr signal ratios (Appendix A, Figure A18). The PXRD data for  $\text{As}^{\text{V}}$ -exposed materials are identical to the data for the corresponding as-synthesized materials (Appendix A, Figure A1), indicating that the crystallinities of the MOF samples are mostly retained even after significant  $\text{As}^{\text{V}}$  uptake and prolonged (24 h) shaking. Interestingly, while ICP-OES analysis of the supernatants from the batch-adsorption experiments

shows no evidence of  $Zr^{IV}$  ions, concurrent analyses of these samples by ESI-MS and high-resolution water-suppression  $^1H$  NMR spectroscopy reveals the presence of some  $H_2BDC$  linker. Although these data support the occurrence of the aforementioned linker-displacement secondary binding mechanism, and thus possible partial degradation of the initial MOF structure, a quantitative assessment is not possible at the present time (see Appendix A, Section A4.2 for further discussion). Additionally, it is worthwhile to note that the As concentrations that we explored for the uptake experiments herein are much higher than those that exist in natural water sources (1 ppb - 3 ppm),<sup>80</sup> which could accelerate secondary linker-displacement mechanisms such as those mentioned above.

The importance of site accessibility is also reflected in the faster initial-uptakes behavior by  $HCl-UiO-66|_{9/12}$ , which have larger pores (Appendix A, Figure A5) and whose particles are about four times smaller than those of  $AcOH-UiO-66|_{11/12}$  (Appendix A, Figure A6). The larger pores of  $HCl-UiO-66|_{9/12}$ , in comparison to  $AcOH-UiO-66|_{11/12}$ , can be attributed to a combination of higher number of missing linkers and smaller “capping” ligands ( $HO^-$ ,  $Cl^-$ , or  $H_2O$ ).<sup>81</sup> In the aqueous uptake experiments, these weak-binding ligands can also be more easily displaced by the incoming  $As^V$  moieties in contrast to the coordinating acetate “capping” ligand for  $AcOH-UiO-66|_{11/12}$ . In addition to the increase in accessibility that comes with larger pores, samples with smaller particles should have higher external surface area (Appendix A, Table A2) that also enables faster  $As^V$  chemisorption. Partially supporting this conjecture is the similar initial uptake rates for all three  $HCl-UiO-66|_{x/12}$  samples (Appendix A, Figure A13a,b and Table A4), which have nearly identical average particle sizes (Appendix A, Figure A6).



## 2.4 Improving accessibility to node sites via linker elongation: UiO-67

The aforementioned data prompted us to hypothesize that enlarging the pore aperture of UiO-66, through the use of a longer linker, would enhance diffusion and facilitate accessibility to binding sites that are deeper inside a MOF crystal, as demonstrated by Li and coworkers<sup>82</sup> for the capture of As<sup>V</sup> by mesoporous ZIF-8. Thus, we synthesized HCl-UiO-67<sub>9/12</sub>, a UiO-66 analogue with the longer biphenyl-4,4'-dicarboxylate linker and a similar number of missing linkers as our HCl-UiO-66<sub>9/12</sub> sample (based on TGA estimation of missing-linker sites<sup>83</sup>), again using HCl as a modulator. Fortuitously, this sample has similar particle sizes as HCl-UiO-66<sub>9/12</sub> (~ 280 nm vs ~250 nm, see Appendix A, Figure A6), allowing us to compare their As<sup>V</sup>-uptake behaviors without the need to account for the effects of particle size differences.

Similar to HCl-UiO-66<sub>9/12</sub>, HCl-UiO-67<sub>9/12</sub> displayed a high initial As<sup>V</sup> uptake at ~56% of the total binding sites (1.7:1 As<sup>V</sup>:Zr<sub>6</sub>) within 30 min of exposure to the As<sup>V</sup> testing solution (Figure 2.3, dark blue curve). However, after 6 h, the As<sup>V</sup> uptake for HCl-UiO-67<sub>9/12</sub> has risen above that of HCl-UiO-66<sub>9/12</sub> (70% binding sites vs 60%). The uptake continues to rise, albeit at a slow rate, over the next 18 h, presumably due to the gradual diffusion of As<sup>V</sup> into the internal binding sites of the HCl-UiO-67<sub>9/12</sub> particles, filling 90% of the binding sites (2.7:1 As<sup>V</sup>:Zr<sub>6</sub>). While the uptake clearly has not reached equilibrium at 24 h, this capacity is very close to the expected 3 As<sup>V</sup> oxyanions per Zr<sub>6</sub> node. As in the cases for AcOH-UiO-66<sub>11/12</sub> and HCl-UiO-66<sub>9/12</sub>, the PXRD pattern of the As<sup>V</sup>-exposed HCl-UiO-67<sub>9/12</sub> does not differ from that of the corresponding as-synthesized materials (Appendix A, Figure A3a), which is consistent with a retention of some sample crystallinity. Together, these data clearly indicate that the larger pores

in HCl-UiO-67<sub>9/12</sub> (Appendix A, Table A2) can definitely facilitate uptake by sites that are deeper inside a MOF nanocrystal (see further discussion below).

It is worth noting that the initial uptake profiles (over the first 30 minutes) of all five of our MOF samples discussed thus far fit well to the pseudo-first-order Lagergren kinetic model while the total uptake profiles (over a 24 h period) fit best to the pseudo-second-order Lagergren kinetic model (Appendix A, Figure A12-A13). These results are consistent with the adsorption process being governed initially by the chemisorption of As<sup>V</sup> to the readily accessible binding sites near the surfaces of the nanocrystals and becoming diffusion-limited over time as As<sup>V</sup> anions migrate into the MOF nanoparticles. Among the HCl-UiO-66<sub>x/12</sub> samples, this diffusion-limited behavior becomes most apparent after 3 h, with the sample having the most missing linkers displaying the highest equilibrium capacity. Presumably, the samples with more missing linkers will also have larger pores that facilitate diffusion (see Appendix A, Figure A13 and its caption for further discussion).

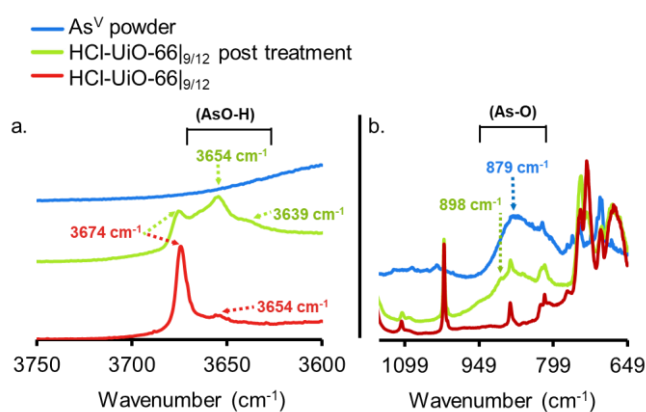


**Figure 2.5** DRIFTS spectra of HCl-UiO-66<sub>9/12</sub> sample before and after As<sup>V</sup> treatment, showing the presence of –As-O-H bonds after exposure. Spectra for powder Na<sub>2</sub>HAsO<sub>4</sub>•7H<sub>2</sub>O are included as reference. Data for AcOH-UiO-66<sub>11/12</sub> can be found in the Appendix A, Figure A14.

As mentioned earlier, phosphonates,<sup>49-50</sup> and vanadates,<sup>73</sup> which have similar structures to arsenates, have been reported to bind strongly to the missing-linker sites on the  $Zr_6(O)_4(OH)_4$  node of UiO-type MOFs through Zr-O-M motifs ( $M = V, P$ ). As such, we also expect arsenates to displace any weakly bound monotopic “capping” ligand (acetates, chlorides, and/or water) at the missing-linker sites (Figure 2.2, bottom portion) in our HCl-UiO-type MOF crystals and form strong Zr-O-M bonds through the so-called anion-exchange mechanism.<sup>35, 76</sup> Analyses of the diffuse-reflectance infrared Fourier-transformed spectroscopy (DRIFTS) data revealed a broad peak (800-900  $cm^{-1}$ ), indicative of the adsorbed  $As^V$ . The blue-shifted shoulder peak at 898  $cm^{-1}$  could be due to formation of As-OZr stretch as observed for zirconium arsenate crystals.<sup>84</sup> The As3d XPS spectrum of  $As^V$ -treated HCl-UiO-67|<sub>9/12</sub> reflected a  $\sim 0.5$  eV blue shift in binding energy in comparison to that for powder  $Na_2HAsO_4 \cdot 7H_2O$  (Figure 2.5a), in agreement with formation of As-O-Zr species<sup>78, 84-85</sup> (see Appendix A, Figures A13-A16 and their captions for further discussion). Interestingly, there is a new peak (3654  $cm^{-1}$ ) in the bridging hydroxide region of the DRIFTS spectra for the  $As^V$ -treated MOF samples (Figure 2.5a and Appendix A, Figure A14b), which we attribute to a combination of As(OH) and  $AsO \cdots H \cdots OZr$  species, similar to the  $PO \cdots H \cdots OZr$  species reported by Deria et al.<sup>19</sup> Together, these data leads us to believe that the arsenate oxyanions are coordinated to the  $Zr_6(O)_4(OH)_4$  node (possible binding motifs shown in Figure 2.2 and Appendix A, Figure A14).

## 2.5 Chelation of $As^{III}$ by the organic thiol-containing linker

To demonstrate that neutral  $As^{III}$  species can also be captured by the UiO-66 platform using thiolated ligand sites, we prepared UiO-66(SH)<sub>2</sub> using both AcOH and HCl modulators (see

Appendix A, Section A2 for experimental details), which afforded thiolated MOFs with the same amount of defects ( $\text{Zr}_6\text{O}_4(\text{OH})_4(-\text{CO}_2)_{10.5/12}$ ; see Appendix A, Section A5). When exposed to aqueous solutions of  $\text{As}^{\text{III}}$ ,<sup>86</sup> both  $\text{AcOH-UiO-66}(\text{SH})_2$  and  $\text{HCl-UiO-66}(\text{SH})_2$  showed much higher uptake compared to the non-thiolated controls (Figure 2.6a), confirming our hypothesis that thiol can be used to chemoselectively capture  $\text{As}^{\text{III}}$ . Further supporting the importance of the thiol functionalities is the observation that  $\text{HCl-UiO-66}(\text{OH})_2$ , the hydroxylated analogue of  $\text{HCl-UiO-66}(\text{SH})_2$ , does not uptake any significant amount of  $\text{As}^{\text{III}}$  under the same condition (Figure 2.6a). While  $\text{HCl-UiO-66}(\text{SH})_2$ , with higher total pore volume and higher micropore surface area (see Appendix A, Table A2), is expected to have a higher  $\text{As}^{\text{III}}$ -adsorption capacity, the uptake amount (40 mg/g, 1:1  $\text{As}^{\text{III}}:\text{Zr}_6$ ) is twice that obtained for  $\text{AcOH-UiO-66}(\text{SH})_2$ . We attribute this to the non-negligible size of the acetate “capping” ligand in the latter, which can significantly narrow the surface apertures of the MOF crystals and reduce the amount of uptake by subsurface sites. As mentioned above, the chelating nature of the acetate ligand made it less likely to be displaced by  $\text{HO}^-$  or  $\text{H}_2\text{O}$  ligands during the uptake experiments, making this mechanism of pore-aperture-narrowing more significant for the “acetate-capped” materials. Notably, sequential exposure of both  $\text{HCl-UiO-66}(\text{SH})_2$  and  $\text{HCl-UiO-66}|_{9/12}$  to  $\text{As}^{\text{V}}$  (Figure 2.6b) and then to  $\text{As}^{\text{III}}$  (Figure 2.6c), showed a stark contrast of the two materials: the latter only binds  $\text{As}^{\text{V}}$  while the former can still bind a notable amount of  $\text{As}^{\text{III}}$  (10 mg/g at 6 h, 0.26:1  $\text{As}^{\text{III}}:\text{Zr}_6$ ) after significant  $\text{As}^{\text{V}}$  uptake (40 mg/g at 6 h, 1:1  $\text{As}^{\text{V}}:\text{Zr}_6$ ). This 1:1  $\text{As}^{\text{V}}:\text{Zr}_6$  stoichiometry corresponds to 67% of the defect sites on  $\text{HCl-UiO-66}(\text{SH})_2$  and is comparable to that of  $\text{AcOH-UiO-66}|_{11/12}$  (cf Figures A6b and A3). Consistent with its low level of defects, exposing  $\text{HCl-UiO-66}(\text{SH})_2$  to an  $\text{As}^{\text{V}}$  solution (30 mL of

50 ppm  $\text{As}^{\text{V}}$ ) for 24 h does not appear to degrade it (< 1% BDC-SH linker is found in solution via ICP-OES sulfur analysis; see Appendix A, Section A4.2).

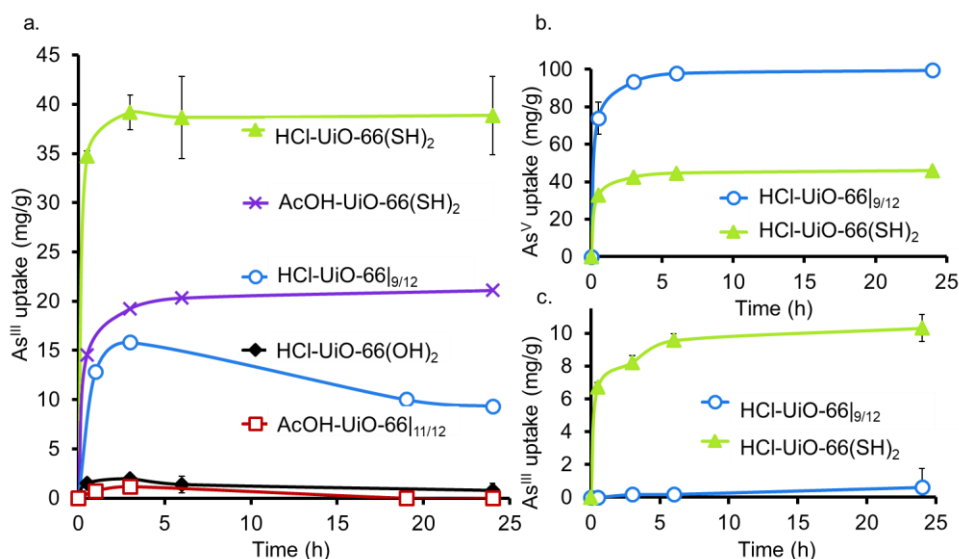


**Figure 2.6** (a)  $\text{As}^{\text{III}}$ -uptake profiles by thiolated UiO-66 samples and non-functionalized analogues confirming the important role of the soft thiol ligands in capturing  $\text{As}^{\text{III}}$ . While the  $\text{AcOH-UiO-66}_{11/12}$  and  $\text{HCl-UiO-66}_{9/12}$  controls show some initial uptake of  $\text{As}^{\text{III}}$ , this appears to be semi-reversible, not unexpectedly if we consider the weaker binding nature of the soft  $\text{As}^{\text{III}}$  ion to the hard missing-linker sites of the nodes, especially under slightly acidic conditions. (b-c) In sequential exposures to  $\text{As}^{\text{V}}$  (b) and  $\text{As}^{\text{III}}$  (c),  $\text{HCl-UiO-66}(\text{SH})_2$  shows good uptakes for both  $\text{As}^{\text{V}}$  and  $\text{As}^{\text{III}}$  compared to  $\text{HCl-UiO-66}_{9/12}$ , which only binds  $\text{As}^{\text{V}}$ . See Figure A9 for data concerning the reverse exposure order. Experimental conditions: batch exposure of a sample of MOF (10 mg) to the appropriate As-containing solution (30 mL; 50 ppm initial concentration).

Interestingly, sequential exposure of  $\text{HCl-UiO-66}(\text{SH})_2$  to  $\text{As}^{\text{III}}$  and then to  $\text{As}^{\text{V}}$  solutions (Appendix A, Figure A9) shows a reverse ordering of uptake capacities (40 mg/g at 6 h of the first exposure plus 10 mg/g of  $\text{As}^{\text{V}}$  at 6 h of the second exposure). These data suggest that while  $\text{HCl-UiO-66}(\text{SH})_2$  has capability for binding both  $\text{As}^{\text{III}}$  and  $\text{As}^{\text{V}}$ , the total capacity may again be limited by sterics. Full uptake of the first species, regardless of the oxidation state, invariably results in a

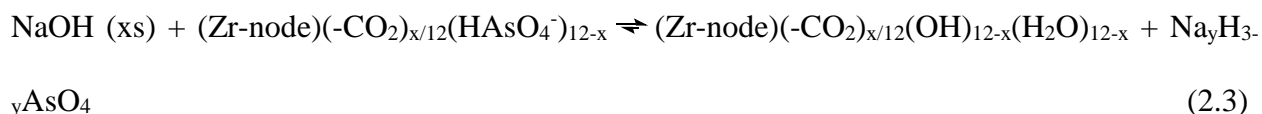
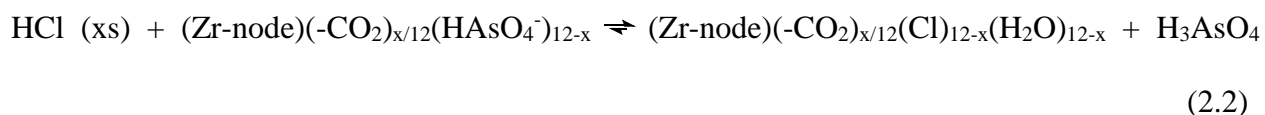
narrowed pore that lowers the accessibility of the binding sites deeper inside the nanocrystals. Such a case would result in lower uptakes of the second species compared to the available binding sites.

## 2.6 The binding reversibility of As<sup>III</sup> and As<sup>V</sup>

To identify some possible post-adsorption regeneration strategies for these promising MOF sorbents, we examined the reversibility of As binding in them (see additional discussion in Appendix A, Section A9). Given that [As<sup>III</sup>(OH)<sub>3</sub>]<sub>n</sub> species are known to bind to sulfur-containing enzymes and thiol-rich chelators presumably through the exchange of the hydroxyl group with RSH moieties, we hypothesized that the (BDC-S)<sub>x</sub>As(OH)<sub>3-x</sub> species present in As<sup>III</sup>-treated HCl-UiO-66(SH)<sub>2</sub> is best decomposed into soluble As<sup>III</sup> moieties and intact MOF via competitive ligand exchange with excess soluble thiols (Eq. 2.1). Indeed, about 30% of As<sup>III</sup> can be removed from As<sup>III</sup>-treated UiO-66(SH)<sub>2</sub> within 3 h when treated with a 0.5 M solution of thiophenols (~90 equiv in excess) at 50 °C under stirring. No As was removed without stirring or heating, consistent with a thermodynamically driven equilibrium that is limited by slow diffusion through the crystal. Also consistent with this hypothesis are the observations that treatments with a smaller excess of thiophenols and the use of less acidic alkylthiols did not work as well (Appendix A, Table A5). Notably, Zr<sup>IV</sup> ions and BDC-(SH)<sub>2</sub> linkers were not observed in the treatment solution, suggesting that HCl-UiO-66(SH)<sub>2</sub> is completely stable under these conditions. The stability of this MOF to regeneration is highly beneficial as it can be reused in applications that aim to remove As<sup>III</sup>, which is the more toxic and prevalent form of arsenic in anaerobic groundwater streams.<sup>42</sup>



The desorption of As<sup>V</sup> from As<sup>V</sup>-treated AcOH-UiO-66|<sub>11/12</sub> and HCl-UiO-66|<sub>9/12</sub> is slightly more problematic given their strong coordination to the nodes (Figure 2.1), which can only be disrupted by treatment with either a strong acid or base (Eqs 2.2 and 2.3); however, such treatments may also facilitate some decomposition of the MOF.<sup>87</sup> Indeed, while subjecting As<sup>V</sup>-treated HCl-UiO-66|<sub>9/12</sub> to either a 3.3 M HCl (~16000 equiv/node) or a 3.3 M NaOH (>1000 equiv/node) solution led to the desorption of a significant amount of As<sup>V</sup>; a small amount of Zr<sup>IV</sup> ions was also released (Appendix A, Table A4). From the limited set of data that had been obtained to date, we are optimistic that this loss of Zr<sup>IV</sup> ions can be minimized with proper optimization of exposure time and acid (or base) concentrations.



We note that exposing As<sup>V</sup>-treated HCl-UiO-66|<sub>9/12</sub> to solutions with pH 2, 7, or 12 did not lead to any noticeable As release until pH 12 (Appendix A, Figure A22). This observation is in agreement with a previous report by Wang *et al.*, where UiO-66 exhibits the lowest As<sup>V</sup> uptake at pH 11 in the 2-11 pH range that was studied.<sup>76</sup> Interestingly, exposing As<sup>V</sup>-treated AcOH-UiO-66|<sub>11/12</sub> to the same series of pH solutions led to a more noticeable desorption of As<sup>V</sup> that increases proportionally with the basicity of the solution (Appendix A, Figure A22). This process may be attributed to the removal of the weakly bound As<sup>V</sup> that originally adsorbed onto AcOH-UiO-66|<sub>11/12</sub> through secondary binding mechanisms (see discussion above).

## 2.7 Conclusion

In summary, we have successfully demonstrated the respective use of the nodes and linkers in a series of UiO-MOFs to chemoselectively capture anionic  $\text{As}^{\text{V}}$  and neutral  $\text{As}^{\text{III}}$ . Missing-linker sites on the  $\text{Zr}_6(\text{O})_4(\text{OH})_4$  nodes are excellent binders for  $\text{As}^{\text{V}}$  oxyanions, thiolated linkers can selectively chelate  $\text{As}^{\text{III}}$ , and both of these recognition motifs can be incorporated into the same framework for dual-capture purposes. Our results also suggest that the full capacity of this dual-binding feature is best realized when the binding sites internal to the MOF crystals are made easily accessible, either by enlarging the pore aperture size or by reducing the particle sizes. Notably, the binding of both  $\text{As}^{\text{V}}$  and  $\text{As}^{\text{III}}$  appear to be reversible with the proper post-adsorption treatments, suggesting that the dual-capture strategy can be incorporated into the design of regenerable/reusable adsorbents capable of efficiently capturing multiple pollutants or toxic agents that exist as diverse species in aqueous environments

## 2.8 Experimental Section

Please see Appendix A



### **Chapter 3**

#### **Delineating pore architectures in defect-containing UiO-66 derivatives and its significance to adsorbent design.**

Portions of this chapter will appear in the following manuscript:

Audu, C. O.; Liu, M.; Anderson, R. M.; McConnell, M. S.; Malliakas, C. D.; Snurr, R. Q.; Farha, O. K.; Hupp, J. T.; Gualdrón, D. A. G.; Nguyen, S. T. *manuscript in preparation*.

### 3.1 Introduction

The intentional incorporation of defects into crystalline metal-organic frameworks (MOFs) has sparked a tremendous interest in recent years, as it can introduce larger pores<sup>88-91</sup> and labile node coordination sites into MOFs for applications in gas storage,<sup>14, 20, 54, 92-95</sup> chemical sensing,<sup>96-97</sup> separations,<sup>46, 92, 98-99</sup> and catalysis.<sup>92, 100-104</sup> In the previous chapter, we discussed how these sites can be engineered for arsenate removal in a manner that afforded fast initial adsorption and high capacity. However, it remained unclear just how such traits were endowed into UiO-66 without sacrificing the framework stability – a crucial factor in the design of porous adsorbents. As such there was a critical need to understand the pore structure surrounding these defect sites in a manner that exceeds the long-range structures obtainable through crystallographic analysis. With this knowledge, effective structure-property correlations can be applied in the design of stable and efficient adsorbent frameworks for practical applications.

For this purpose, a combination of analytical techniques<sup>105</sup> including sophisticated diffraction methods that can detect features with short-range ordering (e.g., EXAFS, PDF, synchrotron XRD, etc)<sup>106-112</sup> have been employed. However, for MOFs with small particle sizes or having randomly distributed missing-linker or missing-cluster sites (i.e., not periodically present throughout the crystallite and often viewed as defect sites), delineating these structural details through crystallographic analysis remains non-trivial.<sup>108-109 113-114</sup> Thus, it would be desirable to have additional analytical methods that can complement X-ray-based methods to facilitate structure determinations in a broader selection of MOF morphologies, especially in those that exist as very small particles or have been made with non-periodic defect sites.

With its high sensitivity to structural changes in microporous materials,<sup>115-117</sup> the analysis of adsorption isotherms has served as a powerful characterization tool<sup>118-128</sup> that can be used in conjunction with crystallographic analyses to provide structural information for MOFs. For example, insights into the MOF structure—such as adsorbed solvents and ligands,<sup>129-130</sup> collapsed pore structure,<sup>58</sup> and interpenetration,<sup>131-132</sup> to name a few—can be obtained from adsorption isotherms by comparing the measured surface areas and saturation loadings to theoretical values determined from crystal structures or structural models derived from powder X-ray diffraction (PXRD) data. However, such comparisons are quite difficult to make for MOFs with very complex PXRD patterns,<sup>133</sup> with disordered defect structures,<sup>15, 81, 108, 111, 114, 134</sup> or with small particle sizes,<sup>106</sup> as has been reviewed recently.<sup>15, 113</sup> A physical strategy to address these challenges is to expand the experimental parameters used in adsorption experiments (e.g., type of probing gas molecule and pressure range) to deduce structural information and properties beyond the Brunauer–Emmett–Teller (BET) areas and saturation loadings, as demonstrated in the analysis of the complex hierarchical pore structure in NU-1301<sup>133</sup> and others.<sup>118</sup> Alternatively, one can also employ a more chemically oriented strategy by synthesizing a series of MOF derivatives that are distinguishable in compositions, examining their N<sub>2</sub>-adsorption profiles, and deducing structural information through comparative analysis against a series of logically constructed structural models. Such an approach (i.e., the combined efforts of tunable chemical synthesis/modification and systematic modeling) could even address certain structural ambiguity in MOF derivatives with the same topology and building blocks but containing varying levels of disordered defect structures.

Given that the N<sub>2</sub>-pore-filling process for micropores (0.4-2 nm) of different sizes can be clearly observed as distinguishable stages in the N<sub>2</sub>-adsorption isotherm,<sup>118-120</sup> we surmised that small, yet distinct changes to the pore structure (e.g., pore sizes, shape, hierarchy, and volume) of a MOF—such as changes in the number of linkers, as well as the number and types of node-capping ligands—would be reflected in its N<sub>2</sub>-adsorption isotherm (Figure 3.1).<sup>128</sup> If this is the case, the observed changes can be compared against those generated in the simulated isotherms of a libraries of *in silico* models that have been systematically generated by integrating available crystallographic data (i.e., from a known parent structure or a good guess) along with sensible chemical information that is obtainable from compositional analysis. If such a methodical analysis results in a best match, detailed information regarding the structure of the experimental sample can be inferred from those of the *in silico* models.

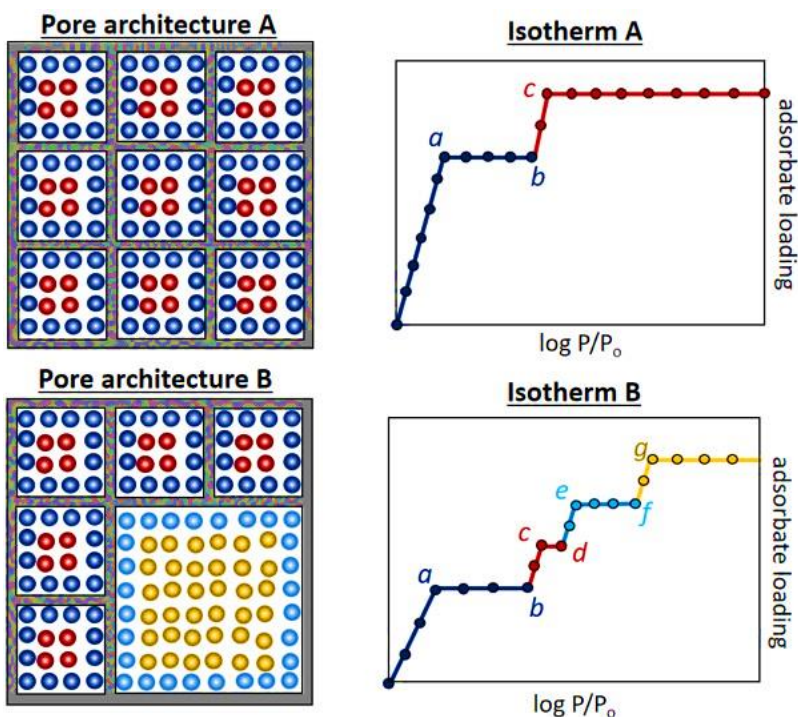


**Figure 3.1** An illustration of how modifications of the pore architecture can affect the pore-filling process in a gas-adsorption experiment and introduce discernable changes in the adsorption isotherm. For pore architecture A, the first and second isotherm steps reflect monolayer formation (dark blue spheres) and pore filling (red spheres). For pore architecture B, a third and fourth steps are introduced due to the monolayer formation (light blue spheres) and pore filling (yellow spheres) occurring in the newly introduced larger pore. While the spheres are color-coded to correlate with the different steps in the adsorption process, they represent molecules of the same type (e.g., N<sub>2</sub>).

In this chapter, we demonstrate the successful elucidation of the pore structures of a series of UiO-66 MOFs synthesized with different modulators under different conditions, thus possessing a broad range of defects, with the most-defective one possessing a linker/node ratio of 4 (out of 6 total in a defect-free UiO-66). These materials were obtained in small particle sizes ( $\leq 1 \mu\text{m}$ ) and with a substantial amount of non-periodic defects, from missing benzene-1,4-dicarboxylate (BDC) linkers to missing Zr<sub>6</sub>-oxohydroxo cluster nodes, based on compositional analysis. From a crystallographic perspective, these defect sites deviate from the ideal fcu topology where each node is connected to twelve carboxylates. While it is known that these highly rigid frameworks can withstand fewer connections per node when linkers are absent, or when there are missing clusters, the resulting vacant sites have ambiguous chemophysical environments that are difficult to elucidate by conventional diffraction analysis,<sup>15</sup> partly due to the disordered nature of these sites and the limitations for crystallographic analysis on these systems.<sup>113</sup> We found that these ambiguities can be fully resolved through a combination of compositional analysis and thorough investigation of the pore-filling processes in N<sub>2</sub>-adsorption studies over a broad range of relative pressures ( $10^{-7} < P/P_0 < 1$ ). In particular, we showed that the N<sub>2</sub>-pore-filling process is highly sensitive to changes in local pore environments that comprise only a few unit cells (our modeling was carried out on  $2 \times 2 \times 2$  supercells) and can readily discriminate changes in the number of

defects and their distribution patterns within adjacent unit cells. Notably, we generated new MOF derivatives that differ from the parent samples in types of capping ligands through post-synthesis modifications and showed that these changes can be detected with our systematic composition/modeling analysis strategy. Together, these results suggest that our approach can provide a highly complementary addition to the suite of techniques available for the better and more-accurate structure elucidation of defect-containing MOFs.

### 3.2 Preparation and experimental analyses of defect-containing UiO-66 derivatives

We prepared three different derivatives of UiO-66 using acetic acid,<sup>60</sup> hydrochloric acid,<sup>59</sup> and benzoic acid<sup>72</sup> modulators, respectively. These materials are denoted as AcOH-UiO-66|<sup>5.2/6</sup>, HCl-UiO-66|<sup>4.2/6</sup>, and BzOH-UiO-66|<sup>4.0/6</sup>, where the acid name before the “UiO-66” name indicates the modulator that was used in the synthesis and the superscripted  $y/6$  ratio after the | sign indicates how the linker/node (L/N) ratio  $y$  deviates from the ideal ratio of 6 (as in  $[\text{Zr}_6\text{O}_4(\text{OH})_4](\text{Linker})_6$  formula unit). As determined by a combination of  $^1\text{H}$  NMR spectroscopy<sup>135</sup> and ICP-OES analysis,<sup>105</sup> the L/N ratios for all three materials are consistent with the presence of defects that can be as high as 2 missing linker/node (i.e., 4 carboxylate sites/node).<sup>136</sup>

Quantitative  $^1\text{H}$  NMR analyses of the digested AcOH-UiO-66|<sup>5.2/6</sup> and BzOH-UiO-66|<sup>4.0/6</sup> samples clearly showed the presence of acid modulators (Appendix B, Figure B8-9) at stoichiometries that are consistent with them acting as monocarboxylates “caps” to the missing-linker sites on the node (Appendix B, Table B4, entries 1 and 3). For the digested HCl-UiO-66|<sup>4.2/6</sup> sample, a significant amount of formic acid (FOH) is observed in the  $^1\text{H}$  NMR spectrum,

presumably due to the decomposition of DMF in the presence of HCl,<sup>137</sup> Given the strong interactions between carboxylates and the  $Zr_6O_4(OH)_4$  node,<sup>19, 138-139</sup> formate can act as capping ligand<sup>81</sup> for the node in  $HCl-UiO-66|^{4.2/6}$ . However, since it is present in a stoichiometry that is not enough to completely account for all the missing-linker sites on the node (Appendix B, Table B4, entry 2), we attribute the “caps” of the defect sites in  $HCl-UiO-66|^{4.2/6}$  to a combination of formates and possibly  $[\mu_1-Cl + \mu_1-H_2O]$ .<sup>59, 140</sup>

The defects in our three materials have been originally attributed to the absence of linkers connecting adjacent nodes (typically referred to as “missing linkers”<sup>15, 36, 60, 89, 112</sup>) and/or the absence of whole oxometallic cluster nodes and surrounding linkers (commonly referred to as “missing nodes”<sup>110</sup> or “missing cluster”<sup>15, 81, 111</sup>; Figure 3.2. Theoretically, these defects could be randomly distributed<sup>89</sup> or aggregated into “defect-rich” domains, as has recently been shown by synchrotron PXRD experiments<sup>108</sup> on (Hf)UiO-66 to be dominated by the 8-connected, 4-linker/node *reo* topology (Figure 3.2).<sup>81, 108</sup> However, such analysis would have been difficult to carry out for the analogous (Zr)UiO-66 materials, where the signal intensity will be reduced. As an example, the absence of low-angle peaks in the conventional PXRD patterns (Appendix B, Figure B1a) of our  $HCl-UiO-66|^{4.2/6}$  and  $BzOH-UiO-66|^{4.0/6}$  samples could have been mistakenly interpreted as consistent with the absence of *reo* defects. While synchrotron PXRD analysis (Appendix B, Figure B1b) of these materials reveals a low-angle peak that hints at the presence of an 8-connected domains, this peak is quite broad and low in intensity, so we cannot confidently associate it with *reo* features. Its broadness also raises the possibility that *reo* features are not the only ones present and that other types of defects are present and are randomly distributed throughout the MOF crystallite. Thus, we set out to resolve the differences between these

possibilities by N<sub>2</sub>-adsorption studies with the hypothesis that the different pore architectures generated by these defects can be detected by signatures at the low-pressure region (see above).

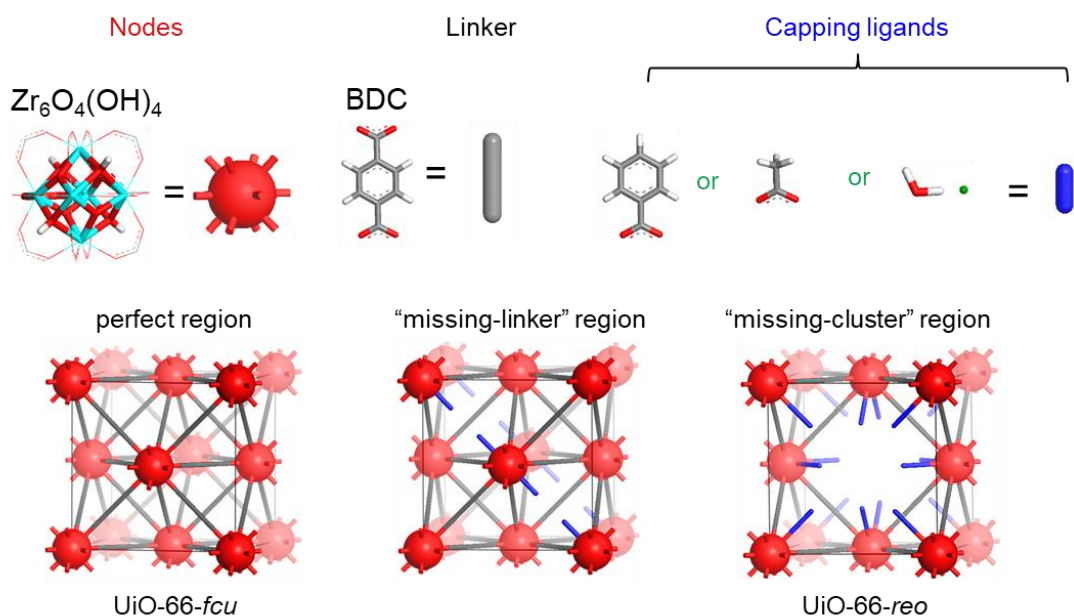


**Figure 3.2** A schematic of the UiO-66 unit cells comprising perfect UiO-66 regions (UiO-66-*fcu*),<sup>62, 71</sup> “missing-linker” regions (UiO-66-*ml*),<sup>60, 81</sup> and “missing-cluster” regions (UiO-66-*reo*).<sup>81, 108</sup>

The experimental N<sub>2</sub> adsorption isotherms for AcOH-UiO-66<sup>|5.2/6</sup>, HCl-UiO-66<sup>|4.2/6</sup>, and BzOH-UiO-66<sup>|4.0/6</sup> (Figure 3.3) show very different saturation-loadings. While the isotherm for AcOH-UiO-66<sup>|5.2/6</sup> exhibits a saturation loading approaching that simulated for a defect-free UiO-66 crystal,<sup>81, 128</sup> those for BzOH-UiO-66<sup>|4.0/6</sup> and HCl-UiO-66<sup>|4.2/6</sup> show successively higher loadings that are consistent with their higher levels of defects. The isotherm for HCl-UiO-66<sup>|4.2/6</sup> also presents a much broader curvature than the other two as it approaches saturation, signifying the presence of larger pores.<sup>128</sup> These observations are supported by the pore-size distribution



(PSD) profiles (Figure 3.10c), which show BzOH-UiO-66<sup>|4.0/6</sup> and HCl-UiO-66<sup>|4.2/6</sup> to have successively larger micropores (~14 Å and ~18 Å, respectively).<sup>141</sup>

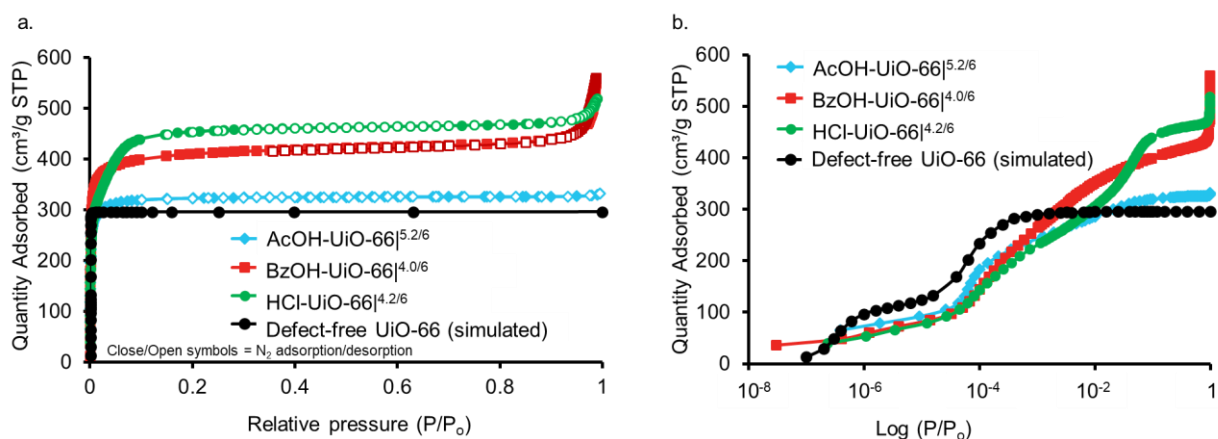


**Figure 3.3** Experimentally obtained N<sub>2</sub> isotherms for AcOH-UiO-66<sup>|5.2/6</sup>, HCl-UiO-66<sup>|4.2/6</sup>, and BzOH-UiO-66<sup>|4.0/6</sup> plotted on a normal scale (a) and a semi-log scale (b) of just the adsorption-branch data. The N<sub>2</sub>-adsorption isotherm for the defect-free UiO-66 model was generated using grand canonical Monte Carlo simulations with the open source code RASPA.<sup>142,143</sup>

While saturation loading or BET area is a useful parameter to consider for identifying defect-containing MOFs from their defect-free analogues,<sup>60, 108, 144-146</sup> alone, it cannot account for subtle structural differences that are necessary to construct an accurate model that describes the resulting pore structures of these defect-containing MOFs. For example, that the saturation loading for our low-defect-density AcOH-UiO-66<sup>|5.2/6</sup> mirrors that of a defect-free material may make it tempting to attribute its defects solely to missing linkers.<sup>147</sup> However, for BzOH-UiO-66<sup>|4.0/6</sup> and HCl-UiO-66<sup>|4.2/6</sup>, where the defect densities are much higher and similar, conclusions regarding the nature of the defects cannot be made solely based on changes in the saturation loadings.

Gómez-Gualdrón *et al* have previously simulated the pore-filling behaviors of N<sub>2</sub> molecules for a wide range of MOFs and showed that, in spite of the small differences in pore diameter, the tetrahedral ( $d = 6.9$  and  $7.3$  Å)<sup>148</sup> and octahedral ( $d = 7.9$  Å) cages in UiO-66 exhibited different pore-filling behaviors at low-pressure regions ( $10^{-7} < P/P_0 < 10^{-4}$ ).<sup>128</sup> Indeed, distinct pore-size-dependent filling behaviors can be simulated for other MOFs possessing pores that cover a broad 11-33 Å range in pore sizes. Such sensitivity suggests that a close scrutiny of the N<sub>2</sub>-adsorption profiles for our three materials at low  $P/P_0$  range may provide a means for distinguishing their pore structures. This is indeed the case: when the experimental isotherms for our three UiO-66 materials were replotted against a logarithmic  $P/P_0$  scale (Figure 3.3b), they appear very distinctive from each other. AcOH-UiO-66<sup>|5.2/6</sup> displays two clear steps in this semi-logarithmic adsorption profile, while HCl-UiO-66<sup>|4.2/6</sup> and BzOH-UiO-66<sup>|4.0/6</sup> display three and one step, respectively. These steps occur at different pressure ranges and have unique curvature, especially in the  $10^{-8} < P/P_0 < 10^{-2}$  range, that can serve as a unique fingerprint for each sample. This data prompted us to carry out a series of simulations to elucidate how defect-induced deviations from the ideal UiO-66 pore structures can manifest into observable differences in the pore-filling process.

### 3.3 Construction of the computational models for defect-containing UiO-66 derivatives

We generated seven unique models per potential “capping” species (i.e., acetates, benzoates, formates (FOH), and a [ $\mu_1$ -Cl +  $\mu_1$ -H<sub>2</sub>O] combination that could reside on any site of the node that is not connected to the linker carboxylate) by systematically varying the L/N ratio between 4 and 6 (L/N = 6 for an ideal UiO-66 crystal (UiO-66-*fcu*, see Figure 3.2)). To obtain each L/N ratio, we introduced either missing-linker or missing-cluster defects (see Figure 3.4 for

those based on the AcOH-UiO-66 derivative and Appendix B, Figures B11-B13 for the other derivatives) by modulating the linker/node composition of the defect-free model in a  $2 \times 2 \times 2$  cubic supercell ( $a = 4.519$  nm). While previous work has centered on the modification of a single cubic unit cell ( $a = 2.097$  nm) of UiO-66-*fcu*,<sup>59, 81</sup>, this small-sized model would limit the L/N ratio attainable with missing clusters strictly to 4. The  $2 \times 2 \times 2$  supercell (comprising 32  $Zr_6O_4(OH)_4$  nodes and 192 BDC linkers for UiO-66-*fcu*, denoted herein as *UiO-66*<sub>(192/32)</sub> provides a large enough system for us to accurately simulate how defects (either missing-linker or missing-cluster) impact the pore-filling processes in different UiO-66 pore structures without being computationally cumbersome.

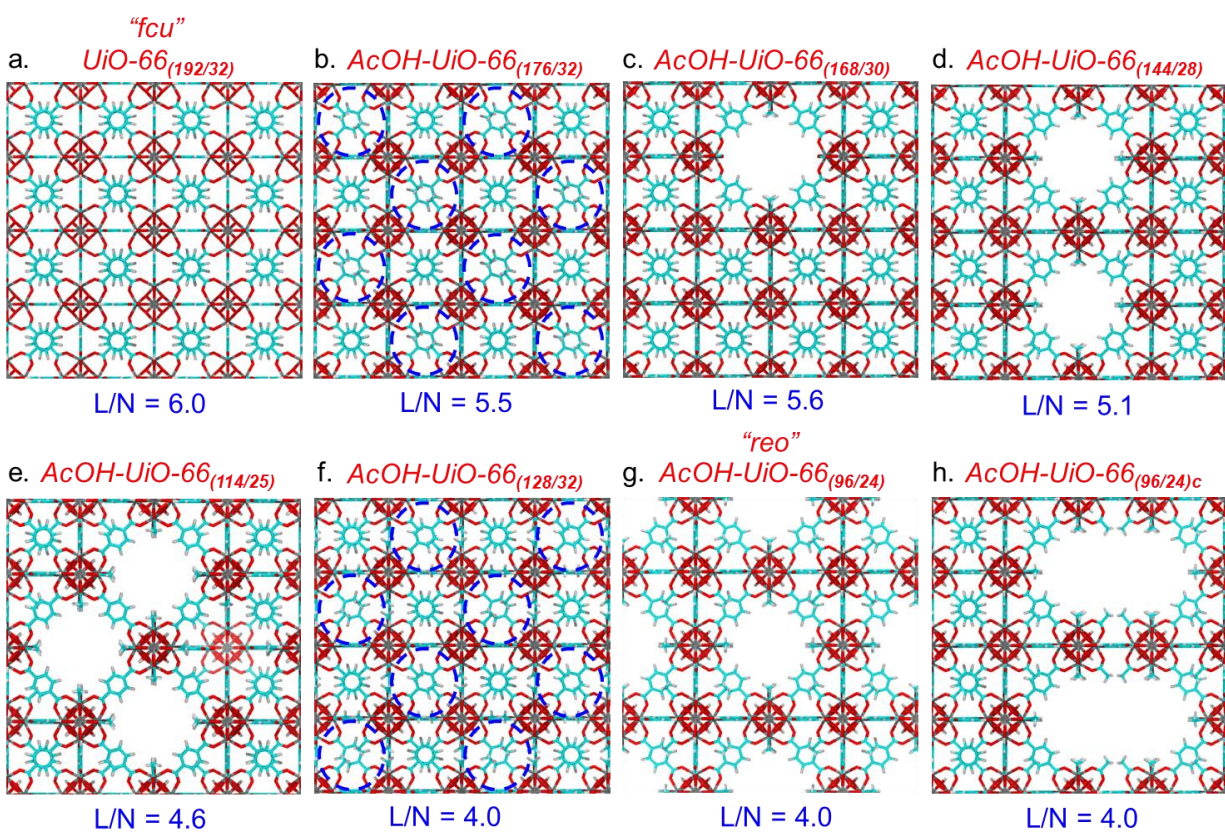


**Figure 3.4** The ideal UiO-66 supercell (a) and a set of seven *in silico* structural models for AcOH-UiO-66 with different defective regions based on either missing linker or missing cluster defects (b-h). Models b and f were constructed by removing linkers from the ideal UiO-66 supercell, but not nodes. The locations of removed linkers that are noticeable in this 2D view are circled. Models c, d, e, g, and h were constructed by removing nodes and the associated linkers (i.e., generating missing-cluster defects). In the *AcOH-UiO-66*<sub>(*l*/*n*)</sub> notation, *l* indicates the total number of linkers and *n* indicates the total number of nodes in the supercell. Models a and g correspond to UiO-66-*fcu* and UiO-66-*reo*, respectively. Models g and h have similar missing-cluster defects but *AcOH-UiO-66*<sub>(96/24)*c*</sub> possess defect regions that coalesced together.

For each type of “capped” MOF (e.g., AcOH-UiO-66), missing-linker defects were installed in our model by removing BDC linkers from the defect-free UiO-66 supercell (*UiO-66*<sub>(192/32)</sub>). Missing-cluster defects were installed by removing both the Zr<sub>6</sub>O<sub>4</sub>(OH)<sub>4</sub> nodes and the associated BDC linkers randomly from the 2 × 2 × 2 supercell. Under-coordinated nodes were capped with the appropriate modulator species (e.g., acetate caps in models for the AcOH-UiO-66 derivatives). Among the seven models that were generated are several hybrids that include both UiO-66-*reo* and UiO-66-*fcu* “domains” (i.e., with 8- and 12-connected nodes, Figure 3.4c-e,h), which can account for samples with mixed domains.<sup>149</sup> In addition, models with similar L/N ratios can have drastically different pore architectures (cf. Figures 3.4f,g, and h for L/N = 4.0; cf. Figures 4b,c with L/N ~ 5.5).

As described above, our series of models (Figure 3.4 and Appendix B, Figure B11-B13) comprises a range of UiO-66 supercells that should encompass representative local defect-containing regions in the experimentally obtained AcOH-UiO-66<sup>5.2/6</sup>, HCl-UiO-66<sup>4.2/6</sup>, and BzOH-UiO-66<sup>4.0/6</sup>. While employing larger supercells would generate larger sets of models with more-complex pore structures,<sup>108</sup> we surmised that our simple series can be used to elucidate key

structural details of these three defect-containing UiO-66 derivatives. We hypothesized that if the L/N ratio, along with the simulated data (i.e., the steps in the simulated isotherm, the N<sub>2</sub> saturation loading, the BET area, and the pore size distribution) for a particular structural model are *all* consistent with the experimental data for a given UiO-66 sample, then that structural model captures the key features of the pore architecture and nanostructure of the synthesized material.

### 3.4 Simulated N<sub>2</sub> adsorption isotherms and their use in structure elucidation of samples

N<sub>2</sub> isotherms were determined *in silico* for each of the 29 constructed models [(4 capping species × 7 defect architecture models) + 1 defect-free model] using grand canonical Monte Carlo (GCMC) simulations. The simulated N<sub>2</sub> isotherms (Appendix B, Figure B16) are all distinctive from each other in either N<sub>2</sub> saturation loadings or their adsorption steps (i.e., the number and location) or both. For instance, the simulated isotherm for the defect-free *UiO-66*<sub>(192/32)</sub> and a slightly defective (L/N = 5.6) UiO-66 model (*AcOH-UiO-66*<sub>(168/30)</sub>) are clearly different in both saturation loadings and adsorption steps (Figure 3.5, cf the profiles in panels a and b). Notably, the missing-cluster model has additional steps in the isotherm due to adsorption phenomena in a missing-cluster-derived cavity not found in the defect-free model. As shown in the snapshots that accompany Figure 3.5b, these steps correspond to formation of a N<sub>2</sub> monolayer around the cavities created by missing-cluster defects and filling of these cavities, successively.

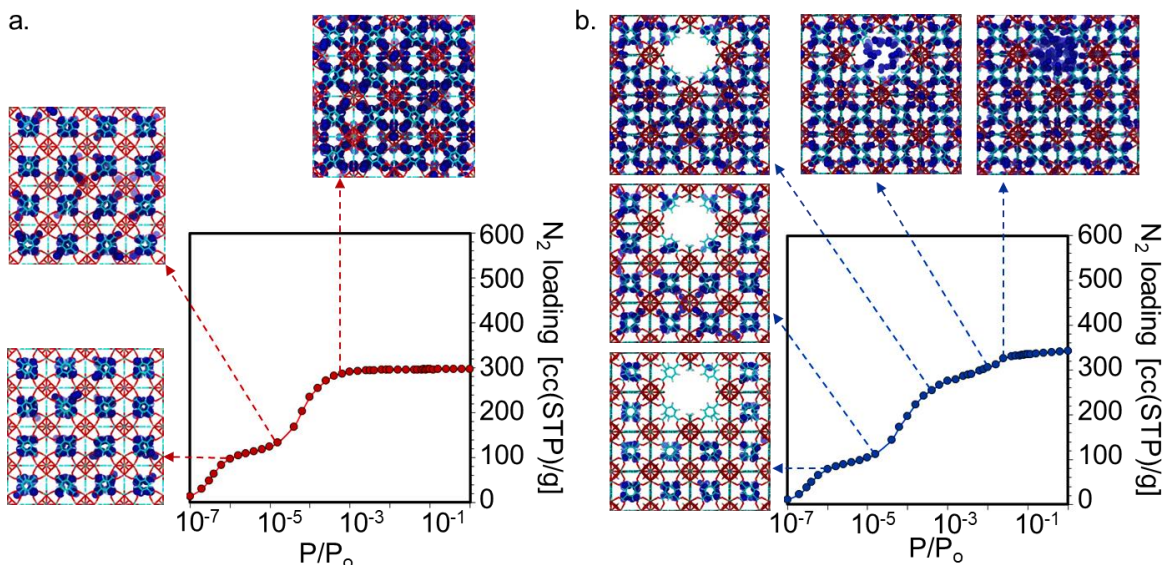


**Figure 3.5** Simulated  $N_2$ -adsorption isotherms along with “step-related” simulation snapshots for  $UiO-66_{(192/32)}$  and  $AcOH-UiO-66_{(168/30)}$ . (a) For the defect-free  $UiO-66_{(192/32)}$ , the steps correspond to filling of the tetrahedral pores by  $N_2$  molecules (purple objects in the snapshots), followed by filling of the octahedral pores. (b) For  $AcOH-UiO-66_{(168/30)}$ , which represents a UiO-66 sample that has a low density of missing clusters (2 out of 32), the steps correspond to filling of the tetrahedral pores, filling of the octahedral pores, formation of a  $N_2$  monolayer around the cavities created by missing-cluster defects, and filling of these cavities, successively

Notably, the simulated isotherms for models  $AcOH-UiO-66_{(128/32)}$  (missing-linker defects, Figure 3.4f) and  $AcOH-UiO-66_{(96/24)}$  (missing-cluster defects, Figure 3.4g), both with  $L/N = 4$ , showed large differences in both their  $N_2$  saturation loadings ( $\Delta \sim 200 \text{ cm}^3 \text{ (STP)/g}$ ) and adsorption steps (Figure 3.6a). This same  $L/N$  ratio (4) can also be modeled as  $AcOH-UiO-66_{(96/24)c}$  (Figure 3.4h), which has similar missing-cluster defects as  $AcOH-UiO-66_{(96/24)}$  but with defect regions that coalesced<sup>90</sup> together. The simulated adsorption isotherms for both of these missing-cluster models show similar saturation loadings ( $\sim 500 \text{ cm}^3 \text{ (STP)/g}$ ) but with noticeable differences in the low-pressure adsorption range  $10^{-4} < P/P_0 < 10^{-2}$  (Figure 3.6b). These data clearly show that even for



models with the same capping species and the same L/N ratio, differences in pore structures lead to distinguishable differences in the adsorption behaviors.

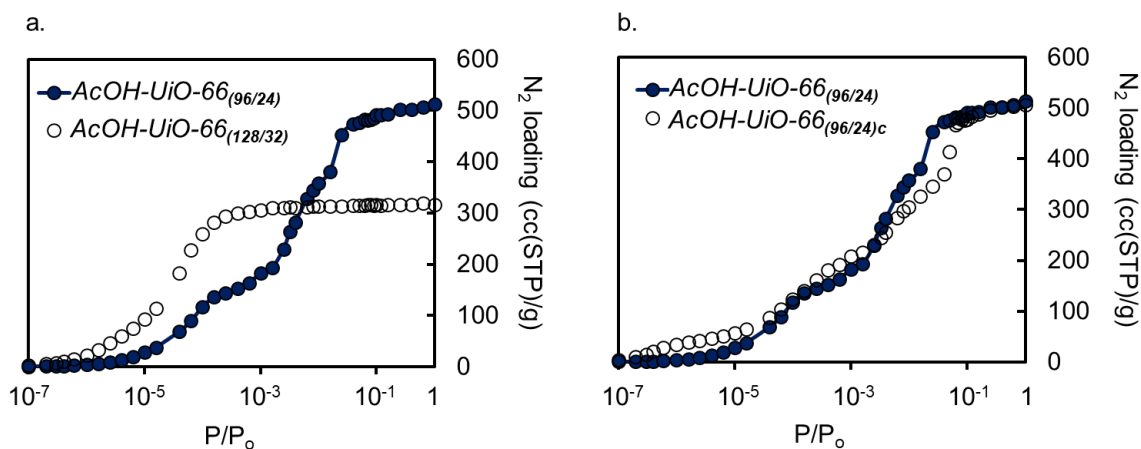


**Figure 3.6** Comparison between the simulated isotherms for models with similar L/N ratio of four. a) Comparing  $AcOH-UiO-66_{(96/24)}$  to  $AcOH-UiO-66_{(128/32)}$  shows that the most notable difference is in their respective saturation loadings. The former represents a sample with missing-cluster defects whereas the latter represents a sample with missing-linker defects. b) Comparing  $AcOH-UiO-66_{(96/24)}$  to  $AcOH-UiO-66_{(96/24)c}$  reveals that the most notable difference is in the isotherm steps. Both models exhibit missing-cluster defects, but the former corresponds to the traditional UiO-66-*reo* representation, whereas the latter corresponds to consecutive or “coalesced” missing-clusters.

Together, the aforementioned observations suggest that if the experimental isotherms are to be correlated with the simulated ones, both saturation loadings and adsorption steps should be considered. Because the adsorption steps are sensitive to the finer details of the pore structure, such a correlation should yield information regarding the “local”<sup>150</sup> distribution of defect-containing regions in  $AcOH-UiO-66$ <sup>5.2/6</sup>,  $HCl-UiO-66$ <sup>4.2/6</sup>, and  $BzOH-UiO-66$ <sup>4.0/6</sup>. Consistent with our expectations, structures such as  $AcOH-UiO-66_{(176/32)}$ , which has regularly distributed missing linkers, have isotherms steps that are very close to that of the defect-free  $AcOH-UiO-$

$66_{(192/32)}$ , with only a minor difference in the filling of the tetrahedral pores (purple box in Appendix B, Figure B17).

For each derivative of UiO-66, the simulated  $N_2$  isotherms for all eight structural models (i.e., 1 defect free model plus 7 defect-containing model with the same capping agent (Appendix B, Figures B11-B13)) were plotted on semi-log ( $\log(P/P_o)$  vs. cc/g) scales (Appendix B, Figure B16) and compared to the experimental  $N_2$  isotherms. The best fit between the simulated isotherms and the experimental isotherm was determined based on “concurrently best-matching” three criteria: i) the L/N ratio of the sample and the model, ii) the saturation loading, and iii) the isotherm shape (i.e., number, locations, and pressure range of the steps in the isotherm). Based on these criteria, the structural model that corresponds to the best-fit simulated isotherm was deemed most likely to describe pore structure for the synthesized UiO-66 derivatives.

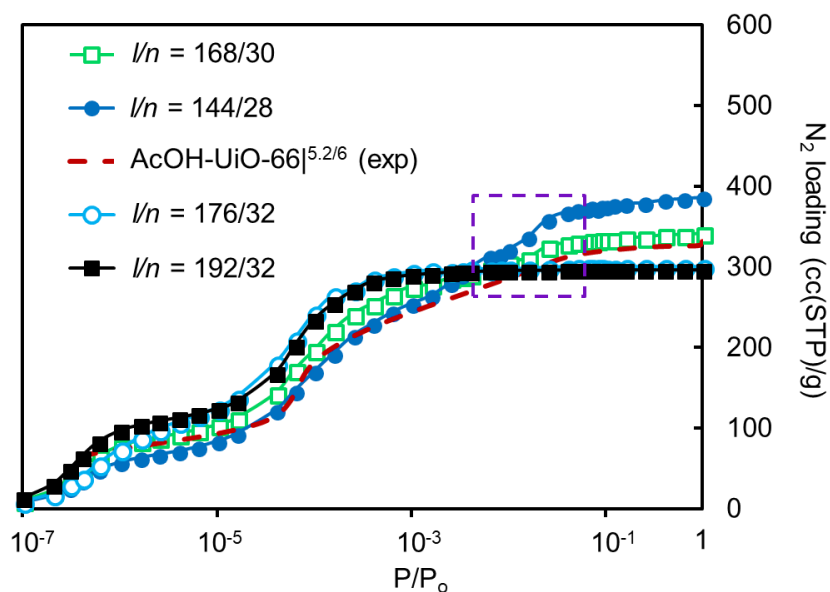


**Figure 3.7** Comparison of experimentally obtained isotherm for  $AcOH-UiO-66_{(5.2/6)}$  with simulated isotherms in  $AcOH-UiO-66_{(l/n)}$  supercell models.



As an illustration, the synthesized  $\text{AcOH-UiO-66}|^{5.2/6}$  derivative, with the lowest defect density in all of our samples, was compared to models with high L/N ratios and acetate caps:  $\text{UiO-66}_{(192/32)}$  (L/N = 6, defect-free UiO-66),  $\text{AcOH-UiO-66}_{(176/32)}$  (L/N = 5.5, missing-linker defects),  $\text{AcOH-UiO-66}_{(168/30)}$  (L/N = 5.6, missing-cluster defects), and  $\text{AcOH-UiO-66}_{(144/28)}$  (L/N = 5.1, missing-cluster defects). Plotting all the isotherms on the same semi-log plot (Figure 3.7) reveals  $\text{AcOH-UiO-66}_{(168/30)}$  model to be the best match for  $\text{AcOH-UiO-66}|^{5.2/6}$  as both the isotherm shape and the saturation loading are nearly identical to the those obtained experimentally. In particular, both the experimental and simulated isotherms possess a subtle step at  $P/P_0 \sim 1.5 \times 10^{-2}$  that corresponds to pore filling of the extra cavities created by the missing-cluster defects (purple box in Figure 3.7).

Interestingly, the simulated isotherm for  $\text{AcOH-UiO-66}_{(176/32)}$  (L/N = 5.5, missing-linker defects) is quite close to that of the defect-free  $\text{UiO-66}_{(192/32)}$ , suggesting that missing-linker defects alone in near-perfect samples will be difficult to detect using our model-matching strategy, which relies on the detection of changes in the pore structure. In contrast, low-level differences of missing-cluster defects can be easily discerned: while the L/N ratio for  $\text{AcOH-UiO-66}|^{5.2/6}$  is closest to that for  $\text{AcOH-UiO-66}_{(144/28)}$ , with four missing clusters per supercell, the fit is better with  $\text{AcOH-UiO-66}_{(168/30)}$ , with only two missing clusters per supercell. Together, these observations allow us to infer that while  $\text{AcOH-UiO-66}|^{5.2/6}$  is most likely to have “two missing clusters/supercell” as well-simulated by  $\text{AcOH-UiO-66}_{(168/30)}$  (L/N = 5.6), it also has additional missing linkers as indicated by its smaller L/N ratio; however, these missing linker defects do not change the pore structure significantly. Such a conclusion highlights the potential synergism that can be obtained with our combined experiment-modeling approach to allow for a detailed analysis

of the pore structure for UiO-66-type of materials. In addition, the good match between the experimental isotherm for AcOH-UiO-66<sup>5.2/6</sup> and the simulated isotherm for *AcOH-UiO-66*<sub>(168/30)</sub> supports the appropriateness of our choice for the  $2 \times 2 \times 2$  supercell.

Similar comparative analyses (see Appendix B, Figure B18) were carried out to determine top candidate models for HCl-UiO-66<sup>4.2/6</sup> and BzOH-UiO-66<sup>4.0/6</sup>. As mentioned earlier, the nodes of HCl-UiO-66<sup>4.2/6</sup> were found to be primarily capped with formate (instead of a [ $\mu_1$ -Cl +  $\mu_1$ -H<sub>2</sub>O] combination, as would have been expected with an HCl-modulated synthesis) through <sup>1</sup>H NMR analysis. This observation provides us with an opportunity to test the sensitivity of our simulated models against the steric nature of the experimentally found capping agent. To this end, we searched for the best-fit simulated isotherm to the experimentally determined isotherm for HCl-UiO-66<sup>4.2/6</sup> from each set of *FOH-UiO-66* and *HCl-UiO-66* (i.e., terminated with the [ $\mu_1$ -Cl +  $\mu_1$ -H<sub>2</sub>O] combination) models (Appendix B, Figures B12-B13) and plotted them together (Appendix B, Figure B18a). Gratifyingly, the best match to the experimentally determined isotherm for HCl-UiO-66<sup>4.2/6</sup> was with the simulated isotherm for *FOH-UiO-66*<sub>(114/25)</sub> (L/N = 4.6) (Figure 3.8b) the best-fit model for the *FOH-UiO-66* set, instead of that for *HCl-UiO-66*<sub>(114/25)</sub> (L/N = 4.6) the best-fit model for the *HCl-UiO-66* set: The steps in the former correlate quite well with those in the experimental isotherm, while those for the latter consistently overestimate the gravimetric adsorption.<sup>151</sup>

For BzOH-UiO-66<sup>4.0/6</sup>, the two possible models are *BzOH-UiO-66*<sub>(96/24)</sub> and *BzOH-UiO-66*<sub>(96/24)*c*</sub>, having the same L/N ratio (4.0) but different structures: the missing-cluster defects are regularly distributed throughout the supercell in *BzOH-UiO-66*<sub>(96/24)</sub> (i.e., UiO-66-*reo*) but coalesced together in *BzOH-UiO-66*<sub>(96/24)*c*</sub> (i.e., comprising both UiO-66-*fcu* and UiO-66-*reo*

domains; cf Figures 3.4g,h). Both simulated isotherms exhibit the same saturation loadings (at  $P/P_0 \sim 0.1$ , SI, Appendix B, Figure B18b) as the experimental isotherm, indicating that the amount and types of defects in  $\text{BzOH-UiO-66}^{4.0/6}$  are appropriately captured by the two models. The simulated isotherm for  $\text{BzOH-UiO-66}_{(96/24)c}$  matches better to the experimental isotherm (Figure 3.8c, see also Appendix B, Figure B18b), signifying that  $\text{BzOH-UiO-66}^{4.0/6}$  is most likely comprised of coalesced missing clusters and defect-free regions.

A careful examination of the gravimetric loadings in the  $0.001 < P/P_0 < 0.1$  region for all three isotherms suggests that the  $\text{BzOH-UiO-66}^{4.0/6}$  crystallites most likely contain a distribution of missing nodes and defect-free domains that is more heterogeneous than that in  $\text{BzOH-UiO-66}_{(96/24)c}$ . The good match between the experimental isotherm and the simulated isotherm for  $\text{BzOH-UiO-66}_{(96/24)c}$  in the  $10^{-5} < P/P_0 < 10^{-3}$  region suggests the presence of both  $\text{UiO-66-reo}$  and  $\text{UiO-66-fcu}$  domains. However, the smooth, almost stepless rise in the  $10^{-5} < P/P_0 < 10^{-2}$  region of the experimental isotherm (Appendix B, Figure B18b, boxed region) is also consistent with the presence of a broad range of cavities (e.g., inherent octahedral cavities and the pores from the missing-node defects) being filled at the same time. Such a situation can potentially occur if these domains are more randomly distributed than in our  $2 \times 2 \times 2$  supercell.

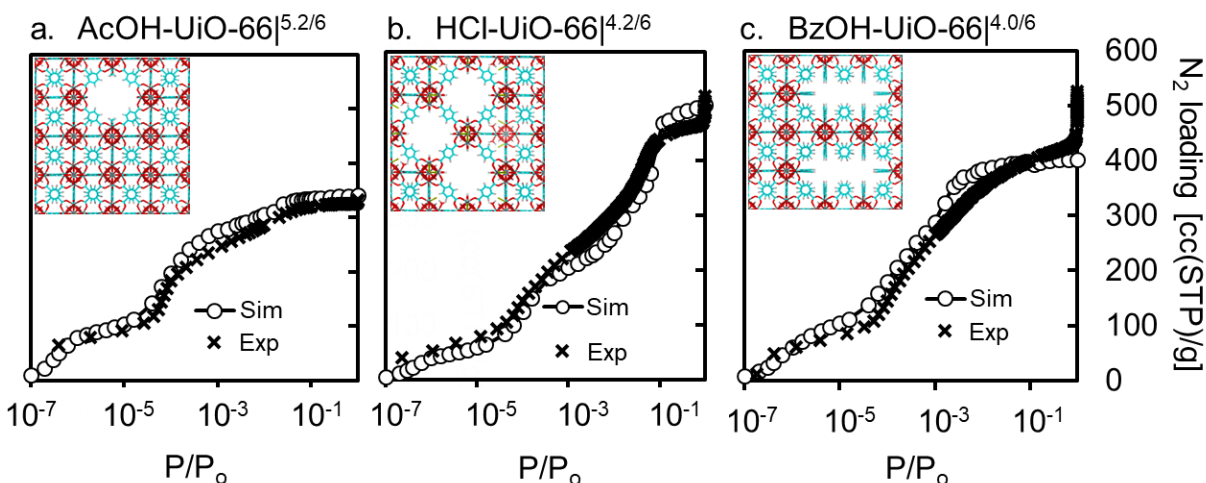


**Figure 3.8** Best match between measured and simulated isotherms for each tested sample. The model representing each sample is shown as inset in each panel. a) Measured isotherm in  $\text{AcOH-UiO-66}|^{5.2/6}$  vs. simulated isotherm in  $\text{AcOH-UiO-66}_{(168/30)}$ . b) Measured isotherm in  $\text{HCl-UiO-66}|^{4.2/6}$  vs. simulated isotherm in  $\text{FOH-UiO-66}_{(114/25)}$ . c) Measured isotherm in  $\text{BzOH-UiO-66}|^{4.0/6}$  vs. simulated isotherm in  $\text{BzOH-UiO-66}_{(96/24)c}$ .

**Table 3.1** Summary of measured properties for UiO-66 samples and simulated properties in the corresponding *in silico* models. Simulated values in parenthesis.

Sample	Model	L/N	BET area (m <sup>2</sup> /g)	V <sub>p</sub> [cc/g]
$\text{AcOH-UiO-66} ^{5.2/6}$	$\text{AcOH-UiO-66}_{(168/32)}$	5.2 (5.6)	1328 (1405)	0.50 (0.54)
$\text{HCl-UiO-66} ^{4.2/6}$	$\text{FOH-UiO-66}_{(114/25)}$	4.2 (4.6)	1802 (1772)	0.73 (0.78)
$\text{BzOH-UiO-66} ^{4.0/6}$	$\text{BzOH-UiO-66}_{(96/24)c}$	4.0 (4.0)	1628 (1694)	0.65 (0.62)
$\text{de-BzOH-UiO-66} ^{4.0/6}$	$\text{FOH-UiO-66}_{(96/24)c}$	4.0 (4.0)	1700 (1826)	0.80 (0.86)
$\text{de'-BzOH-UiO-66} ^{4.0/6}$	$\text{HCl-UiO-66}_{(96/24)c}$	4.0 (4.0)	1700 (1810)	0.76 (0.82)

### 3.5 Molecular modelling-assisted property-prediction

Prompted by the success of our model in elucidating the pore architectures of three very different, experimentally obtained UiO-66 derivatives, we set out to test its capability to delineate small changes in pore architecture when the capping ligands for the  $\text{BzOH-UiO-66}|^{4.0/6}$  derivative are completely modified by post-synthesis treatments. Thus, we subjected this derivative to an

HCl-in-DMF treatment<sup>152</sup> to replace the carboxylate “caps” with formates, as verified for *HCl-UiO-66*<sub>(114/25)</sub>, and later an HCl-in-butanol treatment to probe the MOF without formate or benzoate caps (Figure 3.9). We anticipated that these replacements would maintain the original framework for the MOFs and can be elucidated through changes in the adsorption isotherms.

As expected, compositional analyses of the HCl-in-DMF “decapped” samples (see Appendix B, Figure B6-B8 and accompanying discussion) showed that formates have successfully replaced the modulator carboxylate caps of *BzOH-UiO-66*<sup>4.0/6</sup> to give the “decapped” MOF *de-BzOH-UiO-66*<sup>4.0/6</sup>. <sup>1</sup>H NMR analysis of digested samples of these decapped derivatives shows L/N ratios that are very similar to those of the parent MOFs with no traces of their respective modulator caps. The high amounts of formic acid (Appendix B, Figure B9, Table B4 entry 4) support our earlier observations that formates can indeed serve as replacement capping ligands to the nodes. SEM images (Appendix B, Figure B4) and PXRD profiles (Appendix B, Figures B1-B2) for *de-BzOH-UiO-66*<sup>4.0/6</sup> displayed no observable difference in the particle size/morphology and crystallinity as a result of the HCl treatment, consistent with no alterations in structural connectivities from that of the parent MOF. The measured BET areas for the decapped analogue also increased, consistent with the replacement of the larger initial capping benzoates with the smaller formates (Appendix B, Table B1, cf entry 3 vs 4). From the shape of the isotherms (Appendix B, Figure B3) and their corresponding pore size distribution (Figure 3.10c), when the bulky benzoate caps are absent, as in the case of *de-BzOH-UiO-66*<sup>4.0/6</sup>, the size of the new micropores increases by ~4 Å, which results in a pore large enough<sup>128</sup> to broaden the saturation step; similar to for HCl-*UiO-66*<sup>4.2/6</sup>.

As  $\text{BzOH-UiO-66}^{4.0/6}$  was matched best to  $\text{BzOH-UiO-66}_{(96/24)c}$ , we expect that  $\text{de-BzOH-UiO-66}^{4.0/6}$  should closely resemble  $\text{FOH-UiO-66}_{(168/30)c}$ . This is indeed the case as shown in Figure 3.9a: The experimental  $\text{N}_2$  adsorption isotherm of  $\text{de-BzOH-UiO-66}^{4.0/6}$  matches much better to the simulated isotherm for  $\text{FOH-UiO-66}_{(168/30)c}$  than  $\text{HCl-UiO-66}_{(168/30)c}$ . The only slight discrepancy is in the  $0.1 < P/P_0 < 1$  region, where the simulation isotherm shows a step and the experimental isotherm has a smooth, almost-stepless rise. As discussed at the end of the previous section, this latter behavior is consistent with the presence of a broad range of large cavities, being filled in at the same time. Again, such a situation is possible if the  $\text{UiO-66-reo}$  and  $\text{UiO-66-fcu}$  domains are more randomly distributed in the experimental  $\text{de-BzOH-UiO-66}^{4.0/6}$  sample than is modeled by our  $2 \times 2 \times 2$  supercell, leading to a higher level of heterogeneity.

As a last test of our model, we subjected  $\text{BzOH-UiO-66}^{4.0/6}$  to an HCl-in-butanol treatment (to give  $\text{de}'\text{-BzOH-UiO-66}^{4.0/6}$ ), where the carboxylate capping ligands could be replaced with coordinating alcohol molecules,<sup>153</sup> a  $[\mu_1\text{-Cl} + \mu_1\text{-H}_2\text{O}]$  or a  $[\mu_1\text{-OH} + \mu_1\text{-H}_2\text{O}]$  combination and should afford a change that is detectable by the adsorption isotherm.  $^1\text{H}$  NMR analysis of  $\text{de}'\text{-BzOH-UiO-66}^{4.0/6}$  sample revealed that neither formates nor butanol caps were present on the MOF. Thus to probe if the defect sites were capped with  $[\mu_1\text{-Cl} + \mu_1\text{-H}_2\text{O}]$  or  $[\mu_1\text{-OH} + \mu_1\text{-H}_2\text{O}]$  we compared the  $\text{N}_2$  isotherms. As shown in Appendix B, Figure B3, the adsorption isotherms for  $\text{BzOH-UiO-66}^{4.0/6}$ ,  $\text{de-BzOH-UiO-66}^{4.0/6}$ , and  $\text{de}'\text{-BzOH-UiO-66}^{4.0/6}$  are fully distinguishable in the semi-log plot. While the adsorption isotherms of the two decapped samples are quite similar, that for  $\text{de}'\text{-BzOH-UiO-66}^{4.0/6}$  has a higher gravimetric loading in the  $0.001 < P/P_0 < 0.1$  regions, not surprisingly given the slightly smaller size of the  $[\mu_1\text{-Cl} + \mu_1\text{-H}_2\text{O}]$  or  $[\mu_1\text{-OH} + \mu_1\text{-H}_2\text{O}]$  caps as compared to formate caps. Interestingly, from the comparisons with the simulated isotherms

(Figure 3.9b, bottom panel), the best-fit simulated isotherm (when considering the number of distinct steps) can be generated from the model with  $[\mu_1\text{-Cl} + \mu_1\text{-H}_2\text{O}]$  caps suggesting this combination as the primary caps for the defect sites.<sup>154</sup> Together, this sequence of experiments and the good agreement with the simulations provide a strong endorsement for the ability of our model to capture or predict chemical changes in the MOF crystallites after post-synthesis modification – even to the point of delineating sterics surround the node.

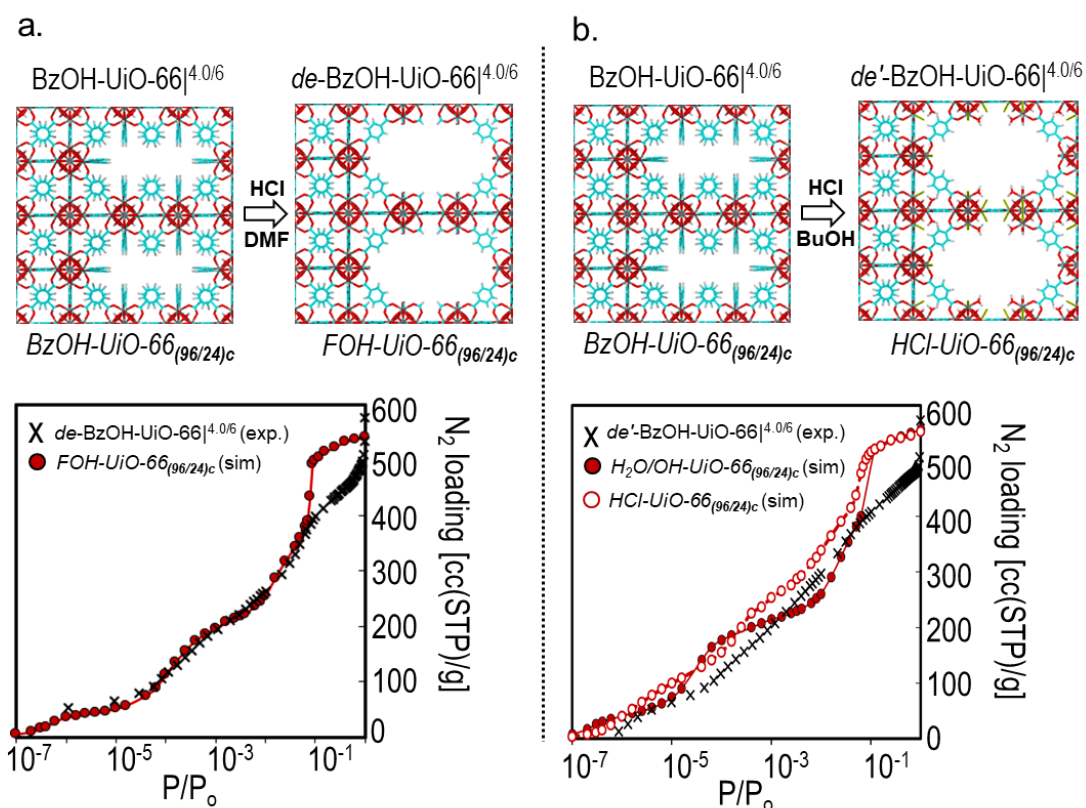


**Figure 3.9** Comparison between measured isotherms for each post-synthetically modified (decapped) sample of  $BzOH\text{-}UiO\text{-}66|^{4.0/6}$  ( $BzOH\text{-}UiO\text{-}66_{(96/24)c}$ ) and the simulated isotherms in the corresponding models predicted based on the expected changes in the structure due to differences in treatment. a) Measured isotherm in  $de\text{-}BzOH\text{-}UiO\text{-}66|^{4.0/6}$  and simulated isotherm in  $FOH\text{-}UiO\text{-}66_{(96/24)c}$ . b) Measured isotherm in  $de'\text{-}BzOH\text{-}UiO\text{-}66|^{4.0/6}$  and simulated isotherm in  $H_2O/OH\text{-}UiO\text{-}66_{(96/24)c}$  and  $HCl\text{-}UiO\text{-}66_{(96/24)c}$ . The experiment-simulation match was comparable to the one

obtained for the non-treated versions (Figure 3.8), indicating our prediction to be correct, which was further verified by subsequently obtained experimental data.

### 3.6 Correlation to pore-size distributions, framework stability, and crystallinity

Based on all the experimental and simulation data discussed thus far, we can completely delineate the evolution of the pore architecture found in our different UiO-66 derivatives depending on the modulator and post-synthesis treatment (Figure 3.10). Although AcOH-UiO-66<sup>5.2/6</sup>, HCl-UiO-66<sup>4.2/6</sup>, and BzOH-UiO-66<sup>4.0/6</sup>, our three initial MOFs, could all possess missing-linker and missing-cluster defects, the missing-cluster defects are more readily detected by low-pressure adsorption data and can be used as a primary handle for structure elucidation. For AcOH-UiO-66<sup>5.2/6</sup>, the derivative with the lowest density of defects, the structure is comprised mostly of defect-free regions with some missing-cluster regions. For HCl-UiO-66<sup>4.2/6</sup> and BzOH-UiO-66<sup>4.0/6</sup>, the two starting UiO-66 derivatives with similarly high defect densities, the density of missing-cluster defects greatly increases; however only the latter possesses regions of coalesced missing-cluster defects. Such differences are attributed to the ability of the bulky benzoate capping ligands to modulate the synthesis and introduce such defects.



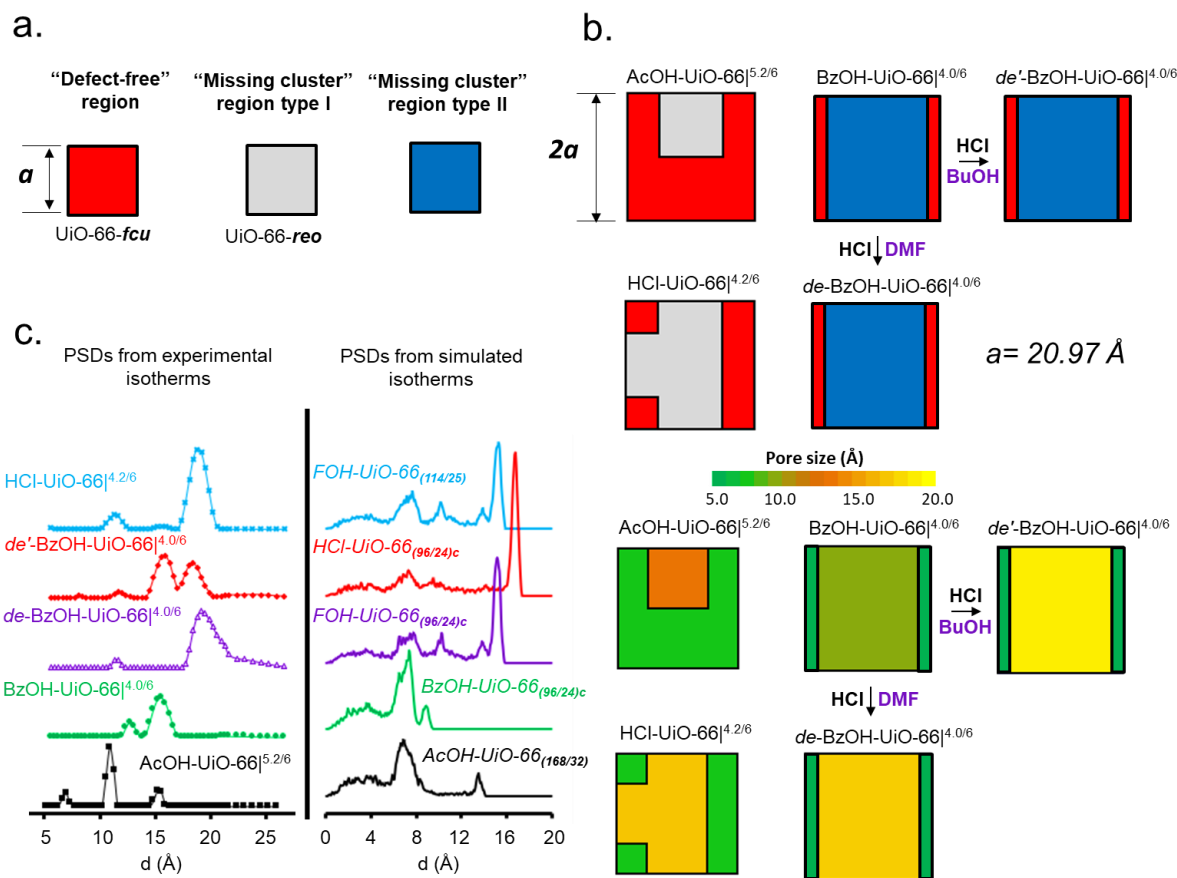


**Figure 3.10** a) Nomenclature for schematics in panel *b*. Square size represents a unit cell size. b) Schematics summarizing the structural changes in the supercells of UiO-66 samples as a result of missing-cluster types (top panel) and pore sizes (bottom panel). c) Pore size distributions (PSDs) obtained by applying classical density functional theory (DFT) to the measured isotherms, along with PSDs obtained geometrically in the structural model representing the sample. Note that the missing cluster region type II has a higher density of defects than the type I.

Through the post-synthesis treatment of the  $\text{BzOH-UiO-66}^{4.0/6}$  material, we showed that the pre-assigned models can be used to predict the structural behavior when the acid caps are replaced. As surmised in Figure 3.10b, not only are the missing cluster models best suited for describing these materials, but the replacement of the capping agents does not change the

framework. However, the pore sizes (Figure 3.10c), are slightly larger and changes to their N<sub>2</sub> saturation behavior can now be observed and elucidated in their corresponding isotherms.

The difference in pore structure between HCl-UiO-66<sup>|4.2/6</sup> and BzOH-UiO-66<sup>|4.0/6</sup> can be manifested into observable differences in physical stabilities. When the benzoate capping ligands in BzOH-UiO-66<sup>|4.0/6</sup> are replaced by formates, the resulting *de*-BzOH-UiO-66<sup>|4.0/6</sup> material is compositionally quite similar to those of the as-synthesized HCl-UiO-66<sup>|4.2/6</sup>. However, the coalesced-missing-cluster pores of *de*-BzOH-UiO-66<sup>|4.0/6</sup> appear to be mechanically less stable than the non-coalesced-missing-cluster pores of HCl-UiO-66<sup>|4.2/6</sup> based on water uptake-desorption studies (Appendix B, Figure B25 and accompanying discussion). Compared to other samples, the water-vapor-uptake capacity of *de*-BzOH-UiO-66 quickly degrades upon cycling, suggesting that its pores are quite susceptible to collapse induced by capillary forces.

Lastly, further experimental support for the assumption that the crystalline MOF samples with high defect density comprises both UiO-66-*fcu* (ideal) and UiO-66-*reo* (defect-containing) regions can be seen in the PXRD data obtained with synchrotron radiation (Appendix B, Figure B1) as briefly discussed at the beginning of this work. Low-intensity broad peaks in the  $5^\circ < 2\theta < 7^\circ$  region were clearly observed in the PXRD profiles for HCl-UiO-66<sup>|4.2/6</sup>, BzOH-UiO-66<sup>|4.0/6</sup>, and *de*-BzOH-UiO-66<sup>|4.0/6</sup>. That these peaks are not as high-intensity and as sharp as the peaks simulated for UiO-66-*reo* in this same region is consistent with the presence of a mixture of domains<sup>108</sup> and with local ordering similar to those shown in our models.

### 3.7 Conclusion

In summary, we have demonstrated how the pore structure of various defect-containing derivatives of UiO-66 can be successfully elucidated by modeling their N<sub>2</sub> adsorption isotherms

over a broad range of pressure ( $10^{-7} < P/P_0 < 1$ ). Compositional analyses of the MOF derivatives allowed us to deduce their L/N ratio and the type of capping ligands in each experimental sample. Based on this data, a series of models with different levels and types of defects was constructed and used to generate a series of  $N_2$  adsorption isotherms using GCMC simulations. Identifying the best match for the isotherm of a sample among these simulated isotherms enables a good correlation of the pore structure in the model to that in the experimental sample. This process allows us to infer that  $BzOH-UiO-66|^{4.0/6}$  and  $HCl-UiO-66|^{4.2/6}$ , with similar L/N ratio, can have very different pore structures, where the missing-cluster defects in the former can coalesce into large regions, a difference that manifests into differences in stabilities during water-vapor-uptake studies. Notably, this comparative modeling strategy can be used to elucidate the adsorption behaviors when the bulky benzoate caps in  $BzOH-UiO-66|^{4.0/6}$ , the derivative with the highest defect density, were replaced with smaller capping ligands.

In conjunction with the many studies that have been published on the nature of defects in UiO-66, the strategy outlined in this work can serve as a powerful tool for elucidating the pore structure of MOFs possessing defects, especially as a function of synthetic conditions and post-synthesis modification. The high sensitivity of the isotherm to minute changes in the steric environment at the node, as reflected through the pore-filling behaviors at low  $P/P_0$  regions, can reveal local chemical information at the node that is difficult to obtain with conventional X-ray techniques. In addition, the rich information (steps and rises in the isotherms) that can be inferred through data obtained using only commercially available equipment, and made apparent in the semi-log plot, can allow researchers to deduce the heterogeneity level in the distributions of the defects. While we only demonstrated the possibilities with a small  $2 \times 2 \times 2$  supercell, larger

model sets that span across more unit cells and comprise a broader range of defect distributions should allow for better and more accurate structure elucidation of defect-containing MOFs.

## Chapter 4

### **Correlating transport diffusion of linear hydrocarbons through MOF pores to their level of van der Waals interactions with the pore environment**

Portions of this chapter appear in the following manuscript:

Audu, C. O.; Chen, D.; Kung, C. W.; Snurr, R. Q.; Nguyen, S. T.; Farha, O. K.; Hupp, J. T.;

“Transport diffusion of linear alkanes (C<sub>5</sub>-C<sub>16</sub>) through thin films of ZIF-8 as assessed by quartz crystal microgravimetry.” *manuscript under revision.*

## 4.1 Introduction and Overview

The increasing interest in using these tunable porous MOFs for gas storage,<sup>155-156</sup> separations,<sup>157</sup> and chemical sensing,<sup>43</sup> has led to several iterative designs of adsorbents where the sorptive sites are chemically engineered onto a MOF's linkers or nodes (similar to the approach shown in Chapters 2), but in a structurally benign manner to prevent degradation (as discussed in Chapter 3). As mentioned in Chapter 1, a third approach for installing sorptive sites into a MOF is through the pore itself. This method, though not as developed as the other two strategies, uses pore environment collectively to sequester a single substrate (Chapter 1, Figure 1.1). These scenarios typically feature larger substrates that are slightly smaller than the pore diameters and apertures. Optimal implementation of these strategy towards the aforementioned applications, necessitates the ability to easily screen and understand how target molecules diffuse/effuse through the pores of these materials.

To this end, transport diffusivity ( $D$ ) has emerged as an instructive property of guest molecules in porous crystalline MOFs.<sup>158-159</sup> A chemically simple, but conceptually interesting set of systems consists of linear alkanes and ZIF-8, a methyl-imidazolate based MOF featuring the sodalite topology. ZIF-8 contains sizable, roughly-spherical cavities ( $\sim 11.6$  Å diameter,  $\sim 820$  Å<sup>3</sup> volume), interconnected by six-ring windows with a crystallographic width of  $\sim 3.4$  Å (as well as narrower four-ring windows connected to smaller pores).<sup>160-161</sup> For comparison, minimum equilibrium cross-sectional diameters for linear alkanes comprising three or more carbons are more-or-less identical, with a value of  $\sim 4.3$  Å, which is significantly greater than the window crystallographic width.<sup>161</sup> Nevertheless, numerous "over-sized" species (*i.e.*, species with kinetic diameters,  $K_D$ , greater than  $3.4$  Å) including *n*-propane, *iso*-butane ( $K_D \sim 5.0$  Å),<sup>162</sup> Xe ( $K_D \sim 4.0$

Å),<sup>163</sup> SF<sub>6</sub> (K<sub>D</sub> ~ 5.5 Å),<sup>163</sup> and benzene (K<sub>D</sub> ~ 5.8 Å),<sup>164</sup> have been observed to permeate and diffuse through ZIF-8.<sup>162, 164-166</sup> In a key computational study, Fairen-Jimenez and co-workers, persuasively showed that hinge-like movement of methyl-imidazolate ligands on pairs of mono-zinc(II) nodes can reversibly expand ZIF-8 window widths sufficiently to permit passage of seemingly over-sized molecules.<sup>161</sup> These authors and others have additionally explicated the role of molecule/linker interactions in defining the energetic cost for reversibly expanding framework windows.<sup>167-169</sup>

Self-diffusivities within MOFs have been experimentally measured via pulse-field-gradient nuclear magnetic resonance<sup>165, 170-175</sup> and by quasi-elastic neutron scattering,<sup>176-177</sup> while transport diffusivities have been measured via gas pressure decay<sup>162</sup> and via single-crystal infrared microscopy.<sup>169</sup> Yet another MOF-applicable approach, specifically for transport diffusivities, is quartz crystal microgravimetry (QCM).<sup>178</sup> Indeed, QCM has been used to assess MOF-based, molecular transport diffusivities and/or uptake capacities for pyridine,<sup>179</sup> ferrocene,<sup>180</sup> chlorinated benzenes,<sup>181</sup> common organic solvents (*e.g.*, acetone, methanol, ethanol, propanol, isopropanol),<sup>182</sup> and other analytes/sorbates.<sup>46, 157, 159, 183-196</sup>

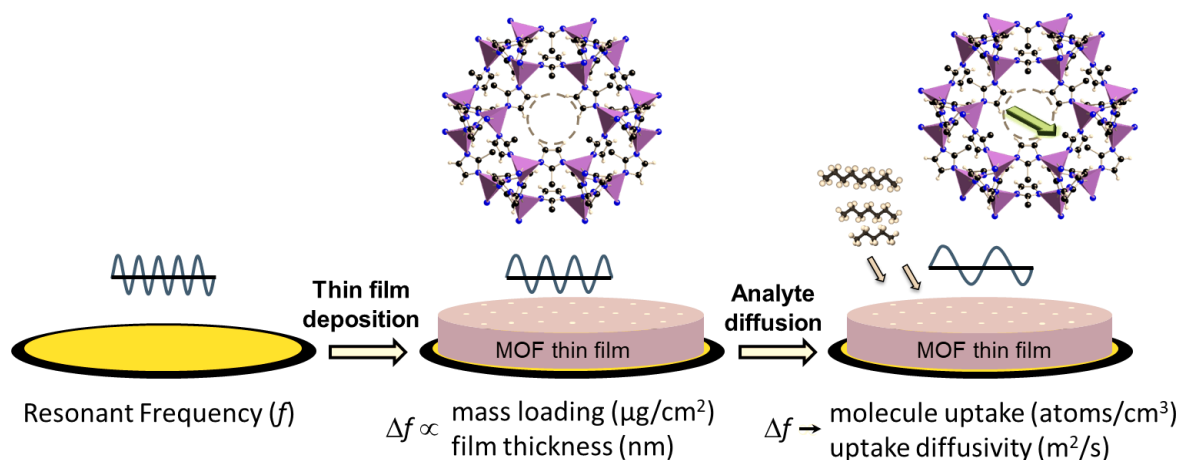


**Figure 4.1** A schematic showing how a QCM can be used to obtain key properties pertaining to MOF thin films (i.e., mass and thickness) and subsequent analyte diffusion studies (i.e., mass/molecule uptake and diffusivities)

As qualitatively illustrated in Figure 4.1, QCM measures changes in resonant frequency ( $\Delta f$ ) of an underlying, gold-electrode-driven, piezoelectric material (quartz), in response to mass-loading – either directly onto the oscillator or within a rigid or semi-rigid, analyte-permeable coating (such as a crystalline MOF). Response times and limits of detection, under optimal conditions, are  $\sim 20$  measurements/sec and  $\sim 0.4$  ng/cm<sup>2</sup>, *i.e.* low enough for quantitative evaluation of submonolayer amounts of molecular adsorbate on flat surfaces or fractions of a percent of guest uptake capacity for porous MOF films of thickness 100 nm or greater. Here we report uptake capacities and transport diffusivities for each of eight linear alkanes (ranging from C<sub>5</sub> to C<sub>16</sub>) in quartz-crystal-supported films of solvent-evacuated ZIF-8 crystals. As described and discussed below, we find that: a) measured uptake capacities are in good agreement with expectations based on fully guest-accessible MOF pores, b) transport dynamics are governed by guest diffusion through MOF crystallites rather than by rates of entry into films at the MOF/vapor permeation, and c) transport times can be substantially shortened (without changes in diffusivity) by replacing



closely packed films of nanocrystallites (dominant 1D intracrystalline diffusion) with loosely packed, electrophoretically deposited films<sup>197-198</sup> (dominant 3D intracrystalline diffusion). While not developed here, the combined results have potentially favorable implications for the development of kinetic separation schemes<sup>169, 199-203</sup> for closely related, and otherwise challenging to separate, linear hydrocarbons.

#### **4.2 Synthesis and characterization of ZIF-8 thin films**

ZIF-8 was initially deposited solvothermally onto gold-electrode-coated quartz crystals as described in Appendix C, Figure C1. The commercial piezoelectric crystals used here oscillate at *ca.* 5 MHz, with the frequency systematically decreasing as mass is deposited; thus, frequency changes can be used to quantify both the amount of ZIF-8 deposited and the amount of molecular guest taken up.

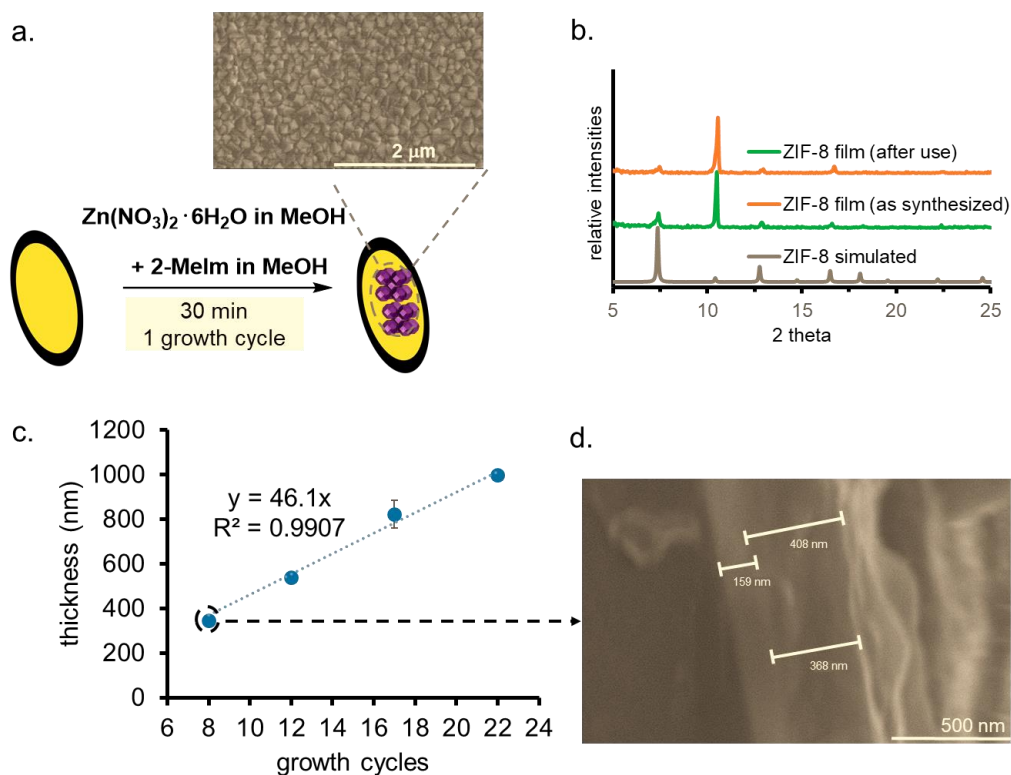


**Figure 4.2** (a) ZIF-8 thin film fabrication via solvothermal growth with an SEM image of the surface of the Au-QCM sensor. (b) XRD patterns of the ZIF-8 thin films grown solvothermally on the Au-QCM electrodes. (c) Plot of thicknesses of solvothermally grown films (determined by QCM) as a function of number of growth cycles. (d) Cross-sectional SEM image of a QCM electrode after 8 growth cycles

As shown in Figure 4.2 presents scanning electron micrographs of representative solvothermally grown films. The shown cross-sectional micrograph (Figure 4.2d), for a film prepared via eight solvothermal growth cycles, indicates a reasonably uniform thickness film (~400 nm), while the top view (Figure 4.2a), showcases the surface morphology consisting of intergrown ZIF-8 nanoparticles consistent with previous work from our lab.<sup>193</sup> X-ray diffraction (XRD) measurements (panel *b*) establish that the films are crystalline and that growth occurs preferentially in the 110 direction

Via the Sauerbrey equation (Equation 4.1),<sup>204</sup> measured shifts in resonator frequency,  $\Delta F$ , yielded mass increases,  $\Delta m$ , ranging from  $\sim 4$  to  $96 \mu\text{g}/\text{cm}^2$  for ZIF-8 deposition. In this equation,  $C_f$  is a constant whose value is determined by the resonant frequency (5 MHz), the piezoelectrically active area of the quartz crystal, the shear modulus of AT-cut quartz, and the density of quartz. Assuming the density of the deposited film,  $\rho_{\text{ZIF-8}}$ , is similar to that of a ZIF-8 single crystal ( $0.95 \text{ g}/\text{cm}^3$ )<sup>160, 205-207</sup> these masses correspond to thicknesses of  $\sim 43$  to  $920 \text{ nm}$  (Equation 4.2, and Appendix C, Figures C3-C4):

$$\Delta m = \frac{\Delta F}{C_f} \quad (4.1)$$

$$\text{Film thickness}(nm) = \frac{\Delta m}{\rho_{\text{ZIF-8}}} \quad (4.2)$$

Consistent with our previous findings,<sup>193</sup> the thicknesses of solvothermally grown ZIF-8 films increase linearly with the number of synthesis cycles (Figure 4.2c). Notably, thicknesses estimated in this way agree with film thicknesses determined from cross-sectional scanning electron microscopy (SEM) images (Figures 4.2d and Appendix C, Figure C3) with high reproducibility (see Appendix C, Section C5),<sup>208</sup> implying that the crystallites constituting the solvothermal films are closely packed.

#### 4.2 Determining the intracrystalline diffusivity in thin films

Our starting assumption is that transport of linear alkanes through solvothermally grown thin films of ZIF-8 is one-dimensional and governed by diffusion through the crystallites pores (*i.e.*, “intracrystalline diffusion” Figure 4.3a). A conceivable alternative, intentionally explored below for EPD grown films, is rapid permeation of voids between crystallites (effectively one-

dimensional diffusion if the film thickness is large compared with crystallite-crystallite spacing), followed by radial (three-dimensional) intracrystalline diffusion of guests simultaneously toward the centers of each of the many particles making up the films. To assess this alternative, we measured the uptake of *n*-hexane ( $K_D = 4.3 \text{ \AA}$ )<sup>209</sup> which we expected would fully occupy the large pores ( $\sim 12 \text{ \AA}$  diameter pores) of the crystallites, and compared it with cyclohexane ( $K_D = 6.0 \text{ \AA}$ )<sup>209</sup> a species known to be sterically excluded<sup>193, 209</sup> from pristine ZIF-8 (where the crystallographic width of ZIF-8's six-linker aperture is  $3.4 \text{ \AA}$ <sup>160</sup> with an estimated maximum flexible width of  $\sim 5 \text{ \AA}$ ).<sup>162, 164, 210-211</sup>

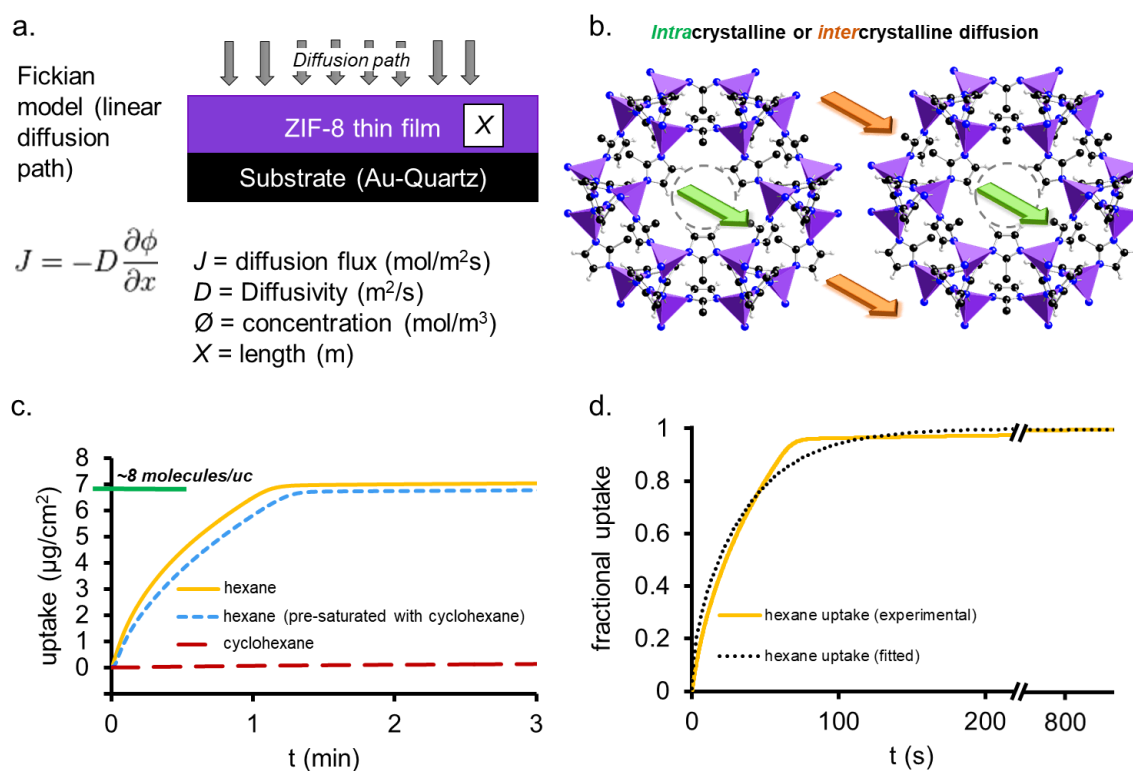


**Figure 4.3** (a) Linear diffusion model used to evaluate the alkane uptake by flat, compact, solvothermally grown films of ZIF-8. (b) Schematic representation of of intra- versus inter-crystalline through films of ZIF-8. (c) Experimental uptake (DA method) of hexane in the presence of air, hexane in the presence of cyclohexane

vapor, and cyclohexane in the presence of air. (d) Measurement and fit of the hexane uptake plot to Equation C2, Appendix C.

Figure 4.3c shows plots of guest uptake ( $\mu\text{g}/\text{cm}^2$ ) versus time for *n*-hexane and cyclohexane, for a representative film of thickness  $\sim 300$  nm. From the plots, it is evident that uptake of the linear alkane is much larger ( $\sim 50 \times$ ) than that of the cyclic alkane and corresponds to *ca.* 8 linear hexane molecules per unit cell.<sup>191,212</sup> The large difference in uptake capacity is consistent with comparatively close packing of ZIF-8 microcrystallites, exclusion of cyclohexane from the MOF interior space, and the presence of only a marginal amount of guest-accessible, defect sites (e.g., from missing linkers) or intercrystalline void space.<sup>213</sup> These observations suggest the applicability of a simple one-dimensional diffusion model (Equation C2). Implicit in Equation C2, Appendix C, is the applicability of Fick's first law (Figure 4.3a), where we assume that diffusion proceeds from top of the film (as sketched, *i.e.* the film/vapor interface) to the bottom, and that the concentration ( $\phi$ ) of the guest at the outermost edge of the film is maximal and constant throughout the course of each diffusion experiment.<sup>214</sup> Additionally, we assume that because measurements are made using saturated vapor, the equilibrium state (final state) of the system is one in which all guest-accessible space within the film (whether pores or voids (or both)) is occupied by linear guest molecules.

Figure 4.3d shows a fit of uptake data for *n*-hexane to Appendix C, Equation C2, which returns a transport diffusivity of  $1.0 \times 10^{-15}$   $\text{m}^2/\text{s}$ . For cyclohexane, where uptake is limited to film voids, the apparent transport diffusivity is  $3.5 \times 10^{-17}$   $\text{m}^2/\text{s}$  (Appendix C, Figure C8). Given the 30-fold difference, we conclude that *n*-hexane infiltrates solvothermally prepared ZIF-8 films via entry at the outermost edge of the film, followed by one-dimensional diffusion through the interior

of the MOF, rather than by rapid filling of voids between crystallites, followed by entry into, and diffusion through, individual crystallites from multiple directions.<sup>215</sup>

Close inspection of Figure 4.3d shows that while the fit to Appendix C, Equation C2 appears to capture the essence of the diffusivity (for example, for 50% occupancy, the fit returns nearly the same uptake time as does the experiment), the fit curve rises slightly more rapidly than the experimental curve at early times (low occupancy), while lagging the experimental curve at 90% occupancy. An assumption in our fits is that the value of the transport diffusivity is insensitive to the extent of pore occupancy. Results for related systems – for example C<sub>1</sub>-C<sub>4</sub> in ZIF-4 – show that transport diffusivities can vary, and even increase, with guest fractional occupancy.<sup>169</sup> With this possibility in mind, we extracted transport diffusivities in the low-uptake limit by turning to Equation 4.3:<sup>179</sup>

$$f(t) \approx \frac{2}{\sqrt{\pi}} \sqrt{\frac{Dt}{L^2}} \quad (4.3)$$

where  $L$  is the film thickness. In using Equation 4.3, we assume that the thickness of the diffusion field is less than  $L$ , a condition that should be satisfied at early times.  $D$  is available from slopes of plots of fractional uptake versus  $t^{1/2}$  at early times and low guest uptake ( $0 < f(t) \leq 0.25$  fractional uptake). For *n*-hexane, the limiting low-occupancy value of the transport diffusivity is  $1.4 (\pm 0.2) \times 10^{-15} \text{ m}^2/\text{s}$ , *i.e.*, only marginally different than the value obtained by fitting the full uptake curve to Appendix C, Equation C2 (See Figure 4.4a, below.)

#### 4.4 Rate-limiting interface permeation?

One further possibility, not yet excluded, is that *n*-hexane transport through solvothermal films is kinetically limited by entry into the film, rather than by diffusion through the film.<sup>216</sup> A

high-density of collapsed pores at the outer edge of the film, for example, could lead to a large interfacial resistance to mass transport.<sup>216-217</sup> If this were the case, the apparent transport diffusivity would increase with increasing film thickness. Appendix C, Figure C13a-c shows instead, that the putative transport diffusivity for *n*-hexane, decane, and dodecane is more or less invariant for films ranging in thickness from ~ 250 nm to 880 nm. From these sets of data, we conclude that intracrystalline diffusion, rather than vapor-phase to MOF-phase guest transfer, is the rate-limiting process for guest uptake.

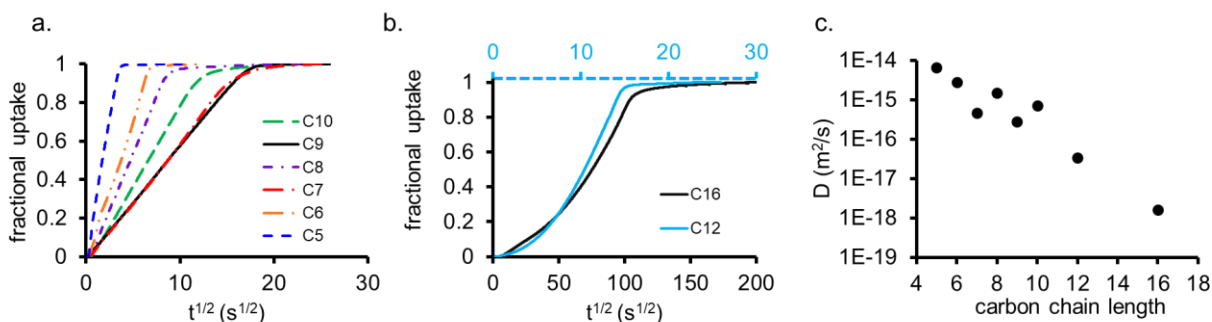


**Figure 4.4** Fractional uptake versus  $t^{1/2}$  for (a) *n*-pentane through *n*-decane and (b) *n*-dodecane and *n*-hexadecane. (c) Semi-log plot of the obtained diffusivities for C<sub>5-16</sub> versus carbon chain length (please see Appendix C, Figure C11 for the corresponding  $D$  values and section C4 for further discussion on their reproducibility). Diffusivities for all guests were determined from application of Equation 4.3 to the plots in panels *a* and *b* in the region of initial uptake. On average, each additional carbon decreases the transport diffusivity by a factor of two. Closer examination appears to indicate an “odd-even” effect, where alkanes having even numbers of carbon atoms display transport diffusivities that are larger than one would expect based on comparisons to alkanes having odd numbers of carbons.

The QCM-based evaluation of transport diffusivity was extended to encompass C<sub>5</sub>-C<sub>10</sub>, C<sub>12</sub>, and C<sub>16</sub>. Figure 4.4a shows plots of fractional uptake versus  $t^{1/2}$  for *n*-pentane through *n*-decane. The individual curves are surprisingly linear, up nearly to saturation loading. Thus, Equation 4.3 was used to obtain  $D$  values – although as shown in Appendix C, Figure C11 these

values differ only marginally from those returned by Appendix C, Equation C2. Figure 4.4b shows results for *n*-dodecane and *n*-hexadecane. The shapes of the  $f(t)$  vs.  $t^{1/2}$  plots are strikingly different and appear to indicate, for both guests, that the value of  $D$  systematically increases with increasing guest occupancy (*e.g.*, by up to ~ 55 fold for C<sub>12</sub> from ~ 2% to ~72% occupancy). Further study will be needed in order to understand the effect; but, we note that precedents of guest occupancy-dependent diffusivities exist for other systems, including C<sub>1</sub>-C<sub>4</sub> in ZIF-4.<sup>169</sup> For purposes of comparison with transport diffusivities for C<sub>5</sub>-C<sub>10</sub> (in ZIF-8), we used  $D$  values for C<sub>12</sub> and C<sub>16</sub> corresponding to limiting low uptakes.

Figure 4.4c shows a semi-log plot of transport diffusivity versus carbon chain length. The plot spans almost four orders of magnitude in  $D$ , and is broadly linear – indicating a roughly exponential decrease in transport diffusivity with alkane length. Expressed differently, each added carbon, *on average*, decreases  $D$  by just over a factor of 2. Lacking charges or even significant bond dipoles, the alkanes presumably interact with the MOF mainly via induced polarizability, *i.e.* London dispersion forces, with greater interaction translating to slower diffusion. A combined computational and experimental study of uptake C<sub>1</sub>-C<sub>4</sub> by ZIF-8 showed that Henry’s Law adsorption constants increase by about a factor of 7 for each added carbon.<sup>191</sup> At the temperature investigated, a factor of 7 would be equivalent to a *ca.* -5 kJ/mol per carbon change in the free energy of adsorption.<sup>218</sup> Since a molecular guest need not completely detach from a pore wall in order to diffuse, it seems qualitatively reasonable that a 7-fold increase (per alkane carbon) in Henry’s Law constants would impose much less than a 7-fold penalty on the magnitude of the transport diffusivity.



Closer inspection of Figure 4.4c shows that superimposed on the general decrease in transport diffusivity with increasing carbon chain length is an apparent odd-even variation with number of carbons. Thus, heptane diffuses less rapidly than octane, and nonane diffuses less rapidly than decane, while the ratio of transport diffusivities for hexane versus heptane is *ca.* 5, rather than the above-mentioned factor of  $\sim 2$ . Odd-even variations have been reported for a wide variety of properties for linear alkanes and their derivatives. These properties include melting points,<sup>219</sup> heats of sublimation,<sup>220</sup> and packing energies for self-assembled monolayers<sup>221</sup> – with lower energies usually associated with having odd numbers of carbon atoms. Curiously, the transport diffusivity variations observed here point to lower barriers for even-numbered alkanes. Potentially related are observations by Hwang, *et al.* of transport diffusion of ethane, propane, *n*-butane, *n*-pentane, and *n*-hexane through ZIF-4;<sup>169</sup> they reported anomalously fast transport diffusion of *n*-pentane, with Monte Carlo simulations implicating chain-length-dependent pore-confinement effects as the cause. It is tempting to assume that pore-confinement effects for alkanes in ZIF-8 are somehow responsible for the odd-even diffusivity variations here; it will be interesting to see if evidence for such effects can be obtained from molecular dynamics simulations.

#### **4.5 Determining the intracrystalline diffusivity in coarser thick films**

An attractive alternative to solvothermal fabrication of MOF films is electrophoretic deposition from suspensions of MOF crystallites in low-polarity solvents.<sup>197-198</sup> MOF films formed by EPD typically feature sizeable voids between crystallites. That indeed is the case for ZIF-8, as shown previously and as evinced by electron microscopy; see Figure 4.5c,d. We reasoned that for molecular transport and uptake, these low-density films might behave as

collections of quasi-independent crystallites. Thus, transport could occur in hierarchical fashion: rapid vapor permeation of large voids, followed by uptake and three-dimensional diffusive transport of guest molecules toward the center of each particle. Under these circumstances, and as implied by Equation C3, Appendix C, the distances relevant for defining rates of uptake would be the radii of individual crystallites, rather than the overall thicknesses of films. For comparatively thick films and small crystallites, molecular uptake via the hierarchical three-dimensional diffusion scheme should be much faster than via one-dimensional film-diffusion of the type discussed above. Values of molecular diffusivities, however, should be insensitive to these details.

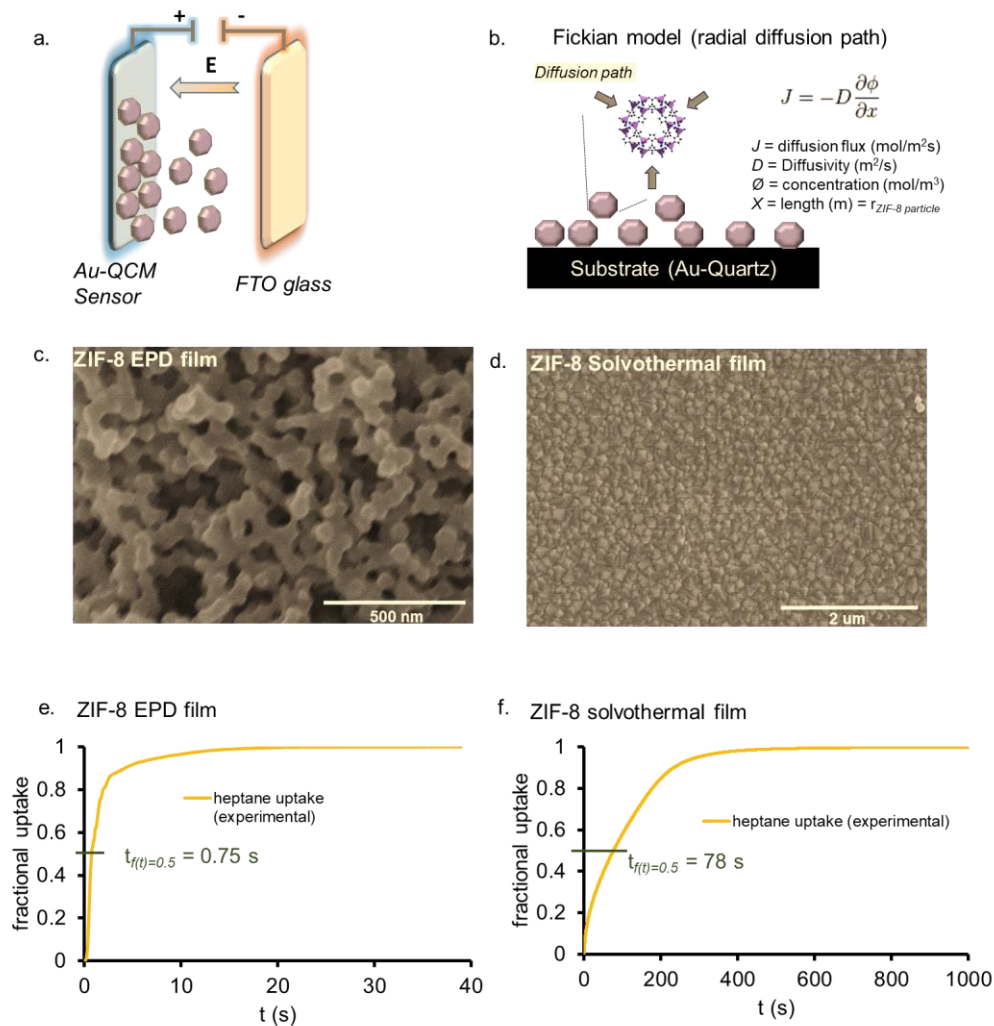


**Figure 4.5** (a) Schematic representation of electrophoretic deposition of ZIF-8 nanoparticles onto a QCM support. (b) Schematic depiction of radial diffusion model used to obtain transport diffusivities from mass versus time plots for EPD films. (c-d) SEM images of the top surfaces of ZIF-8 films prepared via EPD (c) or grown solvothermally (d). (e-f) Time course of heptane uptake by QCM-supported ZIF-8 films prepared by electrophoretic deposition (e) or by solvothermal growth (f). Note the roughly 100-fold shorter timescale for uptake by the EPD film.

Figure 4.5, panels (e) and (f) presents QCM-measured curves for uptake of heptane by EPD and solvothermal films, respectively. While the EPD film's mass, in this example, is 2.4 times that of the solvothermal film, the time required to reach 50% of the maximum uptake is ~100-fold

shorter for the EPD-formed film than the solvothermal film. From fits to the early portions of each curve (see box *a* in Appendix C, Figure C15 for details), the corresponding transport diffusivity values are  $2.4 (\pm 0.4) \times 10^{-16} \text{ m}^2/\text{s}$  (EPD) and  $4.6 (\pm 0.4) \times 10^{-16} \text{ m}^2/\text{s}$  (solvothermal). Given the simplifying assumptions made (*e.g.*, spherical crystallites, uniform film thicknesses, uniform crystallite size), we consider the agreement to be close, and cannot conclude that transport diffusivity values are meaningfully different for guests in EPD versus solvothermal ZIF-8 films.

#### 4.6 Conclusion

Approximate transport diffusivities for linear alkanes ranging from C<sub>5</sub> to C<sub>16</sub> can be readily measured via analysis of QCM-determined temporal plots of guest uptake (from vapor) by thin films of ZIF-8, a material whose apertures must expand from their equilibrium width (3.4 Å) in order to accept the hydrocarbons (limiting cross-sectional diameters of 4.3 Å). For solvothermally grown films, transport is governed by intracrystalline diffusion in the direction normal to the QCM electrode, with guest molecules entering films only at the exterior film/vapor interface. Consistent with this picture, the values of putative transport diffusivities are independent of film thickness. Also consistent are the results of QCM experiments with cyclohexane, a molecule that is too large to permeate ZIF-8; these experiments indicate that molecule-accessible defects or intercrystalline voids constitute only a few percent of the film volume and imply that the crystallites constituting the films are comparatively closely packed.

Close examination of measured and fitted curves suggests that diffusivities may increase with extent of guest uptake. As such, we have focused on values derived from the early portions of QCM curves (*i.e.*, diffusivities in the low-uptake limit). For the alkanes examined, these vary from *ca.*  $10^{-14}$  to  $10^{-18} \text{ m}^2/\text{s}$ , with shorter hydrocarbons generally displaying larger diffusivities.<sup>222</sup>

Consistent with our results, this range of diffusivities fall between reported values for n-butane and iso-butane.<sup>162, 223</sup> On average, for each added carbon the transport diffusivity decreases by about a factor of 2. These more detailed comparisons, however, point to an odd-even carbon chain-length alteration effect, with alkanes featuring even numbers of carbons displaying larger values than expected based on a gross correlation of  $\log D$  with chain length. We lack an explanation for the odd-even pattern, but can speculate that alkane confinement within the  $\sim 12$  Å pores of the MOF energetically favors guest alkanes having odd numbers of carbons and, consequently, renders these less mobile diffusively than otherwise expected.

Finally, QCM experiments with coarser films prepared via EPD reveal that guest uptake is much faster than with dense, solvothermally grown films. Electron microscopy shows that films formed by EPD consist of loosely packed crystallites and extensive voids of width similar to individual crystallites. The contrasting guest-uptake dynamics for EPD-formed films can be understood by assuming that guest molecules (vapor) can rapidly enter film voids, and thereby enshroud individual crystallites – with rate-limiting filling of the crystallites occurring via approximately radial intracrystalline diffusion. The relevant distances for determining the rate of diffusive transport, therefore, are the size of the ZIF-8 nanoparticles, in the EPD case, and the overall film thickness, in the solvothermal film case. Consistent with intracrystalline molecular diffusion as the rate-limiting process for both types of films, the values of the putative transport diffusivity for a represent guest, *n*-hexane, are in good agreement for EPD versus solvothermal films. We suggest that the observations regarding: a) alkane uptake dynamics for loose versus compact aggregates of ZIF-8 crystallites, b) apparent odd-even behavior, and c) the roughly four-

orders-of magnitude variation of transport diffusivities for C<sub>5</sub> through C<sub>16</sub> may prove useful for kinetic separations of mixtures of linear alkanes.

#### **4.7 Experimental section**

Please see Appendix C.

**Chapter 5**

**Epilogue**

## 5.1 Overview

As discussed in chapter 1, the versatile and facile tunability of metal-organic frameworks enabled the incorporation of specific sorptive sites at high densities into the metal nodes, organic linkers, and the pores. With the bottom-up construction of MOFs, a wide range of building blocks can be used to engender a single framework that not only exhibits high uptake kinetics and capacity, but also chemoselectively captures multiple analytes, which necessitate a diverse set of sorptive interactions. In chapter 2, we demonstrated this concept in a UiO-66 MOF analogue by utilizing the oxometallic zirconium nodes to chemoselectively remove arsenate ( $\text{As}^{\text{V}}$ ), and the thiol-functionalized linkers to capture arsenites ( $\text{As}^{\text{III}}$ ). However, our work also revealed that uptake kinetics in MOFs adsorbents can be hindered by small MOF pores. To remedy the slow kinetics, we demonstrated that by 1) elongating the organic linkers, or 2) encouraging the structurally benign formation of missing-node defects, pore enlargement can be achieved, leading to improvement in the diffusion rates of analytes to all sorptive sites.

Curiously, the introduction of defects into these UiO-MOFs engendered a series of materials with hierarchical pores structures that, at the time, was not well understood. Thus, in chapter 3, we investigated the pore structures created in high defect-containing derivatives of UiO-66 and how they affect the stability of the UiO-66 analogues. Using a combination of isotherm-based studies (i.e., with  $\text{N}_2$ ,  $\text{H}_2\text{O}$  as probe molecules) and computational modelling, we were able to disclose different pore structures that exist “locally” within a crystallite of defect-containing UiO-66. While in all cases the pores are enlarged considerably, improving diffusion kinetics, the sample with the most defect density featured missing-cluster defects that coalesced and are susceptible to capillary force degradation mechanisms upon removal of water from the pores.



Though larger pore sizes are beneficial for aqueous-based MOF adsorbents, the pore environment small-pore MOFs can also be utilized in vapor-based adsorbent design to separate analytes of similar structures. In chapter 4, we showed that the diffusivities of linear hydrocarbons ( $C_{5-16}$ ) through thin films of ZIF-8, another model MOF, can be correlated to the level of strong vdW interactions between the hydrophobic pore and the incoming analyte using a series of QCM-based experiments. For the longer alkanes ( $C_{12-16}$ ), the small diffusivities ( $\sim 10^{-17} \text{ m}\cdot\text{s}^{-1}$ ) were indicative of strong binding affinities that could be exploited in the sequestration of alkyl-anchored materials (see Appendix D for preliminary work). This sorptive interaction, in addition to those incorporated at the nodes and the linkers, can collectively herald the next generation of efficient adsorbents with the ability to capture or separate multiple analytes at multiple sorptive sites.

## 5.2 Outlook

The findings in this thesis uncover several design principles for developing the next generation of efficient MOF-based adsorbents that can capture multiple species of arsenic or separation of chemically similar linear hydrocarbons. To extend this work, the directions to be considered include: 1) the development of inexpensive and convenient methods that can elucidate the structure of a wide selection of defect-containing MOFs that retain good adsorptive capabilities, 2) the eventual development of defect-free MOF adsorbents with active coordination sites that can exhibit those adsorption capabilities without sacrificing structural stability, and 3) the fundamental investigation on how the anomalous diffusion kinetics observed between odd-numbered and even-numbered linear hydrocarbons can be exploited to encourage selective separation. Possible strategies that build upon the knowledge in this thesis and address these points

are outlined below.

### 5.2.1 Towards complete structural elucidation of defect-containing MOFs

Towards the structural elucidation of defect-containing MOFs, this thesis presents the promising use of adsorption isotherm behavior and linker-node (L/N) ratios to examine the nature of defects in UiO-66 and how it relates to the pore structure of the framework. Thus far we have demonstrated that the elucidative and predictive power afforded by structural models generated from large supercells (i.e.,  $2 \times 2 \times 2$  unit cells with a maximum of 192 linkers and 32 nodes) is limited to the amount of pore-structural variations possible within these models. An obvious extension of this work would involve the use of structural models constructed in larger cells (e.g.,  $6 \times 6 \times 6$  used by Cliffe *et al.*<sup>108</sup>) which would allow for more variations between a mixture of different types of defects, defective domains, and L/N ratios within one supercell. Our premise is that if a database of these models and their simulated isotherms can be built with open access to researchers in porous materials, then the structural elucidation of synthesized materials that contain irregular and non-ordered pore structures can be realized simply through comparisons of the low-pressure N<sub>2</sub> isotherms.

### 5.2.2 Towards hierarchical defect-free MOFs for As<sup>III/V</sup> capture

A complete understanding of how defects in MOF sorbents facilitate the adsorption kinetics and capacity would enable the crystal engineering of better and more stable MOF sorbents. As discussed in chapters 2 and 3, the incorporation of missing-cluster defects can increase the uptake kinetics and capacity of arsenates (As<sup>V</sup>), while coalesced missing-cluster defects can lead to pore collapse upon the removal of water. Based on our work with UiO-66, we surmised that a

carefully designed Zr-MOF sorbent with hierarchical pores, akin to those created by missing clusters in UiO-66, and low linker coordination ratios (e.g.,  $L/N < 6$ ), hence available  $Zr_6$ -node(-OH/-OH<sub>2</sub>) binding sites, would enable the fast uptake of arsenates (As<sup>V</sup>) and arsenites (As<sup>III</sup>). We hypothesize that utilizing MOFs that feature pore structures and undercoordinated L/N ratios in an ordered fashion throughout the crystallite could avoid detrimental framework instability normally associated with high defect densities. For example, favorable non-thiolated, water-stable Zr-MOFs that could be used as template include MOF-800 series<sup>56</sup> and NU-1000.<sup>152</sup> This concept has, in part, already been demonstrated from other members of the Hupp group, in which high and fast uptake of selenates,<sup>35</sup> sulfates,<sup>224</sup> and pertechnetates<sup>225</sup> were realized with NU-1000.

### 5.2.3 Towards the selective separation of linear hydrocarbons.

As discussed in chapter 4, the MOF pore environment can also be exploited in the design of vapor-based adsorbents to separate analytes of similar structures. For the case of linear hydrocarbons, we demonstrated that their diffusivities are inversely proportional to the carbon length due to varying levels of van der Waals interactions. Slightly noticeable disparities between odd- and even-numbered alkanes (Appendix C, Figure C13 and as recently reported by Kärger and coworkers<sup>169</sup>), however, led us to postulate that either: 1) the apparent diffusion rate is influenced by adsorbate-adsorbate interactions leading to smaller diffusivities from even-numbered alkanes which are more closely packed in the pores than the odd-numbered alkanes, or 2) even-numbered alkanes have adsorbent-adsorbate interactions stronger than the odd-numbered alkanes possibly due to the pore geometry. Future work could involve testing these hypotheses either by measuring diffusivities at low vapor pressures or by systematically changing the MOF pore geometries.

Knowledge from such studies would enable the design of sorbents that could enable the facile separation of structurally similar hydrocarbons.

### References

1. Hoskins, B. F.; Robson, R., Infinite polymeric frameworks consisting of three dimensionally linked rod-like segments. *J. Am. Chem. Soc.* **1989**, *111*, 5962-5964.
2. Serpaggi, F.; Férey, G., Hybrid open frameworks (MIL-n). Part 6 Hydrothermal synthesis and X-ray powder ab initio structure determination of MIL-11, a series of lanthanide organodiphosphonates with three-dimensional networks,  $\text{Ln}^{\text{III}}\text{H}[\text{O}_3\text{P}(\text{CH}_2)_n\text{PO}_3]$  ( $n=1-3$ ). *J. Mater. Chem.* **1998**, *8*, 2749-2755.
3. Eddaoudi, M.; Kim, J.; Rosi, N.; Vodak, D.; Wachter, J.; O'Keeffe, M.; Yaghi, O. M., Systematic design of pore size and functionality in isorecticular MOFs and their application in methane storage. *Science* **2002**, *295*, 469-472.
4. Hua, M.; Zhang, S.; Pan, B.; Zhang, W.; Lv, L.; Zhang, Q., Heavy metal removal from water/wastewater by nanosized metal oxides: a review. *J. Hazard. Mater.* **2012**, *211-212*, 317-331.
5. Babel, S.; Kurniawan, T. A., Low-cost adsorbents for heavy metals uptake from contaminated water: a review. *J. Hazard. Mater.* **2003**, *97*, 219-243.
6. Drage, T. C.; Blackman, J. M.; Pevida, C.; Snape, C. E., Evaluation of Activated Carbon Adsorbents for CO<sub>2</sub> Capture in Gasification. *Energy Fuels* **2009**, *23*, 2790-2796.
7. Curdts, B.; Pflitsch, C.; Pasel, C.; Helmich, M.; Bathen, D.; Atakan, B., Novel silica-based adsorbents with activated carbon structure. *Microporous Mesoporous Mater.* **2015**, *210*, 202-205.
8. Hoffmann, F.; Cornelius, M.; Morell, J.; Froba, M., Silica-based mesoporous organic-inorganic hybrid materials. *Angew. Chem., Int. Ed.* **2006**, *45*, 3216-3251.
9. Wilmer, C. E.; Leaf, M.; Lee, C. Y.; Farha, O. K.; Hauser, B. G.; Hupp, J. T.; Snurr, R. Q., Large-scale screening of hypothetical metal-organic frameworks. *Nat. Chem.* **2012**, *4*, 83-89.

10. Stock, N.; Biswas, S., Synthesis of metal-organic frameworks (MOFs): routes to various MOF topologies, morphologies, and composites. *Chem. Rev.* **2012**, *112*, 933-969.
11. Natarajan, S.; Mahata, P., Metal-organic framework structures--how closely are they related to classical inorganic structures? *Chem. Soc. Rev.* **2009**, *38*, 2304-2318.
12. Yang, Q.; Zhong, C., Understanding hydrogen adsorption in metal-organic frameworks with open metal sites: a computational study. *J. Phys. Chem. B* **2006**, *110*, 655-658.
13. Welbes, L. L.; Borovik, A. S., Confinement of metal complexes within porous hosts: development of functional materials for gas binding and catalysis. *Acc. Chem. Res.* **2005**, *38*, 765-774.
14. Dinca, M.; Long, J. R., Hydrogen storage in microporous metal-organic frameworks with exposed metal sites. *Angew. Chem., Int. Ed.* **2008**, *47*, 6766-6779.
15. Taddei, M., When defects turn into virtues: The curious case of zirconium-based metal-organic frameworks. *Coord. Chem. Rev.* **2017**, *343*, 1-24.
16. Planas, N.; Mondloch, J. E.; Tussupbayev, S.; Borycz, J.; Gagliardi, L.; Hupp, J. T.; Farha, O. K.; Cramer, C. J., Defining the Proton Topology of the Zr<sub>6</sub>-Based Metal-Organic Framework NU-1000. *J. Phys. Chem. Lett.* **2014**, *5*, 3716-3723.
17. Noori, Y.; Akhbari, K., Post-synthetic ion-exchange process in nanoporous metal-organic frameworks: an effective way for modulating their structures and properties. *RSC Adv.* **2017**, *7*, 1782-1808.
18. Cohen, S. M., Postsynthetic methods for the functionalization of metal-organic frameworks. *Chem. Rev.* **2012**, *112*, 970-1000.
19. Deria, P.; Bury, W.; Hod, I.; Kung, C. W.; Karagiari, O.; Hupp, J. T.; Farha, O. K., MOF functionalization via solvent-assisted ligand incorporation: phosphonates vs. carboxylates. *Inorg. Chem.* **2015**, *54*, 2185-2192.
20. Xiang, S.; Zhou, W.; Zhang, Z.; Green, M. A.; Liu, Y.; Chen, B., Open metal sites within isostructural metal-organic frameworks for differential recognition of acetylene and extraordinarily high acetylene storage capacity at room temperature. *Angew. Chem., Int. Ed.* **2010**, *49*, 4615-4618.

21. Howarth, A. J.; Liu, Y.; Hupp, J. T.; Farha, O. K., Metal–organic frameworks for applications in remediation of oxyanion/cation-contaminated water. *CrystEngComm* **2015**, *17*, 7245-7253.
22. Zhang, J. P.; Zhang, Y. B.; Lin, J. B.; Chen, X. M., Metal azolate frameworks: from crystal engineering to functional materials. *Chem. Rev.* **2012**, *112*, 1001-1033.
23. Lu, W.; Wei, Z.; Gu, Z. Y.; Liu, T. F.; Park, J.; Park, J.; Tian, J.; Zhang, M.; Zhang, Q.; Gentle, T., 3rd; Bosch, M.; Zhou, H. C., Tuning the structure and function of metal-organic frameworks via linker design. *Chem. Soc. Rev.* **2014**, *43*, 5561-5593.
24. Shimizu, G. K.; Vaidhyanathan, R.; Taylor, J. M., Phosphonate and sulfonate metal organic frameworks. *Chem. Soc. Rev.* **2009**, *38*, 1430-1449.
25. Kim, M.; Cahill, J. F.; Su, Y.; Prather, K. A.; Cohen, S. M., Postsynthetic ligand exchange as a route to functionalization of ‘inert’ metal–organic frameworks. *Chem. Sci.* **2012**, *3*, 126-130.
26. Tanabe, K. K.; Cohen, S. M., Postsynthetic modification of metal-organic frameworks--a progress report. *Chem. Soc. Rev.* **2011**, *40*, 498-519.
27. Deria, P.; Mondloch, J. E.; Karagiari, O.; Bury, W.; Hupp, J. T.; Farha, O. K., Beyond post-synthesis modification: evolution of metal-organic frameworks via building block replacement. *Chem. Soc. Rev.* **2014**, *43*, 5896-5912.
28. Karagiari, O.; Bury, W.; Mondloch, J. E.; Hupp, J. T.; Farha, O. K., Solvent-assisted linker exchange: an alternative to the de novo synthesis of unattainable metal-organic frameworks. *Angew. Chem., Int. Ed.* **2014**, *53*, 4530-4540.
29. Demessence, A.; D'Alessandro, D. M.; Foo, M. L.; Long, J. R., Strong CO<sub>2</sub> binding in a water-stable, triazolate-bridged metal-organic framework functionalized with ethylenediamine. *J. Am. Chem. Soc.* **2009**, *131*, 8784-8786.
30. Lu, Z.; Xing, Y.; Du, L.; He, H.; Zhang, J.; Hang, C., Isostructural functionalization by –OH and –NH<sub>2</sub>: different contributions to CO<sub>2</sub> adsorption. *RSC Adv.* **2017**, *7*, 47219-47224.
31. McDonald, T. M.; D'Alessandro, D. M.; Krishna, R.; Long, J. R., Enhanced carbon dioxide capture upon incorporation of N,N'-dimethylethylenediamine in the metal–organic framework CuBTTri. *Chem. Sci.* **2011**, *2*, 2022-2028.

32. Savonnet, M.; Bazer-Bachi, D.; Bats, N.; Perez-Pellitero, J.; Jeanneau, E.; Lecocq, V.; Pinel, C.; Farrusseng, D., Generic postfunctionalization route from amino-derived metal-organic frameworks. *J. Am. Chem. Soc.* **2010**, *132*, 4518-4519.
33. Wang, Z.; Cohen, S. M., Postsynthetic covalent modification of a neutral metal-organic framework. *J. Am. Chem. Soc.* **2007**, *129*, 12368-12369.
34. Kobielska, P. A.; Howarth, A. J.; Farha, O. K.; Nayak, S., Metal-organic frameworks for heavy metal removal from water. *Coord. Chem. Rev.* **2018**, *358*, 92-107.
35. Howarth, A. J.; Katz, M. J.; Wang, T. C.; Platero-Prats, A. E.; Chapman, K. W.; Hupp, J. T.; Farha, O. K., High efficiency adsorption and removal of selenate and selenite from water using metal-organic frameworks. *J. Am. Chem. Soc.* **2015**, *137*, 7488-7494.
36. Audu, C. O.; Nguyen, H. G. T.; Chang, C. Y.; Katz, M. J.; Mao, L.; Farha, O. K.; Hupp, J. T.; Nguyen, S. T., The dual capture of As(V) and As(III) by UiO-66 and analogues. *Chem. Sci.* **2016**, *7*, 6492-6498.
37. Deng, H.; Doonan, C. J.; Furukawa, H.; Ferreira, R. B.; Towne, J.; Knobler, C. B.; Wang, B.; Yaghi, O. M., Multiple functional groups of varying ratios in metal-organic frameworks. *Science* **2010**, *327*, 846-850.
38. Yadanaparathi, S. K.; Graybill, D.; von Wandruszka, R., Adsorbents for the removal of arsenic, cadmium, and lead from contaminated waters. *J. Hazard. Mater.* **2009**, *171*, 1-15.
39. Bang, S.; Patel, M.; Lippincott, L.; Meng, X., Removal of arsenic from groundwater by granular titanium dioxide adsorbent. *Chemosphere* **2005**, *60*, 389-397.
40. Mohan, D.; Pittman, C. U., Jr., Arsenic removal from water/wastewater using adsorbents-A critical review. *J. Hazard. Mater.* **2007**, *142*, 1-53.
41. Aposhian, H. V.; Aposhian, M. M., Arsenic toxicology: five questions. *Chem. Res. Toxicol.* **2006**, *19*, 1-15.
42. Cullen, W. R.; Reimer, K. J., Arsenic speciation in the environment. *Chem. Rev.* **1989**, *89*, 713-764.
43. Kreno, L. E.; Leong, K.; Farha, O. K.; Allendorf, M.; Van Duyne, R. P.; Hupp, J. T., Metal-organic framework materials as chemical sensors. *Chem. Rev.* **2012**, *112*, 1105-1125.

44. Chidambaram, A.; Stylianou, K. C., Electronic metal–organic framework sensors. *Inorg. Chem. Front.* **2018**, *5*, 979-998.
45. Li, H.; Wang, K.; Sun, Y.; Lollar, C. T.; Li, J.; Zhou, H.-C., Recent advances in gas storage and separation using metal–organic frameworks. *Mater. Today* **2018**, *21*, 108-121.
46. Li, J. R.; Sculley, J.; Zhou, H. C., Metal-organic frameworks for separations. *Chem. Rev.* **2012**, *112*, 869-932.
47. Evans, J. D.; Sumbly, C. J.; Doonan, C. J., Post-synthetic metalation of metal-organic frameworks. *Chem. Soc. Rev.* **2014**, *43*, 5933-5951.
48. DeCoste, J. B.; Demasky, T. J.; Katz, M. J.; Farha, O. K.; Hupp, J. T., A UiO-66 analogue with uncoordinated carboxylic acids for the broad-spectrum removal of toxic chemicals. *New J. Chem.* **2015**, *39*, 2396-2399.
49. Zhu, X.; Li, B.; Yang, J.; Li, Y.; Zhao, W.; Shi, J.; Gu, J., Effective adsorption and enhanced removal of organophosphorus pesticides from aqueous solution by Zr-based MOFs of UiO-67. *ACS Appl. Mater. Interfaces* **2015**, *7*, 223-231.
50. Zhu, X.; Gu, J.; Wang, Y.; Li, B.; Li, Y.; Zhao, W.; Shi, J., Inherent anchorages in UiO-66 nanoparticles for efficient capture of alendronate and its mediated release. *Chem. Commun.* **2014**, *50*, 8779-8782.
51. Carboni, M.; Abney, C. W.; Liu, S.; Lin, W., Highly porous and stable metal–organic frameworks for uranium extraction. *Chem. Sci.* **2013**, *4*, 2396-2402.
52. Yee, K. K.; Reimer, N.; Liu, J.; Cheng, S. Y.; Yiu, S. M.; Weber, J.; Stock, N.; Xu, Z., Effective mercury sorption by thiol-laced metal-organic frameworks: in strong acid and the vapor phase. *J. Am. Chem. Soc.* **2013**, *135*, 7795-7798.
53. Luo, B.-C.; Yuan, L.-Y.; Chai, Z.-F.; Shi, W.-Q.; Tang, Q., U(VI) capture from aqueous solution by highly porous and stable MOFs: UiO-66 and its amine derivative. *J. Radioanal. Nucl. Chem.* **2015**, *307*, 269-276.
54. Sumida, K.; Rogow, D. L.; Mason, J. A.; McDonald, T. M.; Bloch, E. D.; Herm, Z. R.; Bae, T. H.; Long, J. R., Carbon dioxide capture in metal-organic frameworks. *Chem. Rev.* **2012**, *112*, 724-781.



55. Taylor, J. M.; Dawson, K. W.; Shimizu, G. K., A water-stable metal-organic framework with highly acidic pores for proton-conducting applications. *J. Am. Chem. Soc.* **2013**, *135*, 1193-1196.
56. Furukawa, H.; Gandara, F.; Zhang, Y. B.; Jiang, J.; Queen, W. L.; Hudson, M. R.; Yaghi, O. M., Water adsorption in porous metal-organic frameworks and related materials. *J. Am. Chem. Soc.* **2014**, *136*, 4369-4381.
57. Low, J. J.; Benin, A. I.; Jakubczak, P.; Abrahamian, J. F.; Faheem, S. A.; Willis, R. R., Virtual high throughput screening confirmed experimentally: porous coordination polymer hydration. *J. Am. Chem. Soc.* **2009**, *131*, 15834-15842.
58. Mondloch, J. E.; Katz, M. J.; Planas, N.; Semrouni, D.; Gagliardi, L.; Hupp, J. T.; Farha, O. K., Are Zr(6)-based MOFs water stable? Linker hydrolysis vs. capillary-force-driven channel collapse. *Chem. Commun.* **2014**, *50*, 8944-8946.
59. Katz, M. J.; Brown, Z. J.; Colon, Y. J.; Siu, P. W.; Scheidt, K. A.; Snurr, R. Q.; Hupp, J. T.; Farha, O. K., A facile synthesis of UiO-66, UiO-67 and their derivatives. *Chem. Commun.* **2013**, *49*, 9449-9451.
60. Wu, H.; Chua, Y. S.; Krungleviciute, V.; Tyagi, M.; Chen, P.; Yildirim, T.; Zhou, W., Unusual and highly tunable missing-linker defects in zirconium metal-organic framework UiO-66 and their important effects on gas adsorption. *J. Am. Chem. Soc.* **2013**, *135*, 10525-10532.
61. Vermoortele, F.; Bueken, B.; Le Bars, G.; Van de Voorde, B.; Vandichel, M.; Houthoofd, K.; Vimont, A.; Daturi, M.; Waroquier, M.; Van Speybroeck, V.; Kirschhock, C.; De Vos, D. E., Synthesis modulation as a tool to increase the catalytic activity of metal-organic frameworks: the unique case of UiO-66(Zr). *J. Am. Chem. Soc.* **2013**, *135*, 11465-11468.
62. Valenzano, L.; Civalleri, B.; Chavan, S.; Bordiga, S.; Nilsen, M. H.; Jakobsen, S.; Lillerud, K. P.; Lamberti, C., Disclosing the Complex Structure of UiO-66 Metal Organic Framework: A Synergic Combination of Experiment and Theory. *Chem. Mater.* **2011**, *23*, 1700-1718.
63. DeCoste, J. B.; Peterson, G. W.; Schindler, B. J.; Killops, K. L.; Browe, M. A.; Mahle, J. J., The effect of water adsorption on the structure of the carboxylate containing metal-organic frameworks Cu-BTC, Mg-MOF-74, and UiO-66. *J. Mater. Chem. A* **2013**, *1*, 11922-11932.

64. Ameloot, R.; Aubrey, M.; Wiers, B. M.; Gomora-Figueroa, A. P.; Patel, S. N.; Balsara, N. P.; Long, J. R., Ionic conductivity in the metal-organic framework UiO-66 by dehydration and insertion of lithium tert-butoxide. *Chemistry* **2013**, *19*, 5533-5536.
65. CRC Handbook of Chemistry and Physics. <http://www.hbcpnetbase.com/> (accessed January 8).
66. Vivani, R.; Alberti, G.; Costantino, F.; Nocchetti, M., New advances in zirconium phosphate and phosphonate chemistry: Structural archetypes. *Microporous Mesoporous Mater.* **2008**, *107*, 58-70.
67. Lin, K.-Y. A.; Chen, S.-Y.; Jochems, A. P., Zirconium-based metal organic frameworks: Highly selective adsorbents for removal of phosphate from water and urine. *Mater. Chem. Phys.* **2015**, *160*, 168-176.
68. Watanabe, T.; Hirano, S., Metabolism of arsenic and its toxicological relevance. *Arch. Toxicol.* **2013**, *87*, 969-979.
69. Spuches, A. M.; Kruszyna, H. G.; Rich, A. M.; Wilcox, D. E., Thermodynamics of the As(III)-thiol interaction: arsenite and monomethylarsenite complexes with glutathione, dihydrolipoic acid, and other thiol ligands. *Inorg. Chem.* **2005**, *44*, 2964-2972.
70. Ramadan, D.; Rancy, P. C.; Nagarkar, R. P.; Schneider, J. P.; Thorpe, C., Arsenic(III) species inhibit oxidative protein folding in vitro. *Biochemistry* **2009**, *48*, 424-432.
71. Cavka, J. H.; Jakobsen, S.; Olsbye, U.; Guillou, N.; Lamberti, C.; Bordiga, S.; Lillerud, K. P., A new zirconium inorganic building brick forming metal organic frameworks with exceptional stability. *J. Am. Chem. Soc.* **2008**, *130*, 13850-13851.
72. Schaate, A.; Roy, P.; Godt, A.; Lippke, J.; Waltz, F.; Wiebcke, M.; Behrens, P., Modulated synthesis of Zr-based metal-organic frameworks: from nano to single crystals. *Chemistry* **2011**, *17*, 6643-6651.
73. Nguyen, H. G. T.; Schweitzer, N. M.; Chang, C.-Y.; Drake, T. L.; So, M. C.; Stair, P. C.; Farha, O. K.; Hupp, J. T.; Nguyen, S. T., Vanadium-Node-Functionalized UiO-66: A Thermally Stable MOF-Supported Catalyst for the Gas-Phase Oxidative Dehydrogenation of Cyclohexene. *ACS Catal.* **2014**, *4*, 2496-2500.
74. While Wang and coworkers (reference 76) have found the uptake of aqueous AsV by UiO-66 to be best at pH = 2, neutral pH was selected for our study to simulate ground-water environment.

75. This amount of solution was chosen to give an experimental composition of 3.2 As<sup>V</sup> per hexazirconium node in HCl-UiO-66<sub>9/12</sub>, the most defective materials in our study. This ratio corresponds to a maximum replacement of the three missing carboxylate sites per node; the slight excess of As beyond 3 equiv. is intended to facilitate the sampling and analysis for mass balance in the supernatant in case of complete uptake. However, as described later on in this chapter, this situation is not expected to ever occur in our study. See Appendix A, section A11 for detailed calculations.
76. Wang, C.; Liu, X.; Chen, J. P.; Li, K., Superior removal of arsenic from water with zirconium metal-organic framework UiO-66. *Sci. Rep.* **2015**, *5*, 16613-16617.
77. Suzuki, T. M.; Bomani, J. O.; Matsunaga, H.; Yokoyama, T., Preparation of porous resin loaded with crystalline hydrous zirconium oxide and its application to the removal of arsenic. *React. Funct. Polym.* **2000**, *43*, 165-172.
78. Bortun, A.; Bortun, M.; Pardini, J.; Khainakov, S. A.; García, J. R., Synthesis and characterization of a mesoporous hydrous zirconium oxide used for arsenic removal from drinking water. *Mater. Res. Bull.* **2010**, *45*, 142-148.
79. We speculate that the uptake kinetics by the HCl-UiO-66 sample could be strongly influenced by the narrowing of the pore aperture as arsenates are being uptaken (see Appendix A, Figure A21b)
80. Gomez-Camirero, A.; Howe, P.; Hughes, M.; Kenyon, E.; Lewis, D. R.; Moore, M.; Ng, J.; Aitio, A.; Becking, G., *Arsenic and Arsenic compounds [Online]*. 2<sup>nd</sup> ed.; International Programme on Chemical Safety, WHO: Geneva, 2001. <http://www.inchem.org/documents/ehc/ehc/ehc224.htm#3.1> (accessed May 27, 2016)
81. Shearer, G. C.; Chavan, S.; Bordiga, S.; Svelle, S.; Olsbye, U.; Lillerud, K. P., Defect Engineering: Tuning the Porosity and Composition of the Metal–Organic Framework UiO-66 via Modulated Synthesis. *Chem. Mater.* **2016**, *28*, 3749-3761.
82. Wu, Y. N.; Zhou, M.; Zhang, B.; Wu, B.; Li, J.; Qiao, J.; Guan, X.; Li, F., Amino acid assisted templating synthesis of hierarchical zeolitic imidazolate framework-8 for efficient arsenate removal. *Nanoscale* **2014**, *6*, 1105-1112.
83. See Appendix A Section A5 for data and discussion.
84. Poojary, D. M.; Bortun, A. I.; Bortun, L. N.; Trobajo, C.; García, J. R.; Clearfield, A., Synthesis and characterization of a porous zirconium arsenate, [Zr<sub>3</sub>(AsO<sub>4</sub>)<sub>4</sub>(H<sub>2</sub>O)<sub>2</sub>]<sup>-2</sup>H<sub>2</sub>O. *Microporous Mesoporous Mater.* **1998**, *20*, 77-85.

85. Bortun, A. I.; Clearfield, A.; Suárez, M.; Llavona, R.; Rodríguez, J., Synthesis and characterization of  $\gamma$ -zirconium arsenate. *Mater. Chem. Phys.* **1998**, *55*, 152-154.
86. As<sup>III</sup> adsorption was carried out at pH 5 to facilitate the conversion of two As-OH moieties on arsenite into stable chelating As-SR bonds as shown in the reaction of thiol-rich proteins with Lewisite (L. A. Stocken and R. H. S. Thompson, *Biochem. J.*, **1946**, *40*, 529-535.)
87. Howarth, A. J.; Liu, Y.; Li, P.; Li, Z.; Wang, T. C.; Hupp, J. T.; Farha, O. K., Chemical, thermal and mechanical stabilities of metal-organic frameworks. *Nat. Rev. Mater.* **2016**, *1*, 15018/1-15.
88. Barin, G.; Krungleviciute, V.; Gutov, O.; Hupp, J. T.; Yildirim, T.; Farha, O. K., Defect creation by linker fragmentation in metal-organic frameworks and its effects on gas uptake properties. *Inorg. Chem.* **2014**, *53*, 6914-6919.
89. Bueken, B.; Van Velthoven, N.; Krajnc, A.; Smolders, S.; Taulelle, F.; Mellot-Draznieks, C.; Mali, G.; Bennett, T. D.; De Vos, D., Tackling the Defect Conundrum in UiO-66: A Mixed-Linker Approach to Engineering Missing Linker Defects. *Chem. Mater.* **2017**, *29*, 10478-10486.
90. Jiao, Y.; Liu, Y.; Zhu, G.; Hungerford, J. T.; Bhattacharyya, S.; Lively, R. P.; Sholl, D. S.; Walton, K. S., Heat-Treatment of Defective UiO-66 from Modulated Synthesis: Adsorption and Stability Studies. *J. Phys. Chem. C* **2017**, *121*, 23471-23479.
91. Yuan, S.; Zou, L.; Qin, J.-S.; Li, J.; Huang, L.; Feng, L.; Wang, X.; Bosch, M.; Alsalmeh, A.; Cagin, T.; Zhou, H.-C., Construction of hierarchically porous metal-organic frameworks through linker labilization. *Nat. Commun.* **2017**, *8*, 15356/1-10.
92. Furukawa, H.; Cordova, K. E.; O'Keeffe, M.; Yaghi, O. M., The chemistry and applications of metal-organic frameworks. *Science* **2013**, *341*, 1230444/1-12.
93. Alezi, D.; Belmabkhout, Y.; Suyetin, M.; Bhatt, P. M.; Weselinski, L. J.; Solovyeva, V.; Adil, K.; Spanopoulos, I.; Trikalitis, P. N.; Emwas, A. H.; Eddaoudi, M., MOF Crystal Chemistry Paving the Way to Gas Storage Needs: Aluminum-Based soc-MOF for CH<sub>4</sub>, O<sub>2</sub>, and CO<sub>2</sub> Storage. *J. Am. Chem. Soc.* **2015**, *137*, 13308-13318.
94. Lin, L. C.; Kim, J.; Kong, X.; Scott, E.; McDonald, T. M.; Long, J. R.; Reimer, J. A.; Smit, B., Understanding CO<sub>2</sub> dynamics in metal-organic frameworks with open metal sites. *Angew. Chem., Int. Ed.* **2013**, *52*, 4410-4413.

95. He, Y.; Zhou, W.; Qian, G.; Chen, B., Methane storage in metal-organic frameworks. *Chem. Soc. Rev.* **2014**, *43*, 5657-5678.
96. Hu, Z.; Deibert, B. J.; Li, J., Luminescent metal-organic frameworks for chemical sensing and explosive detection. *Chem. Soc. Rev.* **2014**, *43*, 5815-5840.
97. Kreno, L. E.; Leong, K.; Farha, O. K.; Allendorf, M.; Van Duyne, R. P.; Hupp, J. T., Metal-organic framework materials as chemical sensors. *Chem. Rev.* **2012**, *112*, 1105-1125.
98. Banerjee, D.; Cairns, A. J.; Liu, J.; Motkuri, R. K.; Nune, S. K.; Fernandez, C. A.; Krishna, R.; Strachan, D. M.; Thallapally, P. K., Potential of metal-organic frameworks for separation of xenon and krypton. *Acc. Chem. Res.* **2015**, *48*, 211-219.
99. Bae, Y. S.; Lee, C. Y.; Kim, K. C.; Farha, O. K.; Nickias, P.; Hupp, J. T.; Nguyen, S. T.; Snurr, R. Q., High propene/propane selectivity in isostructural metal-organic frameworks with high densities of open metal sites. *Angew. Chem., Int. Ed.* **2012**, *51*, 1857-1860.
100. Gascon, J.; Corma, A.; Kapteijn, F.; Llabrés i Xamena, F. X., Metal Organic Framework Catalysis: Quo vadis? *ACS Catal.* **2013**, *4*, 361-378.
101. Corma, A.; Garcia, H.; Llabres i Xamena, F. X., Engineering metal organic frameworks for heterogeneous catalysis. *Chem. Rev.* **2010**, *110*, 4606-4655.
102. Feng, D.; Gu, Z. Y.; Li, J. R.; Jiang, H. L.; Wei, Z.; Zhou, H. C., Zirconium-metalloporphyrin PCN-222: mesoporous metal-organic frameworks with ultrahigh stability as biomimetic catalysts. *Angew. Chem., Int. Ed.* **2012**, *51*, 10307-10310.
103. Schlichte, K.; Kratzke, T.; Kaskel, S., Improved synthesis, thermal stability and catalytic properties of the metal-organic framework compound  $\text{Cu}_3(\text{BTC})_2$ . *Microporous Mesoporous Mater.* **2004**, *73*, 81-88.
104. Lee, J.; Farha, O. K.; Roberts, J.; Scheidt, K. A.; Nguyen, S. T.; Hupp, J. T., Metal-organic framework materials as catalysts. *Chem. Soc. Rev.* **2009**, *38*, 1450-1459.
105. Howarth, A. J.; Peters, A. W.; Vermeulen, N. A.; Wang, T. C.; Hupp, J. T.; Farha, O. K., Best Practices for the Synthesis, Activation, and Characterization of Metal–Organic Frameworks. *Chem. Mater.* **2016**, *29*, 26-39.
106. Gandara, F.; Bennett, T. D., Crystallography of metal-organic frameworks. *IUCrJ* **2014**, *1*, 563-570.

107. Yakovenko, A. A.; Reibenspies, J. H.; Bhuvanesh, N.; Zhou, H.-C., Generation and applications of structure envelopes for porous metal–organic frameworks. *J. Appl. Crystallogr.* **2013**, *46*, 346-353.
108. Cliffe, M. J.; Wan, W.; Zou, X.; Chater, P. A.; Kleppe, A. K.; Tucker, M. G.; Wilhelm, H.; Funnell, N. P.; Coudert, F. X.; Goodwin, A. L., Correlated defect nanoregions in a metal-organic framework. *Nat. Commun.* **2014**, *5*, 4176/1-8.
109. Trickett, C. A.; Gagnon, K. J.; Lee, S.; Gandara, F.; Burgi, H. B.; Yaghi, O. M., Definitive molecular level characterization of defects in UiO-66 crystals. *Angew. Chem., Int. Ed.* **2015**, *54*, 11162-11167.
110. Dissegna, S.; Epp, K.; Heinz, W. R.; Kieslich, G.; Fischer, R. A., Defective Metal-Organic Frameworks. *Adv. Mater.* **2018**, *30*, 1704501/1-23.
111. Ren, J.; Ledwaba, M.; Musyoka, N. M.; Langmi, H. W.; Mathe, M.; Liao, S.; Pang, W., Structural defects in metal–organic frameworks (MOFs): Formation, detection and control towards practices of interests. *Coord. Chem. Rev.* **2017**, *349*, 169-197.
112. Øien, S.; Wragg, D.; Reinsch, H.; Svelle, S.; Bordiga, S.; Lamberti, C.; Lillerud, K. P., Detailed Structure Analysis of Atomic Positions and Defects in Zirconium Metal–Organic Frameworks. *Cryst. Growth Des.* **2014**, *14*, 5370-5372.
113. Oien-Odegaard, S.; Shearer, G. C.; Wragg, D. S.; Lillerud, K. P., Pitfalls in metal-organic framework crystallography: towards more accurate crystal structures. *Chem. Soc. Rev.* **2017**, *46*, 4867-4876.
114. Cheetham, A. K.; Bennett, T. D.; Coudert, F. X.; Goodwin, A. L., Defects and disorder in metal organic frameworks. *Dalton Trans.* **2016**, *45*, 4113-4126.
115. Schull, C. G., The Determination of Pore Size Distribution from Gas Adsorption Data. *J. Am. Chem. Soc.* **1948**, *70*, 1405-1410.
116. Pierce, C., Computation of Pore Sizes from Physical Adsorption Data. *J. Phys. Chem.* **1953**, *57*, 149-152.
117. Barrett, E. P.; Joyner, L. G.; Halenda, P. P., The Determination of Pore Volume and Area Distributions in Porous Substances. I. Computations from Nitrogen Isotherms. *J. Am. Chem. Soc.* **1951**, *73*, 373-380.

118. Cychoosz, K. A.; Guillet-Nicolas, R.; Garcia-Martinez, J.; Thommes, M., Recent advances in the textural characterization of hierarchically structured nanoporous materials. *Chem. Soc. Rev.* **2017**, *46*, 389-414.
119. Thommes, M.; Kaneko, K.; Neimark Alexander, V.; Olivier James, P.; Rodriguez-Reinoso, F.; Rouquerol, J.; Sing Kenneth, S. W., Physisorption of gases, with special reference to the evaluation of surface area and pore size distribution (IUPAC Technical Report). In *Pure Appl. Chem.*, **2015**, *87*, 1051-1069.
120. Lowell, S., Joan E. Shields, Martin A. Thomas, Mattias Thommes, *Characterization of porous solids and powders: surface area, pore size and density* Springer Science+Business Media: New York, 2004; 365 pp.
121. Sing, K., The use of nitrogen adsorption for the characterisation of porous materials. *Colloids Surf., A* **2001**, *187-188*, 3-9.
122. Ladavos, A. K.; Katsoulidis, A. P.; Iosifidis, A.; Triantafyllidis, K. S.; Pinnavaia, T. J.; Pomonis, P. J., The BET equation, the inflection points of N<sub>2</sub> adsorption isotherms and the estimation of specific surface area of porous solids. *Microporous Mesoporous Mater.* **2012**, *151*, 126-133.
123. De Lange, M. F.; Vlugt, T. J. H.; Gascon, J.; Kapteijn, F., Adsorptive characterization of porous solids: Error analysis guides the way. *Microporous Mesoporous Mater.* **2014**, *200*, 199-215.
124. Nguyen, P. T. M.; Do, D. D.; Nicholson, D., Pore connectivity and hysteresis in gas adsorption: A simple three-pore model. *Colloids Surf., A* **2013**, *437*, 56-68.
125. Landers, J.; Gor, G. Y.; Neimark, A. V., Density functional theory methods for characterization of porous materials. *Colloids Surf., A* **2013**, *437*, 3-32.
126. Bae, Y. S.; Yazaydin, A. O.; Snurr, R. Q., Evaluation of the BET method for determining surface areas of MOFs and zeolites that contain ultra-micropores. *Langmuir* **2010**, *26*, 5475-5483.
127. Walton, K. S.; Snurr, R. Q., Applicability of the BET method for determining surface areas of microporous metal-organic frameworks. *J. Am. Chem. Soc.* **2007**, *129*, 8552-8556.
128. Gomez-Gualdron, D. A.; Moghadam, P. Z.; Hupp, J. T.; Farha, O. K.; Snurr, R. Q., Application of Consistency Criteria To Calculate BET Areas of Micro- And Mesoporous Metal-Organic Frameworks. *J. Am. Chem. Soc.* **2016**, *138*, 215-224.

129. Ferey, G.; Mellot-Draznieks, C.; Serre, C.; Millange, F.; Dutour, J.; Surble, S.; Margiolaki, I., A chromium terephthalate-based solid with unusually large pore volumes and surface area. *Science* **2005**, *309*, 2040-2042.
130. Mondloch, J. E.; Karagiari, O.; Farha, O. K.; Hupp, J. T., Activation of metal-organic framework materials. *CrystEngComm* **2013**, *15*, 9258-9264.
131. Lin, J. B.; Zhang, J. P.; Chen, X. M., Nonclassical active site for enhanced gas sorption in porous coordination polymer. *J. Am. Chem. Soc.* **2010**, *132*, 6654-6656.
132. Haldar, R.; Sikdar, N.; Maji, T. K., Interpenetration in coordination polymers: structural diversities toward porous functional materials. *Mater. Today* **2015**, *18*, 97-116.
133. Li, P.; Vermeulen, N. A.; Malliakas, C. D.; Gomez-Gualdron, D. A.; Howarth, A. J.; Mehdi, B. L.; Dohnalkova, A.; Browning, N. D.; O'Keeffe, M.; Farha, O. K., Bottom-up construction of a superstructure in a porous uranium-organic crystal. *Science* **2017**, *356*, 624-627.
134. Sholl, D. S.; Lively, R. P., Defects in Metal-Organic Frameworks: Challenge or Opportunity? *J. Phys. Chem. Lett.* **2015**, *6*, 3437-3444.
135. Atzori, C.; Shearer, G. C.; Maschio, L.; Civalleri, B.; Bonino, F.; Lamberti, C.; Svelle, S.; Lillerud, K. P.; Bordiga, S., Effect of Benzoic Acid as a Modulator in the Structure of UiO-66: An Experimental and Computational Study. *J. Phys. Chem. C* **2017**, *121*, 9312-9324.
136. In this chapter, the "missing-linker" notation is conveniently used to represent the number of BDC linker that is missing from the ideal 6 BDC linkers/Zr<sub>6</sub> cluster node solely based on chemical analysis. It does not indicate whether some of the nodes are also missing.
137. Brown, R. S.; Bennet, A. J.; Slebocka-Tilk, H., Recent perspectives concerning the mechanism of H<sub>3</sub>O<sup>+</sup>- and hydroxide-promoted amide hydrolysis. *Acc. Chem. Res.* **2002**, *25*, 481-488.
138. Deria, P.; Mondloch, J. E.; Tylianakis, E.; Ghosh, P.; Bury, W.; Snurr, R. Q.; Hupp, J. T.; Farha, O. K., Perfluoroalkane functionalization of NU-1000 via solvent-assisted ligand incorporation: synthesis and CO<sub>2</sub> adsorption studies. *J. Am. Chem. Soc.* **2013**, *135*, 16801-16804.
139. Deria, P.; Bury, W.; Hupp, J. T.; Farha, O. K., Versatile functionalization of the NU-1000 platform by solvent-assisted ligand incorporation. *Chem. Commun.* **2014**, *50*, 1965-1968.



140. Vandichel, M.; Hajek, J.; Vermoortele, F.; Waroquier, M.; De Vos, D. E.; Van Speybroeck, V., Active site engineering in UiO-66 type metal–organic frameworks by intentional creation of defects: a theoretical rationalization. *CrystEngComm* **2015**, *17*, 395-406.
141. BzOH-UiO-66<sup>4.0/6</sup> exhibits pores ~4 Å smaller in than in HCl-UiO-66<sup>4.2/6</sup>, due to the presence of the bulky benzoate caps.
142. Dubbeldam, D.; Calero, S.; Ellis, D. E.; Snurr, R. Q., RASPA: molecular simulation software for adsorption and diffusion in flexible nanoporous materials. *Mol. Simul.* **2015**, *42*, 81-101.
143. As the simulated N<sub>2</sub>-adsorption isotherm for the defect-free UiO-66 can be simulated quite accurately, it has been used as a standard for comparison with the experimental N<sub>2</sub>-adsorption isotherms for UiO-66 samples synthesized under different conditions. See Shearer, G. et al., *Chem. Mater.* **2016**, *28*, 3749-3761 and Gómez-Gualdrón, D. A., et al., *J. Am. Chem. Soc.* **2016**, *138*, 215-224.
144. Dissegna, S.; Hardian, R.; Epp, K.; Kieslich, G.; Coulet, M.-V.; Llewellyn, P.; Fischer, R. A., Using water adsorption measurements to access the chemistry of defects in the metal–organic framework UiO-66. *CrystEngComm* **2017**, *19*, 4137-4141.
145. Shearer, G. C.; Chavan, S.; Ethiraj, J.; Vitillo, J. G.; Svelle, S.; Olsbye, U.; Lamberti, C.; Bordiga, S.; Lillerud, K. P., Tuned to Perfection: Ironing Out the Defects in Metal–Organic Framework UiO-66. *Chem. Mater.* **2014**, *26*, 4068-4071.
146. Rodríguez-Albelo, L. M.; López-Maya, E.; Hamad, S.; Ruiz-Salvador, A. R.; Calero, S.; Navarro, J. A. R., Selective sulfur dioxide adsorption on crystal defect sites on an isorecticular metal organic framework series. *Nat. Commun.* **2017**, *8*, 14457/1-10.
147. Two plausible scenarios that are consistent with this conclusion are: 1) the small number of missing-linker defects per node do not significantly alter the pore architecture of the MOFs, or 2) while there may be few missing-cluster defects exist within the crystallite, they are distributed in a manner that does not alter the N<sub>2</sub> adsorption isotherm (e.g., in small disordered regions in the crystallite).
148. The bridging hydroxyls at the node, which are alternating and not present in all tetrahedral cages, give rise to two slightly different geometrically calculated pore sizes for otherwise identical tetrahedral cages.
149. We note in passing that isotherms obtained from linear combination of UiO-66-*fcu* model (Figure 3.4a) and UiO-66-*reo* model (Figure 3.4g) did not yield any meaningful result (i.e.,

did not match the experimental isotherms as described in the “Determining best-fit structural models for defect-containing UiO-66” subsection), emphasizing the importance of the hybrid super-cell models

150. For the purpose of this study, we define "local" as relevant to features that can be inferred by matching experimental data with the simulation of a  $2 \times 2 \times 2$  cubic supercell
151. The high  $P/P_0$  rise at the end of the experimental isotherm cannot be simulated because uptake in that region of the isotherm is largely influenced by filling of the interparticle space, which is not accounted for in our models.
152. Mondloch, J. E.; Bury, W.; Fairen-Jimenez, D.; Kwon, S.; DeMarco, E. J.; Weston, M. H.; Sarjeant, A. A.; Nguyen, S. T.; Stair, P. C.; Snurr, R. Q.; Farha, O. K.; Hupp, J. T., Vapor-phase metalation by atomic layer deposition in a metal-organic framework. *J. Am. Chem. Soc.* **2013**, *135*, 10294-10297.
153. Yang, D.; Bernales, V.; Islamoglu, T.; Farha, O. K.; Hupp, J. T.; Cramer, C. J.; Gagliardi, L.; Gates, B. C., Tuning the Surface Chemistry of Metal Organic Framework Nodes: Proton Topology of the Metal-Oxide-Like  $Zr_6$  Nodes of UiO-66 and NU-1000. *J. Am. Chem. Soc.* **2016**, *138*, 15189-15196.
154. One reason the HCl-model isotherm may have less distinguishable inflection points (i.e. is closer to linear) is because of the Cl LJ parameters in the force-field used. Epsilon for Cl is significantly larger than the epsilons for C,O,H. Thus, the most favorable adsorption sites in the HCl-model structure are probably around Cl atoms regardless of whether the Cl is in the large pore or the small pore. This would have the effect of “damping” the isotherm inflection as adsorption in the small pores would be more of a secondary binding site.
155. Ma, S.; Zhou, H. C., Gas storage in porous metal-organic frameworks for clean energy applications. *Chem. Commun.* **2010**, *46*, 44-53.
156. Mason, J. A.; Veenstra, M.; Long, J. R., Evaluating metal-organic frameworks for natural gas storage. *Chem. Sci.* **2014**, *5*, 32-51.
157. Li, B.; Wang, H.; Chen, B., Microporous metal-organic frameworks for gas separation. *Chem. Asian J.* **2014**, *9*, 1474-1498.
158. Karger, J., Transport phenomena in nanoporous materials. *ChemPhysChem* **2015**, *16*, 24-51.

159. Borah, B.; Zhang, H.; Snurr, R. Q., Diffusion of methane and other alkanes in metal-organic frameworks for natural gas storage. *Chem. Eng. Sci.* **2015**, *124*, 135-143.
160. Park, K. S.; Ni, Z.; Cote, A. P.; Choi, J. Y.; Huang, R.; Uribe-Romo, F. J.; Chae, H. K.; O'Keeffe, M.; Yaghi, O. M., Exceptional chemical and thermal stability of zeolitic imidazolate frameworks. *Proc. Natl. Acad. Sci. U. S. A.* **2006**, *103*, 10186-10191.
161. Fairen-Jimenez, D.; Moggach, S. A.; Wharmby, M. T.; Wright, P. A.; Parsons, S.; Duren, T., Opening the gate: framework flexibility in ZIF-8 explored by experiments and simulations. *J. Am. Chem. Soc.* **2011**, *133*, 8900-8902.
162. Zhang, C.; Lively, R. P.; Zhang, K.; Johnson, J. R.; Karvan, O.; Koros, W. J., Unexpected Molecular Sieving Properties of Zeolitic Imidazolate Framework-8. *J. Phys. Chem. Lett.* **2012**, *3*, 2130-2134.
163. Breck, D. W., *Zeolite molecular sieves: structure, chemistry, and use*. New York, Wiley, 1973.
164. Zhang, K.; Lively, R. P.; Zhang, C.; Chance, R. R.; Koros, W. J.; Sholl, D. S.; Nair, S., Exploring the Framework Hydrophobicity and Flexibility of ZIF-8: From Biofuel Recovery to Hydrocarbon Separations. *J. Phys. Chem. Lett.* **2013**, *4*, 3618-3622.
165. Mueller, R.; Zhang, S.; Zhang, C.; Lively, R.; Vasenkov, S., Relationship between long-range diffusion and diffusion in the ZIF-8 and polymer phases of a mixed-matrix membrane by high field NMR diffusometry. *J. Membr. Sci.* **2015**, *477*, 123-130.
166. Peralta, D.; Chaplais, G.; Paillaud, J.-L.; Simon-Masseron, A.; Barthelet, K.; Pirngruber, G. D., The separation of xylene isomers by ZIF-8: A demonstration of the extraordinary flexibility of the ZIF-8 framework. *Microporous Mesoporous Mater.* **2013**, *173*, 1-5.
167. Verploegh, R. J.; Nair, S.; Sholl, D. S., Temperature and Loading-Dependent Diffusion of Light Hydrocarbons in ZIF-8 as Predicted Through Fully Flexible Molecular Simulations. *J. Am. Chem. Soc.* **2015**, *137*, 15760-15771.
168. Coudert, F. X., Molecular Mechanism of Swing Effect in Zeolitic Imidazolate Framework ZIF-8: Continuous Deformation upon Adsorption. *ChemPhysChem* **2017**, *18*, 2732-2738.
169. Hwang, S.; Gopalan, A.; Hovestadt, M.; Piepenbreier, F.; Chmelik, C.; Hartmann, M.; Snurr, R. Q.; Karger, J., Anomaly in the Chain Length Dependence of n-Alkane Diffusion in ZIF-4 Metal-Organic Frameworks. *Molecules* **2018**, *23*, 668.

170. Cotts, R. M.; Hoch, M. J. R.; Sun, T.; Markert, J. T., Pulsed field gradient stimulated echo methods for improved NMR diffusion measurements in heterogeneous systems. *J. Magn. Reson.* **1989**, *83*, 252-266.
171. Cohen, Y.; Avram, L.; Frish, L., Diffusion NMR spectroscopy in supramolecular and combinatorial chemistry: an old parameter--new insights. *Angew. Chem., Int. Ed.* **2005**, *44*, 520-554.
172. Ford, D. C.; Dubbeldam, D.; Snurr, R. Q.; Kunzel, V.; Wehring, M.; Stallmach, F.; Karger, J.; Muller, U., Self-Diffusion of Chain Molecules in the Metal-Organic Framework IRMOF-1: Simulation and Experiment. *J. Phys. Chem. Lett.* **2012**, *3*, 930-933.
173. Wehring, M.; Gascon, J.; Dubbeldam, D.; Kapteijn, F.; Snurr, R. Q.; Stallmach, F., Self-Diffusion Studies in CuBTC by PFG NMR and MD Simulations. *J. Phys. Chem. C* **2010**, *114*, 10527-10534.
174. Stallmach, F.; Groger, S.; Kunzel, V.; Karger, J.; Yaghi, O. M.; Hesse, M.; Muller, U., NMR studies on the diffusion of hydrocarbons on the metal-organic framework material MOF-5. *Angew. Chem., Int. Ed.* **2006**, *45*, 2123-2126.
175. Thoma, R.; Karger, J.; de Sousa Amadeu, N.; Niessing, S.; Janiak, C., Assessing Guest-Molecule Diffusion in Heterogeneous Powder Samples of Metal-Organic Frameworks through Pulsed-Field-Gradient (PFG) NMR Spectroscopy. *Chem. Eur. J.* **2017**, *23*, 13000-13005.
176. Jobic, H.; Theodorou, D. N., Quasi-elastic neutron scattering and molecular dynamics simulation as complementary techniques for studying diffusion in zeolites. *Microporous Mesoporous Mater.* **2007**, *102*, 21-50.
177. Mendes, P. A. P.; Horcajada, P.; Rives, S.; Ren, H.; Rodrigues, A. E.; Devic, T.; Magnier, E.; Trens, P.; Jobic, H.; Ollivier, J.; Maurin, G.; Serre, C.; Silva, J. A. C., A Complete Separation of Hexane Isomers by a Functionalized Flexible Metal Organic Framework. *Adv. Funct. Mater.* **2014**, *24*, 7666-7673.
178. Johannsmann, D., *The Quartz Crystal Microbalance in Soft Matter Research*. Springer International Publishing: Switzerland, 2015; 387 pp.
179. Zybaylo, O.; Shekhah, O.; Wang, H.; Tafipolsky, M.; Schmid, R.; Johannsmann, D.; Woll, C., A novel method to measure diffusion coefficients in porous metal-organic frameworks. *Phys. Chem. Chem. Phys.* **2010**, *12*, 8092-8097.

180. Heinke, L.; Woll, C., Adsorption and diffusion in thin films of nanoporous metal-organic frameworks: ferrocene in SURMOF Cu<sub>2</sub>(ndc)<sub>2</sub>(dabco). *Phys. Chem. Chem. Phys.* **2013**, *15*, 9295-9299.
181. Shen, D.; Ma, X.; Cai, T.; Zhu, X.; Xin, X.; Kang, Q., Investigation on kinetic processes of zeolitic imidazolate framework-8 film growth and adsorption of chlorohydro-carbons using a quartz crystal microbalance. *Anal. Methods* **2015**, *7*, 9619-9628.
182. Shekhah, O.; Eddaoudi, M., The liquid phase epitaxy method for the construction of oriented ZIF-8 thin films with controlled growth on functionalized surfaces. *Chem. Commun.* **2013**, *49*, 10079-10081.
183. Lu, G.; Farha, O. K.; Kreno, L. E.; Schoenecker, P. M.; Walton, K. S.; Van Duyne, R. P.; Hupp, J. T., Fabrication of metal-organic framework-containing silica-colloidal crystals for vapor sensing. *Adv. Mater.* **2011**, *23*, 4449-4452.
184. Wang, T. C.; Hod, I.; Audu, C. O.; Vermeulen, N. A.; Nguyen, S. T.; Farha, O. K.; Hupp, J. T., Rendering High Surface Area, Mesoporous Metal-Organic Frameworks Electronically Conductive. *ACS Appl. Mater. Interfaces* **2017**, *9*, 12584-12591.
185. Hirai, K.; Sumida, K.; Meilikhov, M.; Louvain, N.; Nakahama, M.; Uehara, H.; Kitagawa, S.; Furukawa, S., Impact of crystal orientation on the adsorption kinetics of a porous coordination polymer-quartz crystal microbalance hybrid sensor. *J. Mater. Chem. C* **2014**, *2*, 3336-3344.
186. Biemmi, E.; Darga, A.; Stock, N.; Bein, T., Direct growth of Cu<sub>3</sub>(BTC)<sub>2</sub>(H<sub>2</sub>O)<sub>3</sub>·xH<sub>2</sub>O thin films on modified QCM-gold electrodes – Water sorption isotherms. *Microporous Mesoporous Mater.* **2008**, *114*, 380-386.
187. Campbell, M.; Dincă, M., Metal–Organic Frameworks as Active Materials in Electronic Sensor Devices. *Sensors* **2017**, *17*, 1108.
188. Paschke, B.; Wixforth, A.; Denysenko, D.; Volkmer, D., Fast Surface Acoustic Wave-Based Sensors to Investigate the Kinetics of Gas Uptake in Ultra-Microporous Frameworks. *ACS Sens.* **2017**, *2*, 740-747.
189. Mosier, A. M.; Larson, H. L.; Webster, E. R.; Ivos, M.; Tian, F.; Benz, L., Low-Temperature Adsorption and Diffusion of Methanol in ZIF-8 Nanoparticle Films. *Langmuir* **2016**, *32*, 2947-2954.

190. Herm, Z. R.; Bloch, E. D.; Long, J. R., Hydrocarbon Separations in Metal–Organic Frameworks. *Chem. Mater.* **2013**, *26*, 323-338.
191. Fairen-Jimenez, D.; Galvelis, R.; Torrisi, A.; Gellan, A. D.; Wharmby, M. T.; Wright, P. A.; Mellot-Draznieks, C.; Duren, T., Flexibility and swing effect on the adsorption of energy-related gases on ZIF-8: combined experimental and simulation study. *Dalton Trans.* **2012**, *41*, 10752-10762.
192. Diestel, L.; Bux, H.; Wachsmuth, D.; Caro, J., Pervaporation studies of n-hexane, benzene, mesitylene and their mixtures on zeolitic imidazolate framework-8 membranes. *Microporous Mesoporous Mater.* **2012**, *164*, 288-293.
193. Lu, G.; Hupp, J. T., Metal-organic frameworks as sensors: a ZIF-8 based Fabry-Perot device as a selective sensor for chemical vapors and gases. *J. Am. Chem. Soc.* **2010**, *132*, 7832-7833.
194. Demessence, A.; Boissière, C.; Grosso, D.; Horcajada, P.; Serre, C.; Férey, G.; Soler-Illia, G. J. A. A.; Sanchez, C., Adsorption properties in high optical quality nanoZIF-8 thin films with tunable thickness. *J. Mater. Chem.* **2010**, *20*, 7676-7681.
195. Chang, N.; Gu, Z. Y.; Yan, X. P., Zeolitic imidazolate framework-8 nanocrystal coated capillary for molecular sieving of branched alkanes from linear alkanes along with high-resolution chromatographic separation of linear alkanes. *J. Am. Chem. Soc.* **2010**, *132*, 13645-13647.
196. Bux, H.; Chmelik, C.; van Baten, J. M.; Krishna, R.; Caro, J., Novel MOF-membrane for molecular sieving predicted by IR-diffusion studies and molecular modeling. *Adv. Mater.* **2010**, *22*, 4741-4743.
197. Hod, I.; Bury, W.; Karlin, D. M.; Deria, P.; Kung, C. W.; Katz, M. J.; So, M.; Klahr, B.; Jin, D.; Chung, Y. W.; Odom, T. W.; Farha, O. K.; Hupp, J. T., Directed growth of electroactive metal-organic framework thin films using electrophoretic deposition. *Adv. Mater.* **2014**, *26*, 6295-6300.
198. Zhu, H.; Liu, H.; Zhitomirsky, I.; Zhu, S., Preparation of metal–organic framework films by electrophoretic deposition method. *Mater. Lett.* **2015**, *142*, 19-22.
199. Lee, C. Y.; Bae, Y. S.; Jeong, N. C.; Farha, O. K.; Sarjeant, A. A.; Stern, C. L.; Nickias, P.; Snurr, R. Q.; Hupp, J. T.; Nguyen, S. T., Kinetic separation of propene and propane in metal-organic frameworks: controlling diffusion rates in plate-shaped crystals via tuning of pore apertures and crystallite aspect ratios. *J. Am. Chem. Soc.* **2011**, *133*, 5228-5231.

200. Li, K.; Olson, D. H.; Seidel, J.; Emge, T. J.; Gong, H.; Zeng, H.; Li, J., Zeolitic imidazolate frameworks for kinetic separation of propane and propene. *J. Am. Chem. Soc.* **2009**, *131*, 10368-10369.
201. Pimentel, B. R.; Lively, R. P., Enabling Kinetic Light Hydrocarbon Separation via Crystal Size Engineering of ZIF-8. *Ind. Eng. Chem. Res.* **2016**, *55*, 12467-12476.
202. Wang, Y.; Zhao, D., Beyond Equilibrium: Metal–Organic Frameworks for Molecular Sieving and Kinetic Gas Separation. *Cryst. Growth Des.* **2017**, *17*, 2291-2308.
203. Xue, D. X.; Belmabkhout, Y.; Shekhah, O.; Jiang, H.; Adil, K.; Cairns, A. J.; Eddaoudi, M., Tunable Rare Earth fcu-MOF Platform: Access to Adsorption Kinetics Driven Gas/Vapor Separations via Pore Size Contraction. *J. Am. Chem. Soc.* **2015**, *137*, 5034-5040.
204. Sauerbrey, G., Verwendung von Schwingquarzen zur Wagung dünner Schichten und zur Mikrowgung. *Z. Phys.* **1959**, *155*, 206-222.
205. Song, Q.; Nataraj, S. K.; Roussanova, M. V.; Tan, J. C.; Hughes, D. J.; Li, W.; Bourgoïn, P.; Alam, M. A.; Cheetham, A. K.; Al-Muhtaseb, S. A.; Sivaniah, E., Zeolitic imidazolate framework (ZIF-8) based polymer nanocomposite membranes for gas separation. *Energy Environ. Sci.* **2012**, *5*, 8359-8369.
206. Tan, J. C.; Bennett, T. D.; Cheetham, A. K., Chemical structure, network topology, and porosity effects on the mechanical properties of Zeolitic Imidazolate Frameworks. *Proc. Natl. Acad. Sci. U. S. A.* **2010**, *107*, 9938-9943.
207. Khaletskaya, K.; Turner, S.; Tu, M.; Wannapaiboon, S.; Schneemann, A.; Meyer, R.; Ludwig, A.; Van Tendeloo, G.; Fischer, R. A., Self-Directed Localization of ZIF-8 Thin Film Formation by Conversion of ZnO Nanolayers. *Adv. Funct. Mater.* **2014**, *24*, 4804-4811.
208. Application of the Sauerbrey equations is justified in that the films deposited are rigid and uniform across the QCM sensor while for all cases the change in resonant frequencies are less than 2% of the initial frequency of the sensor.
209. Karagiariidi, O.; Lalonde, M. B.; Bury, W.; Sarjeant, A. A.; Farha, O. K.; Hupp, J. T., Opening ZIF-8: a catalytically active zeolitic imidazolate framework of sodalite topology with unsubstituted linkers. *J. Am. Chem. Soc.* **2012**, *134*, 18790-18796.

210. Krokidas, P.; Castier, M.; Moncho, S.; Brothers, E.; Economou, I. G., Molecular Simulation Studies of the Diffusion of Methane, Ethane, Propane, and Propylene in ZIF-8. *J. Phys. Chem. C* **2015**, *119*, 27028-27037.
211. Moggach, S. A.; Bennett, T. D.; Cheetham, A. K., The effect of pressure on ZIF-8: increasing pore size with pressure and the formation of a high-pressure phase at 1.47 GPa. *Angew. Chem., Int. Ed.* **2009**, *48*, 7087-7089.
212. Previous computational studies by Fairen-Jimenez et al., (*Dalton Trans.* **2012**, *41*, 10752-10762) based on small alkanes (C<sub>1-4</sub>) yield maximum-capacity estimates for ZIF-8 of around 40-45 carbons per unit cell (uc). For n-hexane, this estimate translates to about 7 molecules/uc. Given a 300 nm solvothermally grown film, and assuming a range of 6-8 hexane molecules/uc, we obtained a capacity range of 5.2-7.0  $\mu\text{g}/\text{cm}^2$  (see Appendix C, Section C5) which is congruent with our experimental observation of uptake at 8 molecules/uc (Figure 4.3c)
213. Uptake of hexane plateaus at 7.02  $\mu\text{g}/\text{cm}^2$  within 3 minutes while cyclohexane only reaches an overall low uptake capacity of 0.13  $\mu\text{g}/\text{cm}^2$  during the same time frame
214. Throughout the course of this experiment, the analyte (1 mL) in the experimental jar never dried out, which means that the vapor pressure throughout the experiment was constant. Additionally, we assume that the evaporation rate is significantly faster than diffusion through the thin films.
215. As one further test, we followed the uptake n-hexane by a 300 nm ZIF-8 film that had been pre-exposed to cyclohexane vapor to fill molecule-voids between crystallites. The resulting QCM curve is included in Figure 4.3c. The total uptake of n-hexane is diminished by a few percent, while the transport diffusivity returned by Equation 4.2 agrees within experimental uncertainty with the value obtained without pre-exposure to cyclohexane ( $9.6 \pm 0.9 \times 10^{-16}$  vs.  $1.0 \pm 0.1 \times 10^{-15}$   $\text{m}^2/\text{s}$ )
216. Heinke, L.; Gu, Z.; Woll, C., The surface barrier phenomenon at the loading of metal-organic frameworks. *Nat. Commun.* **2014**, *5*, 4562/1-6.
217. Hibbe, F.; Chmelik, C.; Heinke, L.; Pramanik, S.; Li, J.; Ruthven, D. M.; Tzoulaki, D.; Karger, J., The nature of surface barriers on nanoporous solids explored by microimaging of transient guest distributions. *J. Am. Chem. Soc.* **2011**, *133*, 2804-2807.
218. By convention, isosteric energies of adsorption for MOFs are typically described as increasingly positive for increasing strength of interaction. Here we describe increasingly favorable adsorption in terms of increasingly negative free energies of adsorption.



219. Yang, K.; Cai, Z.; Jaiswal, A.; Tyagi, M.; Moore, J. S.; Zhang, Y., Dynamic Odd-Even Effect in Liquid n-Alkanes near Their Melting Points. *Angew. Chem., Int. Ed.* **2016**, *55*, 14090-14095.
220. Costa, J. C. S.; Mendes, A.; Santos, L. M. N. B. F., Chain Length Dependence of the Thermodynamic Properties of n-Alkanes and their Monosubstituted Derivatives. *J. Chem. Eng. Data* **2017**, *63*, 1-20.
221. Nerngchamnong, N.; Yuan, L.; Qi, D. C.; Li, J.; Thompson, D.; Nijhuis, C. A., The role of van der Waals forces in the performance of molecular diodes. *Nat. Nanotechnol.* **2013**, *8*, 113-118.
222. We note, in passing, that these diffusivities are surprisingly similar to reported MOF-based redox conductivity diffusion constants ( $10^{-10}$  to  $10^{-14}$  cm<sup>2</sup>/s) (see *Chem. Soc. Rev.*, **2017**, *46*, 3185-3241 and *J. Am. Chem. Soc.* **2018**, *140*, 2985–2994) and comparisons between the transport behavior of charges and vapors could shed meaningful insight on ion diffusion pathways during electrochemical operations.
223. Eum, K.; Jayachandrababu, K. C.; Rashidi, F.; Zhang, K.; Leisen, J.; Graham, S.; Lively, R. P.; Chance, R. R.; Sholl, D. S.; Jones, C. W.; Nair, S., Highly tunable molecular sieving and adsorption properties of mixed-linker zeolitic imidazolate frameworks. *J. Am. Chem. Soc.* **2015**, *137*, 4191-4197.
224. Howarth, A. J.; Wang, T. C.; Al-Juaid, S. S.; Aziz, S. G.; Hupp, J. T.; Farha, O. K., Efficient extraction of sulfate from water using a Zr-metal-organic framework. *Dalton Trans.* **2016**, *45*, 93-97.
225. Drout, R. J.; Otake, K.; Howarth, A. J.; Islamoglu, T.; Zhu, L.; Xiao, C.; Wang, S.; Farha, O. K., Efficient Capture of Perrhenate and Pertechnetate by a Mesoporous Zr Metal–Organic Framework and Examination of Anion Binding Motifs. *Chem. Mater.* **2018**, *30*, 1277-1284.
226. Vial, L.; Ludlow, R. F.; Leclaire, J.; Perez-Fernandez, R.; Otto, S., Controlling the biological effects of spermine using a synthetic receptor. *J. Am. Chem. Soc.* **2006**, *128*, 10253-10257.
227. Lippens, B., Studies on pore systems in catalysts V. The t method. *J. Catal.* **1965**, *4*, 319-323.

228. Chakraborty, S.; Colon, Y. J.; Snurr, R. Q.; Nguyen, S. T., Hierarchically porous organic polymers: highly enhanced gas uptake and transport through templated synthesis. *Chem. Sci.* **2015**, *6*, 384-389.
229. Marczewski, A. W. <http://adsorption.org/awm/ads/meso/RIB-ASAP.htm>. (accessed January 5, 2018).
230. <http://www.micromeritics.com/product-showcase/microactive-interactive-data-analysis-software/microactive-interactive-data-analysis-reports.aspx>. (accessed January 5, 2018).
231. Li, P.; Klet, R. C.; Moon, S. Y.; Wang, T. C.; Deria, P.; Peters, A. W.; Klahr, B. M.; Park, H. J.; Al-Juaid, S. S.; Hupp, J. T.; Farha, O. K., Synthesis of nanocrystals of Zr-based metal-organic frameworks with csq-net: significant enhancement in the degradation of a nerve agent simulant. *Chem. Commun.* **2015**, *51*, 10925-10928.
232. These reported % yields are not accurate as these MOFs can trap a significant amount of solvent and water inside their pores.
233. Ghosh, P.; Colón, Y. J.; Snurr, R. Q., Water adsorption in UiO-66: the importance of defects. *Chem. Commun.* **2014**, *50*, 11329-11331.
234. Kercher, A. K.; Nagle, D. C., TGA modeling of the thermal decomposition of CCA treated lumber waste. *Wood Sci. Technol.* **2001**, *35*, 325-341.
235. Abney, C. W.; Taylor-Pashow, K. M. L.; Russell, S. R.; Chen, Y.; Samantaray, R.; Lockard, J. V.; Lin, W., Topotactic Transformations of Metal–Organic Frameworks to Highly Porous and Stable Inorganic Sorbents for Efficient Radionuclide Sequestration. *Chem. Mater.* **2014**, *26*, 5231-5243.
236. As<sup>III</sup> adsorption was carried out at pH 5 to facilitate the conversion of two As-OH moieties on arsenite into stable chelating As-SR bonds as shown in the reaction of thiol-rich proteins with Lewisite (L. A. Stocken and R. H. S. Thompson, *Biochem. J.*, **1946**, *40*, 529-535.)
237. Tossell, J. A., Theoretical studies on arsenic oxide and hydroxide species in minerals and in aqueous solution. *Geochim. Cosmochim. Acta* **1997**, *61*, 1613-1623.
238. Ho, Y. S.; McKay, G., Pseudo-second order model for sorption processes. *Process Biochem. (Amsterdam, Neth.)* **1999**, *34*, 451-465.
239. Zhu, B.-J.; Yu, X.-Y.; Jia, Y.; Peng, F.-M.; Sun, B.; Zhang, M.-Y.; Luo, T.; Liu, J.-H.; Huang, X.-J., Iron and 1,3,5-Benzenetricarboxylic Metal–Organic Coordination Polymers

- Prepared by Solvothermal Method and Their Application in Efficient As(V) Removal from Aqueous Solutions. *J. Phys. Chem. C* **2012**, *116*, 8601-8607.
240. Myneni, S. C. B.; Traina, S. J.; Waychunas, G. A.; Logan, T. J., Vibrational spectroscopy of functional group chemistry and arsenate coordination in ettringite. *Geochim. Cosmochim. Acta* **1998**, *62*, 3499-3514.
241. Toby, B. H.; Von Dreele, R. B., GSAS-II: the genesis of a modern open-source all purpose crystallography software package. *J. Appl. Crystallogr.* **2013**, *46*, 544-549.
242. Given that the TGA instrument used for these analyses does not have a reference cell, the TGA profiles are plotted as functions of time to avoid artificial spikes in the measured temperatures of the sample (e.g., due to sample combustion).
243. The numbers represented here slightly differ from the numbers shown in *Chem. Sci.* **2016**, *7*, 6492-6498 as these values were calculated more accurately in accounting for the percent mass gain from O<sub>2</sub> during combustion.
244. See: [http://ws680.nist.gov/publication/get\\_pdf.cfm?pub\\_id=903698](http://ws680.nist.gov/publication/get_pdf.cfm?pub_id=903698) (accessed January 17, 2018)
245. Spectra were taken on an Agilent DD2 500 NMR instrument.
246. Potoff, J. J.; Siepmann, J. I., Vapor-liquid equilibria of mixtures containing alkanes, carbon dioxide, and nitrogen. *AIChE J.* **2001**, *47*, 1676-1682.
247. Rappe, A. K.; Casewit, C. J.; Colwell, K. S.; Goddard, W. A.; Skiff, W. M., UFF, a full periodic table force field for molecular mechanics and molecular dynamics simulations. *J. Am. Chem. Soc.* **1992**, *114*, 10024-10035.
248. Peng, D.-Y.; Robinson, D. B., A New Two-Constant Equation of State. *Ind. Eng. Chem. Fundam.* **1976**, *15*, 59-64.
249. See discussion in Chapter 3 under the section termed "Determining best-fit structural models for defect-containing UiO-66"
250. Gelb, L. D.; Gubbins, K. E., Pore Size Distributions in Porous Glasses: A Computer Simulation Study. *Langmuir* **1999**, *15*, 305-308.

251. Jasuja, H.; Walton, K. S., Experimental Study of CO<sub>2</sub>, CH<sub>4</sub>, and Water Vapor Adsorption on a Dimethyl-Functionalized UiO-66 Framework. *J. Phys. Chem. C* **2013**, *117*, 7062-7068.
252. Schoenecker, P. M.; Carson, C. G.; Jasuja, H.; Flemming, C. J. J.; Walton, K. S., Effect of Water Adsorption on Retention of Structure and Surface Area of Metal–Organic Frameworks. *Ind. Eng. Chem. Res.* **2012**, *51*, 6513-6519.
253. Micromeritics' new innovative MicroActive data analysis software allows users to interactively evaluate isotherm data from Micromeritics' ASAP, TriStar, and Gemini gas adsorption instruments. <http://www.micromeritics.com/Product-Showcase/MicroActive-Interactive-Data-Analysis-Software/MicroActive-Interactive-Data-Analysis-Reports.aspx> (accessed August 2).
254. Cravillon, J.; Münzer, S.; Lohmeier, S.-J.; Feldhoff, A.; Huber, K.; Wiebcke, M., Rapid Room-Temperature Synthesis and Characterization of Nanocrystals of a Prototypical Zeolitic Imidazolate Framework. *Chem. Mater.* **2009**, *21*, 1410-1412.
255. Jafari, S.; Ghorbani-Shahna, F.; Bahrami, A.; Kazemian, H., Effects of Post-Synthesis Activation and Relative Humidity on Adsorption Performance of ZIF-8 for Capturing Toluene from a Gas Phase in a Continuous Mode. *Appl Sci* **2018**, *8*, 310.
256. Titze, T.; Lauerer, A.; Heinke, L.; Chmelik, C.; Zimmermann, N. E.; Keil, F. J.; Ruthven, D. M.; Karger, J., Transport in Nanoporous Materials Including MOFs: The Applicability of Fick's Laws. *Angew. Chem., Int. Ed.* **2015**, *54*, 14580-14583.
257. Crank., J., *The mathematics of diffusion*. 2<sup>nd</sup> ed.; Clarendon Press: Oxford, 1975; 421 pp.
258. Baghbanzadeh, M.; Simeone, F. C.; Bowers, C. M.; Liao, K. C.; Thuo, M.; Baghbanzadeh, M.; Miller, M. S.; Carmichael, T. B.; Whitesides, G. M., Odd-even effects in charge transport across n-alkanethiolate-based SAMs. *J. Am. Chem. Soc.* **2014**, *136*, 16919-16925.
259. Nimmermark, A.; Öhrström, L.; Reedijk, J., Metal-ligand bond lengths and strengths: Are they correlated? A detailed CSD analysis. *Z. Kristallogr.* **2013**, *228*, 311-317.
260. Atilgan, A.; Islamoglu, T.; Howarth, A. J.; Hupp, J. T.; Farha, O. K., Detoxification of a Sulfur Mustard Simulant Using a BODIPY-Functionalized Zirconium-Based Metal-Organic Framework. *ACS Appl. Mater. Interfaces* **2017**, *9*, 24555-24560.

261. Palmer, R. H.; Liu, J.; Kung, C. W.; Hod, I.; Farha, O. K.; Hupp, J. T., Electroactive Ferrocene at or near the Surface of Metal-Organic Framework UiO-66. *Langmuir* **2018**, *34*, 4707-4714.

## **Appendices**

## Appendix A Supplementary to Chapter 2

Portions of this appendix appear in the following manuscript:

Audu, C. O.; Nguyen, H. G. T.; Chang, C.; Katz, M. J.; Mao, L.; Farha, O. K.; Hupp, J. T.; Nguyen, S. T. “The dual capture of As<sup>V</sup> and As<sup>III</sup> by UiO-66 and analogues” *Chem. Sci.* **2016**, 7, 6492-6498.

### A1. Materials and Methods.

Unless otherwise stated, all reagents were used as received. Hydrochloric acid, zirconium chloride, and terephthalic acid were purchased from Aldrich Chemicals Company, Inc. (Milwaukee, WI). Concentrated sulfuric acid and glacial acetic acid were purchased from VWR Scientific, LLC (Chicago, IL). Arsenic, zirconium, and sulfur ICP standards were purchased from Sigma-Aldrich Co. LLC (St. Louis, MI). Conc. HF (49 wt. %) was obtained from Fisher Scientific Inc. (Pittsburgh, PA). 2,5-Dimercaptoterephthalic acid was prepared using the previously reported protocol.<sup>226</sup> Ultrapure deionized water (18.2 MΩ cm resistivity) was obtained from a Millipore system (EMD Millipore, Billerica, MA). Solvents were purchased from either Sigma-Aldrich Co. LLC (St. Louis, MI), Fisher Scientific, Inc. (Pittsburg, PA), or Avantor Performance Materials, Inc. (Center Valley, PA) and used as received. All the gases used for the adsorption and desorption measurements were ultra-high purity grade 5 and were obtained from Airgas Specialty Gases (Chicago, IL).

Powder X-ray diffraction (PXRD) patterns were recorded on a Rigaku X-ray Diffractometer Model ATX-G (Rigaku Americas, The Woodlands, TX) equipped with an 18 kW Cu rotating anode, an MLO monochromator, and a high-count-rate scintillation detector.

Measurements were made over the range  $2^\circ < 2\theta < 40^\circ$  in  $0.05^\circ$  step width with a  $2^\circ/\text{min}$  scanning speed.

$\text{N}_2$  adsorption and desorption isotherms were measured on a Micromeritics Tristar II 3020 (Micromeritics, Norcross, GA) at 77 K. Before each run, samples were activated at 100-150 °C for 24 h (or until outgass rate  $\leq 0.02$  mmHg) under high vacuum on either a MasterPrep (Quantachrome Instruments, Boynton Beach, FL) or a Smart VacPrep (Micromeritics, Norcross, GA). At least 50 mg of sample was used in each measurement. The specific surface areas for  $\text{N}_2$  were calculated using the Brunauer-Emmet-Teller (BET) model in the range of  $0.005 < P/P_0 < 0.1$ . The pore size distributions of the MOFs were calculated from the adsorption-desorption isotherms by density functional theory (DFT) using the carbon slit-pore  $\text{N}_2$ -DFT model.

The micropore volumes, micropore surface areas, and external surface areas for all samples were determined using conventional t-plot methods<sup>227</sup> from  $\text{N}_2$  adsorption data. For most of the MOFs, the values were selected over the 3-5 Å t range by fitting the data to the Harkins-Jura thickness equation. For HCl-UiO-67|<sub>9/12</sub>, whose adsorption isotherm exhibits a mesoporous step (at 0.1-0.2  $P/P_0$ ), the t range values were selected by fitting the data to the Harkins-Jura thickness equation over a range that affords a physically sensible positive value for micropore volume while maintaining a correlation coefficient that is closest to 1. This is the process we used in a recent publication on hierarchical porous organic polymers<sup>228</sup> and is recommended by Prof. A. W. Marczewski<sup>229</sup> as well as the Micromeritics Instrument Corporation.<sup>230</sup> For HCl-UiO-67|<sub>9/12</sub>, the t range was thus selected to be 5.5-6.4 Å. We note that a similar process has also been applied by Li *et al* to characterize a series of mesoporous MOF nanoparticles.<sup>231</sup>



Inductively coupled plasma optical emission spectroscopy (ICP-OES) analyses of As and Zr contents in the supernatants from the arsenic batch-adsorption experiments (Section A3) were conducted on a Varian Vista-MDX model ICP-OES spectrometer (Varian Inc., Walnut Creek, CA) located in the IMSERC facility of Northwestern University. This instrument is equipped with a CCD detector and an argon plasma to cover the 175-to-785 nm spectral range.

ICP-OES analyses of the acid-digested MOF samples (for Zr and S contents) were conducted on a Thermo Scientific™ iCAP™ 7600 ICP-OES spectrometer (Thermo Fisher Scientific Inc., Waltham, MA) located in the QBIC facility of Northwestern University. This instrument is equipped with a high performance solid-state CID86 chip detector, dual view (radial and axial) capability, and an argon plasma to cover the 166-to-847 nm spectral range. In a typical procedure, MOF samples (2-5 mg) were digested in a small amount (1 mL) of a mixture of 3:1 v/v conc.  $\text{HNO}_3$ : $\text{H}_2\text{O}_2$  (30 wt % in  $\text{H}_2\text{O}$ ) by heating in a Biotage SPX microwave reactor (Biotage, Uppsala, Sweden, software version 2.3, build 6250) at 180 °C until the solution became clear (~30 min). This acidic solution was then diluted to 25 mL with ultrapure deionized  $\text{H}_2\text{O}$  and analyzed for Zr (339.198, 343.823, and 349.619 nm) content as compared to standard solutions.

For safety considerations, thiolated MOF samples (~ 2 mg) were digested using either one of the following two methods:

1. Unoptimized procedure, which was used for the preliminary experiments in our study. MOF sample (~2 mg) was combined with dilute aqueous HF (4 mL, prepared by diluting 3 mL of conc. HF to 30 mL with ultrapure deionized water in a 50 mL propylene centrifuge tube) in a 15 mL propylene centrifuge tube. The tube was capped and agitated at room temperature for 24 h on a Fisher Scientific standard vortex mixer (Fisher Scientific, Inc., Pittsburgh, PA) set at 4.5 speed

dial number. After stopping the agitation, conc.  $\text{HNO}_3$  (250  $\mu\text{L}$ ) was then added to the cloudy yellow sample, the tube was recapped and agitated for another 24 h to afford a less-cloudy, light-yellow, but still partially digested mixture. After stopping the agitation, another aliquot of conc.  $\text{HNO}_3$  (500  $\mu\text{L}$ ) was added and the sample was recapped and then agitated for an additional 48 h, leading to no visible change. The agitation was then stopped and the centrifuge tube was transferred to a sonicator inside a well-ventilated hood. After several minutes of sonication, the sample was removed from the sonicator; conc.  $\text{HCl}$  (250  $\mu\text{L}$ ) was added; and the sample was capped and placed in a 60 °C sand bath for 24 h. As the mixture was still visibly cloudy after this, more conc.  $\text{HF}$  (250  $\mu\text{L}$ ) was added to the cooled down sample and the sample was recapped and heated at in a 70 °C sand bath for 24 h. At this point, the sample has become colorless and not cloudy; however, it still contained a few visible white specks of solids. More conc.  $\text{HF}$  (100  $\mu\text{L}$ ) was added to the cooled down sample and the sample was capped and heated in a 70 °C sand bath for 24 h. The resulting clear solution (5.35 mL total volume of approximately 1:1:0.3:4.7 volumetric ratio of conc.  $\text{HNO}_3$ :conc.  $\text{HF}$ :conc.  $\text{HCl}$ : $\text{H}_2\text{O}$ ) was then transferred to a 50 mL propylene centrifuge tube in the hood and diluted to 50 mL with ultrapure deionized  $\text{H}_2\text{O}$  using a 5 mL Eppendorf Research mechanical pipettor. This acid-digested sample was then analyzed for Zr (339.198, 343.823, and 349.619 nm) and S (180.731 and 182.034 nm) contents as compared to standard solutions. **Caution:** *HF is very toxic and dangerous to handle without proper safety training. PPE must include Silvershield gloves and goggles. Acid digestions and subsequent dilutions should be carried out in a well-ventilated hood.*

2.Optimized procedure, which was used for the later experiments in our study. A digestion solution (5.35 mL total volume in 1:1:0.3:4.7 volumetric ratios of conc.  $\text{HNO}_3$ :conc.  $\text{HF}$ :conc.

HCl:H<sub>2</sub>O) was prepared by combining the reagents in the following order: conc. HNO<sub>3</sub> (750  $\mu$ L), conc. HCl (250  $\mu$ L), H<sub>2</sub>O (3.6 mL), and conc. HF (750  $\mu$ L). MOF sample (~2 mg) was combined with this mixture in a 15 mL propylene centrifuge tube, capped, and heated in a 70 °C sand bath for 3 h. The resulting clear solution was then transferred to a 50 mL propylene centrifuge tube in the hood and diluted to 50 mL with ultrapure deionized H<sub>2</sub>O using a 5 mL Eppendorf Research mechanical pipettor. This acid-digested sample was then analyzed for Zr (339.198, 343.823, and 349.619 nm) and S (180.731 and 182.034 nm) contents as compared to standard solutions.

Thermogravimetric analysis (TGA) experiments were carried out on a Q500 thermogravimetric analyzer (TA Instruments Inc., New Castle, DE). Samples (~20 mg) were heated from room temperature to 600 °C under an O<sub>2</sub>-rich (30 vol % in nitrogen) gas flow (90 mL/min) at a heating rate of 5 °C/min.

X-ray photoelectron spectroscopy (XPS) measurements were carried out at the Keck-II/NUANCE facility at Northwestern University (NU) on a ESCALAB 250 Xi instrument (Thermo Scientific, Waltham, MA) (Al K $\alpha$  radiation,  $h\nu = 1486.6$  eV) equipped with an electron flood gun. XPS data was analyzed using Thermo Scientific Avantage Data System software (v5.926) and all spectra were referenced to the adventitious C1s peak (284.5 eV). To have enough for sample for analysis, 5-6 MOF samples (~10 mg/MOF per sample) were subjected to the same arsenic batch-adsorption experimental conditions (Section A3), combined, and vacuum-filtered over a Büchner funnel (Whatman filter paper Grade 2: 8  $\mu$ m). The collected solids were subsequently rinsed over the Büchner funnel with water (2  $\times$  20 mL), acetone (1  $\times$  20 mL), and suction-dried for several hours. Prior to XPS measurements, the solid samples were thermally activated at 120 °C under high vacuum to remove water from the pores.

Diffuse reflectance infrared Fourier-transformed spectroscopy (DRIFTS) experiments were carried out on a Nicolet Nexus 870 FTIR spectrometer (Thermo Scientific, Waltham, MA) equipped with an MCT detector. MOF samples (from the remaining sample prepared for XPS; see above) were first activated at 120-150 °C under high vacuum for 24 h. These activated MOF samples (~ 3 wt %) were then combined with anhydrous KBr, grounded up thoroughly, and then loaded into the instrument as a powder. The spectra were collected at 1 cm<sup>-1</sup> resolution over 64 scans under N<sub>2</sub> purge. A sample of powder KBr was utilized as the background. Spectra were converted to Kubelka-Munk units and normalized to the most prominent peak within the specified region.

Scanning electron microscopy (SEM) images were obtained at Northwestern University's EPIC/NUANCE facility on a SU8030 FE-SEM (Hitachi High Technologies America, Inc., Dallas, TX) microscope with an acceleration voltage of 10 kV. Prior to imaging, activated MOF samples were coated with either a film of Au/Pd or Os (~10-20 nm thickness) using either a Denton Desk III TSC Sputter Coater (Denton Vacuum, Moorestown, NJ) or a Filgen Osmium Coater Model OPC-60A (Filgen, Nagoya, Japan), respectively. Size measurements were obtained from sample populations of >70 particles, which were used to construct the standard normal distribution plots (mean ± 3 standard deviation units) and the histograms. Data are shown in Figure A6.

Transmission electron microscopy (TEM) images and energy-dispersive X-ray spectroscopy (EDS) line scans were collected at Northwestern University's EPIC/NUANCE facility on a Hitachi HT-7700 Biological S/TEM (Hitachi High Technologies America, Inc., Dallas, TX) equipped with a Bruker EDS system with an accelerating voltage of 120 kV. MOF samples (1-2 mg) were sonicated in ethanol (~10 mL) until a well-dispersed solution was obtained.

About 1-2 drops of the resulting solution was spotted on the TEM-grid and allowed to air-dry for a few minutes before TEM imaging.

High-resolution water-suppression  $^1\text{H}$  NMR spectra of aqueous samples were obtained on an Agilent DD2 600 NMR spectrometer (Agilent Technologies, Santa Clara, CA) equipped with a triple resonance (HCN) cold probe w/ Z-gradient and a sensitivity of  $^1\text{H} = 4300$  and  $^{13}\text{C} = 250$ . This high-resolution  $^1\text{H}$  NMR instrument, located in the IMSERC facility of Northwestern University, was necessary to observe the BDC aromatic resonances at  $\mu\text{M}$  concentration under water-suppression mode.

ESI-MS spectra was collected in negative mode by Saman Shafaie on an Agilent 6210 LC-TOF instrument located in the IMSERC facility of Northwestern University

## **A2. Synthesis of UiO MOF analogues.**

**AcOH-UiO-66**<sub>11/12</sub>. In a 2 L Erlenmeyer flask,  $\text{ZrCl}_4$  (1.86 g, 8 mmol) was dissolved by stirring in dimethylformamide (DMF, 500 mL) before being combined with glacial acetic acid (144 g, 137.3 mL, 2.4 mol). In a separate 1 L Erlenmeyer flask, terephthalic acid (1.33 g, 8 mmol) was dissolved completely in DMF (500 mL). This terephthalic acid solution was then added slowly to the  $\text{ZrCl}_4$  solution and the combined mixture was stirred until homogenized. The resulting solution was partitioned evenly among fifty 8 dram vials. The vials were capped and placed in a 120 °C pre-heated oven for 24 h before being cooled to room temperature. The contents of the vials were combined and filtered over a fine-fritted funnel to afford the crude AcOH-UiO-66<sub>11/12</sub> as a white powder, which was then rinsed with methanol (~ 50-80 mL). The collected materials were then immersed in methanol (~ 35 mL) and kept at 50-60 °C for an additional 24 h.

After cooling, this mixture was filtered over a fine-fritted funnel and allowed to dry under continuous suction from the house vacuum until the white solid become non-sticky and can be collected and stored at room temperature. This solid ( $\sim 1.5$  g,  $\sim 70\%$  yield based on  $\text{ZrCl}_4$ )<sup>232</sup> was activated in portions at  $150$  °C under high vacuum before being used in As-uptake experiments.

We note that the synthesis protocol as described above is quite reliable and can give materials with minimal variations in the amount of linkers ( $\text{AcOH-UiO-66}|_{(11.0 \pm 0.2)/12}$ ) as determined by TGA, see Figure A7), independent of the person who carried out the synthesis. As such, although our work was carried out with several different batches of materials from three different experimenters (H.G.T.N, C.-Y.C, or C.O.A) the results are consistent. For simplicity and clarity in the chapter 2, we refer to all of these materials as  $\text{AcOH-UiO-66}|_{11/12}$ .

**HCl-UiO-66**<sub>9/12</sub>. In an 125 mL Erlenmeyer flask,  $\text{ZrCl}_4$  (1.25 g, 5.4 mmol) was dissolved by sonication in a mixture of DMF (50 mL) and concentrated HCl (10 mL). In a separate 125 mL Erlenmeyer flask, terephthalic acid (1.23 g, 7.4 mmol) was dissolved by sonication in DMF (100 mL). This terephthalic acid solution was then added slowly to the  $\text{ZrCl}_4$  solution and the combined mixture was stirred until homogenized. The resulting solution was then partitioned among ten 8 dram vials. The vials were capped and placed in a  $80$  °C pre-heated oven for 24 h before being cooled to room temperature. The contents of the vials were combined and filtered over a fine-fritted funnel to afford the crude  $\text{HCl-UiO-66}|_{9/12}$  as a white powder, which was then rinsed with DMF ( $2 \times 30$  mL) and either ethanol or methanol ( $2 \times 30$  mL). The collected solid was left on the fritted glass funnel, which was connected to the house vacuum, covered with a glass crystallizing dish to allow for partial air flow through the funnel under reduced pressure, and allowed to be dried overnight in this fashion to give a white solid ( $\sim 1.4$  g,  $>100\%$  yield based on  $\text{ZrCl}_4$ ) that is

then stored at room temperature. Portions of this solid was activated at 150 °C under high vacuum as needed before being used in As-uptake experiments.

**HCl-UiO-66<sub>x/12</sub>-derivatives.** In a 250 mL Erlenmeyer flask, ZrCl<sub>4</sub> (1.5 g, 6.4 mmol) was dissolved by sonicating in a mixture of DMF (60 mL) and concentrated HCl (12 mL) for 1 h. This solution was then evenly distributed (15 mL per flask) into four separate 125 mL Erlenmeyer flasks. To each flask was then added solid terephthalic acid (see Table A1 for the amounts of linker added per each derivative) followed by DMF (30 mL). The resulting mixtures were then homogenized via sonication.

Each of the aforementioned solutions was then evenly transferred to three 8 dram vials (~16 mL each). These vials were capped and placed in a 80 °C pre-heated oven overnight before being allowed to cool to room temperature. The vials of the same composition were combined and filtered over fine-fritted funnels to afford the crude MOFs as white powders, each of which was then rinsed with DMF (2 × 100 mL) and EtOH (2 × 100 mL). The collected solid was left on the fritted glass funnel, which was connected to the house vacuum, covered with a glass crystallizing dish to allow for partial air flow through the funnel under reduced pressure, and allowed to be dried overnight in this fashion to give white solids that are stored at room temperature. Portions of this solid was activated at 150 °C under high vacuum as needed before being used in As-uptake experiments.

**Table A1** Preparative data for HCl-UiO-66<sub>|x/12</sub> ([Zr<sub>6</sub>O<sub>4</sub>(OH)<sub>4</sub>(L)<sub>x</sub>)]<sup>a</sup>

MOFs	Amount of organic linker used	MOF yield (mg)	Specific surface area (m <sup>2</sup> /g)
HCl-UiO-66 <sub> 10.6/12</sub>	801 mg (4.82 mmol)	~510	1400
<sup>b</sup> HCl-UiO-66 <sub> y/12</sub>	534 mg (3.21 mmol)	~430	1600
<sup>b</sup> HCl-UiO-66 <sub> 9/12</sub>	369 mg (2.22 mmol)	~430	1650
HCl-UiO-66 <sub> 8.2/12</sub>	214 mg (1.29 mmol)	~350	1760

<sup>a</sup>See Figure A4 for formula unit determination. <sup>b</sup>Yield, TGA, and As<sup>V</sup>-uptake data suggest no significant difference between these two batches.

**AcOH-UiO-66-(SH)<sub>2</sub>.** In an 125 mL Erlenmeyer flask, ZrCl<sub>4</sub> (110.4 mg, 0.48 mmol) was dissolved by sonication in a mixture of DMF (30 mL) and acetic acid (8.2 mL, 8.5 g, 143 mol). In a separate 125 mL Erlenmeyer flask, 2,5-dimercaptoterephthalic acid (111.6 mg, 0.48 mmol) was dissolved in DMF (30 mL) by sonication. This solution was then added slowly to the ZrCl<sub>4</sub> solution and the combined mixture was stirred until homogenized. The resulting solution was partitioned among three 8 dram vials. These vials were capped and placed in a 120 °C pre-heated oven for 24 h before being cooled to room temperature. The contents of the vials were combined and filtered over a fine-fritted funnel to afford the crude AcOH-UiO-66-(SH)<sub>2</sub> as a light-yellow powder, which was then resuspended in fresh DMF (~20 mL) in a capped 8 dram vial and placed in a 60 °C preheated oven for at least 3 h. After cooling to room temperature, this suspension was then filtered over a fine-fritted funnel; the collected solid was then resuspended in dichloromethane (DCM, ~20 mL) in a capped 8 dram vial and placed in a 60 °C pre-heated oven for at least 3 h. After cooling to room temperature, the suspension was then filtered over a fine-fritted funnel and the collected solid was rinsed with DCM (~20 mL). The collected solid was left on the fritted glass funnel, which was connected to the house vacuum, covered with a glass crystallizing dish to allow for partial air flow through the funnel under reduced pressure and allowed to be dried



overnight in this fashion to give a light-yellow powder (~130 mg, ~79% yield based on  $\text{ZrCl}_4$ ) that is then stored at room temperature. Portions of this solid was activated at 100 °C under high vacuum as needed before being used in As-uptake experiments.

**HCl-UiO-66-(SH)<sub>2</sub>.** In an 8 dram vial,  $\text{ZrCl}_4$  (125 mg, 0.54 mmol) was dissolved by sonication in a mixture of DMF (5 mL) and HCl (1 mL). In a separate 8 dram vial, 2,5-dimercaptoterephthalic acid (170.5 mg, 0.74 mmol) was dissolved by sonication in DMF (10 mL). This solution was then added slowly to the  $\text{ZrCl}_4$  solution and stirred until homogenized. The vial was capped and placed in a 80 °C pre-heated oven for 24 hours before being cooled to room temperature. The solid product was collected over a fine-fritted funnel, resuspended in fresh DMF (~20 mL) in a capped 8 dram vial, and finally placed in a 60 °C preheated oven for at least 3 h. After cooling to room temperature, this suspension was then filtered over a fine-fritted funnel; the collected solid was then resuspended in dichloromethane (~20 mL) in a capped 8 dram vial and placed in a preheated oven at 60 °C for at least 3 h. After cooling to room temperature, the suspension was then filtered over a fine-fritted funnel and the collected solid was rinsed with DCM (~ 20 mL). The collected solid was left on the fritted funnel, which was connected to the house vacuum, covered with a glass crystallizing dish to allow for partial air flow through the funnel under reduced pressure, and allowed to be dried overnight in this fashion to give a light-yellow powder (~190 mg, 100% yield based on  $\text{ZrCl}_4$ ) that is then stored at room temperature. Portions of this solid was activated at 100 °C under high vacuum as needed before being used in As-uptake experiments.

**HCl-UiO-66-(OH)<sub>2</sub>.** In an 8 dram vial,  $\text{ZrCl}_4$  (125 mg, 0.54 mmol) was dissolved by sonication in a mixture of DMF (5 mL) and HCl (1 mL). In a separate 8 dram vial, 2,5-

dihydroxyterephthalic acid (146.6 mg, 0.74 mmol) was dissolved by sonication in DMF (10 mL). This solution was then added slowly to the  $ZrCl_4$  solution and stirred until homogenized. The vial was capped and placed in a 80 °C pre-heated oven for 24 h before being cooled to room temperature. The solid product was collected via centrifugation and resuspended in fresh DMF (~20 mL) in a capped 8 dram vial, and finally placed in a 60 °C preheated oven for at least 3 h. After cooling to room temperature, the solid was separated from the suspension using centrifugation and then resuspended in dichloromethane (~20 mL) in a capped 8 dram vial. This suspension was placed in a preheated oven at 60 °C for at least 3 h. The collected solid was then dried in a vacuum oven overnight to give a light-yellow powder (~183 mg, 100% yield based on  $ZrCl_4$ ) that is then stored at room temperature. Portions of this solid was activated at 100 °C under high vacuum as needed before being used in As-uptake experiments.

**HCl-UiO-67**<sub>9/12</sub>. In a 125 mL Erlenmeyer flask,  $ZrCl_4$  (335 mg, 1.44 mmol) was dissolved by sonicating in DMF (25 mL) and HCl (2.5 mL). In a separate 125 mL Erlenmeyer flask, biphenyl-4,4'-dicarboxylic acid (450 mg, 1.86 mmol) was partially dissolved by sonicating in DMF (25 mL). This dicarboxylic acid solution was then added slowly to the  $ZrCl_4$  solution and stirred until homogenized. The resulting mixture was then partitioned among five 8 dram vials. The vials were capped and placed in an 80 °C pre-heated oven for 24 h before being cooled to room temperature. The contents of the vials were combined and the tan-white powder was collected over a fine-fritted funnel and rinsed with DMF (2 × 30 mL) and ethanol or methanol (2 × 30 mL). The collected solid was left on the fritted glass funnel, which was connected to the house vacuum, covered with a glass crystallizing dish to allow for partial air flow through the funnel under reduced pressure, and allowed to be dried overnight in this fashion to give a white solid

(~777 mg, >100% yield based on  $ZrCl_4$ ) that is then stored at room temperature. Portions of this solid was activated at 150 °C under high vacuum as needed before being used in As-uptake experiments.

### **A3. Arsenic batch-adsorption experiments.**

Stock solutions (1 L) with predetermined concentrations of  $As^{III}$  ( $As_2O_3$ ) and  $As^V$  ( $NaHAsO_4 \cdot 7H_2O$ ) were prepared prior to adsorption experiments. Typically, the solid reagent was dissolved by sonication in ultrapure deionized  $H_2O$  to give a clear solution. The pH of the resulting solution was measured and adjusted to pH ~7 for  $As^V$  and pH ~5 for  $As^{III}$  using HCl and NaOH when necessary. There was no observable changes to the pH values of these solutions for months after preparation and during experimentations. The As concentrations were verified with ICP-OES at the beginning of each batch-adsorption experiment ( $t = 0$ ).

Arsenic batch-adsorption experiments were carried out in 50 mL VWR polypropylene centrifuge tubes. In a typical experiment, activated MOF (~10 mg) was added as a solid to a centrifuge tube containing a 50 ppm solution (30 mL) of  $As^{III}$  ( $As_2O_3$ ) or  $As^V$  ( $NaHAsO_4 \cdot 7H_2O$ ). The tubes were capped and gently agitated using a Barnstead Thermolyne Labquake Shaker Rotisserie Model T400110 (Barnstead International, Dubuque, IA). At specified time intervals, the tubes were centrifuged at 3214 g for either 1 or 10 min (see below) before an aliquot (~3.5 mL) of the supernatant was removed using a disposable syringe and passed through a 0.2  $\mu m$  PTFE syringe filter (VWR International, North American Cat. No. 28145-495) into a 15 mL VWR polypropylene centrifuge tube. The collected liquid samples were then directly analyzed for Zr (327.307, 343.823, and 349.619 nm) and As (188.98 and 228.812 nm) content as compared to

standard solutions. The amount of arsenic uptake at each time point  $t$  is calculated as the difference between the initial As amount and the amount found in the supernatant solution at  $t$ .

For the uptake profiles shown in Figures. A9-11, as well as in Chapter 2 Figures. 2.3 and 2.6, each tube was agitated until a specified amount of time (i.e., 0.5, 3, 6, 24 h), at which the tubes were centrifuged for 10 min before sample aliquots were taken. For the comparative kinetic studies (i.e., data shown in Figures. A12-14), where several data points were taken during the first 30 minutes of contact time, each tube was agitated for 4 min and then centrifuged for 1 min before sample aliquots were taken.

## A4. Characterization of UiO samples

### A.4.1. Data

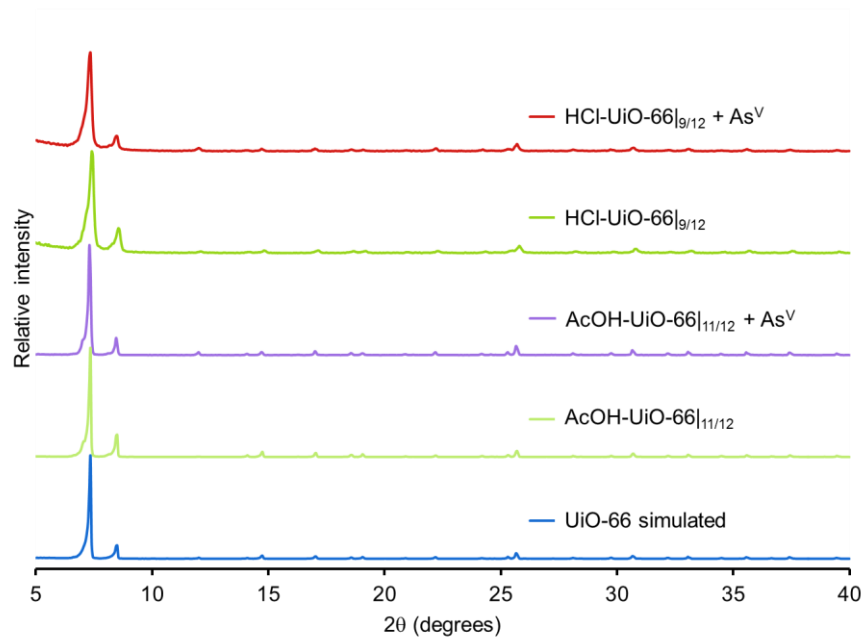


**Figure A1** PXRD patterns of as-prepared UiO-66 analogues before and after exposure to aqueous As<sup>V</sup> solutions for at least 24 h. The simulated PXRD pattern for UiO-66 is also included for comparison. As suggested by this data, the UiO-MOF samples are still crystalline after long exposures to aqueous As<sup>V</sup> solution.

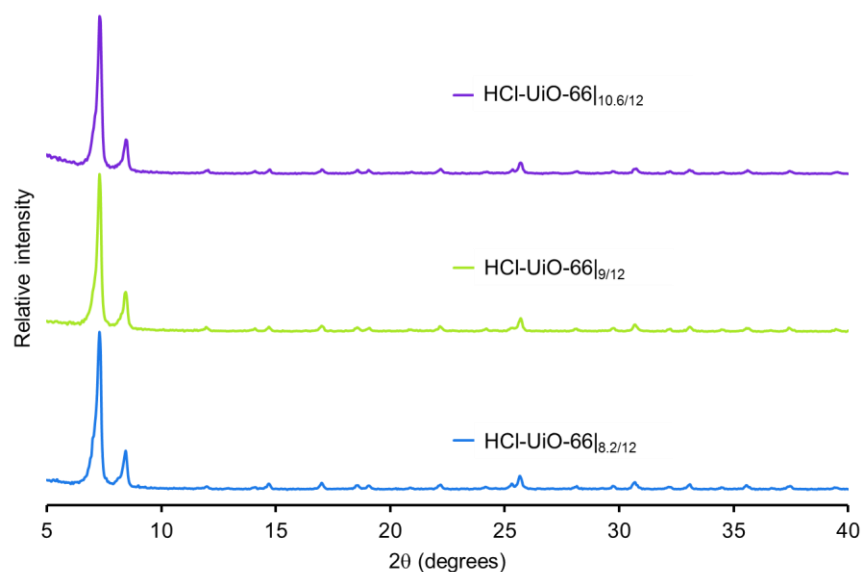


**Figure A2** PXRD patterns of as-prepared HCl-UiO-66<sub>|x/12</sub> derivatives.

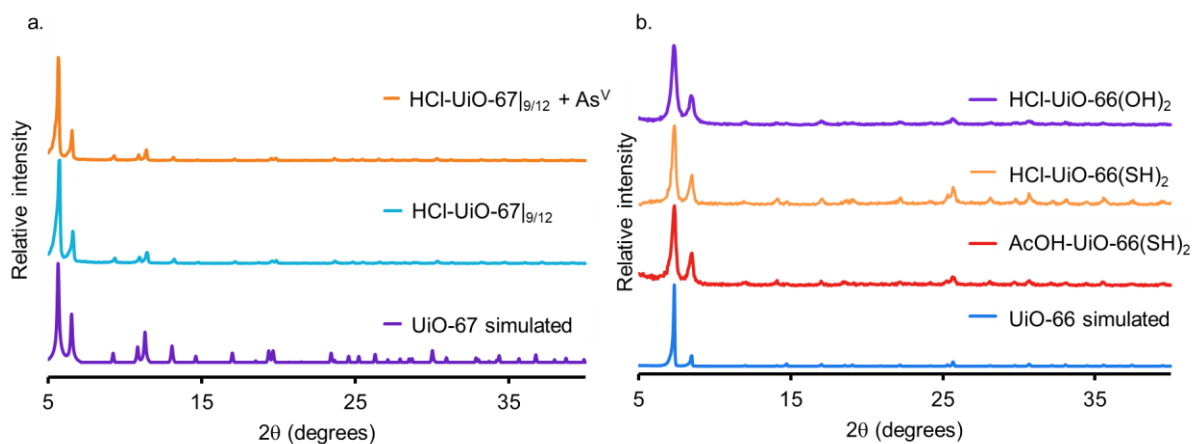


**Figure A3** (a) PXRD patterns of as-prepared HCl-UiO-67<sub>|9/12</sub> before and after exposure to solutions of As<sup>V</sup>. Good PXRD data can be obtained for As<sup>V</sup>-exposed HCl-UiO-67<sub>|9/12</sub> upon solvent exchange to acetone from water and subsequent thermal activation.<sup>58</sup> Although UiO-67 has been reported to be unstable in water or mild acid/base aqueous solutions,<sup>63</sup> this data suggest that our HCl-UiO-67<sub>|9/12</sub> retains crystallinity under our testing conditions. The simulated PXRD pattern for UiO-67 is also included for comparison. (b) PXRD patterns of as-prepared functionalized UiO-66 analogues (AcOH-UiO-66(SH)<sub>2</sub>, HCl-UiO-66(SH)<sub>2</sub> and HCl-UiO-66(OH)<sub>2</sub>). The simulated PXRD pattern for UiO-66 is also included for comparison.

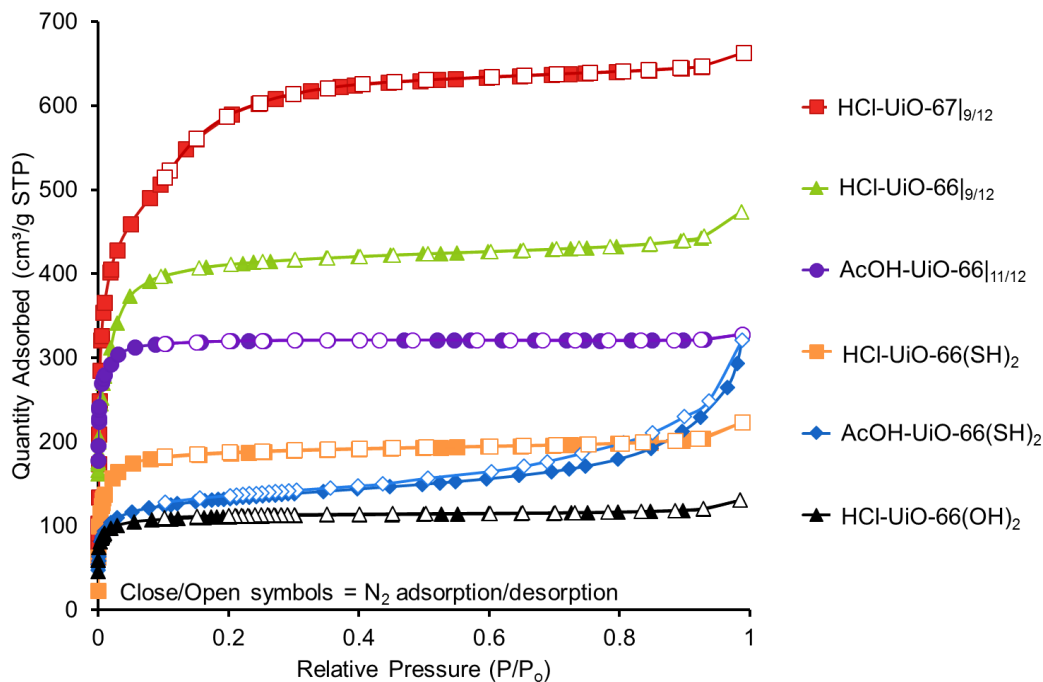


**Figure A4**  $N_2$  isotherms for the UiO-66 analogues used in Chapter 2.

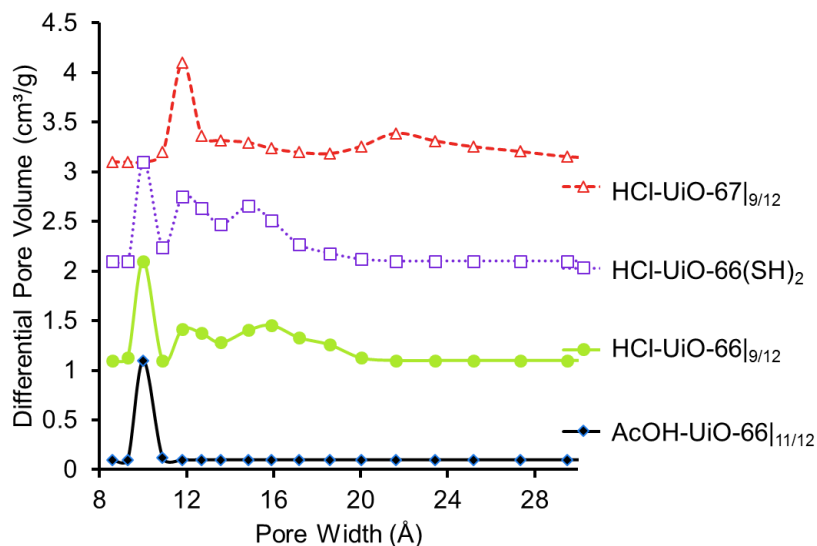


**Figure A5** Relative pore size-distribution profiles for the UiO-66 analogues grown with different acid modulators. Data were collected on a Tristar II 3020 instrument, which does not allow for accurate evaluate of pore sizes  $< 8 \text{ \AA}$ . In comparison to the nearly defect-free AcOH-UiO-66|<sub>11/12</sub> sample, HCl-UiO-66|<sub>x/12</sub> derivatives,

which have many missing-linker sites, clearly have additional larger pores (12-16 Å) that can increase accessibility to the internal binding sites. The appearance of these additional pores as a result of missing linker formation is in agreement with the analysis reported by Katz *et al.* for UiO-66 samples with up to four missing linkers.<sup>59</sup> We note that while the main micropore peak for AcOH-UiO-66<sub>|11/12</sub> (~10 Å) appears to be ~1-1.5 Å greater than the reported value for UiO-66,<sup>59, 73, 233</sup> this is an artificial limitation of the instrumentation and does not affect the conclusion shown in Chapter 2. Consistent with this analysis, HCl-UiO-67, which has a larger diphenyl dicarboxylate linker than HCl-UiO-66, expectedly has a larger main pore (12 Å) which is consistent with the reported value (11.5 Å).<sup>59</sup>

**Table A2** Pore and surface properties of MOFs

MOF	S.A. (m <sup>2</sup> ·g <sup>-1</sup> )	V <sub>pore</sub> (cm <sup>3</sup> ·g <sup>-1</sup> )	V <sub>micropore</sub> (cm <sup>3</sup> ·g <sup>-1</sup> )	S.A. <sub>micropore</sub> (m <sup>2</sup> ·g <sup>-1</sup> )	S.A. <sub>external</sub> (m <sup>2</sup> ·g <sup>-1</sup> )
AcOH-UiO-66 <sub> 11/12</sub>	1150	0.45	0.40	1080	70
HCl-UiO-66 <sub> 8.2/12</sub>	1760	0.72	0.56	1470	290
HCl-UiO-66 <sub> 9/12</sub>	1650	0.68	0.53	1390	260
HCl-UiO-66 <sub> 10.6/12</sub>	1480	0.64	0.47	1230	250
HCl-UiO-67 <sub> 9/12</sub>	2200	1.00	0.90	2100	100
AcOH-UiO-66(SH) <sub>2</sub>	500	0.21	0.13	330	170
HCl-UiO-66(SH) <sub>2</sub>	750	0.32	0.24	640	110
HCl-UiO-66(OH) <sub>2</sub>	440	0.18	0.15	390	50



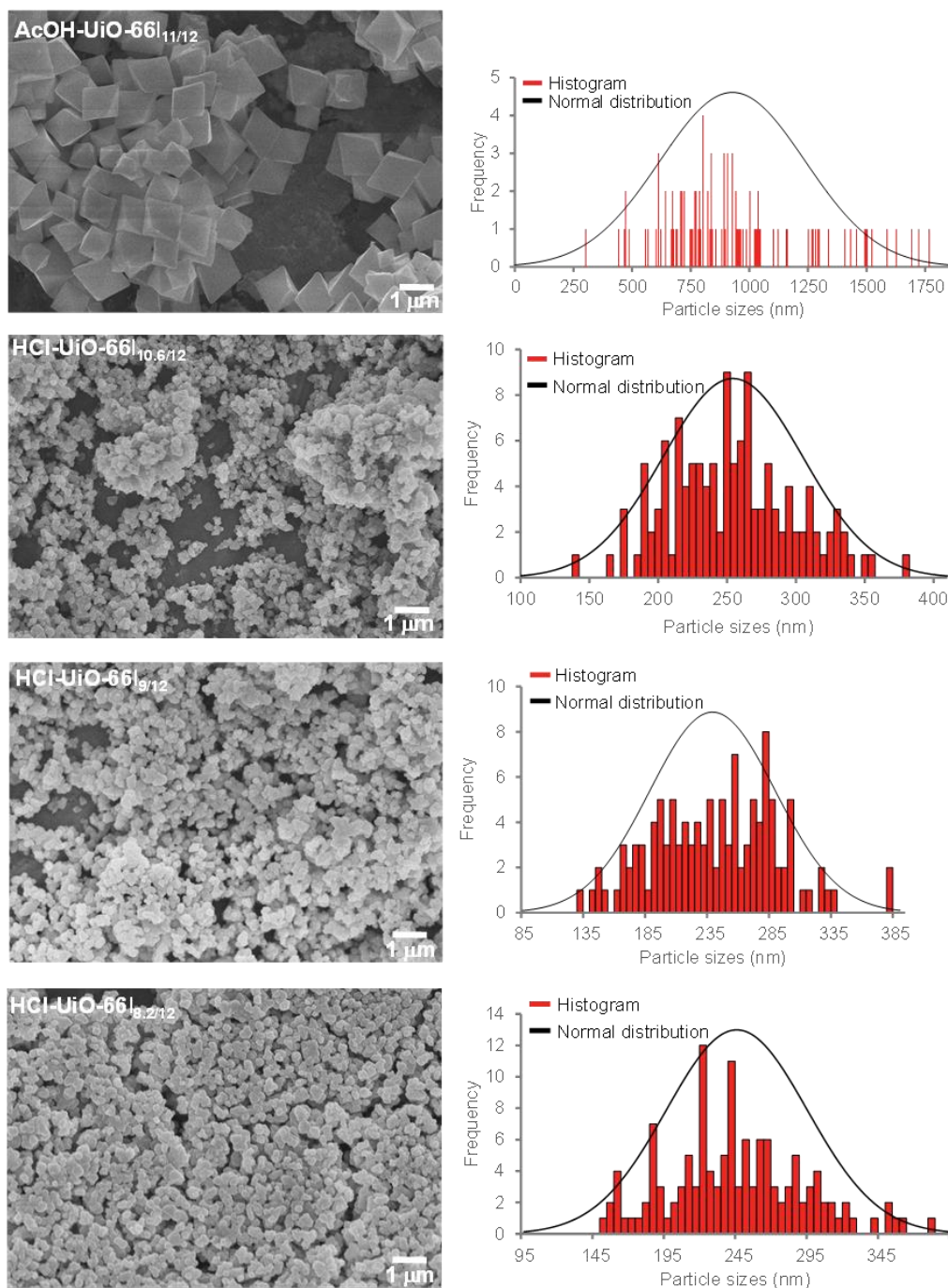


**Figure A6a** Left panels: SEM images of AcOH-UiO66<sub>|11/12</sub> and HCl-UiO66<sub>|x/12</sub> MOFs. Right panels: The corresponding SEM-derived particle-size-distribution profile for the MOF samples; each profile was constructed based on measurements of >70 particles.

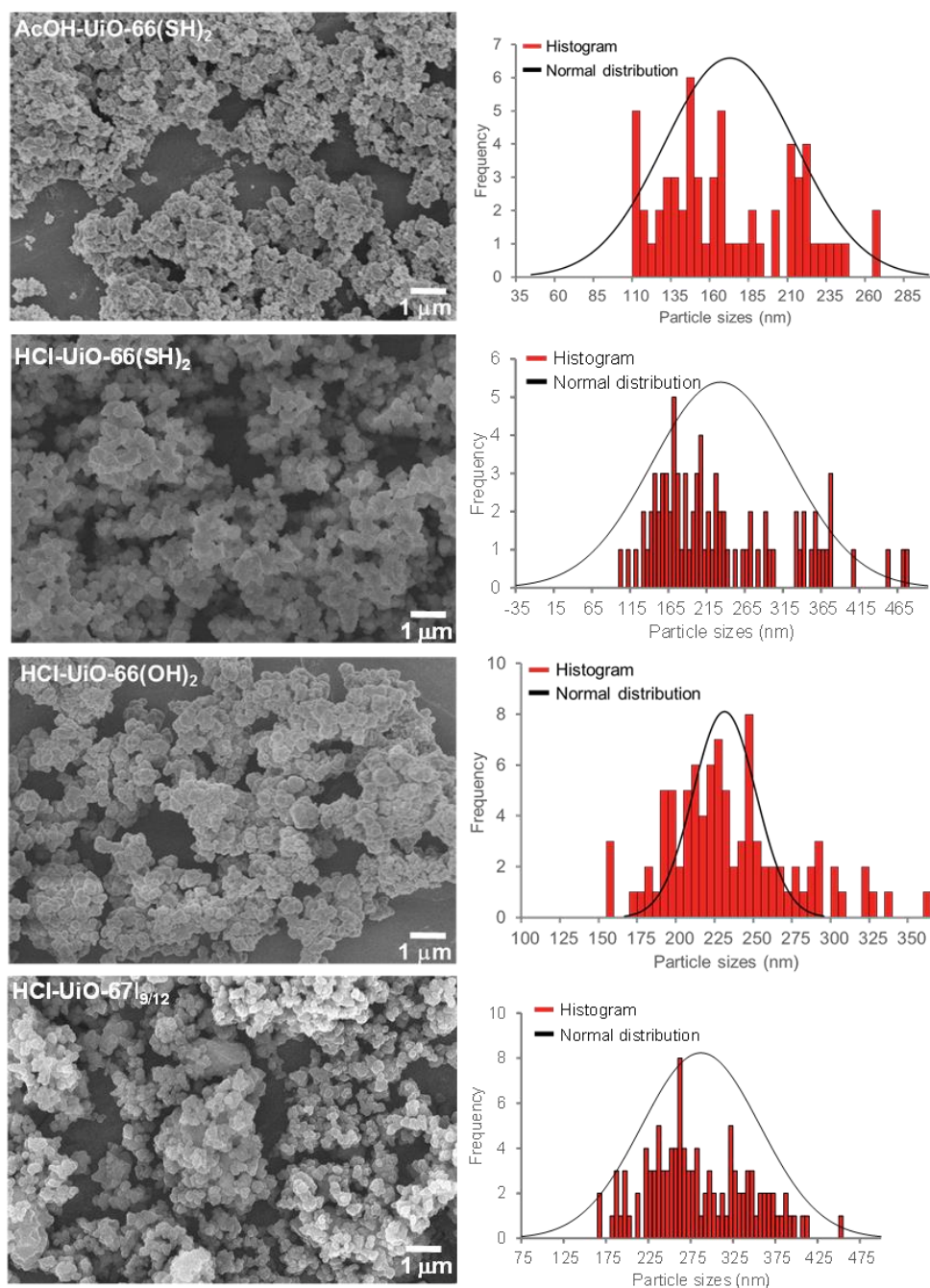


**Figure A6b** Left panels: SEM images of AcOH-UiO-66-(SH)<sub>2</sub>, HCl-UiO-66-(SH)<sub>2</sub>, HCl-UiO-66-(OH)<sub>2</sub>, and HCl-UiO-67|<sub>9/12</sub> MOFs. Right panels: The corresponding SEM-derived particle-size-distribution profile for each of the MOF samples; each profile was constructed based on measurements of >70 particles.

#### A.4.2. Stability of MOFs under batch adsorption conditions

Samples of HCl-UiO-66<sub>|9/12</sub>, AsOH-UiO-66<sub>|11/12</sub>, and HCl-UiO-67<sub>|9/12</sub> were exposed to a 50 ppm solution (30 mL) of As<sup>V</sup> (NaHAsO<sub>4</sub>•7H<sub>2</sub>O) for 24 h, isolated by centrifugation, air-dried, and examined with PXRD. The PXRD pattern of each MOF sample after As<sup>V</sup> treatment (Figures A1, A3) is identical to that of the starting materials, suggesting that the crystallinity of the samples are maintained. Analysis of the remaining As-containing supernatant by ICP-OES does not show any Zr<sup>IV</sup> ions from the MOF samples. In fact, exposing samples of AcOH-UiO-66<sub>|11/12</sub> (10 mg) to a range of solutions with different As<sup>V</sup> concentrations (30 mL of 100-1000 ppm As<sup>V</sup>) does not lead to detectable zirconium ions in any of the solutions after 24 h. (Under these conditions, 1 ppm Zr<sup>IV</sup> in the supernatant is equivalent to 1% MOF degradation).

While we did not observe the loss of sample crystallinity via PXRD and loss of Zr<sup>IV</sup> ions during As<sup>V</sup> batch-adsorption experiments, it is possible that the Zr-containing degradation products, if any, could be amorphous and precipitate out of the solution. A related scenario is when As<sup>V</sup> species would bind around nodes in a MOF unit cell (see Figure A21 below), sterically displace the adjacent BDC linkers, and oligomerize more As<sup>V</sup> ions around the node, as during one of secondary binding processes discussed in Chapter 2. Such a linker-displacement mechanism<sup>76</sup> would allow for more As<sup>V</sup> binding at a node beyond the available defect sites. To address such possibility of ligand loss, we carried out ICP-OES, ESI-MS, and water-suppression <sup>1</sup>H NMR analyses of the supernatant solutions that were separated from three UiO-66 samples (HCl-UiO-66<sub>|9/12</sub>, AcOH-UiO-66<sub>|11/12</sub>, and HCl-UiO-66(SH)<sub>2|10.5/12</sub>) after a batch treatment with arsenates (30 mL of 50 ppm As<sup>V</sup>, 24 h exposure). Consistent with the batch-adsorption experiments described above, Zr-leaching was not observed by ICP-OES for all three As<sup>V</sup>-treated samples. However, the

ESI-MS spectrum of the aqueous supernatant remained after As<sup>V</sup>-treatment of HCl-UiO-66<sub>9/12</sub> sample, which is the most likely to lose ligands due to its high missing-linker density, revealed the presence of the BDC linker. These data are consistent with the possibility described at the beginning of this paragraph where linker replacement occurs without loss of nodes. Unfortunately, TGA analysis of the As-treated MOF could not be conducted due to safety reasons and the potential overlap of the arsenic oxide volatiles at 425 °C,<sup>234</sup> a temperature that is too close to the loss of the H<sub>2</sub>BDC and H<sub>2</sub>BDC(SH)<sub>2</sub> linkers.

Additional ICP-OES sulfur analysis of the batch-experiment supernatant for HCl-UiO-66(SH)<sub>2</sub><sub>10.5/12</sub>, revealed that only  $0.8 \pm 0.2$  % of the MOF linkers was leached into solution after the 24 h batch-adsorption experiment, suggesting that degradation is minimal for this sample. Unfortunately, our attempts to use water-suppression <sup>1</sup>H NMR spectroscopy to directly quantify the amount of BDC linkers in the supernatants isolated from the batch-adsorption experiment for AcOH-UiO-66<sub>11/12</sub> and HCl-UiO-66<sub>9/12</sub> were not successful due to the low solubility of H<sub>2</sub>BDC (1.7 mg/100 mL H<sub>2</sub>O at 20 °C), which prevents the construction of a calibration curve. Attempts to remedy this (i.e., adding DMSO-*d*<sub>6</sub>, dilution, adjusting of the solution pH) all led to the irregular integration values against maleic acid, sodium acetate, and MeOH internal standards, possibly due to the undesired complexation of the remaining arsenates with the linkers. However, qualitative comparison of the water-suppressed <sup>1</sup>H NMR spectra of the three supernatants HCl-UiO-66(SH)<sub>2</sub><sub>10.5/12</sub> does confirm that the amount of leached-out linkers in the supernatant was highest for the more-defective HCl-UiO-66<sub>9/12</sub>, and lowest for HCl-UiO-66(SH)<sub>2</sub><sub>10.5/12</sub>.

Although all of our data to date do not conclusively address the question of MOF stability, it is worthwhile to note that the As concentrations that we explored for the uptake experiments

herein are much higher than those exists in nature (1 ppb - 3 ppm),<sup>80</sup> which could accelerate secondary linker-displacement mechanism such as those mentioned in Chapter 2. With this caveat, our observation of linker loss under these high exposure concentrations is not inconsistent with the linker-displacement binding mechanisms that have been proposed for arsenates<sup>76</sup> and phosphates<sup>235</sup> binding to MOFs with UiO-type nodes. While none of these other studies quantify both Zr<sup>IV</sup> ion and linker loss, Lin and coworkers<sup>235</sup> demonstrated the complete phosphate-replacement of the BDC linkers in UiO-66 at high phosphate exposures (50 mg MOF, 10 mL of 0.25 M H<sub>3</sub>PO<sub>4</sub>, corresponding to a 78.2 P:Zr<sub>6</sub> ratio).

## A5. Quantifying defect sites in UiO analogues

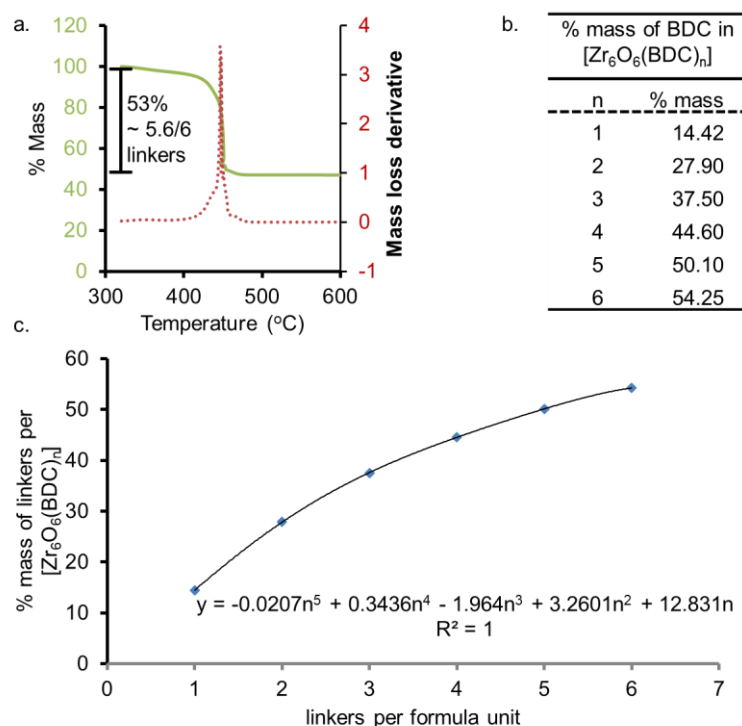


**Figure A7** The calculation of number of missing linkers for MOFs with  $[\text{Zr}_6\text{O}_4(\text{OH})_4(\text{BDC})_n]$  compositions based on TGA profiles. (a) A representative TGA profile (green) for one AcOH-UiO-66<sub>|11/12</sub> sample and the first derivative (red-dotted line) of this profile, used to identify the point of complete linker degradation; where the only materials left is presumably  $\text{ZrO}_2$ . The total mass loss due to the organic linker is calculated from the mass at 320 °C, at which point the MOF is fully activated to the dehydroxylated  $[\text{Zr}_6\text{O}_6(\text{BDC})_n]$  compositions,<sup>62, 145</sup> to the point of complete linker degradation. (b) A table showing theoretical % mass loss as a function of n. These % mass losses are the corrected values for the formation of  $\text{ZrO}_2$  (instead of  $\text{ZrO}$  when derived directly from the  $[\text{Zr}_6\text{O}_6(\text{BDC})_n]$  formula (*ca.* 5.9% mass difference)). (c) Plot of the theoretical % mass vs n as best-fitted ( $R^2 = 1$ ) to a polynomial equation. With this equation, convenient estimates of the amounts of missing linkers can be qualitative obtained from experimental data with a precision of  $11.0 \pm 0.1$  linkers per node, as determined from six repetitive measurements of the same batch of AcOH-UiO-66<sub>|11/12</sub>. Attempts to corroborate this data using the weight percent of Zr in a relatively small (4.5 mg, digestion of larger samples can lead to safety hazards in our equipments) sample of activated AcOH-UiO-66<sub>|11/12</sub> gave us 32 wt % Zr which is 1 wt % off from the theoretical 33 wt % Zr for  $[\text{Zr}_6\text{O}_4(\text{OH})_4(\text{BDC})_{5.5}(\text{AcO}^-)_{0.5}]$ . While this value is in agreement with our formula unit, the error in the ICP-OES method, due to the reliance on accurate mass measurement of a very hygroscopic solid under ambient conditions and/or complete MOF digestion, prevents us from determining the accurate number of missing

linkers. In contrast, the use of TGA allows us to use a much larger sample (20-30 mg) where adsorbed water and solvents can be completely removed prior to the decomposition temperature, and bypass these sources of error. As such, we estimated our amounts of missing linker present in the MOF using linker mass loss from 320-500 °C. It is important to note that the specific surface areas of these MOF samples correlate very well with the number of missing linkers (i.e., the more linkers missing in the sample, the higher the surface area) and these results are in agreement with previously reported observations.<sup>59-60, 145</sup>

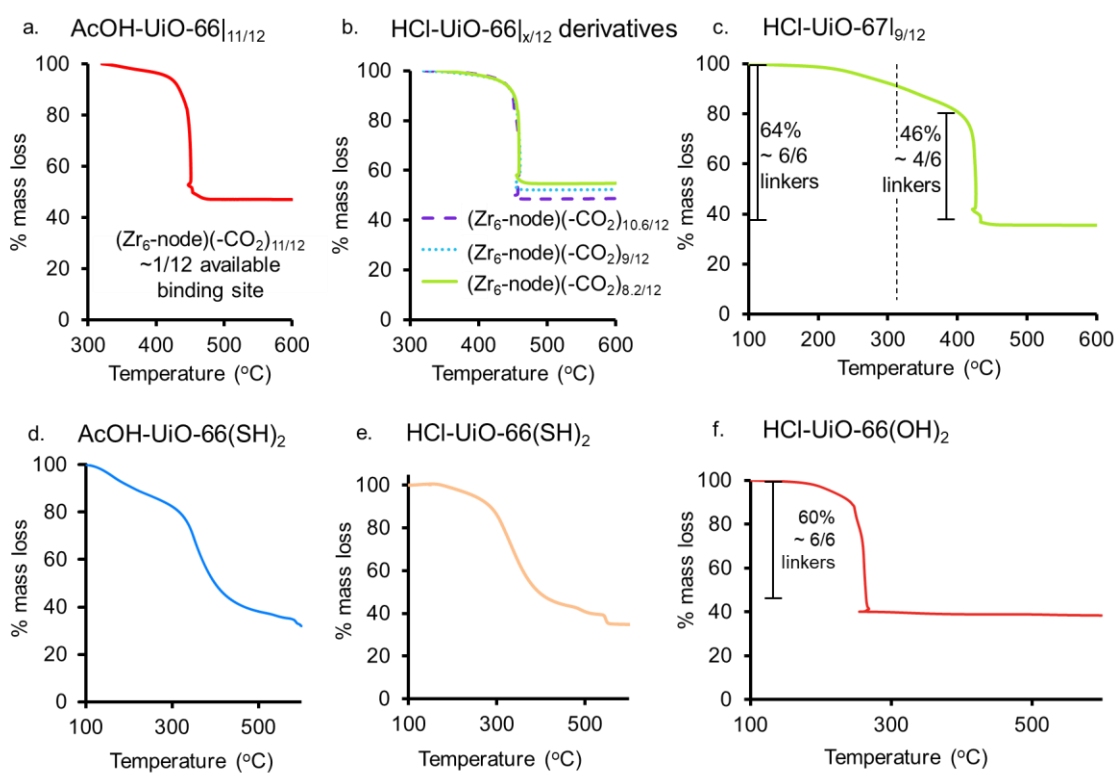


**Figure A8** (a-c) TGA profiles of AcOH-UiO-66<sub>|11/12</sub> (a), HCl-UiO-66<sub>|x/12</sub> derivatives (b), and HCl-UiO-67<sub>|9/12</sub> (c). For the TGA profile of HCl-UiO-67<sub>|9/12</sub>, we set the linker-mass-loss point as 320 °C (dotted line) to be consistent with those for the UiO-66 samples, which were carried out under the same oxygen-enriched atmosphere. While our TGA profile for this sample does not exhibit a clear organic-mass-loss step at ~500 °C as reported by Katz *et al.*,<sup>59</sup> their experiments were carried out in a N<sub>2</sub> atmosphere where complete oxidation of the organic is difficult. (d-f) TGA profiles for AcOH-UiO-66(SH)<sub>2</sub> (d), HCl-UiO-66(SH)<sub>2</sub> (e), and HCl-UiO-66(OH)<sub>2</sub> (f). As the TGA profiles of both thiolated MOFs show a gradual degradation with indistinct steps, predicting the amount of linkers present in them using TGA, as discussed in the caption of Figure A7, is difficult. As such, we relied on the ICP-OES determination of the Zr:S ratio, which does not rely on weight %



measurements and should accurately reflect the node/linker ratio in each sample. For both AcOH-UiO-66(SH)<sub>2</sub> and HCl-UiO-66(SH)<sub>2</sub>, the Zr:S ratio were 1:(1.78 ± 0.03), suggesting that both samples have similar number of missing-linker defects (~10.5/12 carboxylates per node; a non-defective sample would yield a 1:2 Zr:S ratio, corresponding to 12/12 carboxylates per node). We note in passing that this analysis results in a higher number of missing-linker defects for our AcOH-UiO-66(SH)<sub>2</sub> sample than that reported by Yee *et al.*,<sup>52</sup> for a materials synthesized at 3 × [Zr] and with a smaller amount of AcOH modulator. Yee *et al* also estimated node/linker ratio using a combination of TGA under nitrogen flow<sup>5252525252</sup> and CHN combustion analysis, techniques that require estimates of trapped solvent or water.

## A6. Data for the arsenic batch-adsorption analysis

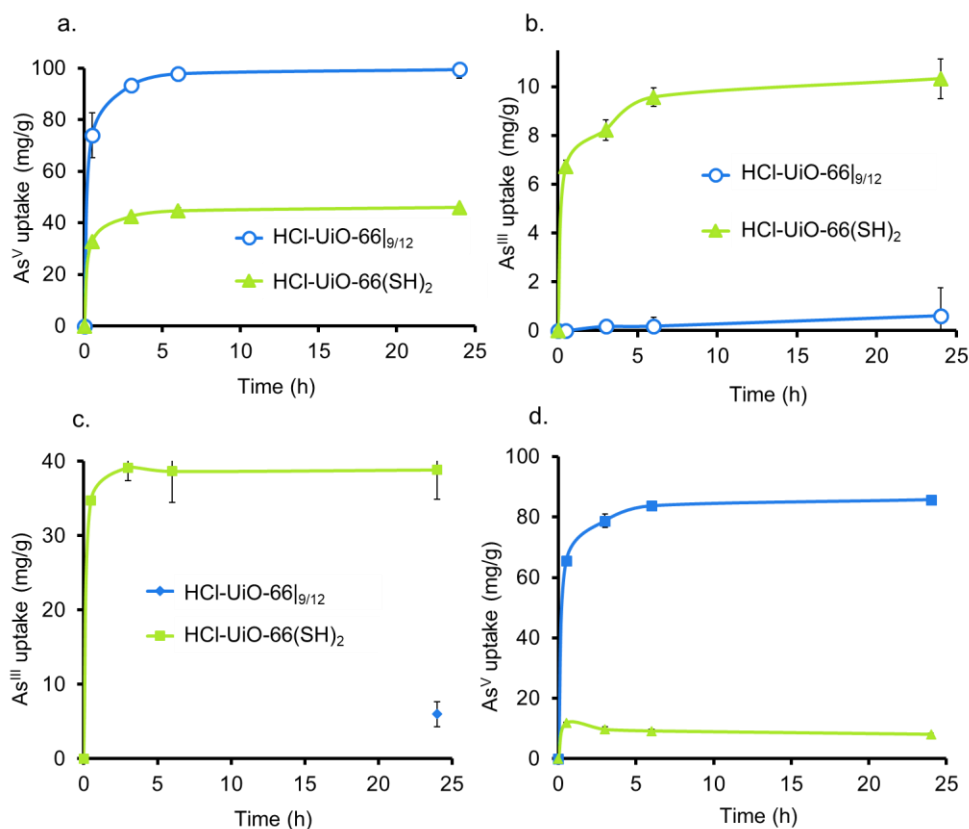


**Figure A9** (a,b) These panels are reproductions of Figure 2.6b-c in the main text for convenience of the readers. Time-dependent arsenic-uptake profiles for HCl-UiO-66|<sub>9/12</sub> and HCl-UiO-66(SH)<sub>2</sub> samples in sequential exposure to As<sup>V</sup> first (a), then As<sup>III</sup> (b). (c,d) Time-dependent arsenic-uptake profiles for HCl-UiO-66|<sub>9/12</sub> and HCl-UiO-66(SH)<sub>2</sub> samples in the reverse exposure order (As<sup>III</sup> first (c), then As<sup>V</sup> (d)). Experimental conditions for all experiments: batch exposure of a sample of



MOF (10 mg) to the appropriate As-containing solution (30 mL; 50 ppm initial concentration, pH ~ 7 for As<sup>V</sup> stock solution and pH ~5 for As<sup>III</sup> stock solution<sup>236</sup>).

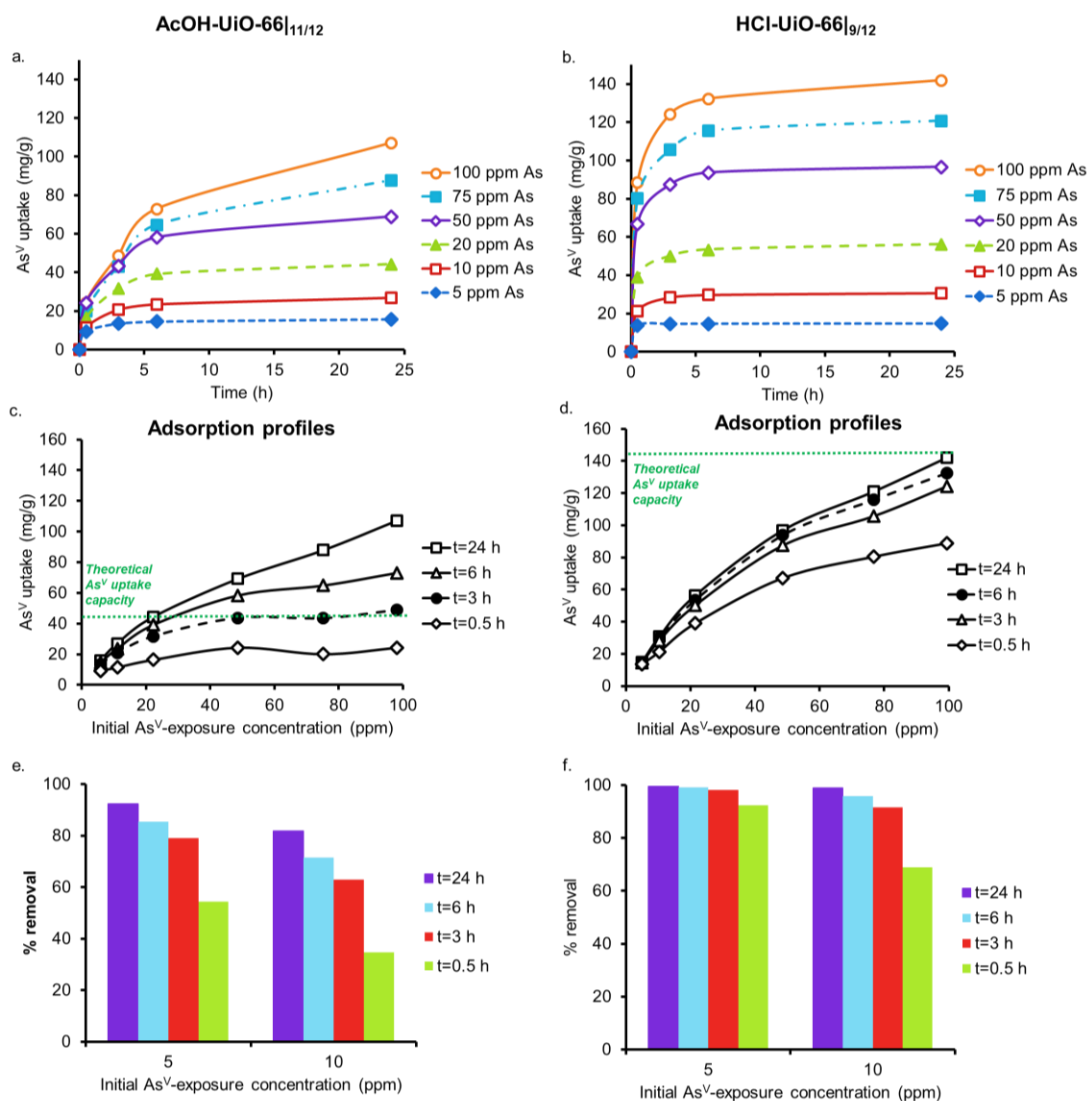


**Figure A10** (a,b) The time-dependent uptake profiles at different concentrations for AcOH-UiO-66<sub>11/12</sub> (a) and HCl-UiO-66<sub>9/12</sub> (b). (c,d) As<sup>V</sup>-adsorption profiles (in mg/g) for AcOH-UiO-66<sub>11/12</sub> (c) and HCl-UiO-66<sub>9/12</sub> (d). The green dashed line across the y axis represents the theoretical As<sup>V</sup>-uptake capacity based on the amount of missing linkers present in the sample. (e,f) % removal of As<sup>V</sup> oxyanions from 30 mL solutions at different times and at low initial As<sup>V</sup>-exposure concentrations for AcOH-UiO-66<sub>11/12</sub> (e) and HCl-UiO-66<sub>9/12</sub> (f). Experimental conditions: batch exposure of a sample of MOF (10 mg) to the appropriate As<sup>V</sup>-containing solution (30 mL; 50 ppm initial concentration).

Interestingly, AcOH-UiO-66<sub>|11/12</sub> and HCl-UiO-66<sub>|9/12</sub> behaves very differently over time with respect to the concentration of the As<sup>V</sup> in solution. When the initial As<sup>V</sup>-exposure concentrations  $\leq 20$  ppm, the time-dependent As<sup>V</sup>-uptake profile for AcOH-UiO-66<sub>|11/12</sub> plateaus after 6 h (Figure A10a). The 6 h plateau behavior for the 20 ppm exposure is notable because it signifies that the AcOH-UiO-66<sub>|11/12</sub> has reached its theoretical capacity based on missing linker sites (Figure A10c). However, at concentrations  $> 20$  ppm, the uptake profiles continues to increase after 6 h (Figure A10a), albeit at a much slower rate than the initial fast uptake. We attribute this behavior to the presence of a secondary uptake mechanism beyond the saturation of the estimated available binding sites due to missing linkers. As mentioned in Chapter 2, such secondary uptake mechanisms could include the formation of As oligomers<sup>237</sup> on the nodes (see Figure A22a for an illustration) and/or linker displacement.<sup>76</sup> These secondary uptake mechanisms are not significant in our time-dependent As<sup>V</sup>-uptake experiments for HCl-UiO-66<sub>|9/12</sub> (Figure A10b) because these missing linker sites have not been fully saturated even at 100 ppm initial As<sup>V</sup>-exposure concentration and after 24 h (Figure A10d).

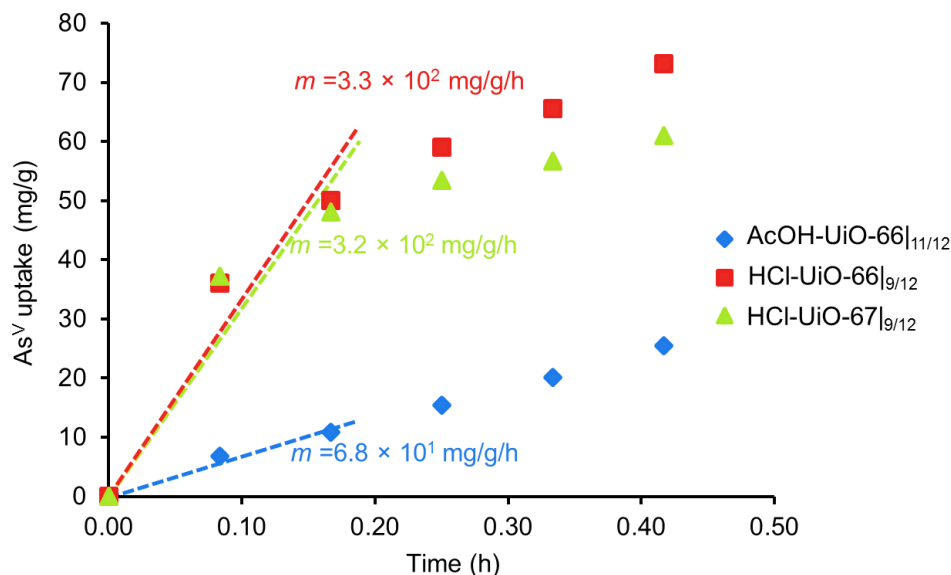


**Figure A11** Initial  $\text{As}^{\text{V}}$ -uptake profiles for MOF samples that have been exposed to a 50 ppm initial concentration of  $\text{As}^{\text{V}}$ . Given the long sampling time of the data-taking processes, only the first 3 data points could be used in the fits to get initial rate data before the pseudo-first-order assumption becomes invalid for HCl-UiO-66|<sub>9/12</sub> and HCl-UiO-67|<sub>9/12</sub> (over 25% of the  $\text{As}^{\text{V}}$  in solution adsorbed). These data clearly show that the rates for HCl-UiO-66|<sub>9/12</sub> and HCl-UiO-67|<sub>9/12</sub> are several times faster than AcOH-UiO-66|<sub>11/12</sub>. We attribute this difference to two different effects: 1) The large particle size differences between AcOH-UiO-66|<sub>11/12</sub> and the HCl-capped MOFs: HCl-UiO-66|<sub>9/12</sub> and HCl-UiO-67|<sub>9/12</sub> have particles that are 4 times smaller in comparison to those for AcOH-UiO-66|<sub>11/12</sub>. 2) The fast diffusion into the first few layers of the MOF particles as a result of larger amounts of defects (hence larger pore sizes) in the HCl-prepared MOFs (see Figures A12-13 for further discussion).

The uptake data for all MOF samples can be fit to either the Lagergren pseudo-first-order (Eq A1) or pseudo-second-order (Eq A2) kinetic model as shown below.<sup>238</sup> We note that such analysis is commonly used to probe for the presence of secondary processes. See further discussion in the caption of Figure A13.

$$\log(q_e - q_t) = \log(q_e) - \frac{k_{s1}}{2.303} t \quad (\text{A1})$$

$$\frac{t}{q_t} = \frac{1}{q_e} t + \frac{1}{k_{s2} q_e^2} \quad (\text{A2})$$

where:

$t$  = time (min)

$q_e$  = equilibrium capacity (mg/g),

$q_t$  = adsorbed quantity at a specific time (mg/g),

$k_{S1}$  = pseudo first-order rate constant ( $\text{min}^{-1}$ ), and

$k_{S2}$  = pseudo second-order rate constant ( $\text{g}/(\text{mg}\cdot\text{min})$ )

The corresponding data fits are shown in Figures A12-13 and the determined rate constants are listed in Table A3.

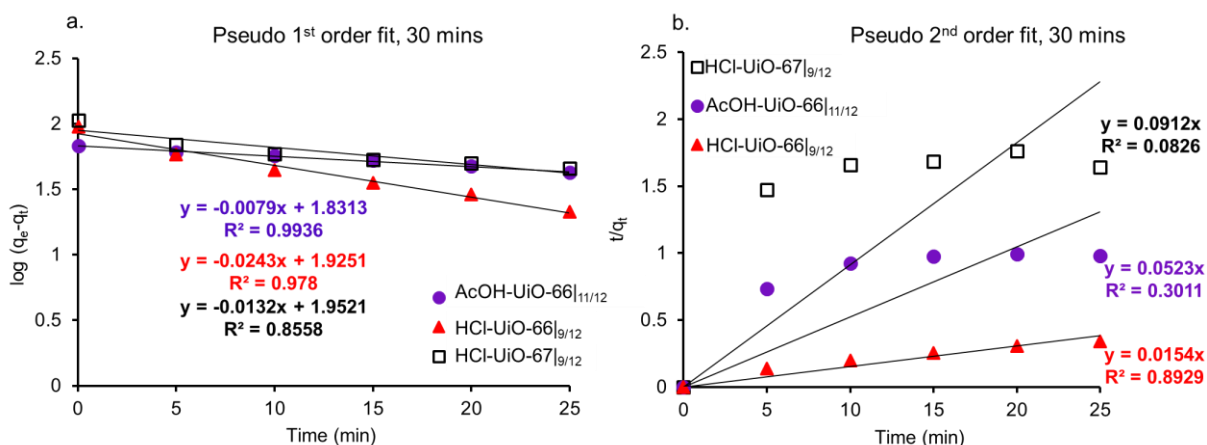


**Figure A12** (a) Lagregren pseudo-first-order and (b) pseudo-second-order model fitting of the initial (within 30 mins) uptake data for samples of UiO-66 and analogues. In all cases (including the other two HCl-UiO-66<sub>x/12</sub> derivatives, data not shown), the Lagregren pseudo-first-order model provided the best fit to this initial uptake data.

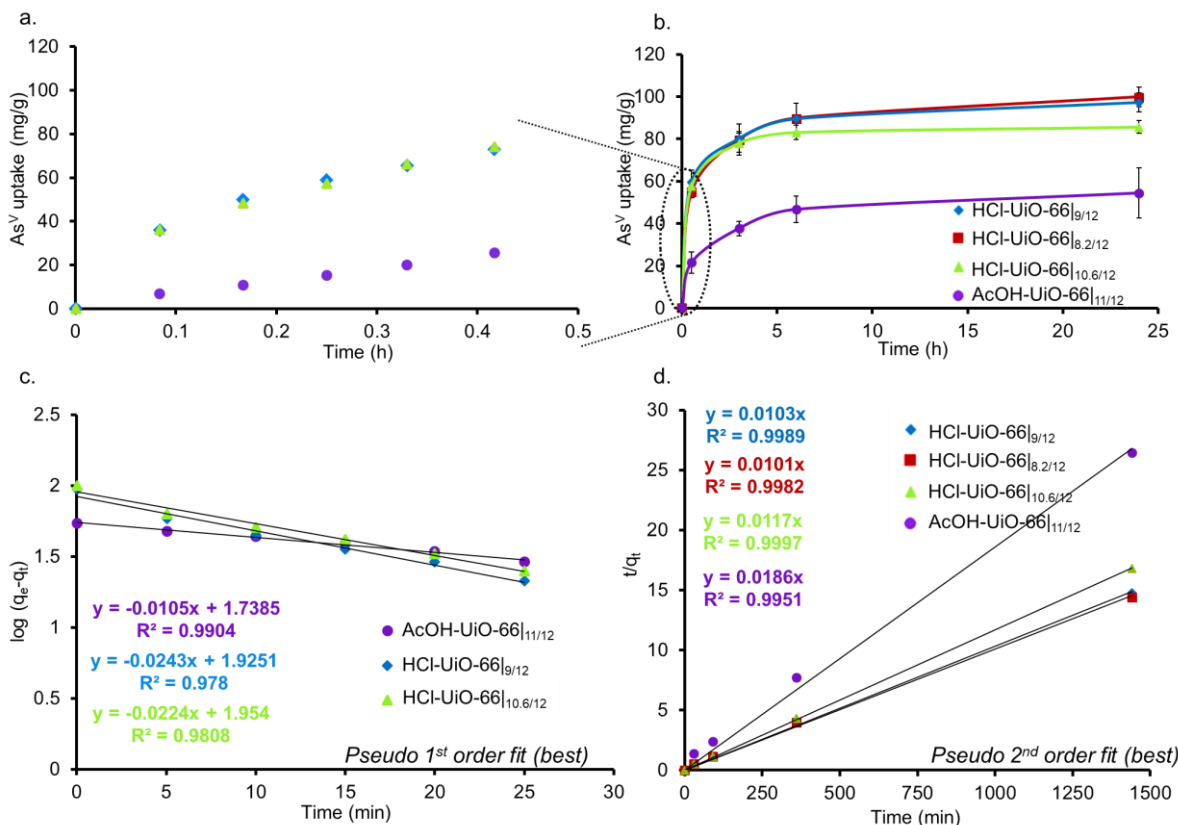


**Figure A13** (a,b): The As<sup>V</sup>-adsorption profiles for AcOH-UiO-66<sub>11/12</sub> and the three HCl-UiO-66<sub>x/12</sub> derivatives under conditions that favor the missing-linker-based uptake mechanism. HCl-UiO-66<sub>x/12</sub> samples with similar particle sizes (Figure A6a) displayed similar initial (i.e., first 30 mins) uptake profiles (a) but diverge at longer times (b). This divergence (i.e., starting at 3 h with HCl-UiO-66<sub>10.6/12</sub> having the lowest uptake) suggests that As<sup>V</sup>-uptake capacity increases with larger amounts of defect density. This is presumably due to the additional binding sites present and larger “average” internal spaces that facilitate As<sup>V</sup> diffusion. AcOH-UiO-66<sub>11/12</sub>, which have particle sizes that are 4 times as large (Figure A6a), has a significantly slower initial uptake profile. These observations suggest that both the particle size and defect density can play important roles in As<sup>V</sup> uptake but their relative contributions change at different stages of the adsorption. (c,d): The best fits of the adsorption profiles to the Lagregren pseudo-first-order (30 min uptake, c) and pseudo-second-order (24 h uptake, d) models. Similarly to that in Figure A11, the initial adsorption profiles for all four MOFs samples fit best to the pseudo-first-order model (bottom left panel) supports our hypothesis that initial uptake is mainly governed by chemisorption to the binding sites on the surface of the MOF particles. This conclusion is also consistent with literature findings<sup>238-239</sup> for Fe-BTC and other porous adsorbents for As<sup>V</sup>. However, the total adsorption profiles over 24 h fit better to a pseudo-second-order model (bottom right panel), affirming the

presence of a second, diffusion-limited process (i.e., binding to the accessible internal binding sites).

**Table A3** Adsorption rates of As<sup>V</sup> in UiO-66<sub>|x/12</sub> MOFs

<i>UiO-66 analogues</i>	<i>Rates</i>	
	<b>*Initial (30 min)</b>	<b>+Overall (1440 min)</b>
AcOH-UiO-66 <sub> 11/12</sub>	$1.50 \times 10^{-2} \text{ min}^{-1}$	$4.81 \times 10^{-4} \text{ g}/(\text{mg} \cdot \text{min})$
HCl-UiO-66 <sub> 10.6/12</sub>	$5.37 \times 10^{-2} \text{ min}^{-1}$	$1.29 \times 10^{-4} \text{ g}/(\text{mg} \cdot \text{min})$
HCl-UiO-66 <sub> 9/12</sub>	$5.27 \times 10^{-2} \text{ min}^{-1}$	$5.88 \times 10^{-4} \text{ g}/(\text{mg} \cdot \text{min})$
HCl-UiO-66 <sub> 8.2/12</sub>	$3.50 \times 10^{-2} \text{ min}^{-1}$	$4.49 \times 10^{-4} \text{ g}/(\text{mg} \cdot \text{min})$

Calculated using Eqs A1\* and A2<sup>+</sup>

## A7. Spectroscopic evidence of adsorption

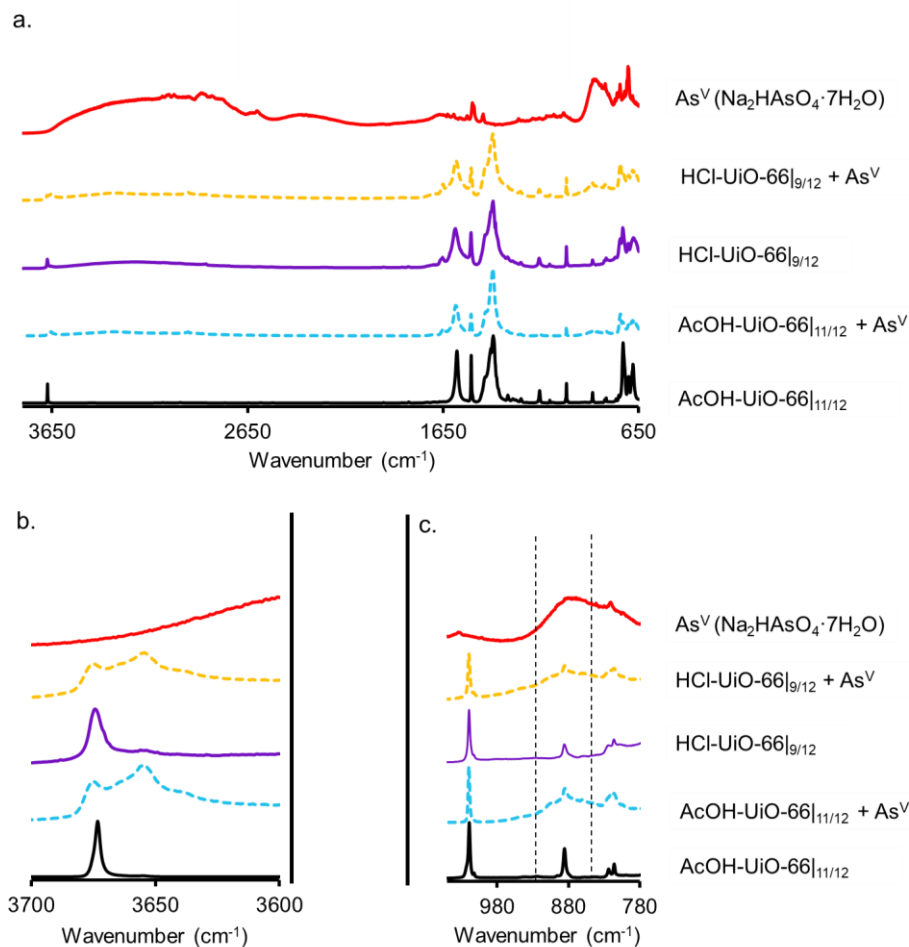


**Figure A14** (a) DRIFT spectra of MOF samples before and after As<sup>V</sup> treatment suggest successful As<sup>V</sup> encapsulation. After As<sup>V</sup> treatment (24 h of exposure to 30 mL of a solution of 50 ppm initial As<sup>V</sup> concentration), samples were washed with DI water (2 × 30 mL) and acetone (1 × 30 mL) and activated at 120 °C overnight. (c) The broad stretch at ~880 cm<sup>-1</sup>, which is attributed to As-O bonds,<sup>237, 240</sup> appears in both As<sup>V</sup>-treated MOF samples with an increased relative intensity in the HCl-UiO-66|<sub>9/12</sub> sample (top gold dotted plot). Additionally, the appearance of new peaks at the bridging hydroxide region (b, 3680-3630 cm<sup>-1</sup>) in the DRIFT spectra of the MOFs after exposure to As<sup>V</sup> suggest the presence of new As(OH) and AsO⋯H species that are similar to the As<sup>V</sup>-O⋯H⋯OM species reported by Myneni *et al.*,<sup>240</sup> and the PO⋯H⋯OZr species reported by Deria *et al.*<sup>19</sup>

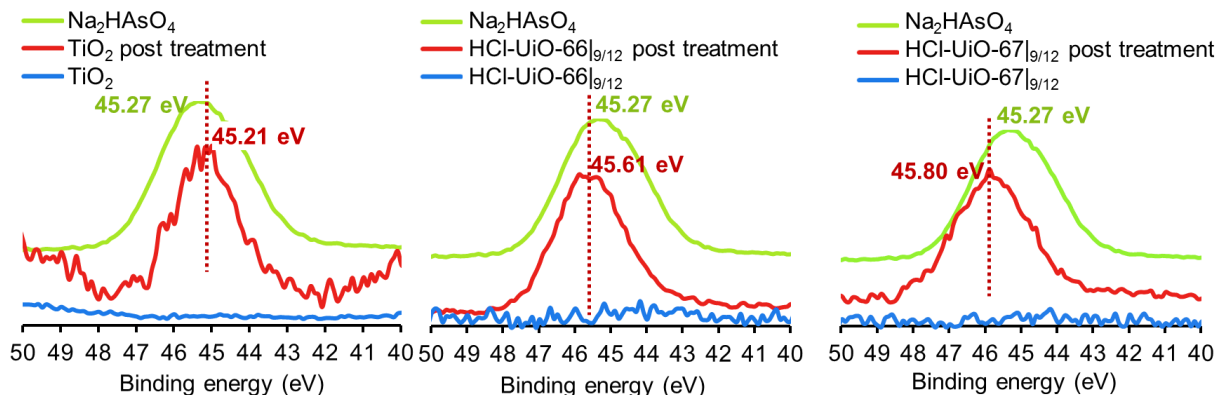


**Figure A15** As<sub>3d</sub> XPS spectra of MOFs and TiO<sub>2</sub> samples that have been exposed to a solution (30 mL) of 50 ppm initial As<sup>V</sup> concentration for 24 h (i.e., at the point of highest As<sup>V</sup> uptake in our study, see Chapter 2, Figure 2.3). The XPS chemical shift for our As<sup>V</sup>-exposed Ti sample is consistent with data previously obtained for As<sup>V</sup>-TiO<sub>2</sub> surface complexation.<sup>39</sup> Together with the data for the parent MOF before exposure and Na<sub>2</sub>HAsO<sub>4</sub>·7H<sub>2</sub>O, the data for the As<sup>V</sup>-exposed MOF samples strongly support the presence of bound As<sup>V</sup>. While it is tempting to note that the binding energies of As<sup>V</sup> bound to the UiO analogues (middle and right spectra) are shifted in a manner that is consistent with the increased presence of bound As<sup>V</sup> (either Zr-O-As or As oligomers) in the MOF (by ~ 0.34 and ~ 0.53 eV for HCl-UiO-66|<sub>9/12</sub> and HCl-UiO-67|<sub>9/12</sub> respectively), these shifts are comparable to the ultimate resolution of our spectrometer (0.4 eV).

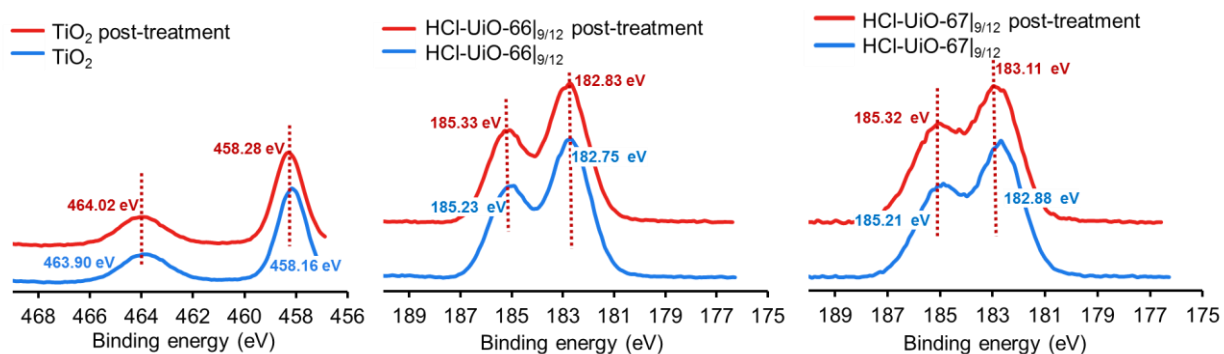


**Figure A16** Ti<sub>2p</sub> and Zr<sub>3d</sub> XPS spectra of the TiO<sub>2</sub> and MOFs, before and after As<sup>V</sup> exposure (24 h of exposure to 30 mL of a solution of 50 ppm initial As<sup>V</sup> concentration).



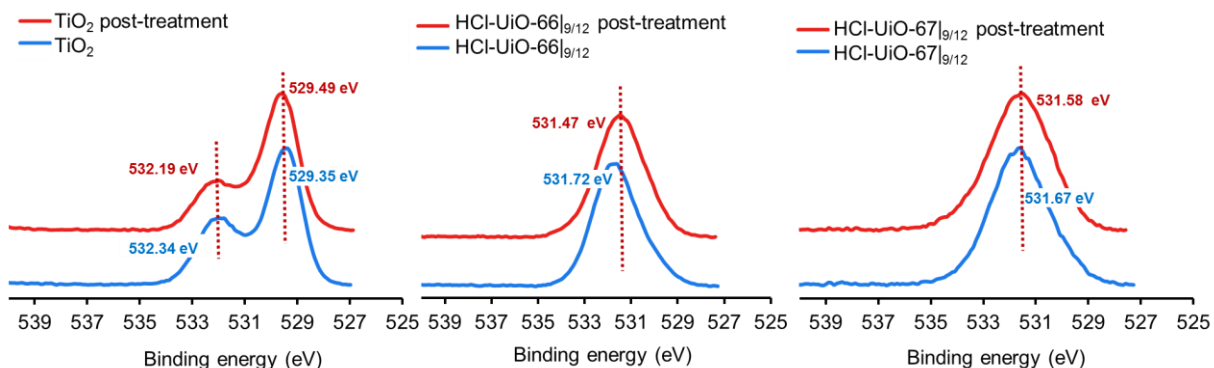


**Figure A17** O1s XPS spectra of the  $\text{TiO}_2$  and MOFs, before and after  $\text{As}^{\text{V}}$  exposure (24 h of exposure to 30 mL of a solution of 50 ppm initial  $\text{As}^{\text{V}}$  concentration).

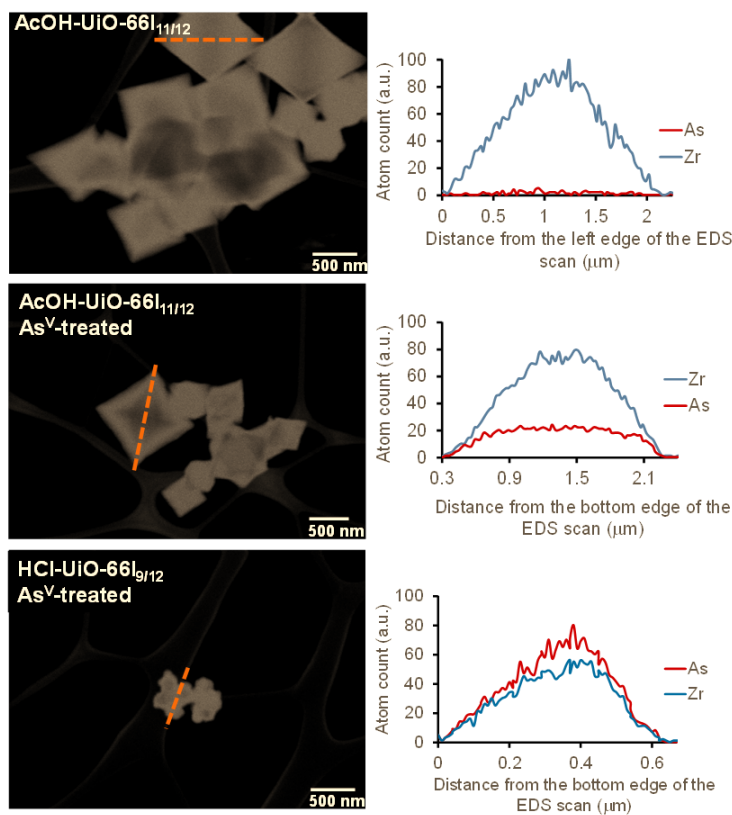


**Figure A18** Left panels: TEM images of  $\text{AcOH-UiO-66}|_{11/12}$  exposed to water and  $\text{AcOH-UiO-66}|_{11/12}$  and  $\text{HCl-UiO-66}|_{9/12}$  exposed to  $\text{As}^{\text{V}}$  solution (30 mL of a solution of 100 ppm initial  $\text{As}^{\text{V}}$  concentration) for 24 h. Right panels: The corresponding EDS line scans showing the amount of arsenic present with respect to zirconium. These data correspond to the scans that are traced by the orange dashed lines in the images on the left.

### A8. Other As<sup>III/V</sup> binding motifs and possibilities

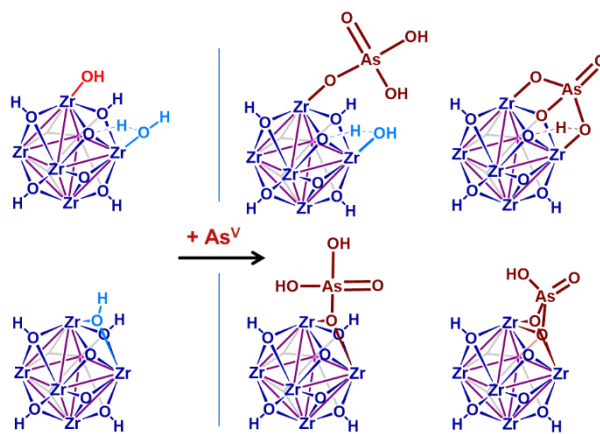


**Figure A19** A schematic illustration showing other potential coordination motifs of As<sup>V</sup> to the nodes of UiO-66 as the exact binding mode was not investigated by direct methods (e.g., pair distribution function). It is quite possible that some combinations of these binding modes will form rather than the energetically unfavorable displacement of the  $\mu^3$ -OH moiety.

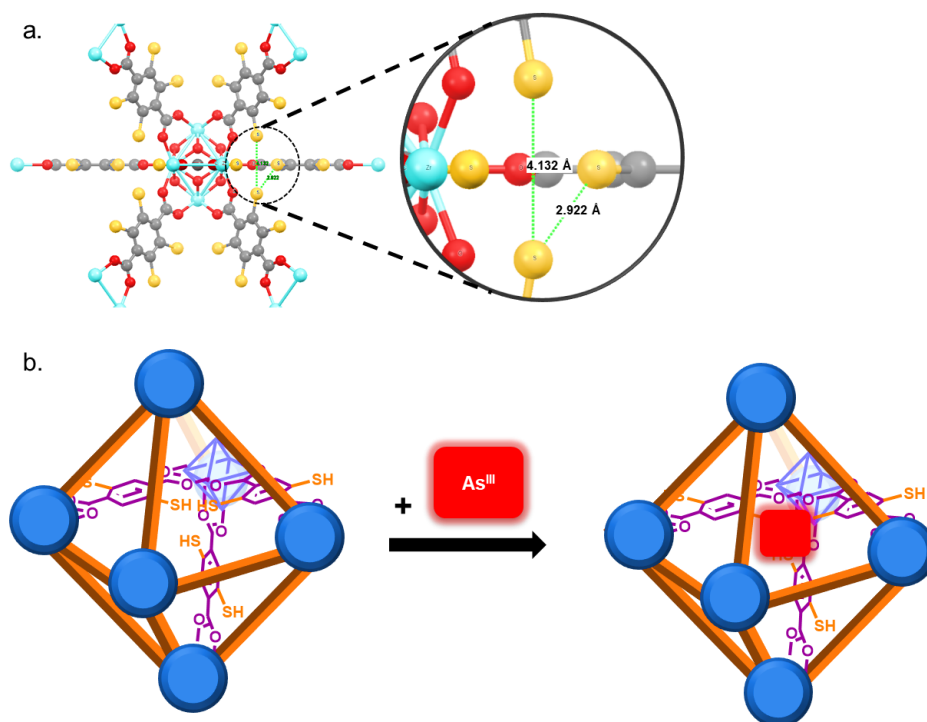


**Figure A20** (a) A schematic representation<sup>52</sup> of the node of UiO-66(SH)<sub>2</sub> where the linkers are shown to have four thiols (as opposed to two) due to potential rotational disorders in the simulated crystal structure.<sup>52</sup> When the pre-oriented thiols are pointing into

the same pore, the bond distances are close enough for synergistic complexation of  $\text{As}^{\text{III}}$ . (b) A schematic illustration showing the proposed binding motif for  $\text{As}^{\text{III}}$  in  $\text{UiO-66}(\text{SH})_2$ . Note that while it may take  $\sim 2\text{-}3$  rightly oriented thiols to bind one  $\text{As}^{\text{III}}$  in a strong, “chelated” fashion,<sup>69</sup> some of the  $\text{As}^{\text{III}}$  may be bound more weakly through only one As-S linkage.

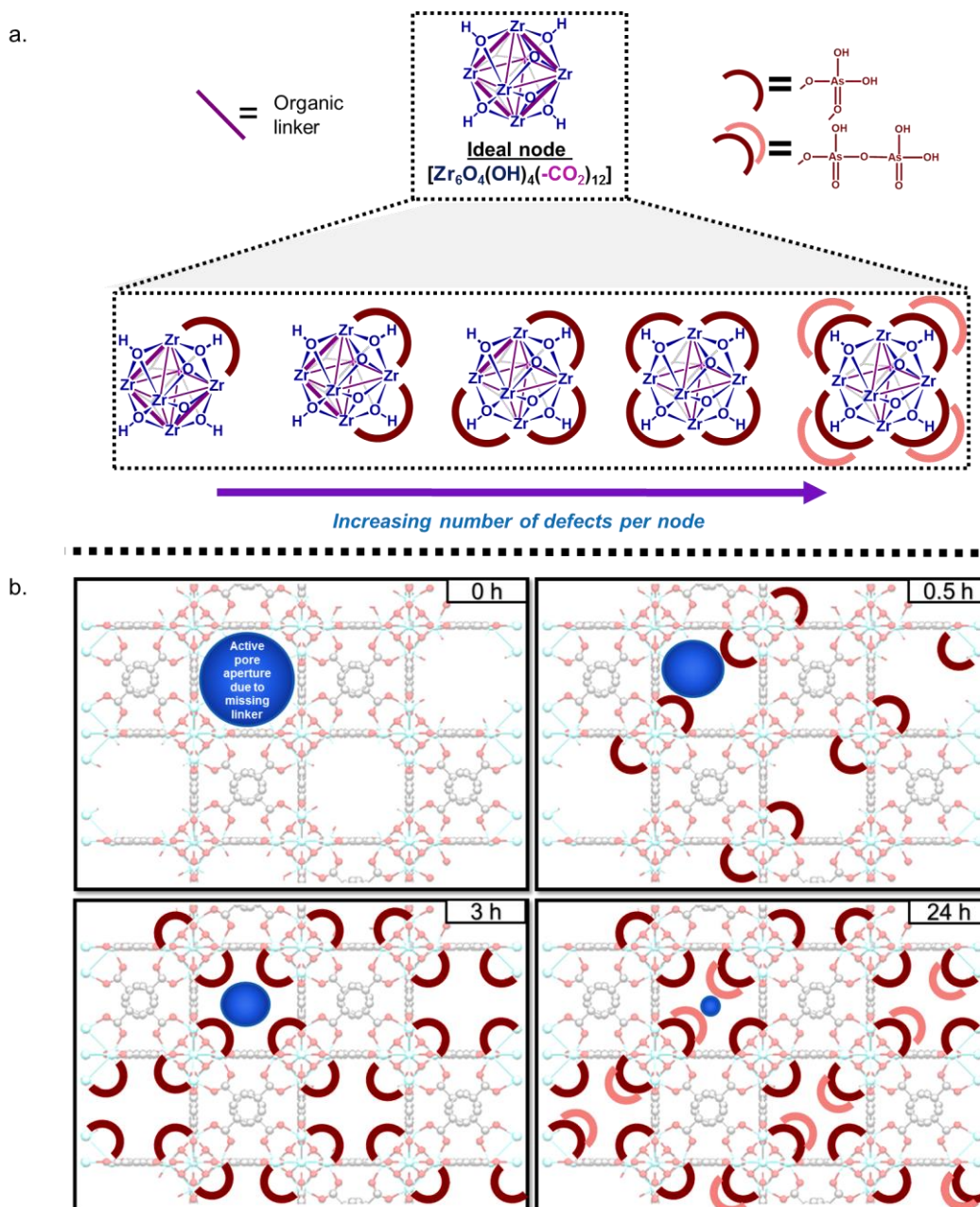


**Figure A21** (a) A schematic illustration of possible  $\text{As}^{\text{V}}$ -binding behavior to the defective nodes in  $\text{HCl-UiO-66}_{x/12}$  MOFs. (b) A perspective view into the first few layers of a

MOF particle that is exposed to an  $\text{As}^{\text{V}}$  solution over time. As time passes, the pore aperture becomes more constricted, slowing down the diffusion rates of  $\text{As}^{\text{V}}$  ions into the internal binding sites.

## A9. Arsenic desorption experiments

### A.9.1. Regeneration of UiO-MOFs after arsenate ( $\text{As}^{\text{V}}$ ) treatment

The regeneration of MOF adsorbents with hexazirconium oxo hydroxo cluster nodes have been investigated after treatments with several oxyanions (i.e., phosphates,<sup>67</sup> amino-bisphosphonates of alendronate,<sup>50</sup> and sulfates<sup>224</sup>). Lin and coworkers found that phosphate-treated UiO-66 could be partially regenerated (up to ~85% of the original capacity) by treatment with a 1% NaCl solution.<sup>67</sup> In a similar study, Shi and coworkers demonstrated that the release of amino-bisphosphonates of alendronate from UiO-66 could be expedited by increasing the acidity (pH 5.5 vs. pH 7.4) of the media at 37 °C. These workers postulated that the release of this phosphonate-containing drug from the UiO-66 is most likely facilitated by the protonation of the phosphonate groups. As such we expected that the desorption of  $\text{As}^{\text{V}}$  oxyanions from  $\text{As}^{\text{V}}$ -treated AcOH-UiO-66<sub>11/12</sub> and HCl-UiO-66<sub>9/12</sub> samples is possible via simple ion-exchange chemistry (Eqs. 2a and b in Chapter 2). See further discussion in Chapter 2 Section 2.6. The relevant data and experimental conditions are summarized in Figure A22 and Table A4 below.

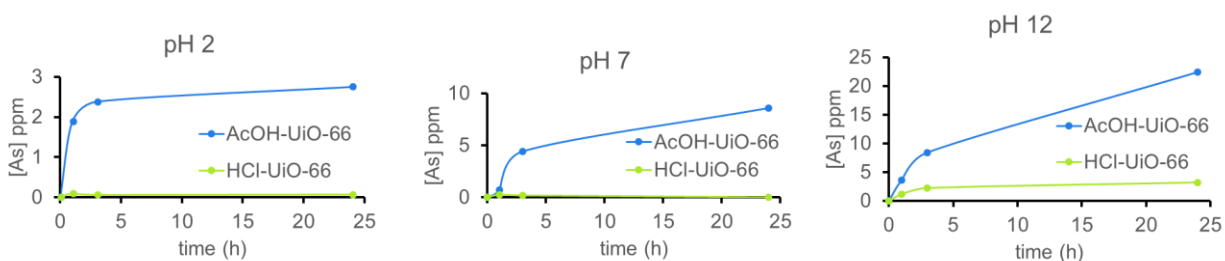


**Figure A22** Qualitative investigation of the effect of pH on the desorption of  $\text{As}^{\text{V}}$ . The plots show the amount of As desorbed, expressed as ppm concentrations in the supernatant, as a function of time in acidic, neutral, and basic solutions. (Full

desorption would yield 112 ppm for As<sup>V</sup>-treated AcOH-UiO-66<sub>11/12</sub> and 135 ppm for As<sup>V</sup>-treated HCl-UiO-66<sub>9/12</sub>.) No Zr<sup>IV</sup> ions leached out at pH 7 and 12, and only trace amounts (<1%) was found in the supernatants after 24 h at pH 2. Experimental conditions: 50 mg of each As<sup>V</sup>-treated UiO-66 sample was placed in a volume (30 mL) of un-buffered solution (pH = 2, 7, or 12), which was gently agitated using a Barnstead Thermolyne Labquake Shaker Rotisserie Model T400110 (Barnstead International, Dubuque, IA). ICP analysis was carried out on aliquots of the supernatant of the mixture after centrifuging at various time points.

**Table A4** Tested desorption conditions for As<sup>V</sup>-treated HCl-UiO-66<sub>9/12</sub>

<b>Desorption agent / node ratio</b>	<b>% As desorbed</b>	<b>% of Zr<sup>IV</sup> ions that leached from MOF sample</b>	<b>Desorption solution</b>
15714 HCl/node	73	16	3.3 M HCl (10 v/v % conc. HCl solution)*
5 HCl/node	0.3	0.008	0.015 M HCl (pH = 1.8**)
10 HCl/node	0.6	0.02	0.03 M HCl (pH = 1.5**)
5 NaOH/node	22	0.08	0.015 M NaOH (pH = 12.2**)
10 NaOH/node	20	0.3	0.03 M NaOH (pH = 12.5**)
1048 NaOH/node	93	2.7	3.3 M NaOH
814 NaCl/node	5	0	1 wt % NaCl solution*

\*Exposed to 30 mL of desorption solution for 24 h. \*\*Calculated values from concentration.

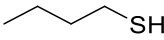
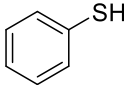
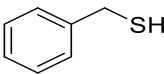
The experimental conditions for the data displayed in Table A4 are as follows: HCl-UiO-66<sub>9/12</sub> was initially exposed to a As<sup>V</sup> solution (32.5 mL of a 45 ppm As<sup>V</sup> in water, pH 7) for 24 h to maintain a similar As:MOF ratio as in the batch treatments described earlier in Section A3. The remaining As concentration after exposure is ~18 ppm, which is comparable to those batch experiments. The MOF samples were then separated from the treatment solutions via centrifugation on a Spin-X centrifuge filter (product # 8161, Corning Inc., Corning, NY). The collected MOF samples were then exposed to the appropriate desorption solutions (2 mL except when noted), gently agitated for ~ 20 minutes, and then passed through a Spin-X centrifuge filter. Depending on the level of acidity and concentrations of the analyzed ions (pre-estimated from

similar experiments), an appropriate amount of the filtrate were collected and analyzed by ICP-OES for As and Zr.

### A.9.2. Regeneration of UiO-MOF after arsenite ( $\text{As}^{\text{III}}$ ) treatment

As most studies on arsenic removal generally focus on the removal of  $\text{As}^{\text{V}}$ , for applications where both  $\text{As}^{\text{III}}$  and  $\text{As}^{\text{V}}$  need to be removed,  $\text{As}^{\text{III}}$  is routinely oxidized to  $\text{As}^{\text{V}}$  prior to adsorbent treatment. However, such treatment involves an extra oxidative step and can potentially oxidize the thiol groups and/or the linker, rendering them unsuitable for reuse. Hence, we proposed that a simpler desorption process from using thiols ligand exchange (Eq. 1 in Chapter 2). See further discussion in the Chapter 2 Section 2.6. The relevant data and experimental conditions are summarized in Table A5 below

**Table A5** Tested desorption conditions for  $\text{As}^{\text{III}}$ -treated HCl-UiO-66( $\text{SH}$ )<sub>2</sub>

Thiols ligands*	%As desorbed	% $\text{Zr}^{\text{IV}}$ ions that leached from MOF sample***	% thiol ligands recovered***
	11	0	20**
	30	0	68
	16	0	69

\*~90 equiv per node. \*\*We suspect that some of this butanethiol evaporated. \*\*Aliquots of the mixture (0.25 mL) were collected, digested in a small amount (2.5 mL) of a mixture of 6:3:1 v/v/v ratios of  $\text{H}_2\text{O}$ :conc.  $\text{HNO}_3$ : $\text{H}_2\text{O}_2$  (30 wt % in  $\text{H}_2\text{O}$ ) inside an unsealed 2-5 mL microwave vial for 10 min at room temperature and then placed in a 70 °C preheated sand bath for ~ 8 h. The samples were then analyzed by ICP-OES for As, S, and Zr

The experimental conditions for data displayed in Table A5 are as follows: HCl-UiO-66( $\text{SH}$ )<sub>2</sub> was initially exposed to an  $\text{As}^{\text{III}}$  solution (30 mL of 50 ppm  $\text{As}^{\text{III}}$  in water, pH 5) for 24 h

at a similar As:MOF ratio as in the As-adsorption batch treatments described in Section A3. The remaining As-concentration after exposure is ~35 ppm, which is comparable to those batch experiments. The MOF samples were then separated from the treatment solutions via centrifugation on a Spin-X centrifuge filter (product # 8161, Corning Inc., Corning, NY), resuspended in the appropriate desorption solutions (1 mL of a 0.486 M thiol solution in EtOH), and stirred for 3 h at 50 °C. Note: heating and stirring are necessary for effective thiol exchange to occur. At room temperature and without stirring, no As<sup>III</sup> release was observed.

For the aforementioned studies, we attempted the regeneration in ethanol solution to maintain the solubility of the thiol ligands. Based on the % of As<sup>III</sup> desorbed from As<sup>III</sup>-treated HCl-UiO-66(SH)<sub>2</sub>, thiophenol is much better than alkylthiols at desorbing As<sup>III</sup> from the MOFs. This is consistent with the ligand-exchange mechanism described in Chapter 2 Eq. 1 where the exchange is thermodynamically favoured with the more reactive thiophenol (pK<sub>a</sub> = 6.6) in comparison to benzyl mercaptan (pK<sub>a</sub> = 9.4) and butane thiol (pK<sub>a</sub> = 10.8).

#### **A10. Miscellaneous Calculations**

For the most defective HCl-UiO-66<sub>9/12</sub> MOF derivative, with a molecular formula of Zr<sub>6</sub>O<sub>4</sub>(OH)<sub>4</sub>(linker)<sub>4.5</sub>Cl<sub>3</sub>(H<sub>2</sub>O)<sub>3</sub> (each missing carboxylate is assumed to be replaced by a Cl ion and a water molecule), exposure to 30 mL of a 50 ppm As (0.02 mmol As) affords a slight excess of arsenic in solution in comparison to the binding sites (i.e., defect sites). This amount is still in excess for the less defective AcOH-UiO-66<sub>11/12</sub> MOF, the less-dense HCl-UiO-67<sub>9/12</sub>, or the denser HCl-UiO-66(SH)<sub>2</sub> and AcOH-UiO-66(SH)<sub>2</sub> (both of which are also less defective). The calculations are as follows:

10 mg of HCl-UiO-66<sub>9/12</sub> (MW = 1578.3 g/mol) = 0.0063 mmol Zr<sub>6</sub>, → 1:3.17 Zr<sub>6</sub>:As

10 mg of AcOH-UiO-66<sub>11/12</sub> (MW = 1641.06 g/mol) = 0.0061 mmol Zr<sub>6</sub>, → 1:3.27 Zr<sub>6</sub>:As

10 mg of HCl-UiO-67<sub>9/12</sub> (MW = 1920.78 g/mol) = 0.0052 mmol Zr<sub>6</sub>, → 1:3.84 Zr<sub>6</sub>:As

10 mg of HCl-UiO-66(SH)<sub>2</sub><sub>10.5/12</sub> (MW = 1957.85 g/mol) = 0.0051 mmol Zr<sub>6</sub>, → 1:3.92 Zr<sub>6</sub>:As

10 mg of AcOH-UiO-66(SH)<sub>2</sub><sub>10.5/12</sub> (MW = 1966.20 g/mol) = 0.0051 mmol Zr<sub>6</sub>, → 1:3.93 Zr<sub>6</sub>:As

10 mg of HCl-UiO-66(OH)<sub>2</sub><sub>12/12</sub> (MW = 1856.10 g/mol) = 0.0054 mmol Zr<sub>6</sub>, → 1:3.71 Zr<sub>6</sub>:As

10 mg of ideal UiO-66 (MW = 1564.08 g/mol) = 0.0060 mmol Zr<sub>6</sub>, → 1:3.33 Zr<sub>6</sub>:As

10 mg of ideal UiO-66(SH)<sub>2</sub> (MW = 2048.82 g/mol) = 0.0049 mmol Zr<sub>6</sub>, → 1:4.08 Zr<sub>6</sub>:As



## Appendix B Supplementary to Chapter 3

Portions of this appendix appear in the following manuscript:

Audu, C. O.; Liu, M.; Anderson, R. M.; McConnell, M. S.; Malliakas, C. D.; Snurr, R. Q.; Farha, O. K.; Hupp, J. T.; Gualdrón, D. A. G.; Nguyen, S. T. *manuscript in preparation*.

### B1. Materials and methods

Unless otherwise stated, all reagents were used as received from commercial sources. Conc. hydrochloric acid, zirconium chloride, and terephthalic acid were purchased from Aldrich Chemicals Company, Inc. (Milwaukee, WI). Concentrated sulfuric acid, and glacial acetic acid were purchased from VWR Scientific, LLC (Chicago, IL). Zirconium ICP standard was purchased from Sigma-Aldrich Co. LLC (St. Louis, MI). Ultrapure deionized water (18.2 M $\Omega$  cm resistivity) was obtained from a Millipore system (EMD Millipore, Billerica, MA). Solvents were purchased from either Sigma-Aldrich Co. LLC (St. Louis, MI), Fisher Scientific, Inc. (Pittsburg, PA), or Avantor Performance Materials, Inc. (Center Valley, PA). All the gases used for the adsorption and desorption measurements were ultra-high purity grade 5 and obtained from Airgas Specialty Gases (Chicago, IL). Conc. HF (49 wt. %) was obtained from Fisher Scientific Inc. (Pittsburgh, PA).

Powder X-ray diffraction (PXRD) patterns were recorded on:

1. Either a Rigaku X-ray Diffractometer Model ATX-G (Rigaku Americas, The Woodlands, TX) equipped with an 18 kW Cu rotating anode (Cu K $_{\alpha 1}$  radiation,  $\lambda = 1.54056 \text{ \AA}$ ), an MLO monochromator, and a high-count-rate scintillation detector **OR** a Rigaku X-ray Diffractometer Model SmartLab (Rigaku Americas, The Woodlands, TX) equipped with a 9 kW Cu rotating anode radiation source coupled to a multilayer optic. Measurements were made over the range 2 $^{\circ}$

$< 2\theta < 40^\circ$  in  $0.05^\circ$  step width with a  $2^\circ/\text{min}$  scanning speed. Data collected from these instruments are shown in Figure B2.

2. A STOE's STADI-MP powder X-ray diffractometer (STOE & Cie. Ltd, Darmstadt, Germany) equipped with an asymmetric curved Germanium monochromator (Cu  $K_{\alpha 1}$  radiation,  $\lambda = 1.54056 \text{ \AA}$ ) and a one-dimensional silicon strip detector (MYTHEN2 1K, DECTRIS Ltd. Baden-Daettwil, Switzerland). The line-focused Cu X-ray tube was operated at 40 kV and 40 mA. The as-received powder was sandwiched between two acetate foils (polymer substrate with neither Bragg reflections nor broad peaks above 10 degrees) and measured in transmission geometry in a rotating holder. Prior to the measurement, the instrument was calibrated against a NIST Silicon standard (640d). Measurements were made over the range  $0.1^\circ < 2\theta < 25.7^\circ$  in 30 mins. Data collected from this instrument are shown in Figure B1a.

3. Beamline 11-ID-B from the Advanced Photon Source synchrotron facility (Argonne National Laboratory, Argonne, IL) using 58.6 keV ( $\lambda = 0.2112 \text{ \AA}$ ) X-rays. Diffraction data were collected using a Perkin Elmer amorphous silicon-based area detector. Geometric corrections and reduction to one-dimensional data were carried out using GSAS-II software.<sup>241</sup> Measurements were made over the range  $0^\circ < 2\theta < 17^\circ$  by averaging 120 scans of 2 seconds exposure each. Data collected from this instrument are shown in Figure B1b.

$\text{N}_2$  adsorption and desorption isotherms were measured on a Micromeritics Tristar II 3020 (Micromeritics, Norcross, GA) or an ASAP 2020 (Micromeritics Instrument Corporation, Norcross, GA) instrument at 77 K. Before each run, samples were activated at  $150^\circ\text{C}$  for at least 12 h (and/or until outgas rate  $\leq 0.02 \text{ mm Hg}$ ) under high vacuum on either an ASAP 2020 (Micromeritics Instrument Corporation, Norcross, GA) activation port or a Smart VacPrep

(Micromeritics, Norcross, GA). At least 60-100 mg of sample was used in each measurement. BET areas were calculated using the four consistency criteria as discussed thoroughly in our previous work.<sup>128</sup> Briefly, it was ensured that only a pressure range where  $N(1-P/P_0)$  increases monotonically was chosen, that the value of  $C$  resulting from the linear regression was positive, that the monolayer loading obtained from the regression falls within the chosen pressure range, and that the monolayer loading obtained from the regression is within 20% of  $1/C^{0.5} + 1$ . Two example calculations are shown in Figure B24. The pore size distributions of the MOFs were calculated from the adsorption branch of the isotherms by density functional theory (DFT) using the  $N_2$ -Cylindrical pores – oxide surface model. Regularization factor was set at a value where the root mean square error of fit, and the roughness of distribution are both minimal.

The micropore volumes, micropore surface areas, and external surface areas for all samples were determined using conventional t-plot method<sup>227</sup> from  $N_2$  adsorption data. For most of the UiO-66 variants, the values were selected over the 3-5 Å t range by fitting the data to the Harkins-Jura thickness equation. For the highly defective HCl treated BzOH-UiO-66, the values were selected over the 5.5-7 Å t range by fitting the data to the Harkins-Jura thickness equation. This is the process that we used in a recent publication on similar samples,<sup>36</sup> and is recommended by Prof. A. W. Marczewski<sup>229</sup> as well as the Micromeritics Instrument Corporation.<sup>230</sup>

Inductively coupled plasma optical-emission spectroscopy (ICP-OES) was conducted on a computer-controlled (QTEGRA software v. 2.2) Thermo iCap 7600 Duo ICP-OES (Thermo Fisher Scientific, Waltham, MA, USA) instrument equipped with a SPRINT valve and a CETAC 520ASX autosampler (Teledyne CETAC, Inc., Omaha, NE, USA). Each sample was acquired using a 5 s sample loop fill (4 mL sample loop), and 6 s loop rinse.

$^1\text{H}$  NMR spectra were recorded on Agilent DD2 600 MHz NMR (Agilent DD2 500 MHz for HCl-UiO-66<sup>4.2/6</sup> sample) spectrometer (Agilent Technologies, Santa Clara, CA), located in the IMSERC facility of Northwestern University, equipped with a triple-resonance (HCN) cold probe w/ Z-gradient and a sensitivity of  $^1\text{H} = 4300$  and  $^{13}\text{C} = 250$ .  $^1\text{H}$  chemical shifts are reported in ppm with maleic acid as an internal standard.

Centrifugation was carried out in an Eppendorf Centrifuge 5804 R, Model AG 22331 (Eppendorf AG, Hamburg, Germany) equipped with an F34-6-38 rotor. Unless otherwise stated, all centrifugations were carried out at 5000-8000 rpm (3214 g) for 10 min.

Thermogravimetric analysis (TGA) was performed on a TA Instruments Q500 Thermogravimetric Analyzer (TA Instruments, Inc., Schaumburg, IL, USA) in a flow of  $\text{O}_2$  (70 vol %, remainder volume is  $\text{N}_2$ ). Sample (~20 mg) was initially heated at a heating rate of 10  $^\circ\text{C}/\text{min}$  from room temperature to 100  $^\circ\text{C}$ , kept at this temperature for 5 min to ensure complete removal of water and volatile organics, and then heated to 600  $^\circ\text{C}$  at a rate of 5  $^\circ\text{C}/\text{min}$ .

Scanning electron microscopy (SEM) images were obtained at Northwestern University's EPIC/NUANCE facility on a SU8030 FE-SEM (Hitachi High Technologies America, Inc., Dallas, TX) microscope with an acceleration voltage of 10 kV. Prior to imaging, activated MOF samples were coated with either a film (~10-20 nm thickness) of Au/Pd using a Denton Desk III TSC Sputter Coater (Denton Vacuum, Moorestown, NJ), or Os using a Filgen Osmium Coater Model OPC-60A (Filgen, Nagoya, Japan).

## B2. Synthesis of UiO MOF analogues.

**AcOH-UiO-66**<sup>5.2/6</sup> and **HCl-UiO-66**<sup>4.2/6</sup> were prepared using previously reported procedures (Appendix A2).<sup>36</sup>

**BzOH-UiO-66**<sup>4.0/6</sup>. In a 500 mL Erlenmeyer flask, benzoic acid (BzOH, 6.963 g, 54 mmol) was dissolved in DMF (206 mL). Zirconium(IV) chloride (ZrCl<sub>4</sub>, 0.424 g, 1.82 mmol) and terephthalic acid (BDC, 0.272 g, 1.64 mmol) were added, and the resulting mixture was sonicated until a clear solution was obtained. This solution was then equally partitioned among eight 8 dram glass vials (~25.5 mL in each vial). The vials were capped and placed in a preheated oven (120 °C) for 24 h and by the end of the reaction either a cloudy solution or a white precipitate was observed. After cooling to room temperature, the content of each vial was poured into a 50 mL centrifuge tube and the solid product was pelletized by centrifugation (3214 g, 15 min). After removing the supernatant, the collected material was immersed in fresh DMF (20 mL) over 8 h to remove unreacted starting materials. The MOF was then pelletized through centrifugation, the supernatant was decanted, and fresh DMF (20 mL) was again added to initiate the second soaking cycle. After three cycles of DMF soaking, the MOF solids was washed using either one of two methods:

1. The supernatant was decanted and the remaining wet solid was immersed in fresh acetone (20 mL) and pelletized by centrifugation (3124 g, 15 min). The supernatant was decanted and the resulting wet solid was immersed in fresh acetone (20 mL) for 8 h, centrifuged, decanted, and then resuspended in another portion (20 mL) of fresh acetone. After three 8 h cycles of acetone soaking, the supernatant was then decanted and the remaining solid in each centrifuge tube was air-dried in the hood (Yield = 0.484 g).

2. The supernatant was decanted and the remaining wet solid was immersed in fresh acetone (20 mL) and pelletized by centrifugation. The supernatant was then decanted and the solid in each centrifuge tube was allowed to air-dry in the hood before being combined into a microscale cellulose Soxhlet extraction thimble (Sigma Aldrich, WHA2800105). Residual solvent in the MOF pores was then removed using Soxhlet extraction ( $\geq 8$  h) over reflux acetone ( $\sim 20$  mL). The MOF solid was then allowed to air-dry inside the thimble prior to collection.

***de-BzOH-UiO-66***<sup>4.0/6</sup>. This material was made from crude **BzOH-UiO-66**<sup>4.0/6</sup> without the need for isolation. The immediately preceding procedure was followed through up to the DMF-soaking step. After three cycles of DMF soaking, the wet solids from the 8 centrifuge tubes were combined and partitioned evenly into two 100 mL glass jars. To each jar was added DMF (60 mL) followed by 8 M HCl<sub>aq</sub> (5 mL). The jars were capped, slightly swirled, and placed in a preheated oven (100 °C) for 24 h. Afterwards, the jars were removed from the oven and allowed to cool to room temperature. The content of each jar was poured into a 50 mL centrifuge tube and the solid product was pelletized by centrifugation. After removing the supernatant, the collected material was immersed in fresh DMF (20 mL) for at least 2 h to remove acid impurities, centrifuged, decanted, and then resuspended in fresh DMF (20 mL). After three cycles of such DMF soaking, the supernatant was decanted and the resulting wet solid was immersed in fresh acetone (20 mL) for 8 h, centrifuged, decanted, and then resuspended in another portion (20 mL) of fresh acetone. After three cycles of such acetone soaking, the resulting solid was isolated via centrifugation and decantation, and air-dried overnight in the open centrifuge tubes at room temperature. The white MOF solids were then collected and combined (0.441 g) and stored for future use.

*de'*-**BzOH-UiO-66**<sup>4.0/6</sup>. This material was made from dry **BzOH-UiO-66**<sup>4.0/6</sup>. Portions of dry **BzOH-UiO-66**<sup>4.0/6</sup> powder (0.150 g, 0.084 mmol of Zr<sub>6</sub> nodes based on the assumed formula [Zr<sub>6</sub>O<sub>4</sub>(OH)<sub>4</sub>](BDC)<sub>4</sub>(BzOH)<sub>3</sub>(H<sub>2</sub>O) (OH)) were each placed into two 8 dram vials. To each vial was added 1-butanol (18 mL) and 8 M HCl (1.5 mL). The vials were covered, slightly swirled, and placed in a preheated oven (100 °C) for 24 h. Afterwards, the reaction vials were removed from the oven and allowed to cool to room temperature. The content of each jar was poured into a 50 mL centrifuge tube and the solid product was pelletized by centrifugation. After removing the supernatant, the resulting solid was immersed in fresh 1-butanol (20 mL) for 2 h, centrifuged, decanted, and then resuspended in fresh 1-butanol (20 mL). After three cycles of 1-butanol soaking, the supernatant was decanted and the resulting wet solid was quickly rinsed in fresh acetone (20 mL) before being pelletized by centrifugation. The supernatant was then decanted and the solid in each centrifuge tube was allowed to air-dry in the hood before being combined into a microscale cellulose Soxhlet extraction thimble (Sigma-Aldrich, part number WHA2800105). Residual solvent in the MOF pores was then removed using Soxhlet extraction (≥ 8 h) over reflux acetone (~ 20 mL). The MOF solid was then allowed to air-dry inside the thimble prior to collection (Yield = 0.260 g).

### B3. Characterization of the UiO-66 samples

#### B3.1. Physical properties of bulk nanoparticles

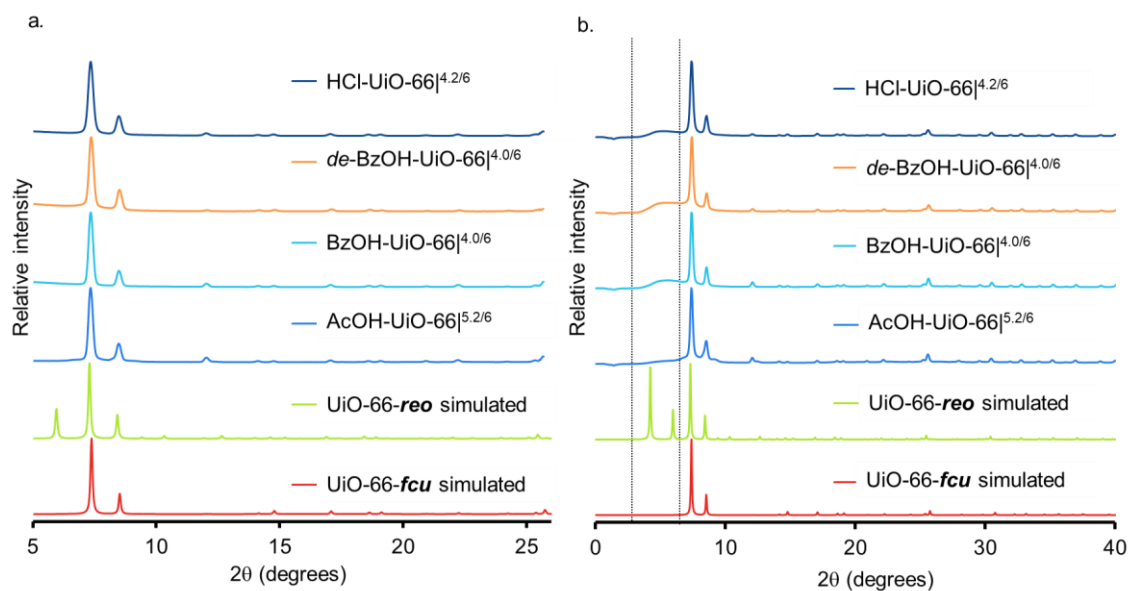


**Figure B1** In-house (a) and synchrotron (b) PXRD patterns of as-prepared UiO-66 variants in comparison to the simulated *fcu* and *reo* PXRD patterns for UiO-66. In-house data was obtained from a STOE's STADI-MP powder X-ray diffractometer.



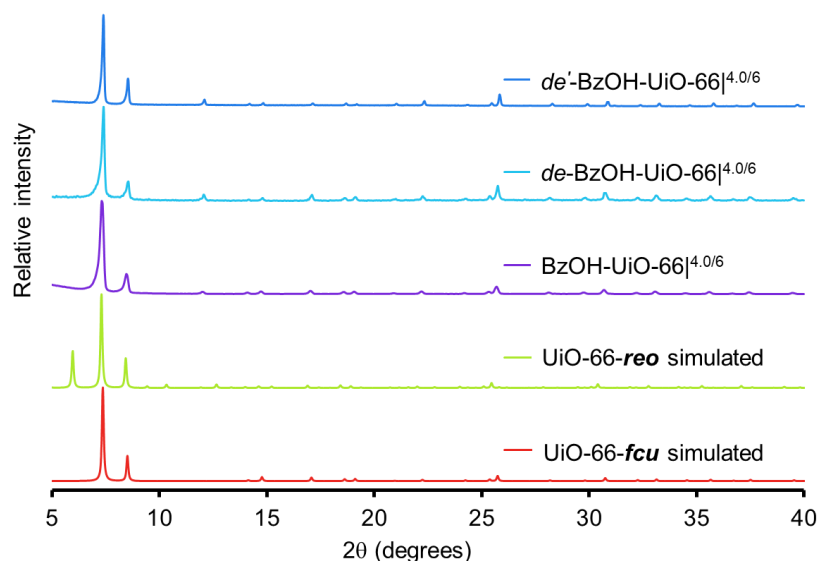


**Figure B2** In-house PXRD patterns of as-prepared of BzOH-UiO-66 variants in comparison to the simulated *fcu* and *reo* PXRD patterns for UiO-66. In-house data was obtained from a Rigaku X-ray diffractometer.

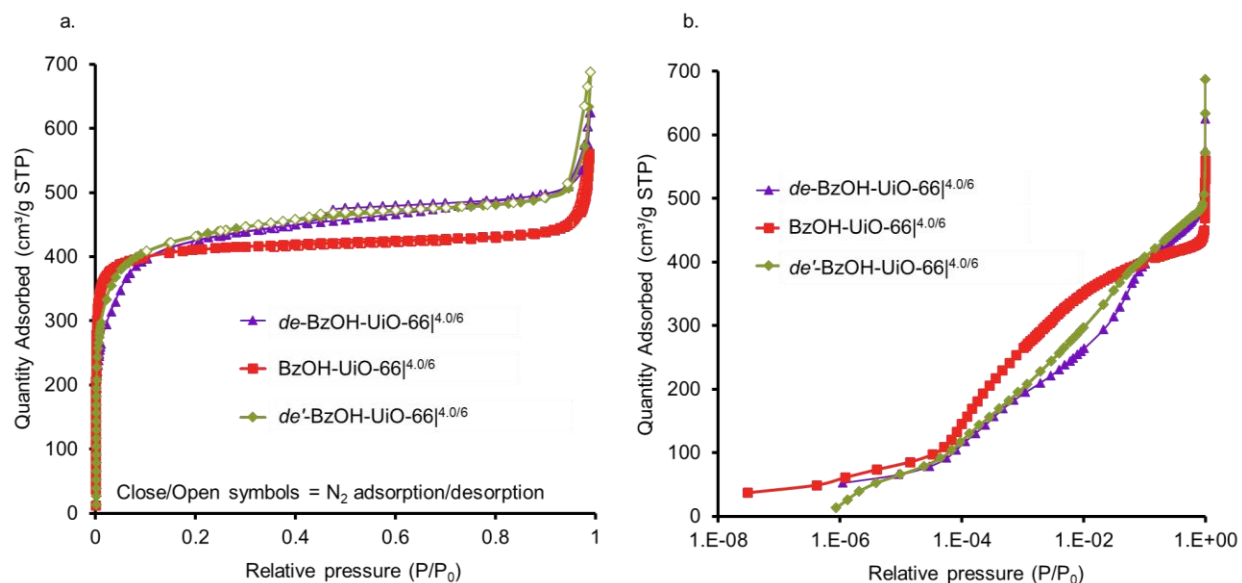


**Figure B3**  $N_2$  isotherms for the BzOH-UiO-66 samples on a normal scale (a) and a semi-log plot scale (b), before and after post-synthesis decapping treatment. The hysteresis in the sample decapped in HCl/DMF (*de*-BzOH-UiO-66) is not observed in the sample decapped in HCl/*n*-butanol (*de'*-BzOH-UiO-66) in the normal scale plot.

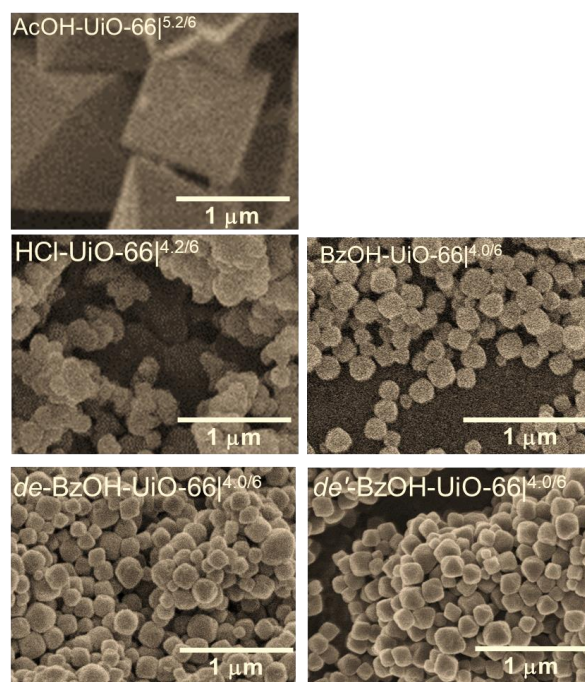


**Figure B4** SEM-images for the UiO-66 variants used in Chapter 3.

### B3.2. Compositional analyses of UiO-66 samples

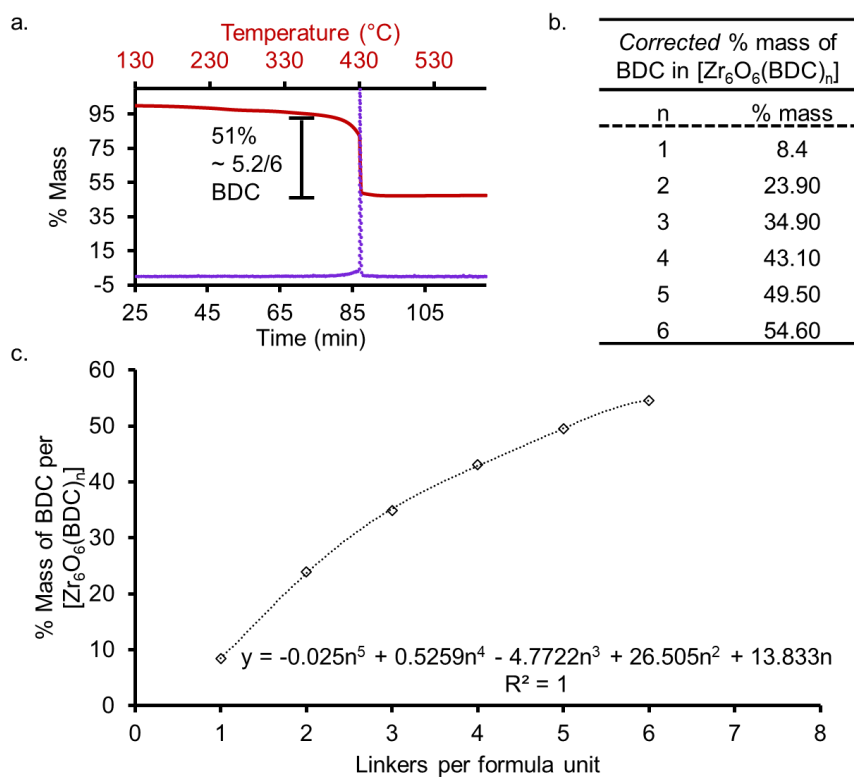


**Figure B5**

The approximation of L/N ratios in the variants of UiO-66 with  $[\text{Zr}_6\text{O}_4(\text{OH})_4(\text{BDC})_n]$  compositions based on TGA profiles.<sup>36</sup> (a) A representative TGA mass-loss profile (red) for the AcOH-UiO-66<sup>5.2/6</sup> sample and the corresponding first derivative (red-dotted line), plotted as functions of time (bottom x-axis) and temperature (top x-axis).<sup>242</sup> These were used to identify the point of complete linker degradation, where the only materials left is presumably  $\text{ZrO}_2$ . The total mass loss due to the organic linker is calculated from the mass at 345 °C (at which point the MOF presumably forms the dehydroxylated  $[\text{Zr}_6\text{O}_6(\text{BDC})_n]$  compositions<sup>62, 145</sup>) to the point of complete linker degradation (600 °C). (b) A table showing theoretical % mass loss as a function of n. These % mass losses are the corrected values for the formation of  $\text{ZrO}_2$  (instead of  $\text{ZrO}$  when derived directly from the  $[\text{Zr}_6\text{O}_6(\text{BDC})_n]$  formula.<sup>243</sup> (c) Plot of the theoretical % mass vs n as best-fitted ( $R^2 = 1$ ) to a polynomial equation. With this equation, convenient estimates of the L/N ratios (Table B4) can be qualitatively obtained from experimental data with a good precision.<sup>36</sup> These measurements corroborate well with the L/N ratios calculated using a joint NMR/ICP strategy as discussed below.

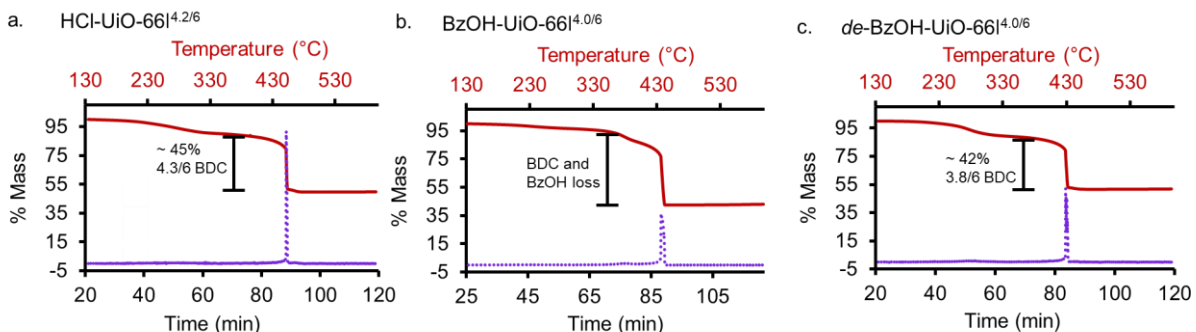


**Figure B6** (a-c) TGA profiles of HCl-UiO-66|<sup>4.2/6</sup> (a), BzOH-UiO-66|<sup>4.0/6</sup> (b), and *de*-BzOH-UiO-66|<sup>4.0/6</sup> (c). For BzOH-UiO-66|<sup>4.0/6</sup>, an accurate L/N ratio could not be determined given the non-distinct mass loss step from both the BzOH cap and the BDC linker.

Given the technical difficulties in identifying the exact point for TGA mass loss, the L/N ratios in UiO-66 were also determined using a combination of <sup>1</sup>H NMR and ICP analyses. The amount of BDC in a MOF sample can be obtained from the <sup>1</sup>H NMR spectrum of a digested sample while the amount of Zr is separately determined from ICP-OES (see procedures a-d below).

**Caution:** HF is very toxic and dangerous to handle without proper safety training. PPE must include Silvershield gloves and goggles. Acid digestions and subsequent dilutions should be carried out in a well-ventilated hood.

**Procedure A: for quantifying the Zr content in MOFs.** In a typical ICP-OES experiment, MOF sample (0.65 mg) was combined with a H<sub>2</sub>SO<sub>4</sub>/HF/H<sub>2</sub>O<sub>2</sub> (6/1/1 v/v/v) mixture and digested in a sealed 15 mL polypropylene centrifuge tube by heating at 80 °C in a sand bath for 1 h. After the tube was allowed to cool to room temperature, the resulting clear solution was diluted to 30 mL with ultrapure deionized water and analyzed for Zr ( $\lambda_{\text{OE}} = 256.887, 257.139, 327.305, 339.198, 343.823, \text{ and } 349.621 \text{ nm}$ ) content with ICP-OES by comparing against a calibration curve constructed from 0, 1, 5, 10, and 20 ppm Zr standard solutions. The obtained Zr content (7.674

ppm) equates to 0.00388 mmol Zr/mg of MOF. The error reported was determined using the standard deviations from three different digested samples of the same material.

**Procedure B: for quantifying the Zr content in MOFs.** The following procedure was employed to reduce the uncertainty associated with the ICP-OES instrumentation.<sup>244</sup> In a 15 mL polypropylene centrifuge tube was added the MOF material (~1 mg), followed by conc. H<sub>2</sub>SO<sub>4</sub> (1.5 mL), H<sub>2</sub>O<sub>2</sub> (0.25 mL), and HF (0.25 mL). The tube was slightly shaken and then sonicated for 1 h until a clear, homogenous solution was observed. The resulting solution was then diluted with deionized water (27.7 mL) and spiked with an yttrium internal standard (0.3 mL of an 500 ppm solution in 3% nitric acid) to make the ICP-OES sample (final volume = 30 mL). This sample was then analyzed for Zr ( $\lambda_{\text{OE}} = 327.305, 339.198, 343.823, \text{ and } 349.621 \text{ nm}$ ) content with ICP-OES (3 ×) by comparing against a calibration curve of standards with known concentrations. The error reported was determined using the standard deviations from three different digested samples of the same material. As an example, the calculations for BzOH-UiO-66 is listed in Table B2.

**Table B1** Sample calculation for Zr content in BzOH-UiO-66.

Sample	[Zr] in ICP sample (ppm) <sup>a</sup>	[Zr] in ICP sample (mmol/L)	Amount of Zr in the MOF sample (mmol)	MOF sample (mg)	Amount of Zr per mass of MOF (mmol/mg)
1	7.73	$8.47 \times 10^{-5}$	$2.54 \times 10^{-3}$	0.65	$3.91 \times 10^{-3}$
2	7.58	$8.31 \times 10^{-5}$	$2.49 \times 10^{-3}$	0.65	$3.84 \times 10^{-3}$
3	7.71	$8.45 \times 10^{-5}$	$2.54 \times 10^{-3}$	0.65	$3.90 \times 10^{-3}$
Avg	7.67 ( $\pm 0.08$ )	$8.41 (\pm 0.09) \times 10^{-5}$	$2.52 (\pm 0.03) \times 10^{-3}$	0.65	$3.88 (\pm 0.04) \times 10^{-3}$

<sup>a</sup>The [Zr] value for each sample was obtained as the average from three different ICP-OES analysis (~ 5 mL each).

**Procedure C: for quantifying the linker content in MOFs.** In a typical NMR experiment, MOF sample (10 mg) was added to a mixture of HF:DMSO-*d*<sub>6</sub> (30  $\mu$ L:570  $\mu$ L) in a 15 mL polypropylene centrifuge tube and vortexed at room temperature until digested (~5 min). An aliquot (12  $\mu$ L,

corresponding to ~0.2 mg of MOF) of this clear solution was added to an NMR tube along with an aliquot of a maleic acid (MA, 12 mM) solution in DMSO- $d_6$  (50  $\mu$ L) and DMSO- $d_6$  (538  $\mu$ L) to give a solution with final MA concentration of 1 mM, which is then analyzed by  $^1\text{H}$  NMR spectroscopy. To ensure accurate integration, a 20 s delay between scans was used, which exceeded the measured T1 relaxation time for BDC (3.7 s) and MA (2.8 s) and the capping agents. The MA:BDC ratios were determined from the average relative integration from spectra of 3 digested samples of the same material. When compared against a calibration curve (constructed from a series of standards with known MA:BDC concentrations (Table B3 and inset of Figure B7)), this value can be correlated to the amount of BDC (mmol)/mass of MOF (mg). Together with the ICP-OES-determined Zr content, the BDC:Zr molar ratio (and thus the L/N ratio) can be determined.

**Procedure D: for quantifying the linker content in MOFs.** The following procedure was employed to minimize the amount of sample and HF usage. In a 15 mL polypropylene centrifuge tube, the MOF material (~ 2 mg) was added, followed by HF (6  $\mu$ L) and DMSO- $d_6$  (114  $\mu$ L) sequentially. The tube was slightly shaken to obtain a well-mixed sample, which is then sonicated until a clear, homogenous solution was observed (~ 1 h). An aliquot (12  $\mu$ L, corresponding to 0.2 mg of sample) of the resulting solution was transferred to an NMR tube, to which were added an aliquot (50  $\mu$ L) of maleic acid internal standard solution (12 mM, in DMSO- $d_6$ ) and DMSO- $d_6$  (538  $\mu$ L). The resulting solution was then analyzed by  $^1\text{H}$  NMR spectroscopy. To ensure accurate integration, the delay between scans was set to 20-50 s, which exceeds the measured T1 relaxation time for BDC (3.7 s), MA (2.8 s), and the capping ligands. The MA:BDC ratios were determined from the average relative integration from spectra of 3 digested sample of the same materials. When compared against a calibration curve (constructed from a series of standards with known

MA:BDC concentrations (see inset in Figures B7), this value can be correlated to the amount of BDC (mmol)/mass of MOF (mg).

**Table B2** Samples for the BDC:MA NMR calibration curve, as prepared from DMSO- $d_6$  stock solutions of BDC (12 mM) and MA (12 mM).

Final concentration (mM) of BDC in DMSO- $d_6$	Amount ( $\mu\text{L}$ ) of BDC stock solution (12 mM in DMSO- $d_6$ ) added	Amount ( $\mu\text{L}$ ) of MA stock solution (12 mM in DMSO- $d_6$ ) added	Amount ( $\mu\text{L}$ ) of DMSO- $d_6$ added	Relative MA:BDC integration
0.1	5	50	545	0.201
0.25	12.5	50	537.5	0.482
0.5	25	50	525	1.001
1.0	50	50	500	1.990
2.0	100	50	450	3.997

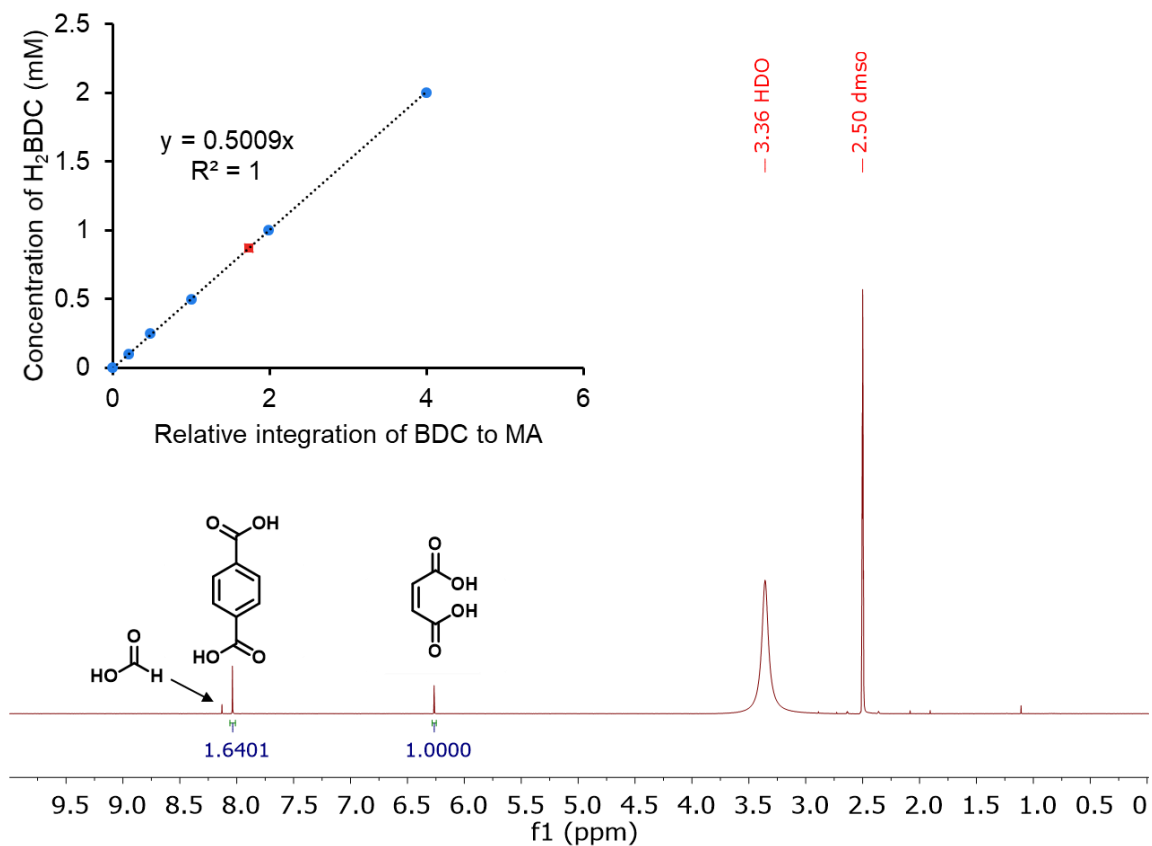


**Figure B7** The  $^1\text{H}$  NMR spectrum of an HF-digested sample of *de*-BzOH-UiO-66 $^{[4.0/6]}$  sample in DMSO- $d_6$ . (Inset) A calibration curve of concentration of terephthalic acid vs

the relative BDC:MA integration ratios (blue circles). The relative BDC:MA integration ratio for a digested MOF sample can then be plotted on this calibration curve (red square) to determine the concentration of BDC in solution. The small peak to the left of the BDC aromatic resonances represents a trace of formic acid that caps the defect sites.

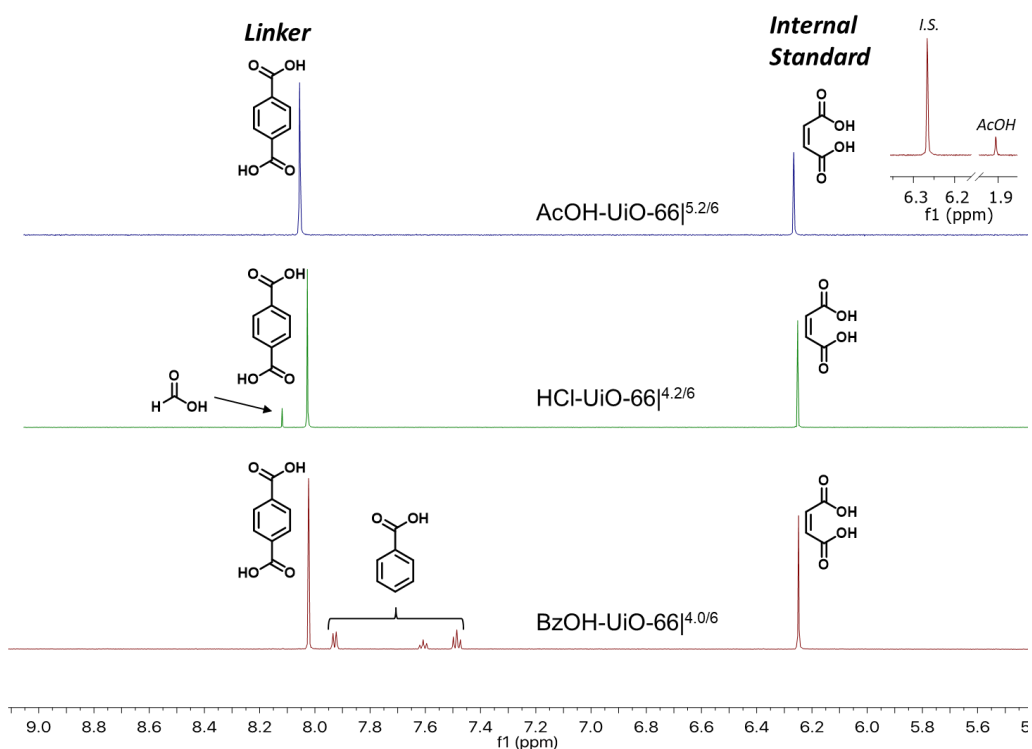


**Figure B8** The  $^1\text{H}$  NMR spectra of HF-digested AcOH-UiO-66 $^{5.2/6}$ , HCl-UiO-66 $^{4.2/6}$ ,<sup>245</sup> and BzOH-UiO-66 $^{4.0/6}$  samples in DMSO- $d_6$ . Inset shows the acetic acid peak with respect to the internal standard (I.S.).



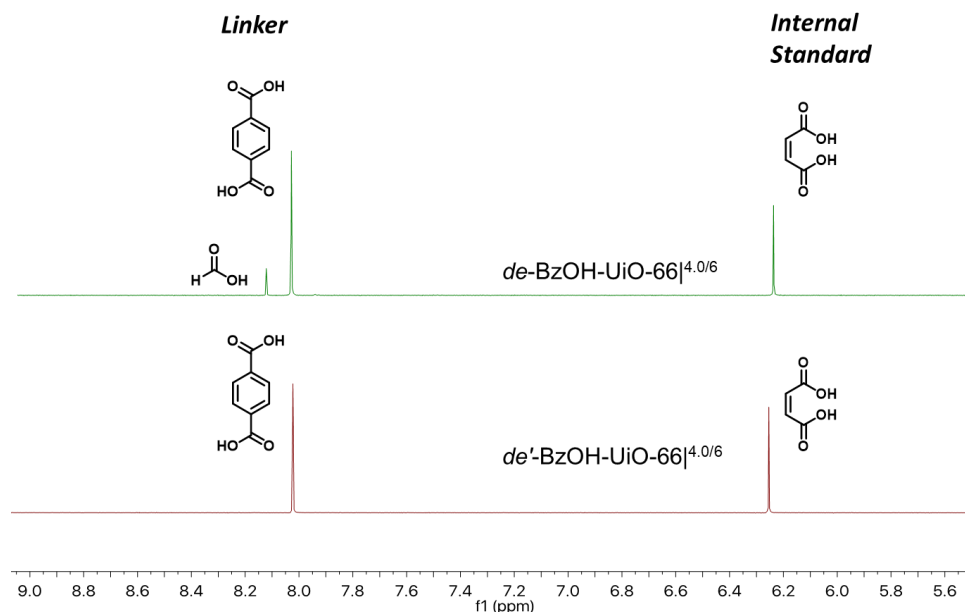


**Figure B9** The  $^1\text{H}$  NMR spectra in  $\text{DMSO-}d_6$  of HF-digested  $de\text{-BzOH-UiO-66}^{4.0/6}$  and  $de'\text{-BzOH-UiO-66}^{4.0/6}$ , obtained after being “decapped” in  $\text{HCl/DMF}$  (top spectrum) and  $\text{HCl}/n\text{-BuOH}$  (bottom spectrum), respectively. The mole ratios of the different species in the top spectrum were obtained from NMR integration against MA internal standards. As shown, formates are no longer present in the bottom spectrum.

As stated in Chapter 3 and shown in Figures B8-B9, the  $^1\text{H}$  NMR spectra of the digested MOF can reveal the identity of the capping ligands present in a particular MOF sample in addition to the expected linkers digested). The amount of each species (mM/mg MOF) can be easily obtained with careful calibration (see procedures c and d above). Of particular interest is the observed presence of formates in the  $\text{HCl-UiO-66}$  sample and in the “decapped” samples. These formates originate from the acid-catalyzed amide-hydrolysis of  $\text{DMF}^{137}$  and can serve as monocarboxylate caps to the defect sites. The large amount of formates present (e.g., from the mole ratios in Figure B11), can be accounted for if one assumes that every missing BDC is replaced with two formate caps, resulting in a  $[\text{Zr}_6\text{O}_4(\text{OH})_4](\text{BDC})_4(\text{HCOO-})_4$  molecular formula for  $\text{BzOH-UiO-66}^{4.0/6}$ . When the decapping procedure was carried out in butanol instead of DMF,

formates were no longer observed (Figure B9), further supporting this formate-from-DMF-decomposition hypothesis, which was also noted by Lillereud's and coworkers.<sup>81</sup>

**Calculations of linker/node ratio.** From the metal content (obtained by ICP-OES analysis) and the linker concentration (determined from <sup>1</sup>H NMR analysis), the L/N ratio for each of our MOF materials can be calculated (Table B4). We exclusively employ these values in the naming convention and model constructions in this work given the difficulty in distinguishing capping agent from the BDC linkers in the TGA profiles (see the discussion in the caption of Figure B7). In addition, there have been alerts of limitations associated with accurate TGA analyses for MOF samples (e.g., obtaining distinct mass loss steps to facilitate the quantification of ligands, linkers, and chemisorbed solvent molecules on the nodes).<sup>81, 105</sup>

**Table B4** Linker-node (L/N) ratio as determined from data obtained from NMR and ICP-OES in comparison to the TGA-based values (defect-free = 6)

Entries	MOF	Zr content (mmol/mg)	BDC content (mmol/mg)	L/N	L/N	Capping ligand (% mol)*
				(NMR -ICP)	(TGA)	
1	AcOH-UiO-66 <sup>a</sup>	3.58×10 <sup>-3</sup>	3.11×10 <sup>-3</sup>	5.2	5.2	AcO- (~34)
2	HCl-UiO-66 <sup>a</sup>	3.74×10 <sup>-3</sup>	2.63×10 <sup>-3</sup>	4.2	4.3	FO- (~46)
3	BzOH-UiO-66 <sup>b</sup>	3.00×10 <sup>-3</sup>	1.98×10 <sup>-3</sup>	4.0	-	BzO- (~67)
4	<i>de</i> -BzOH-UiO-66 <sup>b</sup>	3.88×10 <sup>-3</sup>	2.60×10 <sup>-3</sup>	4.0	3.8	FO- (~ 91)
5	<i>de'</i> -BzOH-UiO-66 <sup>b</sup>	3.41×10 <sup>-3</sup>	2.26×10 <sup>-3</sup>	4.0	NM	none observed

<sup>a</sup>The Zr and BDC contents for these samples were determined by procedures a and c, respectively. <sup>b</sup>The Zr and BDC contents for these samples were determined by procedures b and d, respectively. We recommend the use of procedures b and d as they have been optimized for distinguishing small differences within one class of samples such as the last three materials in this table. \*The mol %, qualitatively estimated from NMR, corresponds to  $\frac{\text{mol monodentate ligand}}{2(\text{mol missing BDC linkers})}$  in which mol % = 100 suggests that all defect sites are capped with the ligand. NM = not measured.

#### B4. Modeling of *in silico* structures for the defect domains in UiO-66 derivatives

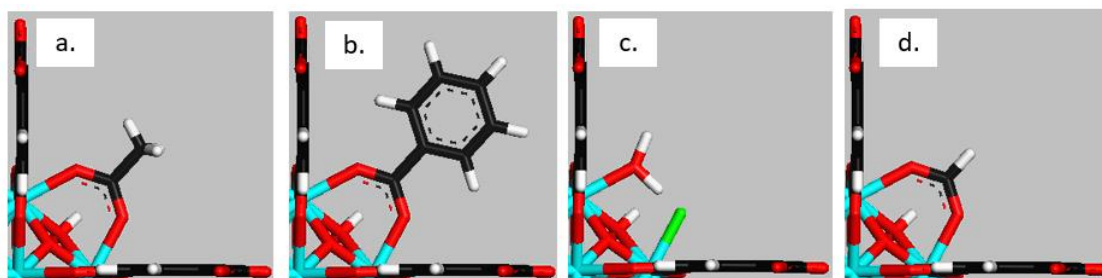


**Figure B10** Proposed capping of under-coordinated nodes in structural models according to synthesis or post-synthesis treatment. a) Proposed model for the acetate capping of UiO-66 synthesized with acetic acid modulator (AcOH-UiO-66). b) Proposed model for the benzoate capping of UiO-66 synthesized with benzoic acid modulator (BzOH-UiO-66). c-d) Two proposed models for the monodentate capping (i.e.,  $[\mu_1\text{-Cl} + \mu_1\text{-H}_2\text{O}]$  (c), formates (d)) of UiO-66 synthesized in DMF with hydrochloric acid as modulator (HCl-UiO-66) or post-synthetically treated with hydrochloric acid in DMF or n-butanol (*de*-BzOH-UiO-66 and *de'*-BzOH-UiO-66)

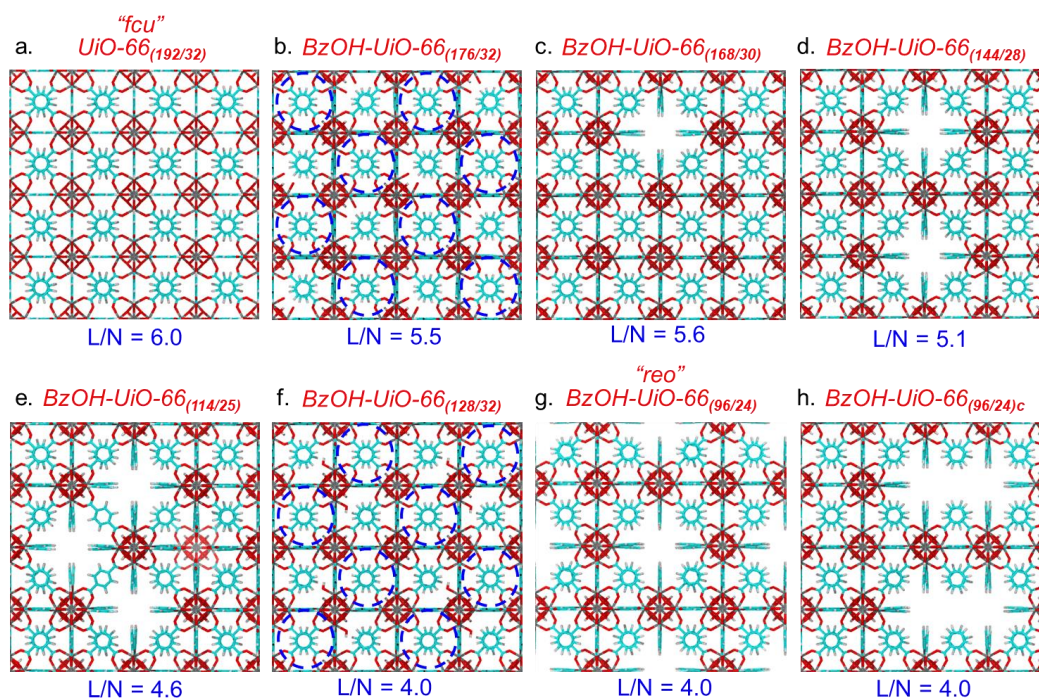


**Figure B11** *In silico* models for defective UiO-66 domains capped with benzoates, i.e.,  $BzOH\text{-}UiO\text{-}66_{(x/y)}$  models where  $x$  indicates the number of linkers and  $y$  indicates number of nodes in the supercell. Models a and g correspond to UiO-66-*fcu* and UiO-66-*reo*, respectively



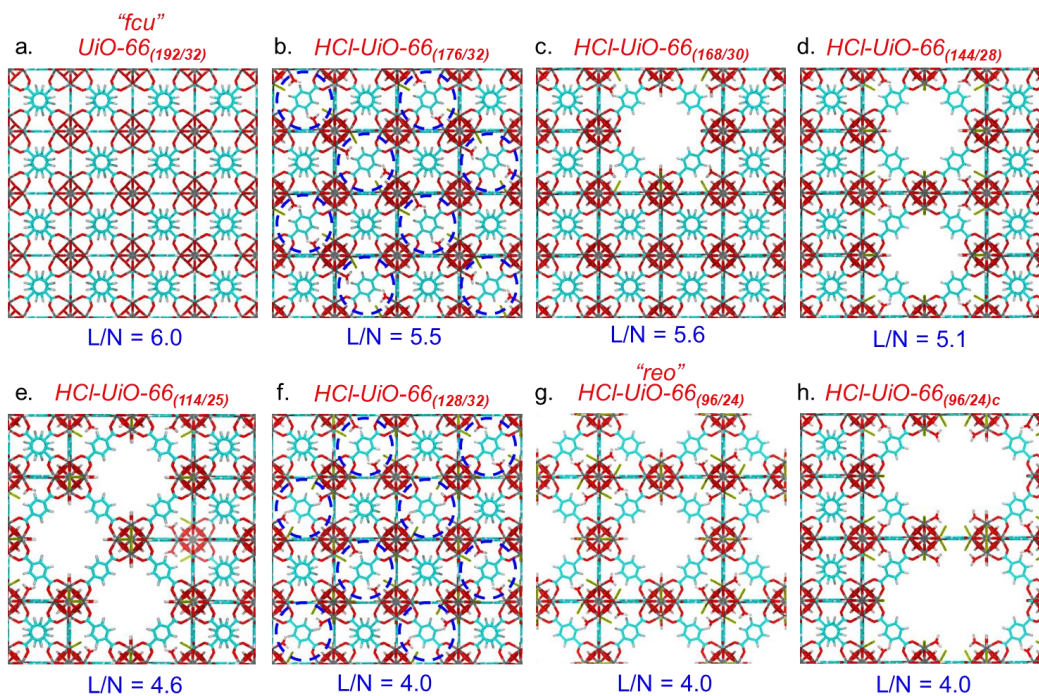


**Figure B12** *In silico* models for defective UiO-66 domains capped with  $[\mu_1\text{-Cl} + \mu_1\text{-H}_2\text{O}]$  groups i.e., *HCl-UiO-66*<sub>(x/y)</sub> models, where *x* indicates the number of linkers and *y* indicates number of nodes in the supercell. Models a and g correspond to UiO-66-*fcu* and UiO-66-*reo*, respectively

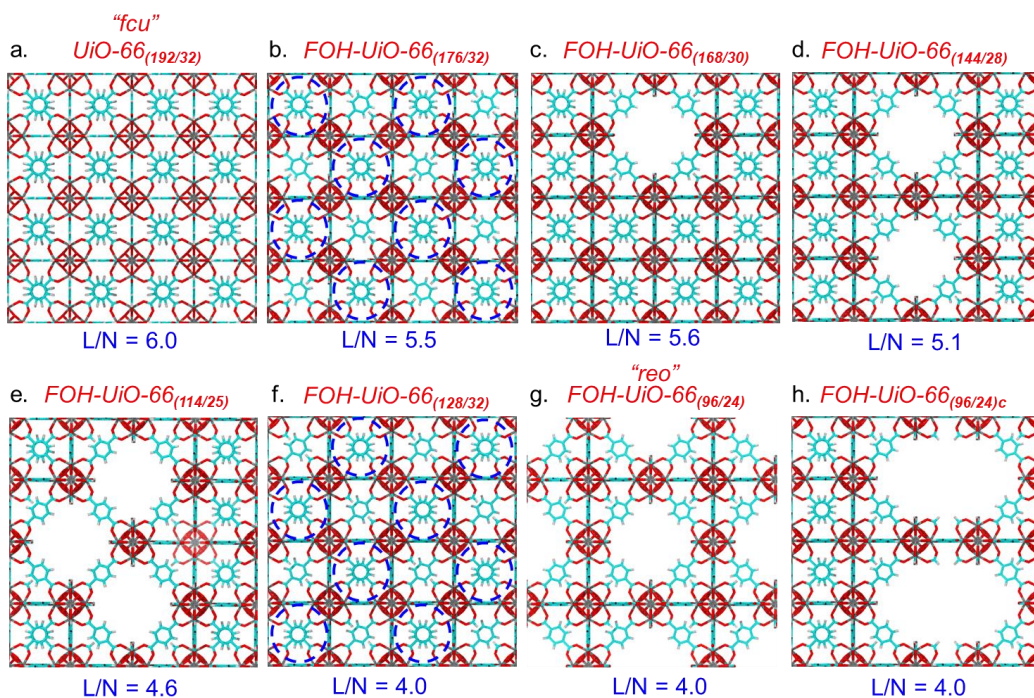


**Figure B13** *In silico* models for defective UiO-66 domains capped with formate groups, i.e., *FOH-UiO-66*<sub>(x/y)</sub> models, where *x* indicates the number of linkers and *y* indicates number of nodes in the supercell. Models a and g correspond to UiO-66-*fcu* and UiO-66-*reo*, respectively.

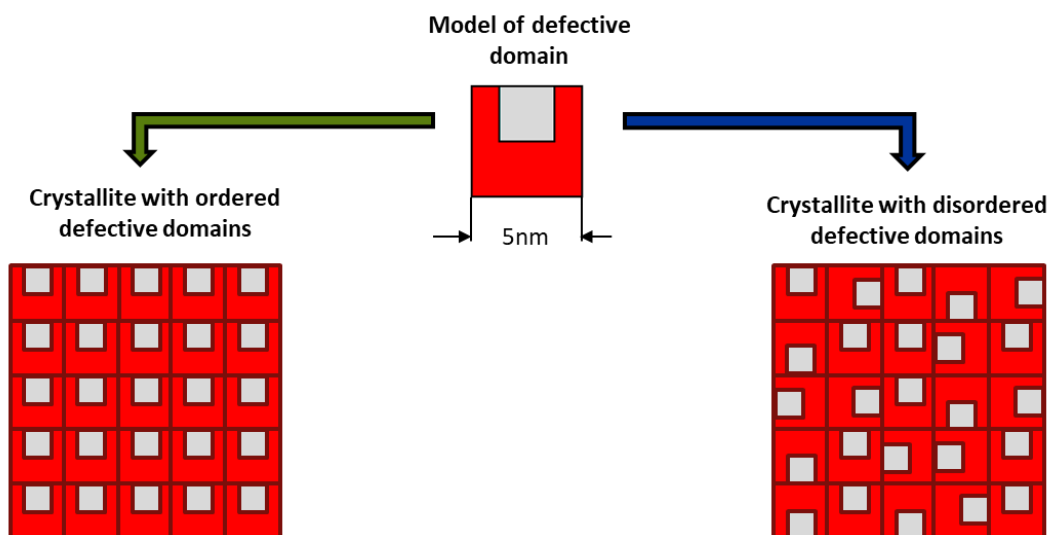


**Figure B14** A schematic showing how the defective domains, modeled by our *in silico* structures, could be present in UiO-66 crystallites. Ordered defective domains (left) would result in additional, highly intense, and low-angle diffraction peaks as shown in the simulated PXRD pattern in Figure B1 and in literature.<sup>81, 108</sup> Disordered defective domains (right) may exhibit (if at all observed) additional and broader peaks in the low-angle regions of the experimental PXRD patterns with weak intensity.<sup>81</sup>

## B5. N<sub>2</sub> isotherm simulations

Nitrogen adsorption isotherms at 77 K were simulated for the *in silico* models shown in Chapter 3, Figure 3.4, and Figure B11-B13 using grand canonical Monte Carlo (GCMC) simulations with the open source code RASPA.<sup>142</sup> Framework atoms were fixed during simulations, while equal probability rotation, translation, insertion and deletion moves were performed for the nitrogen molecules to sample the grand canonical ensemble. Initially 20,000 cycles of N (where N is the maximum between 20 and the number of molecules in the simulation

supercell) Monte Carlo moves were carried out to allow the system to equilibrate, followed by another 20,000 cycles for collection of ensemble averages.

Intermolecular interactions were described by a Lennard-Jones (LJ) plus Coulomb potential. LJ parameters and Coulomb charges for nitrogen molecules were assigned according to the TraPPE model.<sup>246</sup> LJ parameters for framework atoms were assigned according to the Universal Force Field (UFF).<sup>247</sup> Lorentz-Berthelot mixing rules were applied to LJ parameters. No Coulomb charges were applied to framework atoms. Properties of the implicit gas phase were modeled based on the Peng-Robinson equation of state for nitrogen.<sup>248</sup>

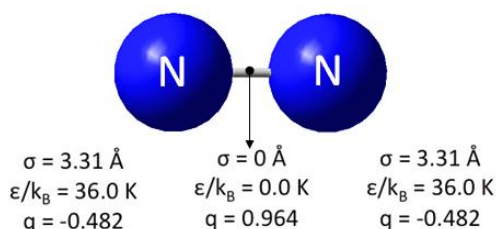


**Figure B15** TraPPE model for nitrogen molecule. This model was parameterized to reproduce vapor-liquid equilibrium curves as well as the quadrupole moment of nitrogen.

**Table B5** Lennard-Jones (LJ) parameters for the framework atoms

Atom	$\sigma$ (Å)	$\epsilon/k_B$ (K)
C	3.43	52.83
Cl	3.52	114.3
H	2.57	22.14
N	3.27	34.75
O	3.12	30.19

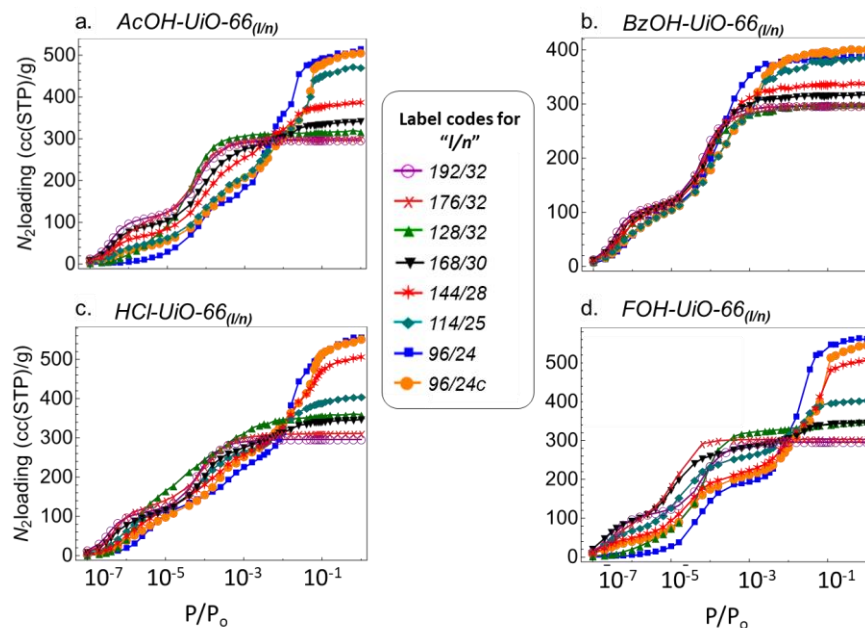


**Figure B16** Different simulated isotherms for the *in silico* models. Simulated isotherms within each panel correspond to the same capping.

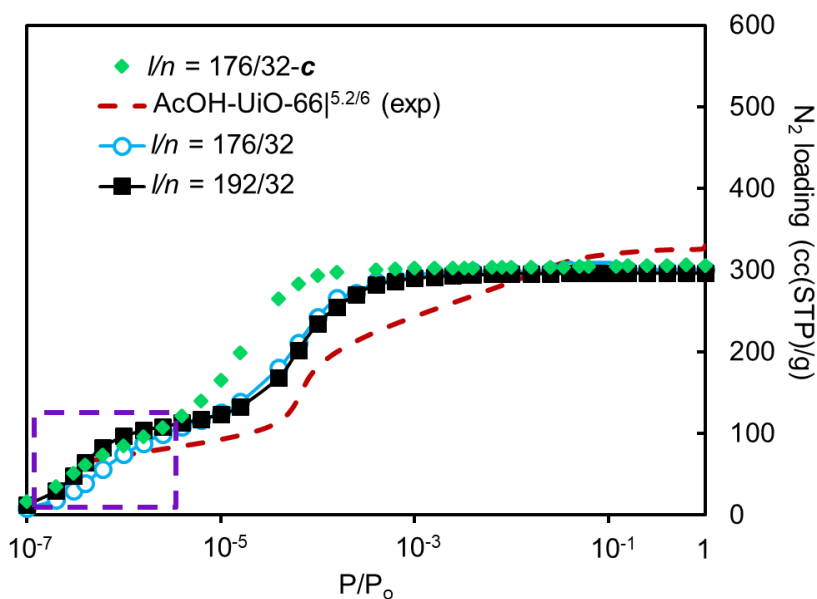


**Figure B17** Clustering vs. randomly distributed missing-linker defects in AcOH-UiO-66<sub>(l/n)</sub>. Comparison between the simulated isotherms for models with high L/N ratios show

that isotherms simulated from a model with randomly distributed missing linkers ( $AcOH-UiO-66_{(176/32)}$ ) matches closest to the defect-free UiO-66 ( $AcOH-UiO-66_{(192/32)}$ ) simulated isotherm except at the pore-filling of the tetrahedral cavities (purple box region). When compared against the isotherm simulated from a model ( $AcOH-UiO-66_{(176/32)c}$ ) comprising of clustering or coalescing missing linkers, the filling of the tetrahedral pore is significantly reduced suggesting the lessened amount of distinct tetrahedral cavities.

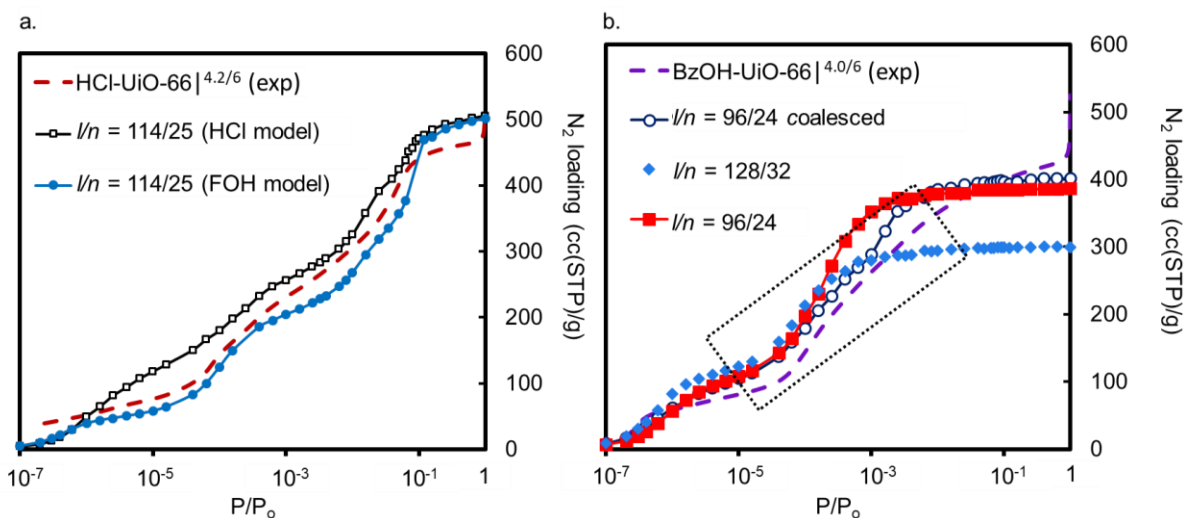


**Figure B18** Comparisons between the experimentally-collected isotherms and those generated from the *in silico* models where only the most reasonable candidates<sup>249</sup> from the models are shown. Comparison between measured and simulated isotherms for a) HCl-UiO-66| $4.2/6$  vs.  $HCl-UiO-66_{(114/25)}$  and  $FOH-UiO-66_{(114/25)}$  models respectively and for b) BzOH-UiO-66| $4.0/6$  vs. select BzOH-UiO-66 $_{(x/y)}$  models. From these, the best fit simulated isotherm to that of the experimental (Chapter 3, Figure 3.8) can be used to justify the assignment of each UiO-66 derivative to a structural model.



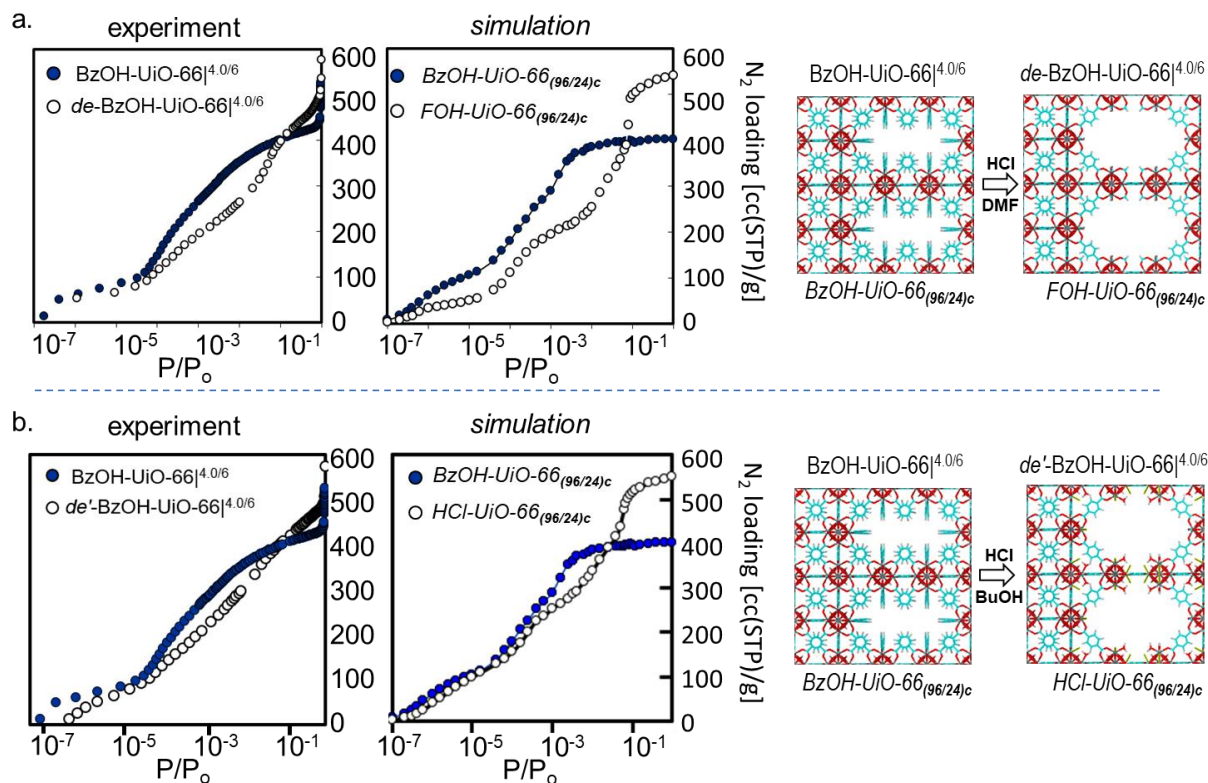


**Figure B19** Expected (simulation) vs. measured (experiment) effects due to post-synthesis decapping. a) Measured isotherms in  $BzOH-UiO-66|^{4.0/6}$  and  $de-BzOH-66|^{4.0/6}$ , and simulated isotherms in  $BzOH-UiO-66_{(96/24)c}$  and  $FOH-UiO-66_{(96/24)c}$ . These models only differ in the capping groups (benzoate vs formate). b) Measured isotherms in  $BzOH-UiO-66|^{5.2/6}$  and  $de'-BzOH-66|^{4.0/6}$ , and simulated isotherms in  $BzOH-UiO-66_{(96/24)c}$  and  $HCl-UiO-66_{(96/24)c}$ . These models only differ in the capping groups (benzoate vs. formate).

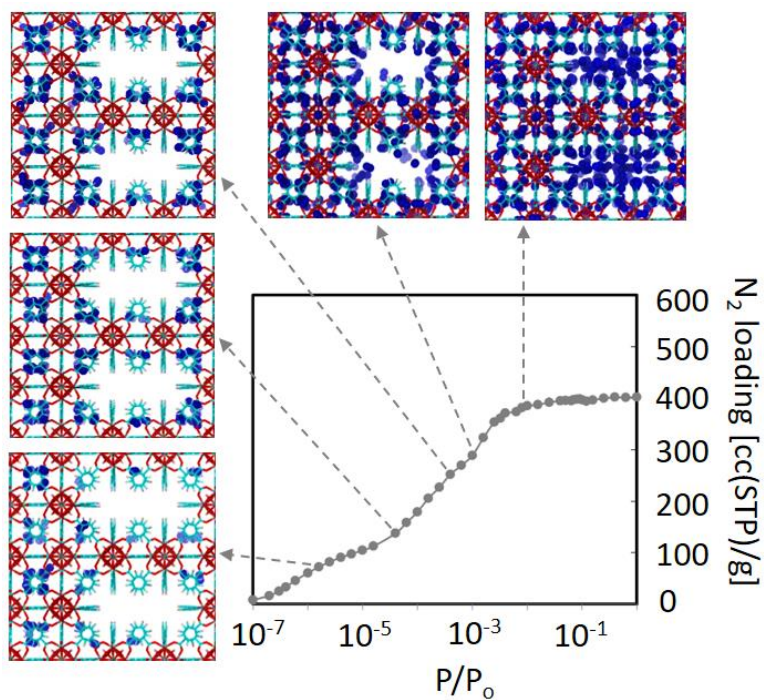


**Figure B20** Simulation snapshots corresponding to steps in isotherm of  $BzOH-UiO-66_{(96/24)c}$  (model for  $BzOH-UiO-66|^{4.0/6}$ ).

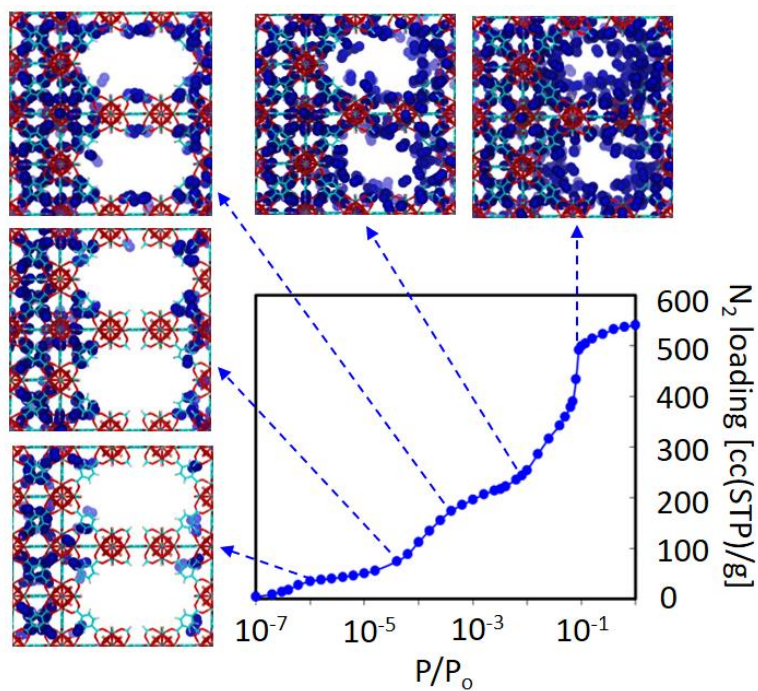


**Figure B21** Simulation snapshots corresponding to steps in isotherm of  $FOH-UiO-66_{(96/24)c}$  (model for  $de-BzOH-UiO-66|^{4.0/6}$ ).

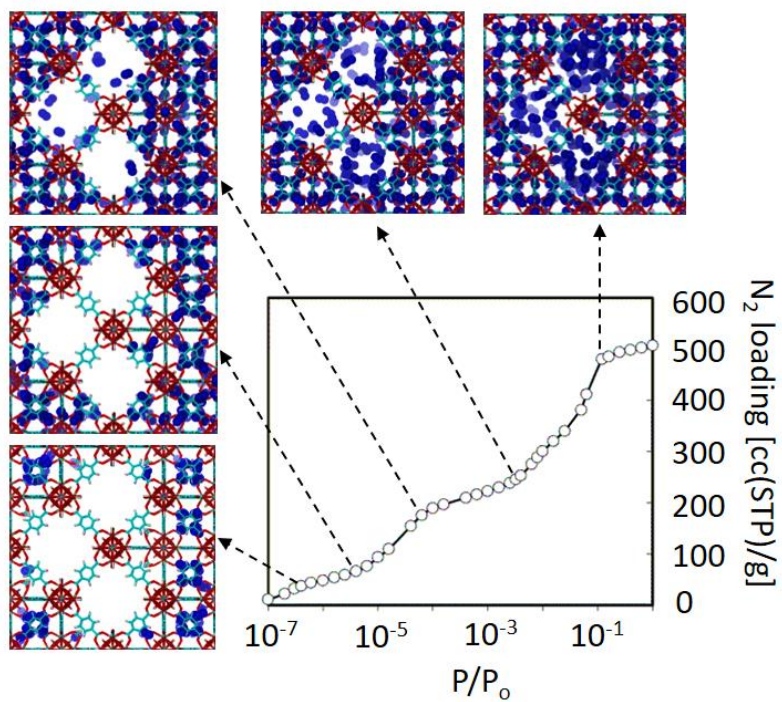


**Figure B22** Simulation snapshots corresponding to steps in isotherm of *FOH-UiO-66*<sub>(114/25)</sub> (model for HCl-UiO-66<sup>4.2/6</sup>).

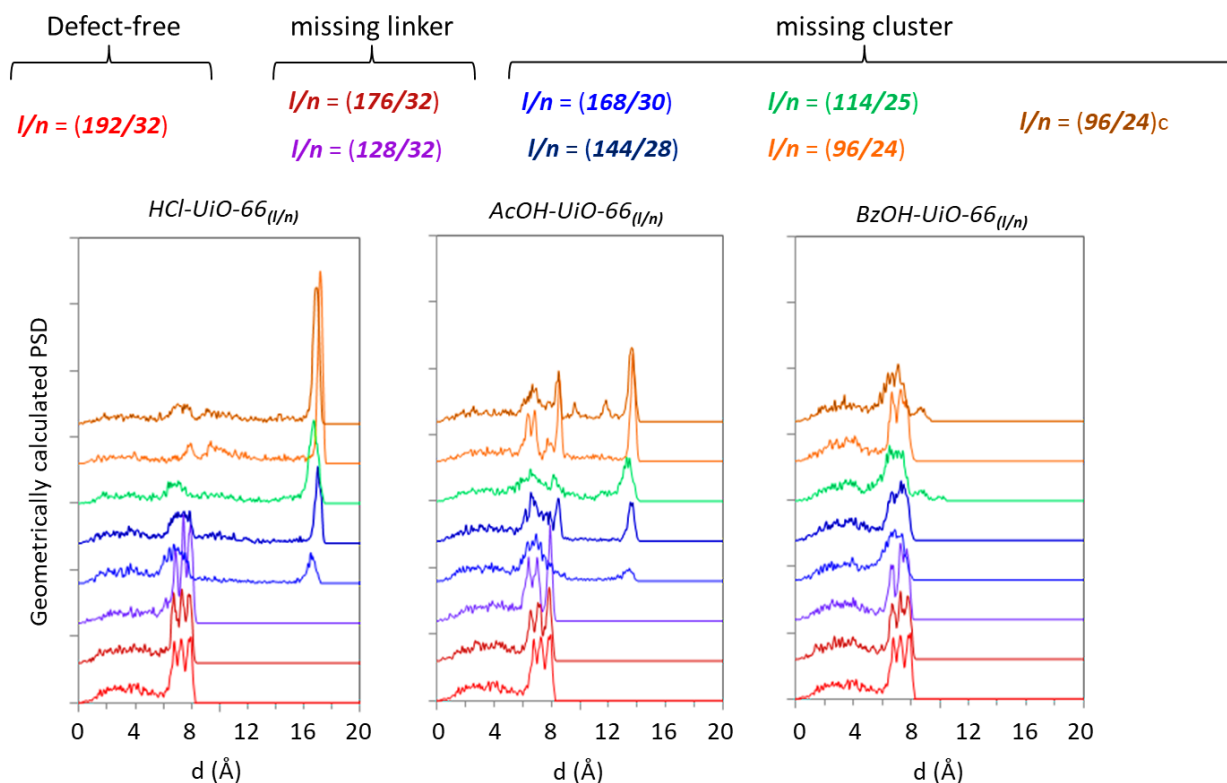


**Figure B23** All pore size distributions (PSD) geometrically calculated for all structural models studied in this work (FOH-UiO-66 models produced similar PSDs to AcOH-UiO-66 models). The PSD were calculated according to the method of Gelb and Gubbins.<sup>250</sup> In this computational method, random points are selected within the pores of a materials and the largest sphere that encloses each point is determined. The resulting histogram corresponds to the PSD.

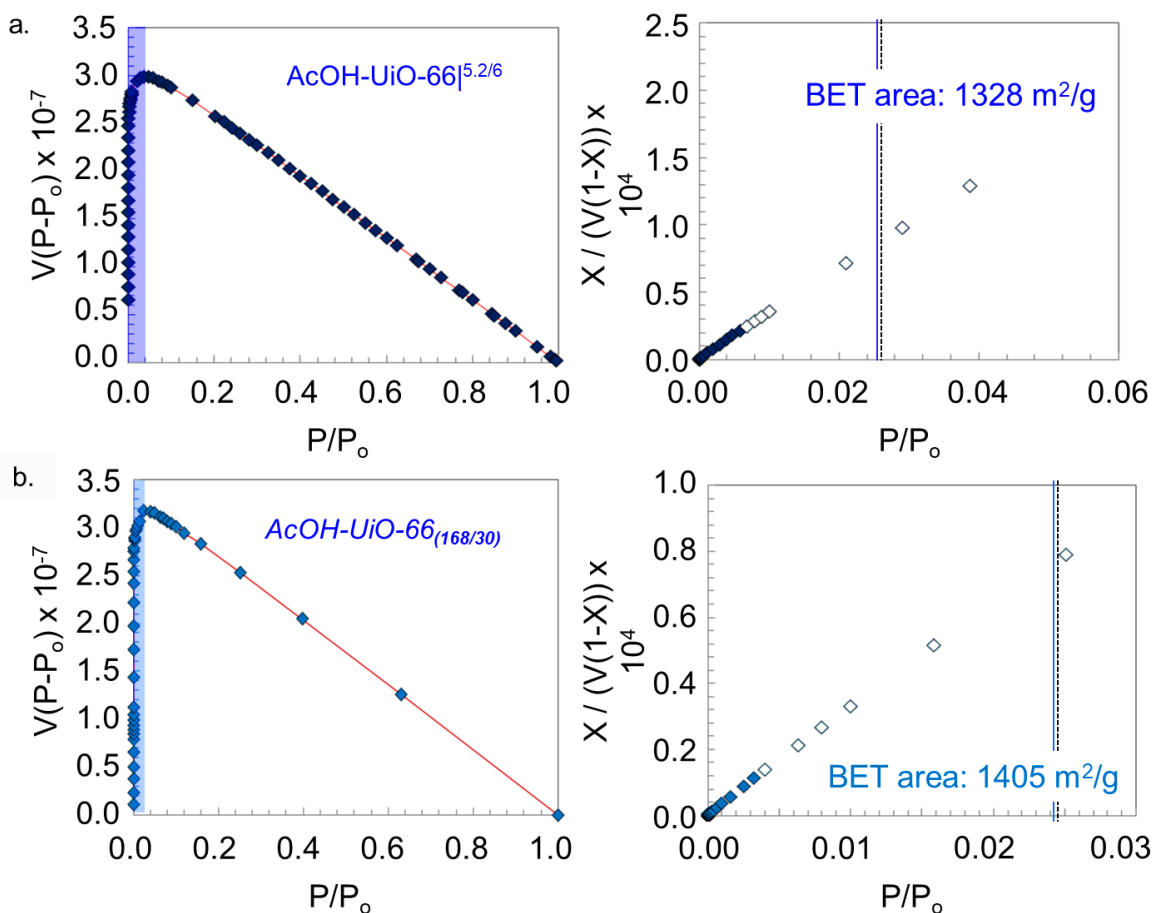


**Figure B24** Example of detailed BET area calculation from the isotherms of synthesized samples (here  $\text{AcOH-UiO-66}^{5.2/6}$ ) and from simulated isotherms corresponding to the *in silico* models (here  $\text{AcOH-UiO-66}_{(168/30)}$ ). Left plots are used to select a pressure range that fulfills the second BET criteria, which is indicated by the shaded region. All points within the shaded region are plotted in the right plots. Open-squared points were utilized for the BET calculation. Solid vertical line indicates the pressure corresponding to the calculated monolayer loading  $A_m$  as read from the isotherm. Dashed line indicates the value of  $(1+C)^{1/2}$  which correspond to the pressure predicted by the BET calculation to correspond to monolayer loading. a) Calculation from measured isotherm for  $\text{AcOH-UiO-66}^{5.2/6}$  b) Calculation from simulated isotherm for the corresponding  $\text{AcOH-UiO-66}_{(168/30)}$  model.

## B6. Water adsorption in UiO-66 variants

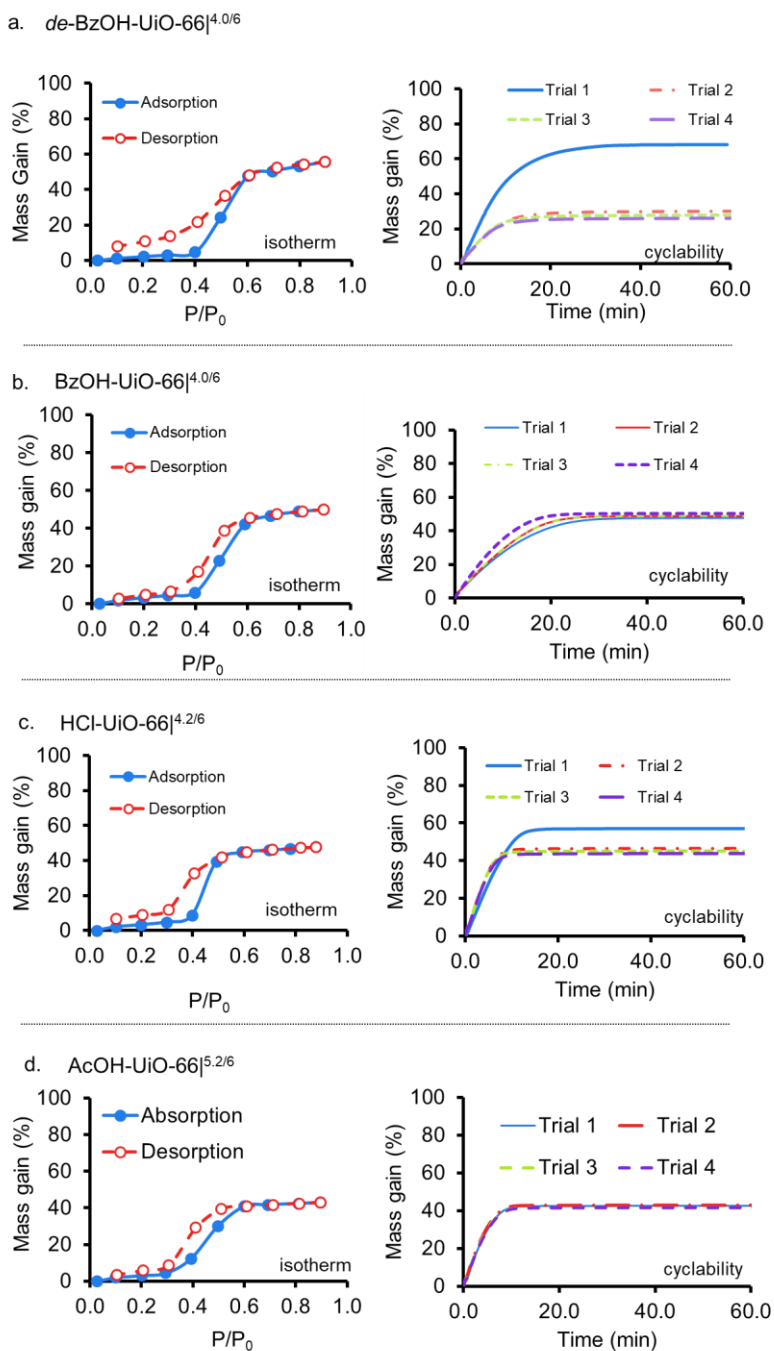


**Figure B25** (a-d) Water isotherms (left panel) and recyclability saturation-point isotherm plots (right panel) of UiO-66 variants. In a typical experiment, the MOF is activated at 120 °C under reduced pressure ( $10^{-3}$  bar) for 30 min followed by an injection of water vapor at  $P/P_0 = 0.9$  at 25 °C. The mass is allowed to equilibrate over 60 min at 25 °C then the sample is activated again to begin the next trial.



With the intriguing differences in pore architectures between the UiO-66 derivatives, we wanted to correlate these structures to their water adsorption behavior. To observe the effect of the delineated pore architectures upon water uptake, we subjected the prepared MOF samples to water isotherms and recyclability studies.<sup>56, 251-252</sup> We observed that the most defective MOF, *de*-BzOH-UiO-66<sup>4.0/6</sup>, achieves the highest water uptake of all the samples (68% mass gain) but partially loses its ability to retain water vapor after the first adsorption/desorption cycle (2<sup>nd</sup>-4<sup>th</sup> cycle plateaus at 30%, Figure B25a, right panel). We speculate that this observation is most likely due to the coalesced pores formed from two adjacent missing cluster defects which exposes the “decapped” node to water molecules. Upon thermal dehydration, these large pores can potentially collapse due to capillary forces in a manner reminiscent of the cases of other Zr-based MOFs featuring larger micropores (e.g., UiO-67) and mesopores (e.g., NU-1000)<sup>58 58 58 58 58 267</sup>. This is within reason as this notable effect is not observed for the BzOH-UiO-66<sup>4.0/6</sup>

## Appendix C Supplementary to Chapter 4

Portions of this appendix appear in the following manuscript:

Audu, C. O.; Chen, D.; Kung, C. W.; Snurr, R. Q.; Nguyen, S. T.; Farha, O. K.; Hupp, J. T.; “Transport diffusion of linear alkanes (C<sub>5</sub>-C<sub>16</sub>) through thin films of ZIF-8 as assessed by quartz crystal microgravimetry.” *manuscript under revision*

### C1. Materials and Methods.

Unless otherwise stated, all reagents were acquired from commercial sources and used without further purification. Ultrapure deionized water (18.2 MΩ cm resistivity) was obtained from a Millipore system (EMD Millipore, Billerica, MA).

Powder X-ray diffraction (PXRD) patterns were recorded on a Rigaku X-ray Diffractometer Model ATX-G (Rigaku Americas, The Woodlands, TX) equipped with an 18 kW Cu rotating anode, an MLO monochromator, and a high-count-rate scintillation detector. Measurements were made over the range  $2^\circ < 2\theta < 40^\circ$  in  $0.05^\circ$  step width with a  $2^\circ/\text{min}$  scanning speed.

N<sub>2</sub> adsorption and desorption isotherms were measured on a Micromeritics Tristar II 3020 (Micromeritics, Norcross, GA) at 77 K. Before each run, samples were thermally activated at 100 °C for 24 h (or until outgas rate  $\leq 0.02$  mmHg) under high vacuum on a Smart VacPrep (Micromeritics, Norcross, GA). At least 50 mg of sample was used in each measurement. The specific surface areas for N<sub>2</sub> were calculated using the Brunauer-Emmet-Teller (BET) model in the range of  $0.005 < P/P_0 < 0.1$ . The pore size distributions of the MOFs were calculated from the adsorption-desorption isotherms by density functional theory (DFT) using the carbon slit-pore N<sub>2</sub>-DFT model. The micropore volumes, micropore surface areas, and external surface areas for all



samples were determined using conventional t-plot methods<sup>227</sup> from N<sub>2</sub> adsorption data. For ZIF-8, the values were selected over the 3–5 Å t range by fitting the data to the Harkins-Jura thickness equation. This is the process recommended by Prof. A. W. Marczewski<sup>229</sup> as well as the Micromeritics Instrument Corporation.<sup>253</sup>

Centrifugation was carried out in an Eppendorf Centrifuge 5804 R, Model AG 22331 (Eppendorf AG, Hamburg, Germany) equipped with an F34-6-68 rotor. Unless otherwise stated, all centrifugations were carried out at 5000 rpm (3214 g) for 10–30 min.

Scanning electron microscopy (SEM) images were obtained at Northwestern University's EPIC-NUANCE facility on a SU8030 FE-SEM (Hitachi High Technologies America, Inc., Dallas, TX) microscope with an acceleration voltage of 10 kV. Prior to imaging, activated MOF samples were coated with either a film of Au/Pd or Os (~10–20 nm thickness) using either a Denton Desk III TSC Sputter Coater (Denton Vacuum, Moorestown, NJ) or a Filgen Osmium Coater Model OPC-60A (Filgen, Nagoya, Japan), respectively.

Research Quartz Crystal Microbalance (RQCM, Maxtekinc. Inc., CA) equipped with a polypropylene QCM holder (CHT-100 crystal holder - Teflon®, Maxtek Inc., CA) was used for diffusivity measurements. A 5 KΩ QCM polished gold electrode sensors (Maxtekinc. Inc., CA) was used as a substrate for ZIF-8 deposition (solvothermally or electrophoretically).

## C2. Preparation of MOF nanoparticles and films.

**Substrate preparation.** A 5 K $\Omega$  QCM polished gold coated, AT-cut quartz crystals (Maxtek Inc., CA) were immersed in a cleaning solution (1:1:5 v/v NH<sub>4</sub>OH (28–30 wt % in H<sub>2</sub>O):H<sub>2</sub>O<sub>2</sub> (30 wt % in H<sub>2</sub>O):H<sub>2</sub>O (distilled ultrapure)) at 75 °C for 5 min, then rinsed with distilled water, and dried under a flow of nitrogen. The gold-coated crystals (resonators) were preheated at 80 °C for 2 h and then allowed to cool down in a dry box until further use. Prior to thin film growth or EPD, the initial resonance frequencies of the resonators were recorded.

**Solvothermal ZIF-8 thin film preparation.**<sup>193</sup> Pre-cleaned QCM resonators were individually dipped in methanol and stacked upright into a Thermo Scientific™ vertical slide staining rack (Catalogue # 143, Thermofisher scientific, Waltham, MA) with two resonators placed back-to-back to prevent ZIF-8 growth on the reverse side (*i.e.*, the contact electrode) of the crystal (Figure B1). The tray was then immersed into a zinc nitrate hexahydrate solution in methanol (100 mL of 12.5 nM Zn(NO<sub>3</sub>)<sub>2</sub>·6H<sub>2</sub>O). This solution was rapidly combined with a 2-methylimidazole solution in methanol (100 mL of 25 nM) and allowed to sit for 30 min at room temperature. The tray was then removed from the solution and dipped in methanol to remove excess linker and metal precursors from the sensors. (For additional growth cycles, the tray containing the resonators can be immersed into a fresh solution of Zn(NO<sub>3</sub>)<sub>2</sub>·6H<sub>2</sub>O in methanol first then 2-methylimidazole in methanol second and then after 30 min, immersed into pure methanol again). After ZIF-8 thin film growth, resonators were removed from the tray, immersed in methanol, and dried under N<sub>2</sub> flow. Synthesis-solvent evacuation (“MOF activation”) was carried out by heating the ZIF-8 films at 100 °C for 2 h in a vacuum oven. The activated samples were then allowed to cool to room temperature, transferred to their original plastic cases, and stored in a drybox until further use.

**Synthesis of ZIF-8 nanoparticles (~140 nm).** ZIF-8 nanoparticles were synthesized via a modified literature procedure.<sup>254</sup>  $\text{Zn}(\text{NO}_3)_2 \cdot 6\text{H}_2\text{O}$  (3 g, 9.8 mmol) was dissolved in methanol (200 mL) and the mixture was combined with a solution of 2-methylimidazole (6.45 g, 79 mmol) in methanol (200 mL). The resulting mixture was then stirred vigorously at room temperature for 1 h. The milky white solid was then isolated via centrifugation and rinsed with methanol ( $3 \times 30$  mL) and dried for ~12 h at 40 °C overnight. Portions of this solid were activated at 100 °C under high vacuum as needed prior to adsorption studies.

**Electrophoretic deposition (EPD) of ZIF-8 nanoparticles.** Activated (*i.e.*, solvent evacuated) ZIF-8 nanoparticles (~12 mg; ~ 140 nm diameter crystallites) were suspended in toluene (30 mL) via sonication for at least 30 s. A precleaned, gold-coated quartz crystal (Maxtek Inc., CA) and a fluorine-doped tin oxide (FTO) glass electrode (15  $\Omega$ /sq, Hartford Glass), separated by 1 cm, were immersed in the suspension and a fixed DC voltage of 90 V was applied using an Agilent (Santa Clara, CA) E3 612A DC power supply. (Toluene ( $K_D = 6.1$ ) is sterically excluded from the interior of pristine and solvent-evacuated ZIF-8,<sup>209</sup> provided exposure times are hours or less.<sup>255</sup>) **Caution:** *Sparks from accidental contact of electrodes can ignite the toluene solution. Appropriate precautions should be taken, including minimizing the amount of toluene suspension used.* Films were dried in a vacuum oven for at least 12 h at 100 °C before diffusivity measurements. Amounts deposited were determined from measured changes in quartz crystal oscillation frequency.

**Post-deposition substrate recovery.** ZIF-8 films were removed from gold-coated crystals (*i.e.*, quartz resonators) as follows: 1) treatment with  $\text{O}_2$  plasma (2 h at 190 W and 10-15 mTorr  $\text{O}_2$ ) in a South Bay Technology, Inc. (San Clemente, CA) Model PC-2000 plasma cleaner, 2)

sonication for 40 mins in water, and then 40 mins in methanol or ethanol, and 3) placement in a preheated oven (80 °C) for 2 h. The cleaned resonators were allowed to cool down in a controlled-atmosphere glovebox, where they were kept until needed. Crystals that were visibly damaged or have an erratic or excessive resistance ( $R > 1,000 \Omega$ ) were deemed unusable and disposed.

**Guest-uptake measurements.** ZIF-8 thin films on gold-coated quartz crystals were mounted on a polypropylene holder and then allowed to equilibrate in a glass jar with a custom fitted cap for 30 min. After the system reached equilibrium, 1 mL of a linear alkane was pipetted into the jar through a resealable hole in the cap (referred to as the *direct-addition (DA) method*, Figure C2b) to provide the saturated pressure of the alkane during thin film kinetic adsorption monitored by a research quartz crystal microbalance at room temperature. Alternatively, for larger alkanes ( $C_{12}$ ,  $C_{16}$ ) that are slow to volatilize, 1 mL of the liquid alkane was first added to a jar and left for at least 30 minutes. A ZIF-8-coated resonator was then quickly transferred to the jar and sealed in place, with measurements of guest-uptake then being initiated. (See Figure C2c for a more detailed description of the *chamber exchange (CE) method*.)

**Analyses of uptake kinetics.**<sup>256-257</sup> For closely packed, resonator-supported films of a MOF material possessing a comparatively high-symmetry sodalite topology, a reasonable starting point for analyzing the kinetics of uptake of molecular guests is to assume that one-dimensional diffusion in the direction normal to the resonator (*i.e.*, normal to the vapor/film interface) is rate-limiting (Figure 4.3a). With this assumption, transport diffusion constants,  $D$ , can be obtained by fitting curves of hydrocarbon uptake (resonator mass loading (oscillation frequency decrease)) versus time – an approach previously used by Wöll and co-workers.<sup>179-180</sup> Following Wöll, we employed MATLAB (Mathworks) software, to fit uptake curves. The ‘fminbind’ minimization

routine determines a value for the variable that minimizes the value of a single-variable function on the user-defined interval. We used the routine to find the value of  $D$  that minimizes the root mean square (RMS) error (Equation C1) between the experimentally observed uptake and the uptake predicted by Equation C2 (a function that describes 1D diffusion through a supported planar film of uniform thickness):

$$RMS\ Error = \sqrt{\frac{\sum(M(t)/M_{\infty} - f(t))^2}{m}} \quad (C1)$$

$$f(t) = 1 - \frac{8}{\pi^2} \sum_{n=1}^{\infty} \frac{1}{(2n+1)^2} \exp\left[-\frac{D(2n+1)^2\pi^2 t}{l^2}\right] \quad (C2)$$

In the equations,  $M(t)$  is the uptake ( $\mu\text{g}$ ) at time  $t$  in seconds,  $M_{\infty}$  is the uptake ( $\mu\text{g}$ ) at infinite time (*i.e.*, equilibrium),  $f(t)$  is the fractional uptake,  $D$  has units of  $\text{m}^2/\text{s}$  to be fitted, and  $l$  is the film thickness. For the sum in Equation C2, fits to between 10 and 20 terms,  $n$ , proved sufficient to return essentially constant values for  $D$ . See Section C4 below for further discussion on the reproducibility and reliability of the values for  $D$ .

For low-density films consisting of loosely packed or aggregated ZIF-8 crystallites (*e.g.*, EPD formed films), treatment of guest-uptake as a one-dimensional diffusion process is likely inaccurate, as the guest, in vapor form, can readily occupy the void spaces between crystallites – and thus, permeate the crystallites from multiple directions. Note that the comparatively high symmetry of ZIF-8's sodalite topology yields apertures along the  $a$ ,  $b$ , and  $c$  crystallographic directions. As such, we employed a second model that idealizes the MOF crystallites as spheres and assumes that intracrystalline guest transport can be approximated as radial diffusion toward the crystallite center.<sup>162</sup> The fitting procedure is similar to that used for closely-packed, solvothermally grown films, but with the predicted fractional uptake at a given time,  $f(t)$ , given by

$$f(t) = 1 - \frac{6}{\pi^2} \sum_{n=1}^{\infty} \frac{1}{n^2} \exp \left[ \frac{-Dn^2\pi^2 t}{r^2} \right] \quad (\text{C3})$$

where  $r$  is the radius of the ZIF-8 crystallite.

### C3. QCM measurement experiment set up.

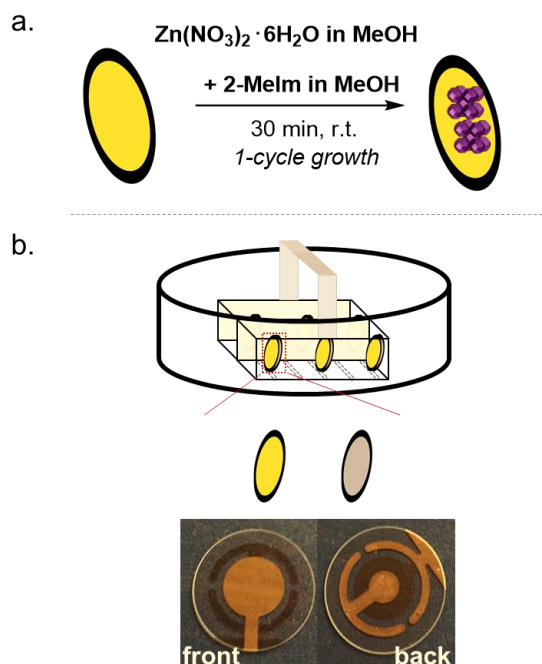


**Figure C1** (a) An illustrative schematic showing the solvothermal ZIF-8 thin film synthesis and growth onto the gold coated QCM sensors. (b) Arrangement of pre-cleaned QCM sensors into a vertical slide staining rack filled with a solution containing  $\text{Zn}(\text{NO}_3)_2 \cdot 6\text{H}_2\text{O}$  and 2-MeIm. 12–24 sensors can be placed into this tray with two sensors placed back-to-back in one slot to prevent ZIF-8 growth on the back side (i.e., contact electrode). For high reproducibility, the QCM sensors should be placed in the same arrangement from batch to batch as increasing or decreasing the amount of sensors placed in the tray can lead to slight deviations in the ZIF-8 film thickness (see Figures C3 and C4 below for more discussion).

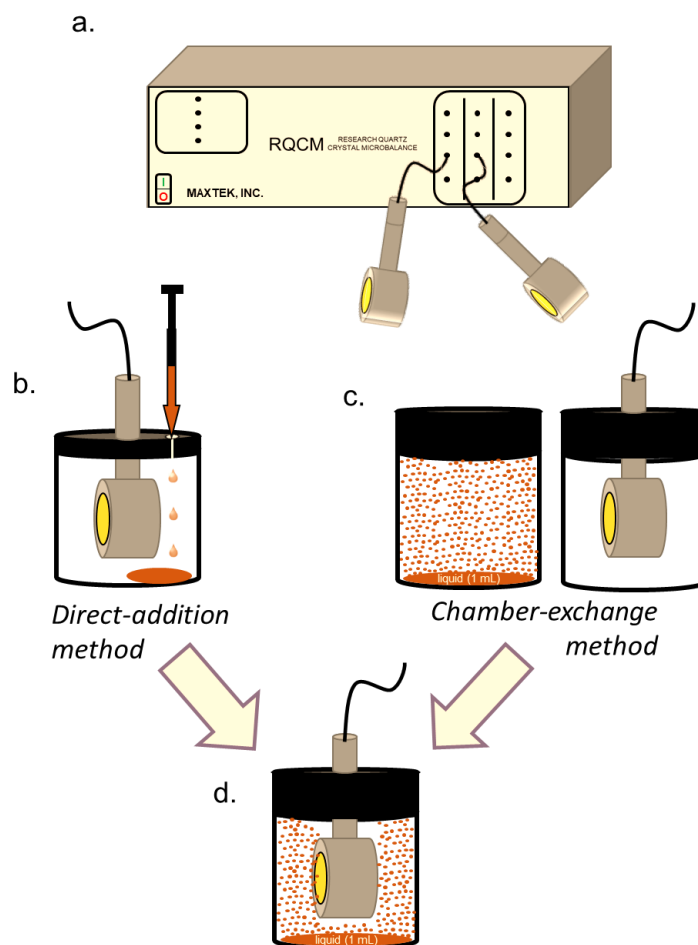


**Figure C2** Diffusivity measurements carried out using a custom made QCM based set-up. (a) RQCM monitor can be readily fitted to the QCM holders. (b) For the *direct-addition method*, the QCM holder can be fitted to a jar with a “sealable hole” on the opposite side of the QCM sensor. Using this hole, ~ 1 mL of analyte can be added quickly using a syringe needle, sealed by tape or with rubber. An alternative method, (c) the *chamber-exchange method*, utilizes two jars, where a second jar containing the analyte is pre-equilibrated for at least 30 min, while the QCM holder is equilibrated in air in the other jar. After 30 minutes, the QCM holder/sensor is then exchanged to the analyte jar exposing the vapor to the sensor as depicted in (d).

#### C4. Film thickness measurements

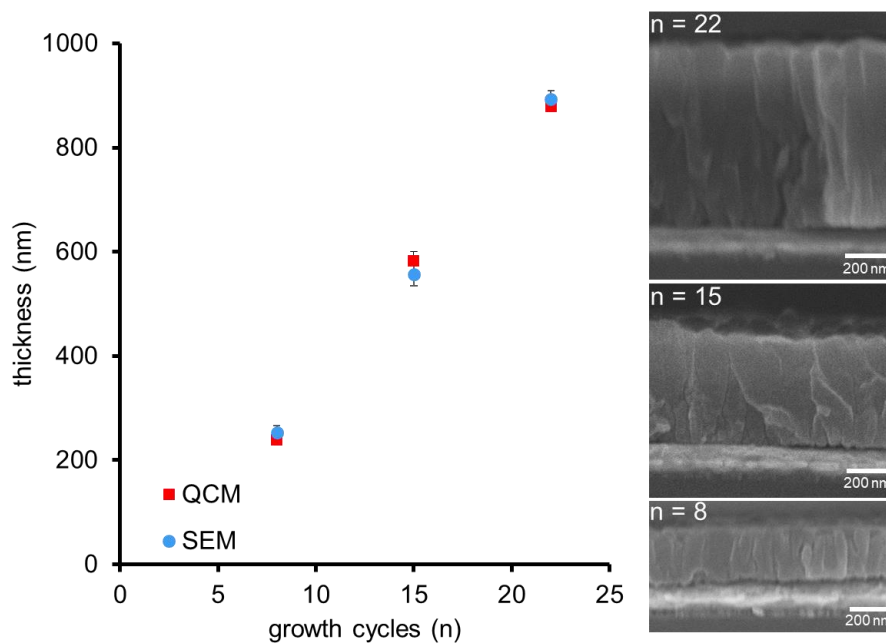


**Figure C3** Film thickness values obtained via QCM, as described in the main text, and by cross-sectional SEM were plotted and show good agreement, thus verifying that the values obtained from QCM for subsequent experiments are representative of the true film thicknesses.



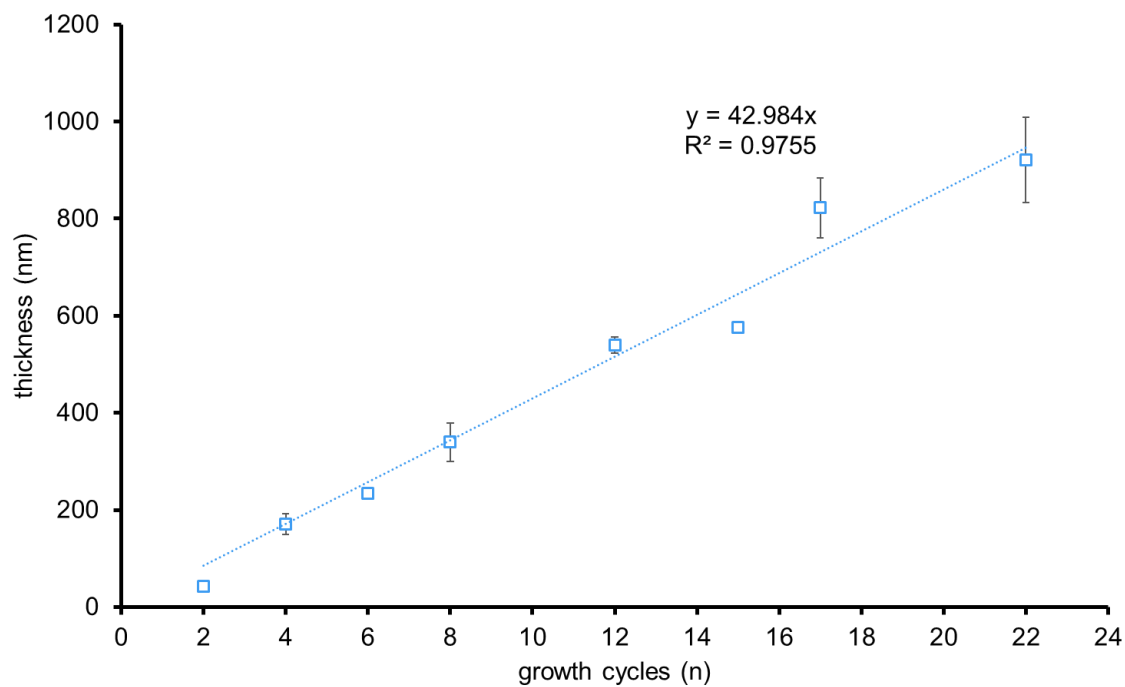


**Figure C4** The combined dataset (including multiple batch runs) of all thin film growth attempts of which the thickness of each film can be controlled by the number of growth cycles (Figure C1a) completed. Each growth cycle on average resulted in an increase in film thickness of *ca.* 43 nm of ZIF-8.

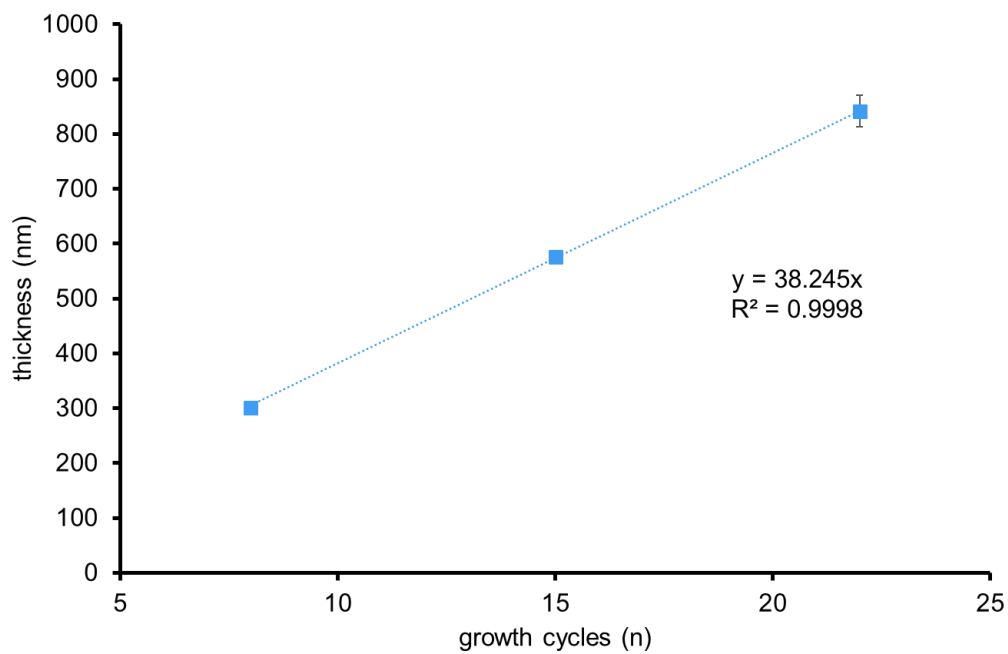


**Figure C5** ZIF-8 thin film growth (one batch) of which some films were isolated from the batch at different cycles. The high linear correlation of this plot demonstrates the high level of control that can be obtained by growing the films solvothermally.

## C5. Reproducibility and reliability in data analyses

To determine the linear alkane diffusivities, we initially obtained the mass uptake time plots using the DA method (Figure C6) with the assumption that the evaporation rate of these analytes was several times faster than the diffusion rates through the films. With this method,  $D$  obtained from fitting the entire time plot were obtained with high reproducibility (Figure C9). However for heavier alkanes ( $> C_{10}$ ) our assumption no longer held as the evaporation rates were much slower, resulting in a distinct *S*-shaped curve (see Figure C7d for representative hexadecane runs). Upon utilizing the CE method, where the vapor for the heavier alkane is given an adequate amount of time to equilibrate in the chamber prior to exposure, the *S*-shaped in the uptake profile was significantly diminished (Figure C7c). Using this method for all alkanes tested also yielded reproducible  $D$  values (Figure C9), similar to those obtained using the DA method – even retaining the same trends. We note that all duplicated runs used for this study were duplicate runs from two different QCM thin films which displayed similar standard deviations to those obtained from recyclability tests (see Figure C12 for representative dataset). From the plot in Figure C9, it is apparent that the diffusivities for pentane and hexane deviate slightly from those obtained through DA method. We suspect that the CE method could be problematic for alkanes with high vapor pressure (as noted in Figure C7ab). Lastly,  $D_{C5-10}$ , calculated from fits to earlier time points were shown to be consistent with  $D$  values determined from full fits. We note that for  $D_{C12,16}$ , can only be reasonably estimated from fits to earlier time points as the diffusion profile of these heavier alkane no longer follow a simple fickian model (possibly due to the high levels of vdW interactions between longer alkyl chains and the pore apertures). We feel confident that our determined values for mass transport diffusivities are reliable as a consistent and reasonable trend was obtained with

high reproducibility regardless of what method was used or how they were calculated (see Figure C9 and C11).

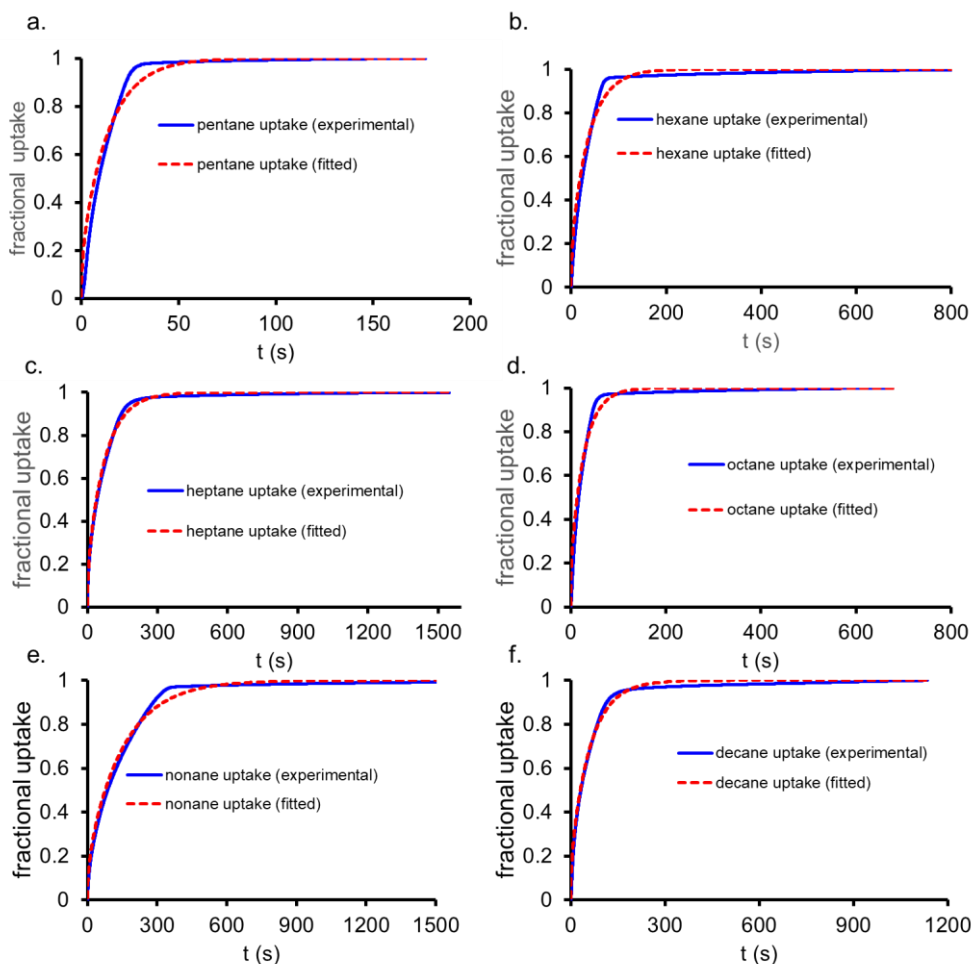


**Figure C6** (a-f) Representative plots and their corresponding fits (to Equation C2, hence called full fits) of linear hydrocarbon diffusion through ZIF-8 thin films as measured with QCM using the DA method (Figure C2b). Fitting the plots to the top-down Fickian model captures the uptake profile for linear alkanes (C<sub>5-10</sub>).

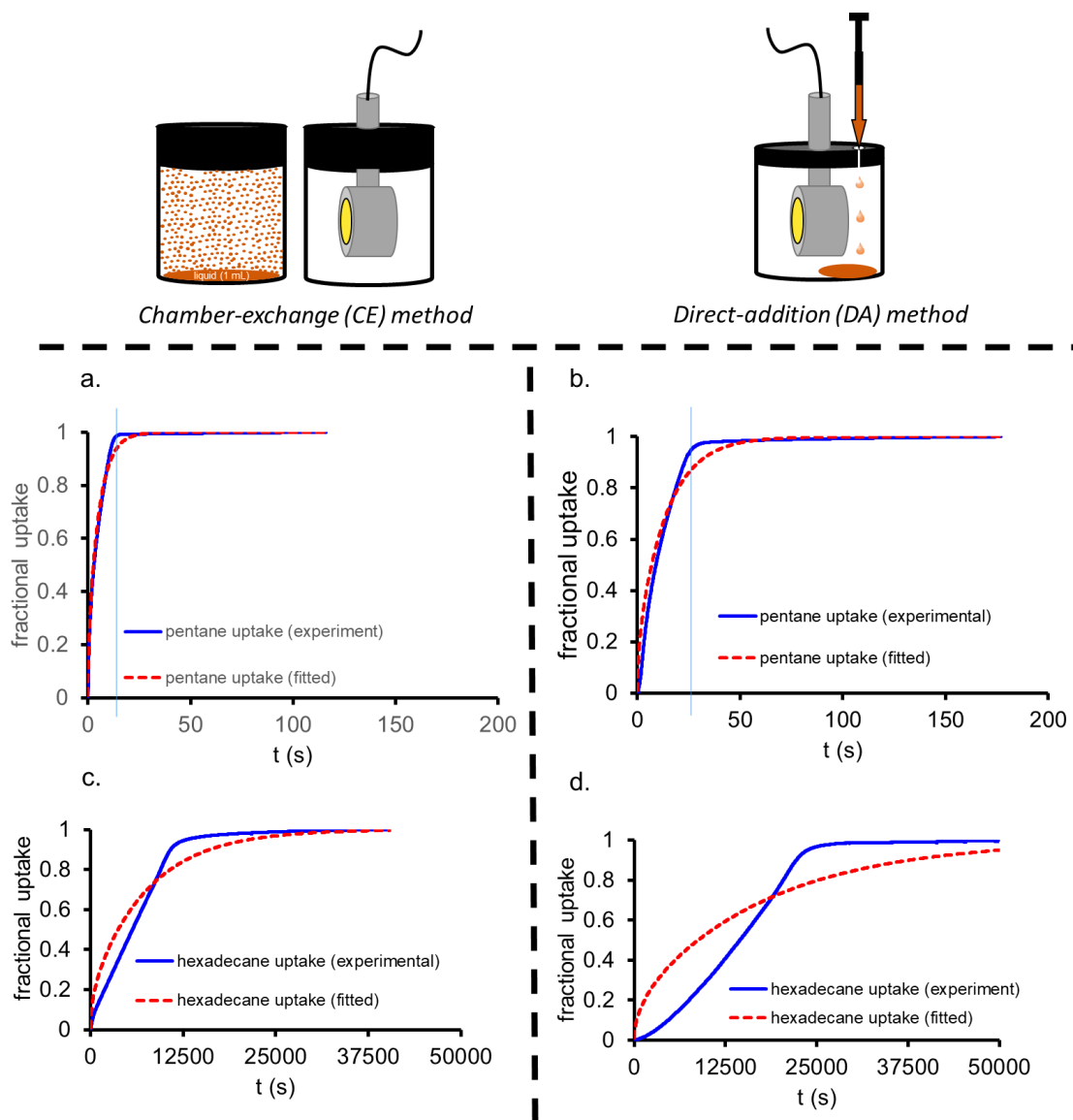


**Figure C7** Comparison between the CE and the DA methods (Figure C2) employed for these studies. Uptake of highly volatile hydrocarbons (e.g.,  $C_{5-6}$ ) are slightly faster in the CE method (a) as opposed to the DA method (b). This could be due to the quick perturbations of the pentane vapor during CE (technique limitation). Hence, we note that DA is better suited for measuring the uptake of smaller hydrocarbons with high vapor pressure. However, in contrast, uptake kinetics of the larger hydrocarbons (e.g.,  $C_{12-16}$ ) through ZIF-8 pores can be measured better using the CE method (c) as opposed to the DA method (d). This is because the DA method relies on very fast evaporation which is problematic for heavier hydrocarbons which causes the inflection in earlier time points  $0 < t \text{ (s)} < 12500$  (d). It is worthy of note that despite the better method, diffusion profiles obtained using the CE method still had poor fits to the simple Fickian model for the entire uptake profile.

As such we surmised that the diffusivities for the heavier alkanes ( $> C_{10}$ ) can be estimated from the earlier stages of adsorption (see Figure C9 below).

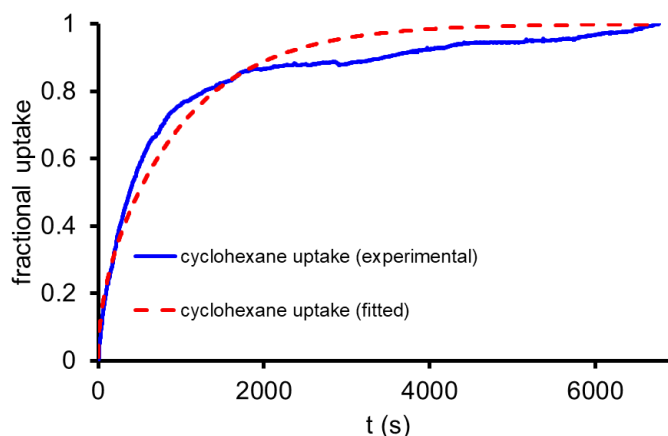


**Figure C8** Plotted fits to cyclohexane uptake (using the DA method) in an  $\sim 300$  nm film over a wider range than shown in Figure 4.3c. From the fits, apparent transport diffusivity was determined to be  $3.5 \times 10^{-17}$  m<sup>2</sup>/s, which we attribute to the filling of the intercrystalline void spaces, given that its large kinetic diameter would sterically hinder it from permeating through the ZIF-8 pores.

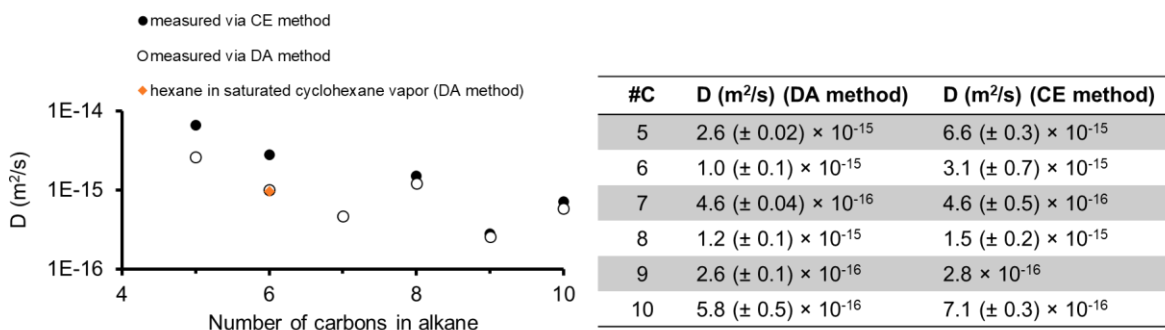


**Figure C9** Combined semi-log plots and table containing both the diffusivities (from full fits) with alkane kinetic time plots obtained using CE and DA method. While the values for pentane and hexane are different for both methods, there seems to be a strong correlation from heptane to decane. In all cases, the longer the alkyl chain the smaller the diffusivity which is expected as van der Waals interaction with ZIF-8 pore increases. The observed trends (i.e., decrease in  $D$ , zig-zag pattern for  $C_7$ - $C_{10}$ ) are visible in both methods indicating a possible odd-even effect as delineated in Figure 4.4c, Chapter 4. Representative standard deviations for each alkane

diffusivity were determined from duplicate runs on different ~300 nm films per each method used.

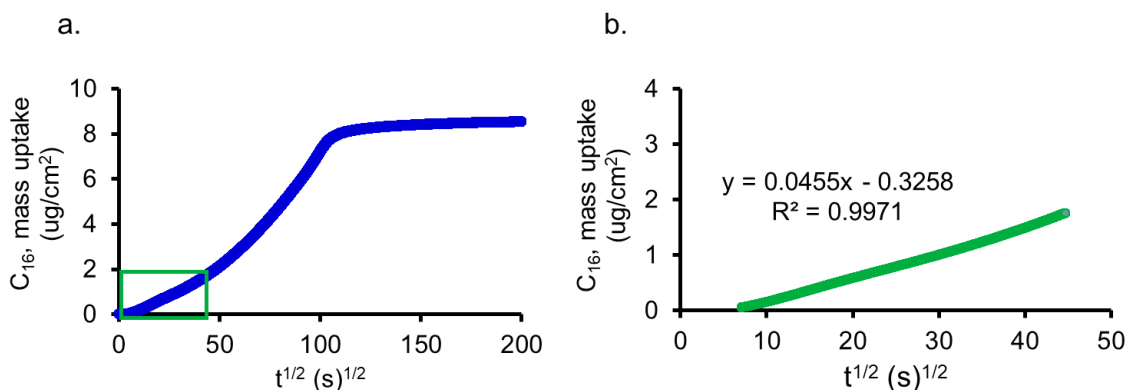


**Figure C10** (a-b) Representative hexadecane plot analysis showing how diffusivity was estimated for the heavier alkanes ( $>C_{10}$ ) by first plotting the mass uptake vs the sqrt(time) (a) and fitting the slope of the early stages of diffusion (green box in (a)) to Equation 4.3.

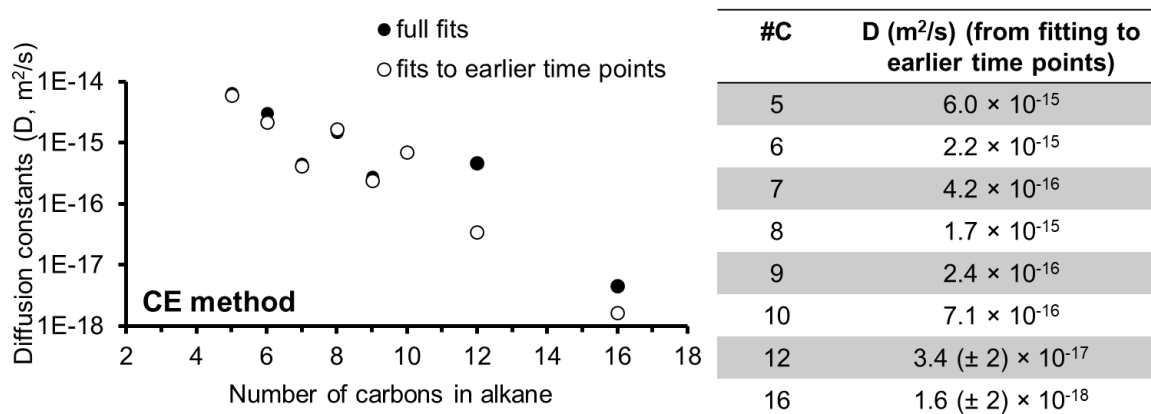


**Figure C11** Comparison between diffusivities obtained from full fits vs. those fitted to earlier time points on a semi-log plot and table. Differences between the regions are marginal for *n*-pentane to *n*-decane but are noticeable for *n*-dodecane and *n*-hexadecane. Values for *D* are shown in the adjacent table. For representative standard deviations (from duplicate runs on different ~ 300 nm films) please see the *D* values for C<sub>6</sub>, C<sub>10</sub>, and C<sub>12</sub> (Figure C13) or from the fits to earlier time points for C<sub>12</sub> and C<sub>16</sub> in the table.

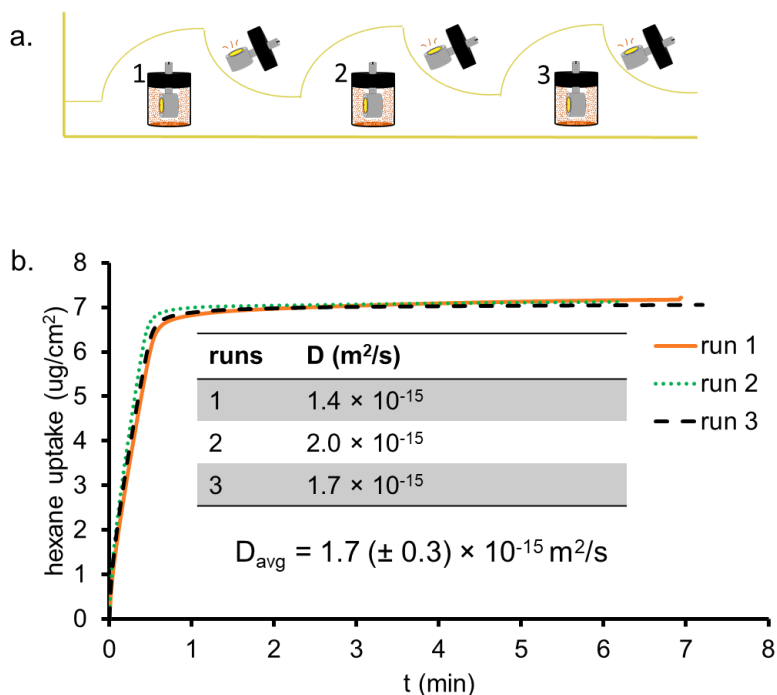


**Figure C12** (a) A schematic of the recyclability experiment showing the diffusion and effusion measurements possible on the ZIF-8 modified-QCM sensors. For each run, the QCM sensor was exposed to the vapor chamber containing hexane and then exposed to air for the hexane to effuse out of the sensors. (b) Plots and statistical data showing reproducibility of the diffusivities obtained

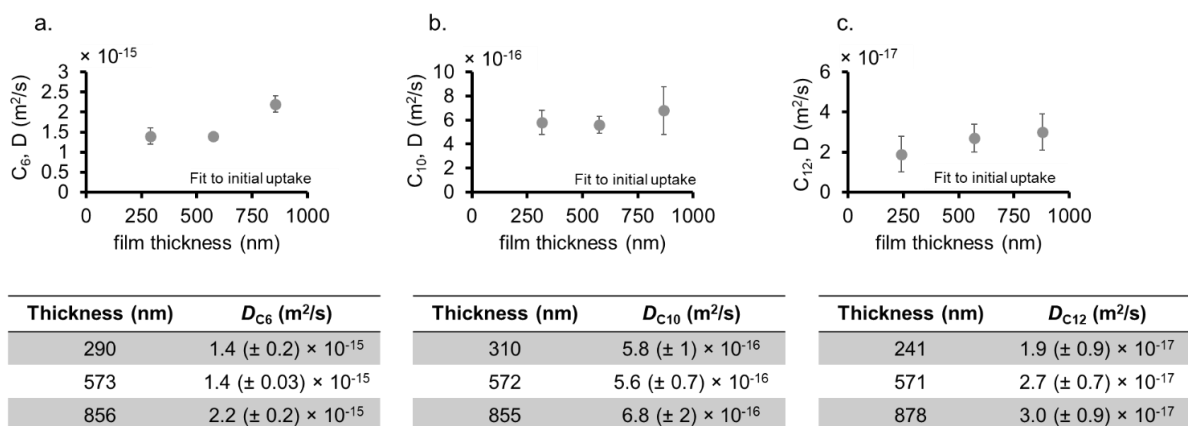


**Figure C13** To verify the validity of the diffusivities obtained, we obtained these diffusion coefficients on films with different film thicknesses and plotted on a semi-log plot



for hexane (a), decane (b), and dodecane (c). As expected, we do not see a dependence on thickness at least for cases where fits to the initial uptake stages (orange dots) were done. If transport were controlled by rate of crossing vapor/MOF interface (but analyzed as diffusivities following Equation 4.3 in Chapter 4) then one should see an  $\sim 12$  fold increase in values for  $D$ . It is worthy of note that fits to full uptake for hexane (a) and decane (b) can be used as good estimates for the true diffusivities around  $\sim 300$  nm, where they overlap with the  $D$  determined from earlier time points. When fit to full uptake plots, it is apparent that the diffusivities drastically increases with film thickness.

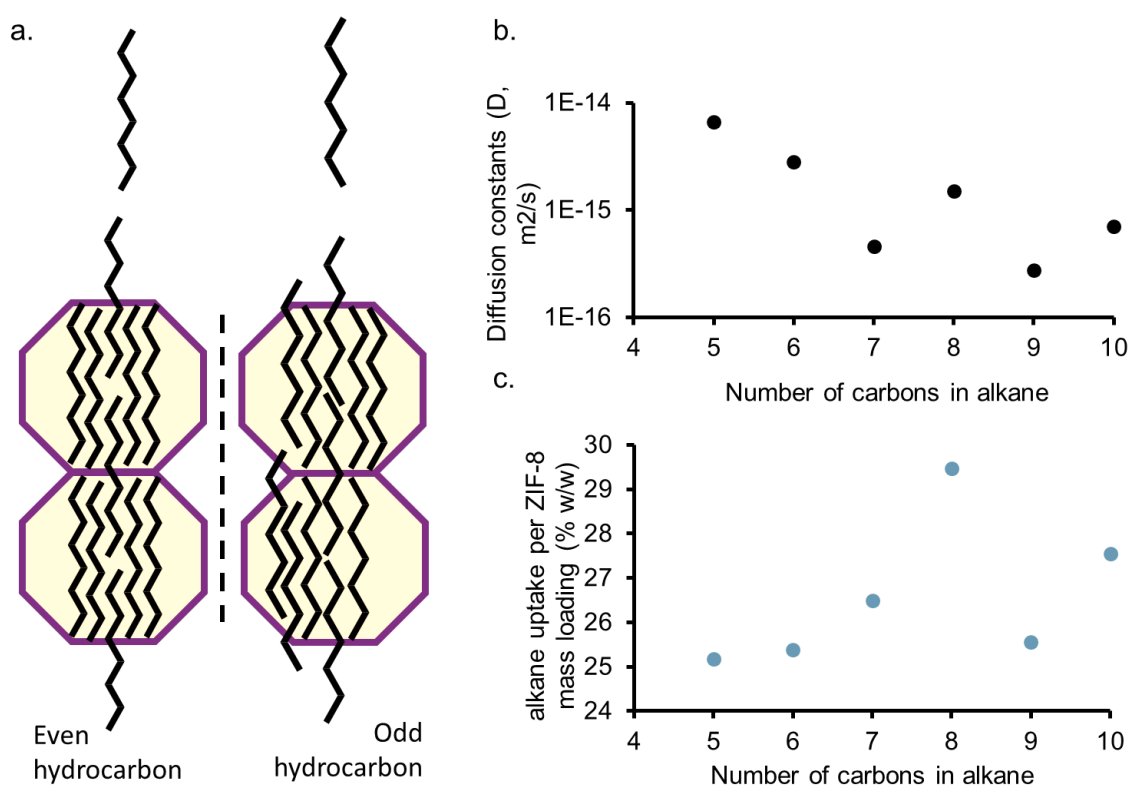


**Figure C14** Assuming that only one linear hydrocarbon ( $K_d = 4.3 \text{ \AA}$ ) can pass through the small pore apertures of ZIF-8 ( $\sim 3.4 \text{ \AA}$ ) at a time, then it is conceivable that single-line confinement<sup>158</sup> in addition to pore filling is a possible diffusion mechanism. As such, it is possible that (a) *even* hydrocarbons can stack closer inside the pores of the ZIF-8 pore under saturated vapor conditions as opposed to the *odd*-hydrocarbons which preferentially stack in one direction of the linear molecule to be closely packed. This packing phenomenon, which is known to cause a similar zig-zag trend in the boiling point trends of these *n*-alkanes and also in the case of charge transport across different length *n*-alkanethiolate based SAMs,<sup>258</sup> could account for the observed zig-zag pattern observed for heptane to decane both in

perspective of the diffusivities shown on the semi-log plot (b) and the % condensed mass loadings/uptake (c) of the alkanes in the pores of the MOF.

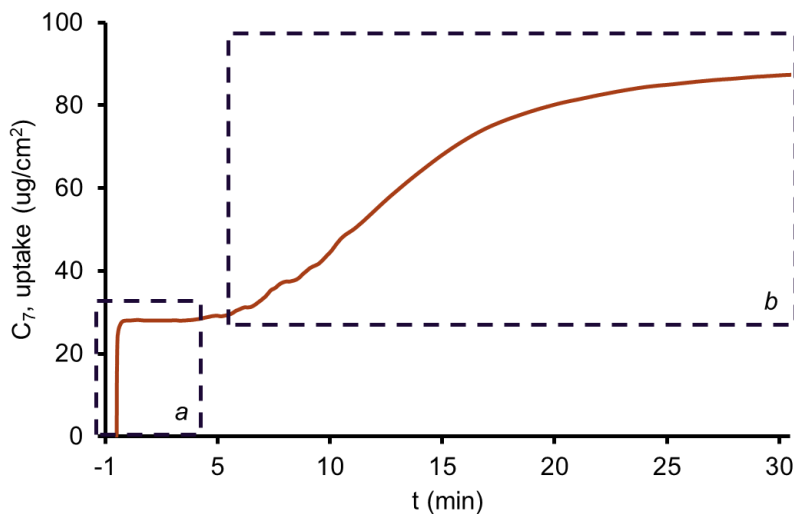


**Figure C15** Diffusion of heptane through EPD film. The first step (boxed section *a*) plateaus near the expected capacities which were determined by correlating the maximum capacity per unit cell ( $\sim 38$   $-\text{CH}_2-$  per UC)<sup>191</sup> to the mass deposited onto the film. Data fits to this first step were then used to obtain intracrystalline diffusivities (Figure 4.5e). The remaining of the uptake profile (boxed section *b*) is a result of the condensation of heptane within the numerous interparticle spaces or voids on the EPD film.

## C6. Theoretical capacity calculations

Alkane theoretical capacity in ZIF-8 was estimated around  $\sim 40$  C/unit cell<sup>191</sup>, which for hexane, translates to  $> 6$  molecules per unit cell. Given a 300 nm solvothermally grown film, and assuming a range of 6-8 molecules of hexane per unit cell, we can estimate a range of the theoretical mass loading ( $\Delta m_T$ ) in  $\mu\text{g}/\text{cm}^2$  expected from the QCM trace as follows:

$$\Delta m_T = \frac{nT(MM_{hex})}{N_A(AA_{QCM})} \quad (C4)$$

Where  $n$  = hexane molecule/unit cell,  $T$  = total number of units cells (UC dimension = 1.7 nm)<sup>191</sup> for a given ZIF-8 film length (300 nm),  $MM_{hex}$  = molecular mass of hexane ( $\mu\text{g}/\text{mol}$ ),  $N_A$  = Avogadro's constant,  $AA_{qcm}$  = active area of the QCM electrode ( $0.3419 \text{ cm}^2$ ) as given in the QCM manual for a 5 MHz sensor. Hence for a lower limit of 6 molecules of hexane/unit cell, we obtain a  $\Delta m_T = 5.24 \mu\text{g}/\text{cm}^2$ , and for the upper limit of 8 molecules of hexane/unit cell, we obtain  $\Delta m_T = 6.99 \mu\text{g}/\text{cm}^2$ .

## Appendix D Supplementary to Chapter 5

Audu, C. O.; Atilgan, A.; Palmer, R.; Howarth, A.; Nguyen, S. T.; Farha, O. K.; Hupp, J. T.

### D1. Project Overview

As shown in Chapter 4, the observed diffusivities of the linear alkanes passing through the hydrophobic ZIF-8 pores decreased with increasing carbon chain length – an attribute to the increasing van der Waals (vdW) interactions. Thus it is possible that a given long linear alkane (e.g.,  $\geq C_{12}$ ) could have high vdW interactions with a ZIF-8 pore and display a binding strength similar to a coordinative bond (for instance a  $\sim 5$  KJ/mol per carbon would give a  $C_{18}$  a 90 KJ/mol, similar to a Cu-N bond strength<sup>259</sup>). If so, it is plausible that an alkyl-containing substrate (where substrate diameter > pore diameter) could be sequestered simply with vdW interactions. Thus we set out to demonstrate that the external surfaces of ZIF-8 can be non-covalently functionalized using alkyl-anchored substrates (Figure D1).

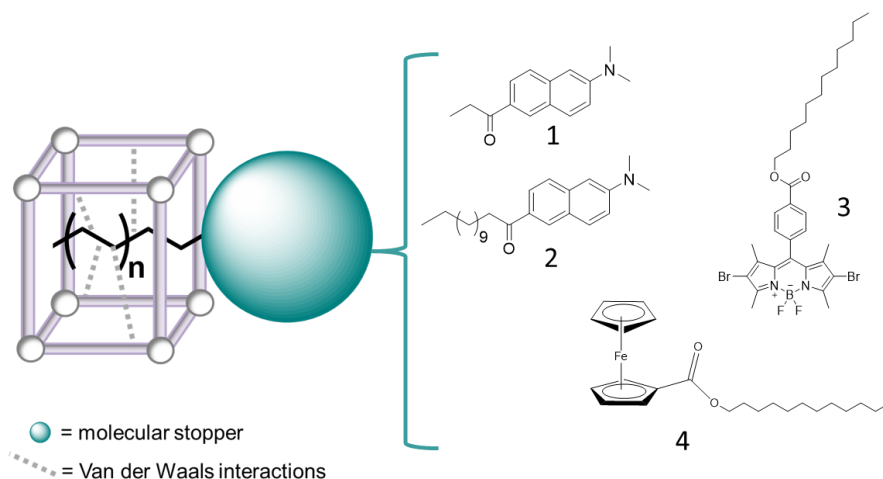


**Figure D1** A schematic illustration of alkyl-anchoring MOFs (AAMOFs) in which the identity of the molecular stopper renders additional sensing (Structures 1,2,4) or catalytic (Structure 3) properties to the MOF.

## D2. Materials and method

Unless otherwise stated, all reagents, including dyes, were acquired from commercial sources and used without further purification. Ultrapure deionized water (18.2 M $\Omega$  cm resistivity) was obtained from a Millipore system (EMD Millipore, Billerica, MA). As seen in Figure D1, N,N-Dimethyl-6-propionyl-2-naphthylamine (Structure 1) and 6-Dodecanoyl-2-dimethylaminonaphthalene (Structure 2) were purchased from Sigma Aldrich (St. Louis, MO). The BODIPY ester (Structure 3) was prepared by A. A using commercially available reagents and an adapted procedure from earlier work.<sup>260</sup> The Ferrocenyl ester (Structure 4) was prepared by R. P. following an adapted procedure from earlier work.<sup>261</sup>

Centrifugation was carried out in an Eppendorf Centrifuge 5804 R, Model AG 22331 (Eppendorf AG, Hamburg, Germany) equipped with an F34-6-68 rotor. Unless otherwise stated, all centrifugations were carried out at 5000 rpm (3214 g) for 10–30 min.

Scanning electron microscopy (SEM) images were obtained at Northwestern University's EPIC-NUANCE facility on a SU8030 FE-SEM (Hitachi High Technologies America, Inc., Dallas, TX) microscope with an acceleration voltage of 10 kV. Prior to imaging, activated MOF samples were coated with either a film of Au/Pd or Os (~10–20 nm thickness) using either a Denton Desk III TSC Sputter Coater (Denton Vacuum, Moorestown, NJ) or a Filgen Osmium Coater Model OPC-60A (Filgen, Nagoya, Japan), respectively.

Powder X-ray diffraction (PXRD) patterns were recorded on a Rigaku X-ray Diffractometer Model ATX-G (Rigaku Americas, The Woodlands, TX) equipped with an 18 kW Cu rotating anode, an MLO monochromator, and a high-count-rate scintillation detector.

Measurements were made over the range  $2^\circ < 2\theta < 40^\circ$  in  $0.05^\circ$  step width with a  $2^\circ/\text{min}$  scanning speed.

Inductively coupled plasma optical emission spectroscopy (ICP-OES) analyses of Zn, Co, and Fe were conducted on a Thermo Scientific™ iCAP™ 7600 ICP-OES spectrometer (Thermo Fisher Scientific Inc., Waltham, MA) located in the QBIC facility of Northwestern University. This instrument is equipped with a high performance solid-state CID86 chip detector, dual view (radial and axial) capability, and an argon plasma to cover the 166-to-847 nm spectral range. In a typical procedure, MOF samples (2-5 mg) were digested in a small amount (1 mL) of a mixture of 3:1 v/v conc.  $\text{HNO}_3:\text{H}_2\text{O}_2$  (30 wt % in  $\text{H}_2\text{O}$ ) by heating in a Biotage SPX microwave reactor (Biotage, Uppsala, Sweden, software version 2.3, build 6250) at  $180^\circ\text{C}$  until the solution became clear (~30 min). This acidic solution was then diluted to 25 mL with ultrapure deionized  $\text{H}_2\text{O}$  and analyzed for the metal content as compared to standard solutions.

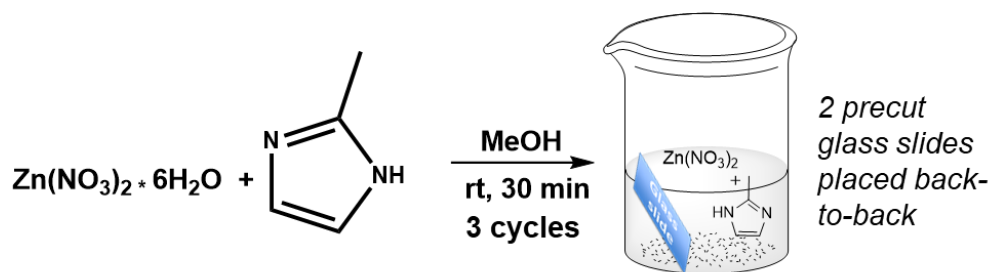
### D3. Preparation of ZIF-8 nanoparticles and thin films

**Substrate preparation.** ColorFrost disposable microscope glass slides (Catalog No. 12-550-423, Fisher Scientific Inc., Waltham, MA) were cut into smaller strips ( $4.5 \times 2.5$  cm) using a diamond-tip pen. The glass strips were then immersed in a piranha solution (3:1 v/v Conc.  $\text{H}_2\text{SO}_4:\text{H}_2\text{O}_2$  (30 wt % in  $\text{H}_2\text{O}$ )) at  $70^\circ\text{C}$  for 30 min, then rinsed with distilled water, and dried under a flow of nitrogen. With the diamond-tip pen, an “X” and a middle-line were etched onto the side of the glass strip where no ZIF-8 will be deposited.

**Synthesis of ZIF-8 nanoparticles (~70 nm).** ZIF-8 nanoparticles were synthesized via a modified literature procedure.<sup>254</sup>  $\text{Zn}(\text{NO}_3)_2 \cdot 6\text{H}_2\text{O}$  (3 g, 9.8 mmol) was dissolved in methanol (200

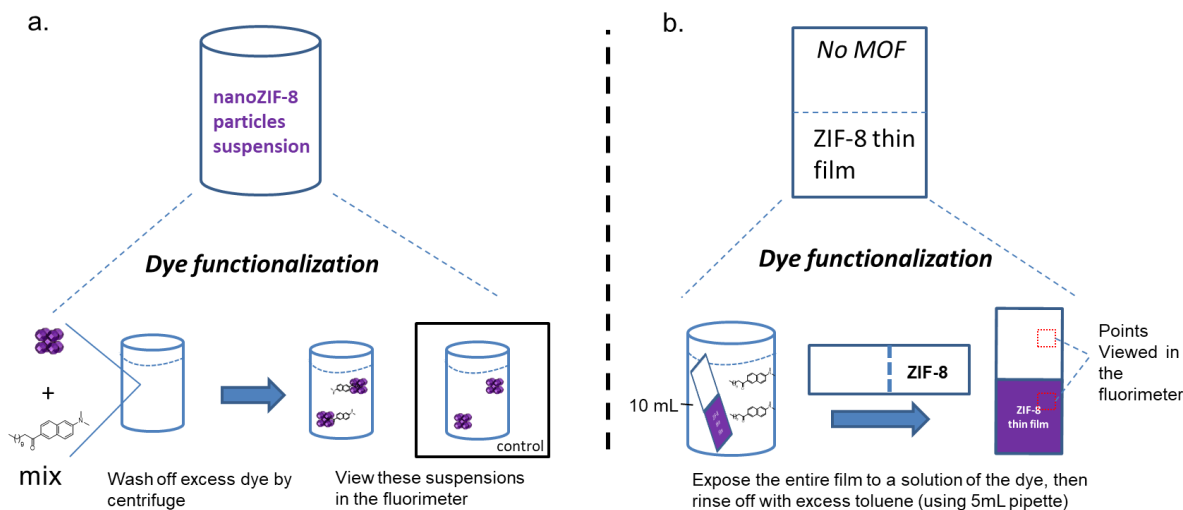
mL) and the mixture was combined with a solution of 2-methylimidazole (6.45 g, 79 mmol) in methanol (200 mL). The resulting mixture was then stirred vigorously at room temperature for 1 h. The milky white solid was then isolated via centrifugation and rinsed with methanol ( $3 \times 30$  mL) and dried for ~12 h at 40 °C overnight. Portions of this solid were activated at 100 °C under high vacuum as needed prior to adsorption studies.

**Thin film preparation.**<sup>193</sup> Pre-cleaned glass strips were individually dipped in methanol and placed upright into a scintillation vial with two strips placed back-to-back to prevent ZIF-8 growth on the reverse side (*i.e.*, the etched side). To each scintillation vial was added zinc nitrate hexahydrate solution in methanol (5 mL of 12.5 nM  $\text{Zn}(\text{NO}_3)_2 \cdot 6\text{H}_2\text{O}$ ) and, subsequently, 2-methylimidazole solution in methanol (5 mL of 25 nM) using a 5-mL pipettor. The mixture was then allowed to sit for 30 min at room temperature. The glass strips was then removed from the solution and dipped in methanol to remove unreacted linker and metal salt. This completes one cycle of growth. For additional growth cycles, the glass strips can be immersed into a fresh solution of  $\text{Zn}(\text{NO}_3)_2 \cdot 6\text{H}_2\text{O}$  in methanol first, then 2-methylimidazole in methanol second, and allowed to sit for another 30 min before rinsing with pure methanol again. A total of 3 cycles were completed to give a more complete and uniform coverage of half the glass strip (see Figure D2). Synthesis-solvent evacuation (“MOF activation”) was carried out by heating the ZIF-8 films at 100 °C for 2 h in a vacuum oven. The activated samples were then allowed to cool to room temperature, and stored in a dry box until further use.



**Figure D2** Solvothermal synthesis of ZIF-8 thin films as conducted in a scintillation vial.

#### D4. Experimental design

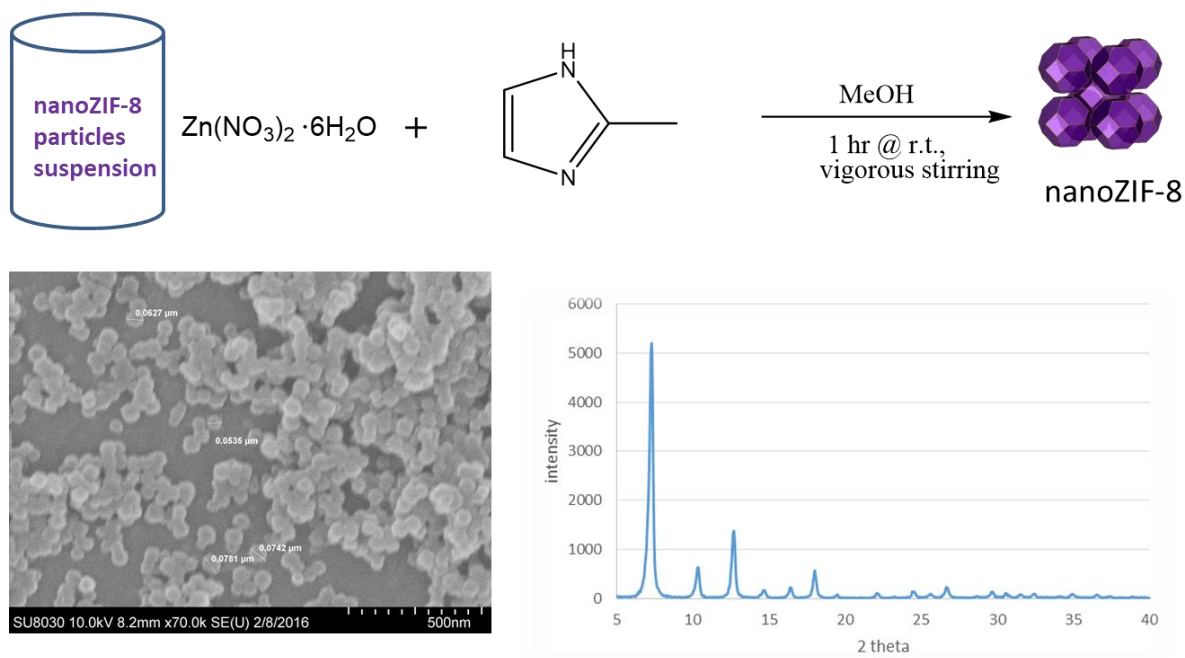


**Figure D3** Dye substrates (Structure 1-2, Figure D1) were exposed to ZIF-8 as a suspension (a) or thin film (b) in a toluene (20 mL, 1.4 nM ZIF-8, 0.2 nM dye). After a 24 h of exposure, the samples were then analyzed by a PTI QuantaMaster 400 fluorometer (Birmingham, NJ).

A proof of concept was demonstrated qualitatively with dyes (Structure 1-2, Figure D1). For the suspension method (Figure D3a), white ZIF-8 nanoparticles (6.4 mg) was suspended in toluene (20 mL) via sonication prior to the addition of the dye – which readily dissolves. The solution was agitated gently for 24 h to keep the suspension from settling and give excess amount of time for functionalization. After exposure, the very light pink solids were collected and washed



copiously with centrifugation ( $\geq 5\times$  with fresh toluene). Each wash can be monitored to see when all residual “untethered” dye have been washed off (see Figure D6 below). The collected wet solids can be analyzed directly on the fluorimeter equipped with a solid phase glass holder. Background scans for the unfunctionalized MOF, glass slides, and solvent were collected as well (Figure D6). The same studies can be completed on a thin film as depicted in the set-up above (Figure D3b). After solvothermal ZIF-8 deposition, half of the glass strips are covered with a ZIF-8 film while the other half is barren. The whole strip was then exposed to the dye solution overnight, washed copiously with fresh toluene ( $5 \times 1$  mL glass pipette squirts) and evaluated by the fluorometer at multiples spots across the entire Strip. As with the suspension set-up, background scans were conducted as well to account for any signal from the solvent and the glass strip itself.

**D5. Preliminary results and discussion**

**Figure D4** Synthesis of ZIF-8 nanoparticles where the embedded SEM image shows the particle sizes of the MOF. The embedded PXRD profile of the crystalline solids is identical to the reported profile for ZIF-8.

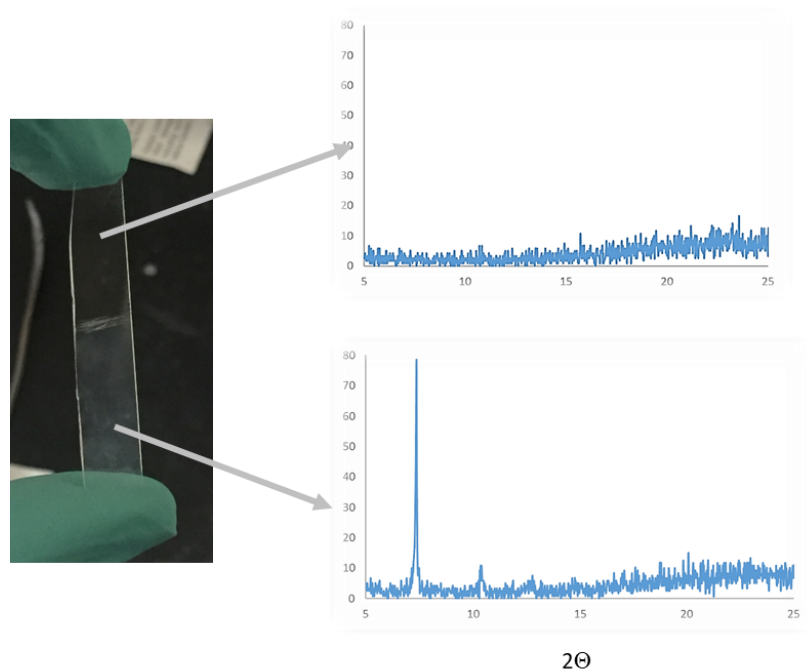


**Figure D5** PXRD scans on the prepared thin films verify the intentionally coated portion is ZIF-8.

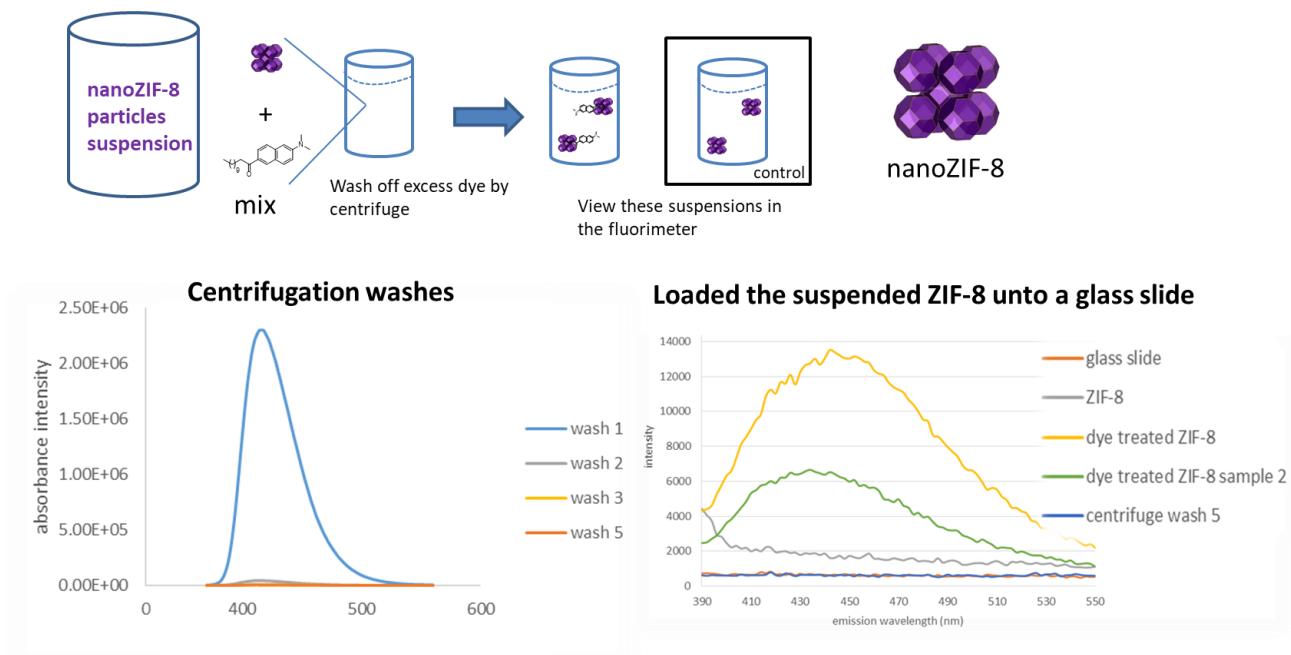


**Figure D6** Fluorescence measurements reveal that after the second washing cycle of the ZIF-8 suspension, all residual “untethered” dye molecules (Structure 2, Figure D1) have been washed off. On the bottom right panel, the high fluorescence signals obtained

are from the surface functionalized ZIF-8 nanoparticles – in comparison to the control scans.

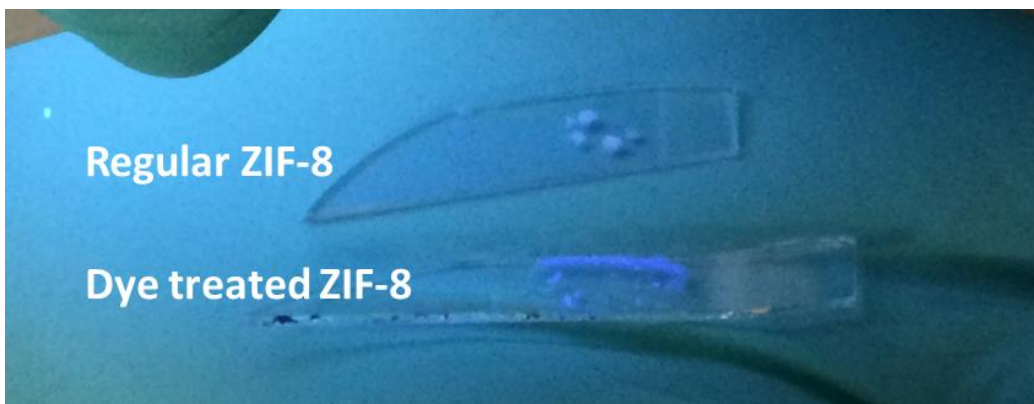


**Figure D7** For visualization, the functionalized ZIF-8 nanoparticles fluoresces when exposed to a 365 UV lamp albeit the distinction is not great (dye emission wavelength = 415 nm).

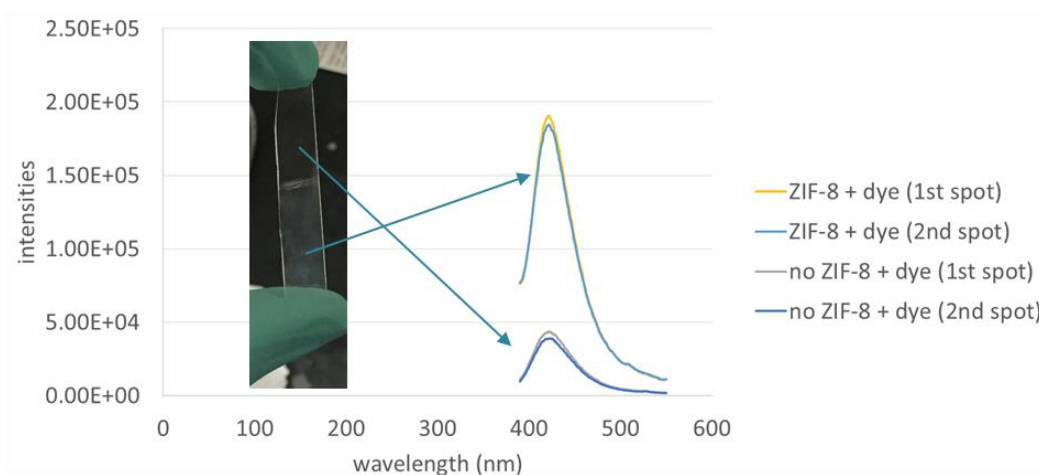


**Figure D8** Fluorescence measurements on the half-coated glass strips (representative trial) showed that the ZIF-8 portion retained the dye molecules more efficiently than the glass surface.

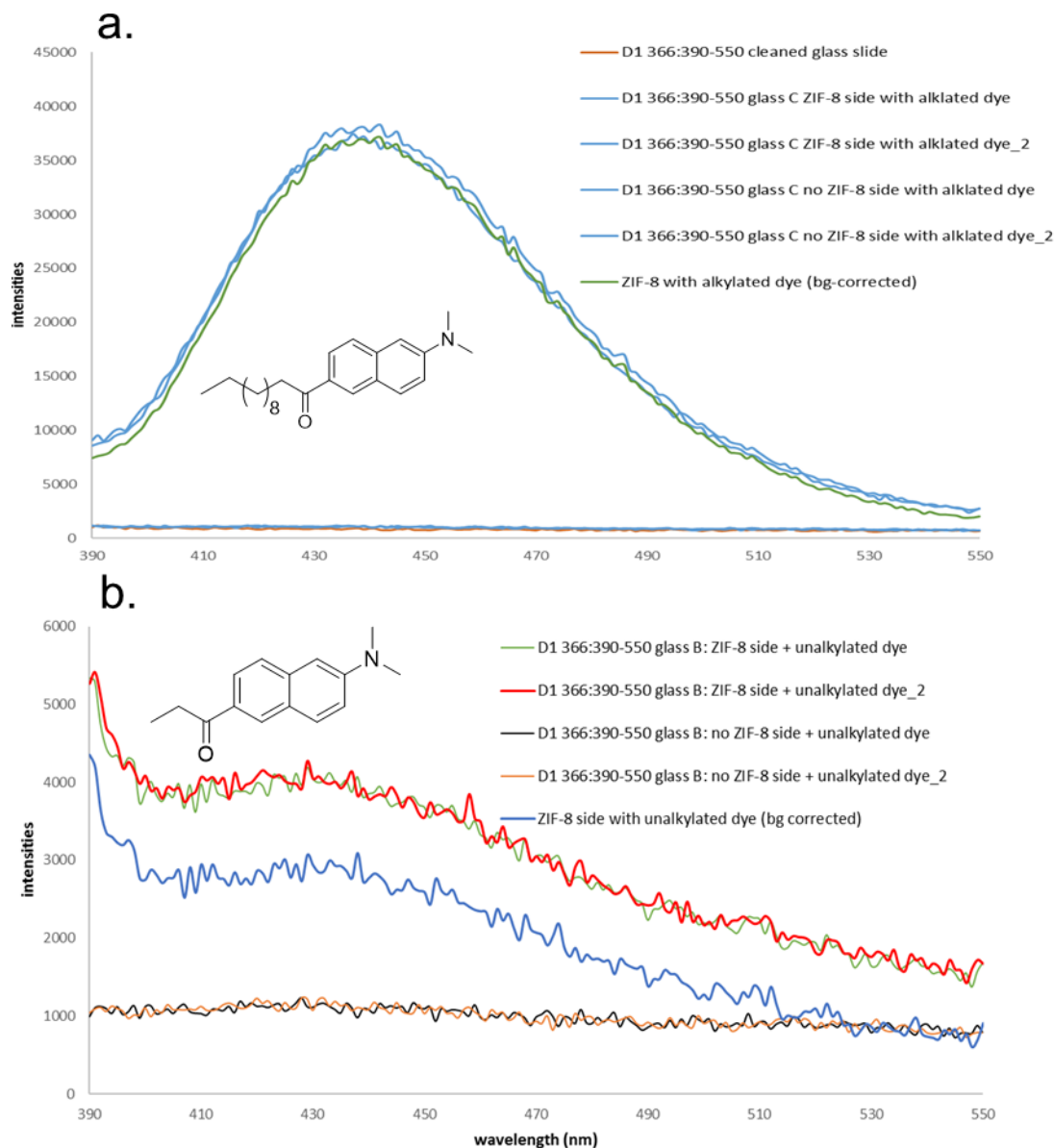


**Figure D9** Fluorescence scans on the dye treated thin films. When the long alkyl chain is present (a), we are able to see high retention on the ZIF-8 surface. When the alkyl chain is much shorter (b), very low retention onto the ZIF-8 surface is observed. This shows that the adhesion to the ZIF-8 surfaces is most likely due to the vdW interactions between the alkyl tail (a) and the pores of ZIF-8.

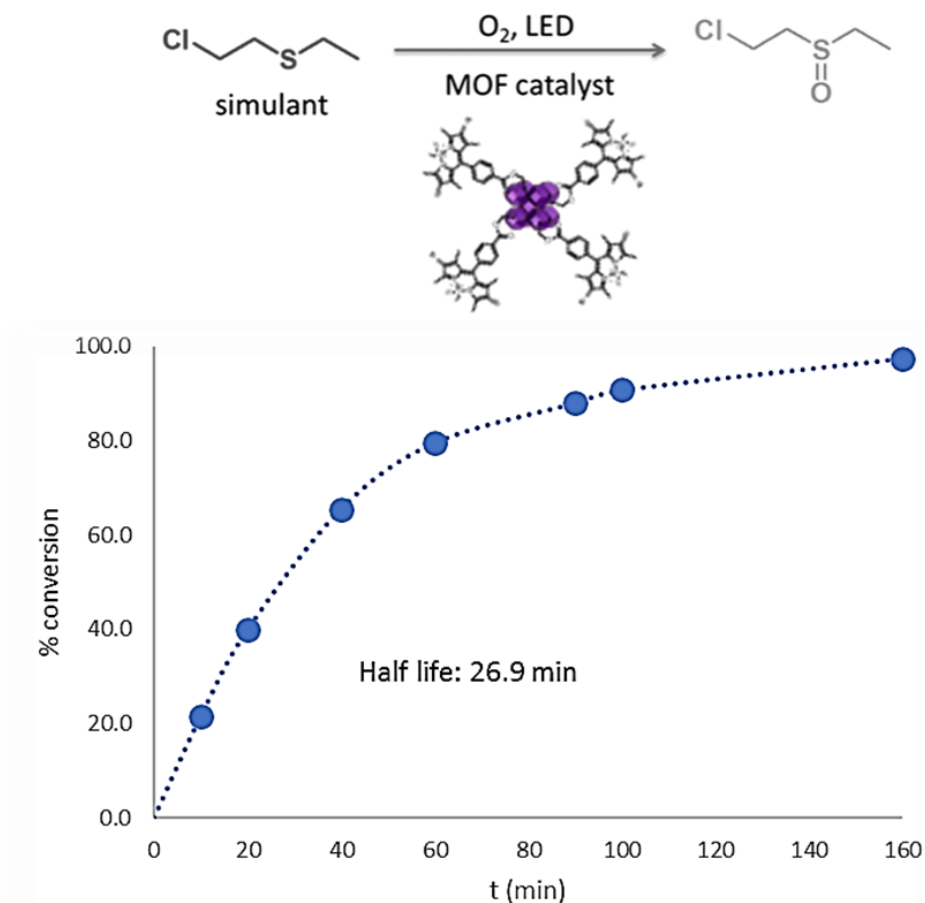


**Figure D10** ZIF-8 nanoparticles were exposed to the BODIPY substrates (Structure 3, Figure D1) and evaluated for catalytic activity. Preliminary work shows that the MOF system is catalytically active towards the photooxidative degradation of a chemical warfare agent (CWA) simulant. However, more controls and leaching experiments will have to be completed before any other conclusions can be made.

Quantification of this systems remains to be completed. Attempts to quantify these surface functionalized ZIF-8 using ICP-OES are ongoing with the ferrocene substrate (Structure 4, Figure D1). Nevertheless the preliminary results show that it is quite possible to non-covalently incorporate additional functionality to a MOF's surface simply using vdW interactions. Future work could entail utilizing this method to install a third active site onto MOFs, leaving the node and linkers free for modifications.

**Appendix E CURRICULUM VITAE****CORNELIUS OKATAHI AUDU**

Place of Birth: Dallas, Texas

**EDUCATION**

Ph.D. in Chemistry  
Northwestern University, Evanston, IL May 2018

- Advisors: Drs. Joseph T. Hupp and SonBinh T. Nguyen
- Thesis Committee: Drs. Omar K. Farha, Franz M. Geiger, Randall Q. Snurr, and Fraser Stoddart (*Nobel Laureate*)
- Thesis: Design and Installation of Sorptive Sites in Metal-Organic Framework Adsorbents

B.S. in Chemistry (minor: math)  
Indiana University-Purdue University Indianapolis (IUPUI) May 2012

- Advisor: Dr. Jingzhi Pu
- Honors senior project: Demonstrated how maltose binding proteins (MBP) recognize substrates using computational simulations

**RESEARCH EXPERIENCE**

Graduate Research, Northwestern University, Evanston, IL 2012-2018

- Advisors: Drs. Joseph T. Hupp and SonBinh T. Nguyen
- Understanding and utilizing structural components of metal-organic frameworks (i.e., metal-node, organic linker, and pore cavities) for preparing adsorbent materials.
- Manager for TGA and RQCM instruments

Undergraduate Research, IUPUI, Indianapolis, IN 2008-2012

- Advisor: Dr. Jingzhi Pu
- Demonstrated how maltose binding proteins (MBP) recognize substrates using computational simulations. Completed at IUPUI, Department of Chemistry and Chemical Biology
- Advisors: Drs. Martin O'Donnell and William Scott

- Synthesized libraries of unnatural amino acids derivatives as potential drug leads using solid-phase combinatorial chemistry. Completed at IUPUI, Department of Chemistry and Chemical Biology with the O'Donnell/Scott Research group
- Advisor: Dr. John Schaus
- Conducted pharmaceutical research under the supervision of John Schaus, PhD, and Joseph Krushinski, MS. where a small library of analogues of a bioactive parent molecule for PET imaging scans was synthesized and submitted them bioassay testing. Completed at Eli Lilly & Co. as a Volt Workforce academic contractor.

## PUBLICATIONS

### In Preparation

1. Audu, C. O.; Liu, M.; Anderson, R. M.; McConnell, M. S.; Malliakas, C. D.; Snurr, R. Q.; Farha, O. K.; Hupp, J. T.; Gualdrón, D. A. G.; Nguyen, S. T. Delineating anomalous pore architectures in common defect-containing derivatives of UiO-66. *Chem. Mater.* **2019**, *in preparation*.
2. Audu, C. O.; Chen, D.; Kung, C. W.; Snurr, R. Q.; Nguyen, S. T.; Farha, O. K.; Hupp, J. T. Transport diffusion of linear alkanes (C<sub>5</sub>-C<sub>16</sub>) through thin films of ZIF-8 as assessed by quartz crystal microgravimetry. *Langmuir.* **2018**, *under revision*.

### Graduate

3. Cui, B., Audu, C. O. (co-first author), Lao, Y., Nguyen, S. T., Farha, O. K, Hupp, J. T., Grayson, M. Thermal conductivity of ZIF-8 thin-film under ambient gas pressure. *ACS Appl. Mater. Interfaces*, **2017**, *9* (34), 28139-28143.
4. Wang, T., Hod, I., Audu, C. O., Vermuelen, N., Nguyen, S. T., Farha, O. K., Hupp, J. T. Rendering high surface area, mesoporous metal-organic frameworks electronically conductive. *ACS Appl. Mater. Interfaces*, **2017**, *9* (14), 12584-12591.
5. Kung, C.W., Audu, C. O., Peters, A. W., Noh, H., Farha, O. K, Hupp, J. T., Copper nanoparticles installed in metal-organic framework thin films are electrocatalytically competent for CO<sub>2</sub> reduction. *ACS Energy Letters*, **2017**, *2* (10), 2394-2401.
6. Audu, C. O., Nguyen, H., Chang, C., Katz, M., Mao, L., Farha, O., Hupp, J.T., Nguyen, S.T. The dual capture of As<sup>V</sup> and As<sup>III</sup> by UiO-66 analogues. *Chem Sci.* **2016**, *7* (10), 6492-6498.



7. Nguyen, H., Mao, L., Peters, A., Audu, C. O., Brown, Z., Farha, O., Hupp, J. T., Nguyen, S. T. Comparative study of titanium-functionalized UiO-66: Support effect on the oxidation of cyclohexene using hydrogen peroxide. *Catal. Sci. Technol.*, **2015**, 5 (9), 4444-4451.

### Undergraduate

8. Audu, C. O.; Pu, J. How maltose binding proteins recognize substrates: insights from computer simulations. *NCUR*. **2012** (online)

### PRESENTATIONS

1. Audu, C. O., Farha, O. K.; Hupp, J. T.; Nguyen, S. T. Sorptive Interactions in Metal-Organic Frameworks and their Versatility in Adsorbent Design. Northwestern University Industrial Associates Meeting. Evanston, IL 2018. (poster)
2. Audu, C. O., Nguyen, H., Chang, C., Katz, M., Mao, L., Farha, O., Hupp, J. T., Nguyen, S. T. Tailoring Zr-based MOFs for the chemoselective dual capture of As<sup>V</sup> and As<sup>III</sup>. 5<sup>th</sup> International conference on metal-organic frameworks & open framework compounds, Long Beach, CA, September 2016. (talk)

### ACADEMIC RELATED ACTIVITIES

- Undergraduate research mentor 2015-2018  
Project mentor – Mentored two undergraduate students on their work on using metal-organic frameworks to sequester inorganic mercury and arsenic from water. This project, continued by a third undergrad (now a Harvard graduate student), focused on improving the uptake kinetics of these toxic analytes (specifically arsenites) into the porous materials and delineating the governing adsorption mechanisms in UiO-66 MOFs.
- Science in the Classroom (SiTC) mentor and team leader 2013-2017  
Team leader – led a team of graduate students in teaching 3<sup>rd</sup> graders about scientific concepts using safe and exciting experiments.
- Lab and Lecture TA for General Chemistry and Organic Chemistry 2009-2017  
TA – As an undergrad TA, my role involved leading recitation courses and guiding students through the lab course component for the Chemistry Department, IUPUI. I continued this role as a graduate student at Northwestern university for both general chemistry courses and organic chemistry courses.

## SKILLS

- **Laboratory** – Experienced in: **(1)** synthesizing porous polymers (e.g., metal-organic frameworks, porous organic polymers) as powders or as thin films; **(2)** surface and total characterization of materials using X-ray-based techniques (i.e., XRD, EDS, and XPS), thermal gravimetric analysis (instrument manager), adsorption isotherms (via ASAP 2020 and Tristar instruments), microscopy (i.e., SEM, confocal), spectroscopy (e.g., infrared (IR), UV-VIS, ICP-OES quantitative analysis); **(3)** using quartz crystal microbalance (QCM) for analyzing thin film deposition, film thickness, and analyte diffusion rates; **(4)** simple molecule analysis using NMR spectroscopy ( $^1\text{H}$ ,  $^{13}\text{C}$ , liquid and solid phase), LCMS, GCMS, and IR spectroscopy.
- **Data analysis/computer**– Proficient with Microsoft office programs such as Word, Excel, PowerPoint, and Windows 2003-latest edition. Experienced in XPS Advantage software, Micromeritics adsorption analysis software, and Mercury (crystal structure analysis software).